UNIVERSIDAD COMPLUTENSE DE MADRID

FACULTAD DE CIENCIAS FÍSICAS

TESIS DOCTORAL

Modelling the wind flow and dispersion of reactive pollutants in cities at microscale

MEMORIA PARA OPTAR AL GRADO DE DOCTORA

PRESENTADA POR

Beatriz Sánchez Sánchez

Directores

José Luis Santiago del Río
Magdalena L. Palacios Gómez

Madrid, 2019

UNIVERSIDAD
COMPLUTENSE
MADRID

FACULTAD DE CIENCIAS FÍSICAS

TESIS DOCTORAL

MODELLING THE WIND FLOW AND DISPERSION OF REACTIVE POLLUTANTS IN CITIES AT MICROSCALE

SIMULACIÓN A MICROESCALA DEL FLUJO ATMOSFÉRICO Y DISPERSIÓN DE CONTAMINANTES REACTIVOS EN CIUDADES

Beatriz Sánchez Sánchez

Directores: José Luis Santiago del Río Magdalena L. Palacios Gómez

Tutor: Gregorio Maqueda Burgos

Mayo 2018

Agradecimientos

Me gustaría agradecer brevemente a todas las personas que me han ayudado en la realización de la tesis, y a las que estoy tremendamente agradecida porque, de una forma u otra, siempre me han brindado su apoyo para que consiguiera alcanzar mi objetivo.

Al Dr. José Luis Santiago por formarme en el ámbito de la modelización, por guiarme en el desarrollo de la tesis, por su valioso trabajo en la revisión de las múltiples versiones de la misma y, sobre todo, por su paciencia y apoyo constante.

A la Dra. Magdalena Palacios por introducirme en el campo de la química atmosférica, por sus sugerencias y consejos a la hora de elaborar la tesis así como, por su apoyo y confianza.

Al Dr. Alberto Martilli por su continua disponibilidad para resolver mis dudas e inquietudes, por su ayuda en la discusión de los resultados, por sus conocimientos transmitidos y su valiosa contribución a lo largo de este trabajo.

Al Dr. Gregorio Maqueda por introducirme en el campo de la micrometeorología y por animarme a iniciar mi camino en el mundo de la investigación, por su interés y labor a lo largo de todo este proceso.

Al Dr. Fernando Martín por acogerme en el grupo de modelización y confiar en mi trabajo.

A la Dra. Marta G. Vivanco por su disposición a ayudarme siempre que lo he necesitado.

También me gustaría agradecer a mis compañeros del grupo de Modelización y Ecotoxidad del CIEMAT por sus continuos ánimos, especialmente a Juan Luis Garrido y Esther Rivas, por animarme siempre cuando creía que no iba a acabar nunca. Y por supuesto, por todos esos cafés que siempre estábais dispuestos a tomaros conmigo para ayudarme desconectar.

Agradecer al CIEMAT por la financiación de este trabajo a través de los proyectos LIFE MINOx-STREET (LIFE12 ENV/ES/000280) y TECNAIRE-CM (S2013/MAE-2972).

Me gustaría agradecer a mis compañeros del grupo de Caracterización de la Contaminación Atmosférica y COPs por facilitarme todos los datos necesarios para realizar la validación de las simulaciones.

Dar las gracias también al grupo de investigación en Tecnologías Ambientales y Recursos Industriales (TARINDUSTRIAL) de la Universidad Politécnica de Madrid, en particular a Christina Quaassdorff, David de la Paz y al Dr. Rafael Borge, por su disponibilidad para discutir los resultados y proporcionarme todos los datos que he necesitado para realizar las simulaciones.

Me gustaría agredecer al grupo de Micrometeorología y Variabilidad Climática de la Universidad Complutese de Madrid por facilitarme los datos meteorológicos usados en la validación de las simulaciones.

Agradecer al Centro Extremeño de Tecnologías Avanzadas (CETA-CIEMAT) por permitirme usar sus recursos computacionales para realizar todas las simulaciones que constituyen este trabajo.

También me gustaría agradecer el apoyo y ánimos que siempre he recibido de ellas durante este proceso, ¡gracias amigas!

Finalmente, quiero agradecer inmensamente a mis padres y a mi hermana que siempre me hayan apoyado y animado para que consiguiera todo lo que me propusiera. Y a mi pareja, que, gracias a él, todo siempre es más fácil.

Resumen

La calidad del aire es, hoy en día, una de las principales preocupaciones ambientales en las ciudades, donde se concentra la mayor parte de la población y se registran niveles altos de contaminantes, especialmente debido al tráfico. Los NO_x (óxidos de nitrógeno), es decir, NO (óxido nítrico) y NO_2 (dióxido de nitrógeno), son unos de los contaminantes más importantes asociados asociados a las emisiones del tráfico rodado. Sin embargo, sólo está legislado el NO_2, por ser perjudicial para la salud. A pesar de las políticas medioambientales adoptadas en los últimos años, los valores límite establecidos por la Unión Europea (EU, en inglés) y la Organización Mundial de la Salud (WHO, en inglés) son ampliamente superados a lo largo de Europa, especialmente en las zonas urbanas. Por este motivo se necesita llevar a cabo estudios exhaustivos, que ayuden a gestionar y planificar estrategias de mitigación para reducir la contaminación atmosférica urbana.

La complejidad de los procesos atmosféricos en las zonas urbanas dificulta la evaluación de la calidad del aire, tanto a través de técnicas de monitorización como de modelos numéricos. El gran número de obstáculos existentes en la ciudad (edificios, vegetación, vehículos...) generan complejas distribuciones del flujo de viento en las calles. Esto unido a la heterogeneidad de las emisiones a lo largo de la ciudad, producen fuertes gradientes de concentración. Por esta razón es necesario resolver con alta resolución espacial los fenómenos atmosféricos urbanos. En este sentido, los modelos de mecánica de fluidos (CFD, en inglés), son herramientas potentes capaces de reproducir en detalle la dispersión de contaminantes en zonas urbanas. Por contra, estas simulaciones requieren un elevado número de puntos de malla (varios millones), que conlleva un alto coste computacional.

Para ese motivo, este tipo de modelos requiere millones de celdas, que permitan resolver adecuadamente los fenómenos atmosféricos urbanos. Por lo tanto, para llevar a cabo una simulación CFD es necesario disponer de altos recursos computacionales.

El objetivo de este trabajo es simular a microescala el flujo de viento y la dispersión de contaminantes reactivos en escenarios urbanos mediante un modelo CFD. La incorporación de reacciones químicas a la simulación es un gran reto en términos de modelización numérica y de recursos computacionales. En este estudio se han implementado las reacciones

químicas gaseosas más relevantes que se producen en la atmósfera urbana durante el periodo diurno. Para ello se tienen en cuenta dos mecanismos químicos: el mecanismo fotoestacionario (reacciones $NO_x{-}O_3$) y un mecanismo más complejo que incluye las reacciones con compuestos orgánicos volátiles (VOC, en inglés) (reacciones $NO_x{-}O_x{-}$VOC). En este trabajo se evalúa la importancia que tiene considerar reacciones químicas para simular adecuadamente la dispersión del NO_2, tanto en geometrías simplificadas como en escenarios reales urbanos. También se estudia el impacto que tendría incluir las reacciones químicas con VOC para simular la concentración del NO_2 en la calle. Las transformaciones químicas dependen, a través de las constantes de reacción, de las variables meteorológicas, como la radiación solar y temperatura del aire. No obstante, existen otros aspectos característicos de las zonas urbanas, como las emisiones de tráfico o la ventilación de la calle, que también afectan a la diferencia que resulta de considerar o no reacciones químicas en el modelo. Por este motivo, se analiza la dispersión de contaminantes reactivos en diferentes condiciones atmosféricas, estudiándose, tanto temporal como espacialmente, el acoplamiento de los procesos dinámicos y químicos a lo largo del periodo diurno. Los resultados muestran cómo la turbulencia y el equilibrio químico juegan un papel importante en la diferencia de concentración debida a las interacciones químicas. Por último, se presenta una aproximación numérica, basada en el uso de modelos a microescala y mesoescala, que permite obtener mapas detallados de concentración para largos periodos de tiempo. De esta manera, se amplía el alcance del uso de los modelos CFD para evaluar la calidad del aire en las ciudades. Este sistema consiste en utilizar los resultados de la simulación a mesoescala para proporcionar la variabilidad temporal de las condiciones atmosféricas a la simulación de microescala. Esto permite obtener la distribución representativa de los contaminantes en cualquier parte de la ciudad.

Por lo tanto, este trabajo contribuye principalmente a comprender el comportamiento de los procesos químicos dentro de la ciudad, teniendo en cuenta la variabilidad temporal y espacial de las condiciones atmosféricas. Los resultados obtenidos muestran diferencias significativas en la concentración del NO_2 al incluir reacciones químicas durante el periodo diurno. El alto coste computacional que requiere incluir estos procesos en la simulación acota el uso del modelo CFD a periodos cortos de tiempo (varias horas). No obstante, estas simulaciones son de gran utilidad para analizar estrategias concretas de reducción de la contaminación en zonas urbanas. Concretamente, para estudiar las condiciones atmosféricas que podrían propiciar superaciones de los valores límite horarios. Finalmente, para evaluar largos periodos de tiempo, la aproximación multiescalar de modelos desarrollada proporciona mapas fiables de concentración de contaminantes, necesarios para la gestión de calidad del aire en zonas de alta contaminación.

Abstract

Air quality is nowadays a priority environmental concern in the cities. High pollution levels have been often observed in urban areas, where both emissions and population are concentrated. The NO_x, namely NO and NO_2, are the primary traffic-related pollutants in gas-phase, but only the NO_2 is legislated given that it is the harmful to human health. Despite the environmental policies adopted in the recent years, the limit values established by the European Union (EU) and the World Health Organization (WHO) are widely exceeded across Europe, especially in urban areas. Accordingly, exhaustive studies are required to manage and plan mitigation strategies for the abatement of urban air pollution.

The complexity of atmospheric processes in urban environments hinders the assessment of air quality in the streets using both monitoring techniques and numerical models. The vast number of obstacles found in an urban area (buildings, vegetation, vehicles...) lead to complex flow patterns in the streets. Additionally, the heterogeneity of pollutant emissions, mainly from road traffic, across the city, gives rise to strong gradients of concentration. Hence the irregular distribution among buildings can only be captured by maps of high spatial resolution. In this sense, the Computational Fluid Dynamics (CFD) models are powerful tools for reproducing the dispersion of pollutants considering realistic features of urban environments.

This work focuses on simulating the wind flow and dispersion of reactive pollutants in urban environments, at microscale, using a CFD model. The implementation of chemical reactions into the CFD simulations over urban areas faces a big challenge in terms of numerical modelling and computational resources. In this study, the relevant chemical reactions in gas-phase that take place in the urban atmosphere at daytime are implemented in the model. To do that two chemical mechanisms are considered: the photostationary state (NO_x-O_3 scheme) and a condensed mechanism including Volatile Organic Compounds (VOC) (NO_x-O_x-VOC scheme).

The influence of the chemical reactions by modelling the NO_2 dispersion at street level is extensively analysed in simplified and real urban scenarios. Moreover, the impact of the VOC reactions on the NO_2 concentration is compared with the use of the NO_x-O_3

mechanism. The reaction rates are closely dependent on the meteorological parameters like the solar radiation and air temperature. Nonetheless, other urban factors, such as traffic emissions or wind flow patterns, bring about variations in the concentration of reactive pollutants. For that reason, the dispersion of reactive pollutants is, temporally and spatially, analysed in urban scenarios under numerous atmospheric conditions. As from this substantial study, the coupling of dynamical and chemical processes show how the turbulence and the chemical equilibrium in the streets can play an important role in the concentration difference caused by chemical conversions. Finally, in an attempt to improve the CFD modelling, a multiscale system is undertaken using the outputs derived from a mesoscale model to provide time-dependent boundary conditions to the microscale model. This system allows to compute the distribution of pollutant concentrations in the streets with high spatial resolution in any part of a city.

This comprehensive study contributes to a better understanding of the coupled behaviour of dynamical and chemical processes in urban environments, taking into account the temporal and spatial variability of the atmospheric conditions. The implementation of chemical reactions in the CFD model improves the accuracy of the simulated concentration of reactive pollutants in the streets. Due to the increase of computational time by including chemical reactions, the CFD model are used to reproduce the temporal variation of pollutant dispersion in a short period of time (several hours). It is especially useful for simulating the detailed distributions of the NO_2 concentration under unfavourable atmospheric conditions, in which the hourly limit values are exceeded. Moreover, the modelling approach used in this study provides reliable concentration maps for long periods of time (e.g. annual average concentration) demanded for the air quality management in urban hot-spots.

Contents

List of Symbols

A_{Em}	Emission area
A_{street}	Area of streets
A_{roof}	Area of buildings roof
C_{back}	Background concentration
C_{local}	Local concentration
C_p	Specific heat at constant pressure
C_{tot}	Total concentration
$C_{d,veg}$	Drag coefficient of vegetation
C_ε	Model constant for ε equation
C_μ	Model constant
d	Zero-plane displacement
D	Molecular diffusivity
Da	Damkhöler number
D_h	Dissipation function
g	Acceleration due to gravity
G_k	Production of turbulent kinetic energy
h_{canop}	Canopy height
H	Building height
H_0	Sensible heat flux at the surface
H_{max}	Tallest building height
i_u	Turbulence intensity
J_{NO_2}	NO_2 photolysis constant
k	Turbulent kinetic energy
k_{NO+O_3}	Rate chemical constant for the NO + O_3 reaction
K_t	Turbulent or eddy diffusivity
F_T	Total flux
F_m	Mean flux
F_t	Turbulent flux

l	Large-eddy scale
L	Obukhov length
L_{ref}	characteristic lenght scale for Re computation
NO_{T}	NO concentration as non-reactive pollutant
$NO_{2\mathrm{T}}$	NO_2 concentration as non-reactive pollutant
NO_{R}	NO concentration as reactive pollutant
$NO_{2\mathrm{R}}$	NO_2 concentration as reactive pollutant
p	Pressure
Pr_t	Turbulent Prandtl number
Q_{NO}	Source emission rate for NO
Q_{NO_2}	Source emission rate for NO_2
Re	Reynolds number
Ri	Richardson number
S	Mean strain-tensor
S_{em}	Emission flux at surface
S_h	Source or sink of heat
S_k	Source or sink of turbulent kinetic energy
S_M	Source or sink of momentum
S_{traff}	Traffic emission scenario
S_{veg,u_i}	Sink of momentum for vegetation modelling
$S_{veg,k}$	Sink of k for vegetation modelling
$S_{veg,\varepsilon}$	Sink of ε for vegetation modelling
S_ϕ	Source or sink of a scalar variable
Sc_t	Turbulent Schmidt number
t	Time
t_s	Time step
T	Temperature
T_0	Reference temperature
U	Mean velocity component
u	Instantaneous velocity
u'	Turbulent velocity component
u_*	Friction velocity
u_τ	Reference velocity (cyclic simulations)
W	Building width
W_{sect}	Wind direction sector
z	Height above a reference plane
z_0	Roughness length

α_h	Thermal diffusivity
β	Thermal expansion coefficient
β_p	Constant for vegetation modelling
β_d	Constant for vegetation modelling
ε	Turbulent dissipation rate
η	Small-eddy scale
δ_{ij}	Kronecker delta
δ_{NO}	Relative differences from non-reactive approach for NO
δ_{NO_2}	Relative differences from non-reactive approach for NO_2
θ	Potential temperature
θ_*	Scale temperature
θ_{ref}	Reference temperature
κ	Von Karman constant
λ_p	Packing density
δ_{eq}	Chemical equilibrium deviation
μ	Dynamic viscosity
μ_t	Turbulent or eddy viscosity
ν	Kinematic viscosity
ν_t	Turbulent or eddy kinematic viscosity
ρ	Air density
σ_k	Turbulent Prandtl number for turbulent kinetic energy
σ_ε	Turbulent Prandtl number for turbulent dissipation energy
σ_θ	Turbulent Prandtl number for temperature
τ	Shearing stress
τ_0	Surface shear stress or drag
τ_{turb}	Turbulent time scale
τ_{react}	Chemical time scale
φ	Zenith angle
ϕ	Scalar variable
Φ	Mean scalar component
ϕ	Turbulent scalar component
ψ	M-O similarity function for normalized velocity

List of acronyms

ABL	Atmospheric Boundary Layer
AADT	Annual Average Daily Traffic
AGL	Above Ground Level
BEP	Building Effect Parametrization
BEM	Building Energy Model
CBM-IV	Carbon Bond Mechanism IV
CCM1/2	$NO_x - O_3 -$VOC scheme with emission VOC/NO_x=1/2
CCM1/5	$NO_x - O_3 -$VOC scheme with emission VOC/NO_x=1/5
chemBM	Chemical Box Model
CHEMATA	CHEmical Mechanism Adaptation to Tropospheric Applications
CFD	Computational Fluid Dynamics
DNS	Direct Numerical Simulation
EU	European Union
EEA	European Enviromental Agency
FAC2	Factor 2
FB	Fractional Bias
LAD	Leaf Area Density
LES	Large Eddy Simulation
LST	Local Solar Time
MCM	Master Chemical Mechanism
NMSE	Normalized Mean Square Error
PDT	Plames-type passive diffusion tubes
R	Correlation coefficient
RACM	Regional Atmospheric Chemistry Mechanism
RAMS	Regional Atmospheric Model System
RANS	Reynolds-averaged Navier-Stokes
RSM	Reynolds Stress Model
RNG	Re-Normalisation Group

PBL	Planetary Boundary Layer
PSS	Photostationary state
UBL	Urban Boundary Layer
UCL	Urban Canopy Layer
VOC	Volatile organic compound
WA CFD-RANS	Weighted Average CFD-RANS methodology
WHO	World Health Organization
WRF	Weather Research and Forcasting
WRF-CHEM	Weather Research Forecasting-CHEMistry

Chapter 1

Introduction and research motivation

1.1 Urban air pollution

Air pollution is nowadays an important environmental and social issue that involves a large and complex challenge in terms of management and mitigation of harmful pollutants (EEA, 2017). The air pollutants can be directly emitted from both anthropogenic and natural sources, called primary pollutants, which in turn chemically react in the atmosphere forming secondary compounds. High pollution levels have often been observed in urban areas, where both emissions and population are concentrated. Nevertheless, the pollutant emitted in cities can be transported and travel long distances, affecting large areas as a result.

Not only has air pollution significant impact on long- and short-term health-related issues in the population, but also, it has an important economic repercussion, e.g. in the increase of medical costs. The most harmful pollutants to human health are the particulate matter, nitrogen dioxide (NO_2) and ground-level ozone (O_3). In 2014, in the European Union (EU), the estimates of the effects in health attributable to air pollution exposure were about 399 000 premature deaths, caused by the long-exposure to the fine particulate matter (PM2.5). Moreover, around 75 000 and 13 600 deaths per year were associated to the exposure to the NO_2 and O_3 respectively (EEA, 2017).

Effective air quality policies call for the cooperation at global, national and local scales in order to act against air pollution. The EU and the World Health Organization (WHO) established specific thresholds for several pollutants, and thus improve air quality and prevent the increasing effects on human health. For that matter, the WHO and EU estimate that the hourly limit value of NO_2 is 200 μg m^{-3}, while the annual average value is 40 μg m^{-3}. Even so, between 2013 and 2015, around 8% of the urban population are exposed to values of NO_2 above the established threshold. Moreover, the annual limit value of NO_2 continues to be widely exceeded across Europe, in around 10% of all the monitoring stations recording

concentrations in 2015 (EEA, 2017). Concerning the hourly limit, it was also exceeded at monitoring stations of some countries, being Spain one of them.

The procedure for reducing the impact of air pollution demands extensive knowledge of its causes. Therefore, more detailed studies are required to face the high levels of harmful pollutants recorded at monitoring stations in an attempt to establish suitable mitigation measures. Accordingly, a comprehensive study of the dynamical and chemical processes that take place in the urban atmosphere and affect air pollution is essential.

1.2 Urban Boundary Layer

The atmosphere can be classified according to the scales of motions, both spatially and temporally, into broad categories; microscale, mesoscale and macroscale, which are also commonly referred to as local, regional and global scales, respectively (Arya, 2001). Therefore, the field of meteorology that deals with the smallest processes in the troposphere is called micrometeorology.

Figure 1.1 illustrates the scales of the atmospheric phenomena and the reference time scales for each category.

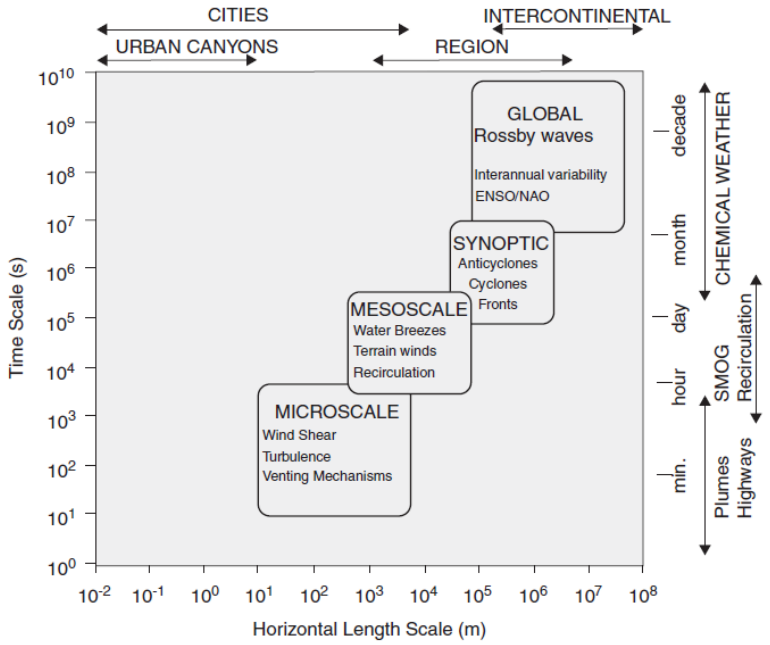

Figure 1.1: Time and spatial scales of chemical and dynamic processes in the urban atmosphere. Source: Salmond and McKendry (2009).

Micrometeorology focuses on the phenomena developed in the atmospheric layer closest to the earth's surface, known as the Planetary Boundary Layer (PBL) or Atmospheric Boundary

Layer (ABL). Thus, the PBL can be defined as the part of the troposphere that results from the interaction with the underlying surface. Hence the atmospheric processes in the PBL are primarily dominated by the exchanges of heat, momentum and mass between the atmosphere and the earth's surface.

The thickness of the PBL is fairly variable in time and space due to its entire dependence on several factors such as the wind strength, the surface roughness or the heating and cooling of the surface (Stull, 2012). Therefore, the variation of the PBL height is linked to atmospheric phenomena at different scales; from the synoptic weather conditions, like high or low pressure systems to the surface energy balance resulted from the interaction of the lowest layers with the surface features (Arya, 2001). Moreover, its temporal variability is closely related to the diurnal cycle as a result of the heating and cooling of the land surfaces, produced by solar radiation. The height and structure of the PBL can vary depending on the topography or the land use of the underlying surface resulting in the surface drag (τ_0/ρ).

Over an urban area, the flow features in the PBL are modified by the great number of obstacles comprising a city. The buildings and other structures considerably increase the surface roughness and modify the surface-energy balance as well. Accordingly, the lowest part of the atmosphere over an urban area is also known as the Urban Boundary Layer (UBL).

Figure 1.2 displays a cross section of the scales in the UBL, which is divided into the Mixing Layer and the Surface Layer. In turn, the latter involves the Inertial Sublayer and the Roughness Sublayer, in which the Urban Canopy Layer is found.

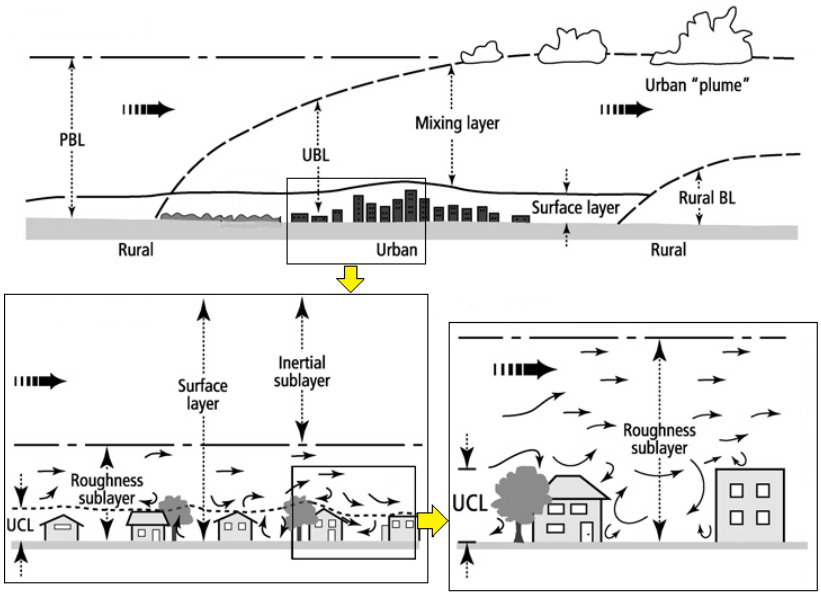

Figure 1.2: Scales of the Urban Boundary Layer. Modified from Oke (1997).

The Inertial Sublayer is a more homogeneous area, where flows are well developed and pollutants are expected to be well mixed. In air pollution, it is commonly referred to as the mixing height or depth, because the emitted pollutants are blended here, giving rise to a strong contrast with the free atmosphere (Arya, 2001). The Roughness Sublayer is characterised by intermittent motions, where the flow is still adjusting to the effects produced by the perturbations found on the surface (Britter and Hanna, 2003). And lastly, below the mean height of buildings is defined the lowest atmospheric layer, known as the Urban Canopy Layer (UCL).

The processes in the lower atmosphere are strongly influenced by the drag force exerted by urban obstacles. Moreover, the energy balance is significantly affected by the heat changes brought about by the activities associated with urban areas. The additional heat fluxes and the heat storage of the urban surface trigger the widely known urban heat island phenomenon (Britter and Hanna, 2003).

The daytime behaviour of the UBL is largely based on the physical processes caused by the wind shear and the buoyancy effects in the city. The vertical gradients of temperature tend to decrease in the roughness sublayer and reach almost zero above it, giving rise to unstable atmospheric conditions. In contrast, the UBL at night comes down on account of the strong stability that suppress the turbulent vertical mixing (Arya, 2001). Therefore, the turbulence processes together with the heat exchanges between surface and atmosphere lead to a thermal stratification of the surface layer, which is subsequently transferred to the entire mixing layer.

The Monin-Obukhov Similarity Theory established an approach to describe the mean flow profiles in a horizontally homogeneous surface layer, by means of the atmospheric stability based on the scale variables of the length, velocity and temperature.

The scale velocity is the so-called friction velocity (u_*), related to the surface drag through $\tau_0/\rho \equiv {u_*}^2$. The surface kinematic heat flux ($H_0/\rho C_p$) is expressed as $H_0/\rho C_p \equiv u_*/\theta_*$, where θ_* is the scale temperature; H_0, the sensible heat flux at the surface; ρ, the air density and C_p, the specific heat at constant pressure. Accordingly, the stability parameter (z/L) is calculated on the length scale L known as Monin-Obukhov length, which is defined as follows:

$$L = -\frac{{u_*}^3}{\kappa(g/T_0)(H_0/\rho C_p)} \tag{1.1}$$

where κ is the von Karman constant (0.4). g is the gravity and T_0, the reference temperature and, thereby, g/T_0 the buoyancy variable. In this way, the ratio z/L provides the relative importance of the buoyancy forces versus the shear effects. Therefore, positive values of z/L stand for unstable atmospheric conditions whereas negative values, do it for stable conditions.

Finally, the wind profiles over a homogeneous surface layer can be described by the following logarithmic vertical profile:

$$u(z) = \frac{u_*}{\kappa} ln \left(\frac{z}{z_0} + \psi(z/L) \right) \tag{1.2}$$

where κ is the Von Karman constant (0.4) and z_0 the roughness parameter (Arya, 2001). The expression $\psi(z/L)$ is the dimensionless function of the Monin-Obukhov theory, that is zero in neutral atmospheric conditions.

In the Inertial Sublayer over urban areas, the atmospheric processes might be adapted to the standard expressions described above (Stull, 2012). The average shear stress over the urban surface gives rise to the friction velocity, which can be used to obtain both the wind and turbulence profiles. In neutral atmospheric conditions, taking into account the effect of buildings, the wind profile is properly defined through the displacement height (d) as follows: $u(z) = \frac{u_*}{\kappa} ln \left(\frac{z-d}{z_0} \right)$.

Figure 1.3 illustrates an approximation of the logarithmic velocity profile in urban environments.

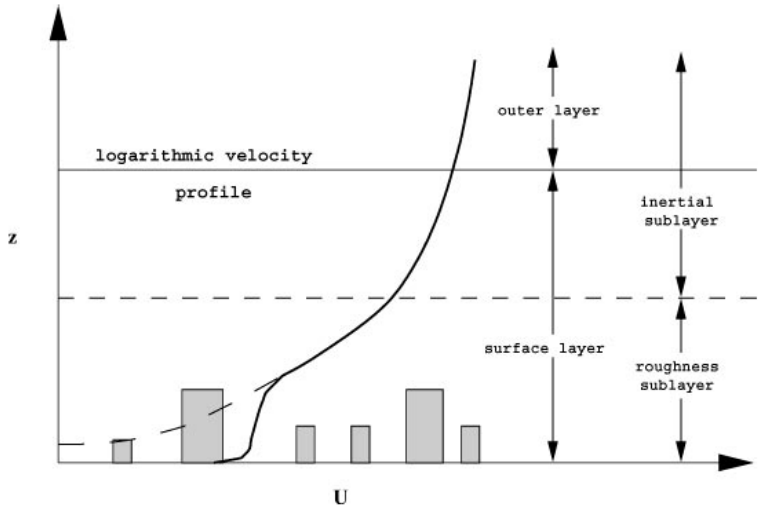

Figure 1.3: The spatially averaged mean velocity profile near an urban area. Source: Britter and Hanna (2003).

Finally, the non-uniformity of buildings layout in urban areas lead to the motions in the UCL are always in a turbulent flow regime.

1.3 Turbulence

The motions in the low atmosphere are defined by the mathematical expressions of the fundamental laws of conservation mass, momentum and energy of an incompressible

newtonian fluid. The continuity equation (Eq. 1.3) states that the divergence of velocity is zero at all times and at every point in the flow. The momentum equations (Eq. 1.4) establish that the rate of change of momentum for a fluid particle is equal to the sum of all the forces on the particle (Newton's Second Law). The energy conservation is based on the First Law of thermodynamics that can be expressed by the temperature equation (Eq. 1.5) (Versteeg and Malalasekera, 2007).

$$\frac{\partial u_i}{\partial x_i} = 0 \tag{1.3}$$

$$\frac{\partial u_i}{\partial t} + u_j \frac{\partial u_i}{\partial x_j} = -\frac{1}{\rho}\frac{\partial p}{\partial x_i} + \nu \frac{\partial^2 u_i}{\partial x_j \partial x_j} + S_M \tag{1.4}$$

$$\frac{\partial \theta}{\partial t} + u_j \frac{\partial \theta}{\partial x_j} = \alpha_h \frac{\partial^2 \theta}{\partial x_j \partial x_j} + D_h + S_h \tag{1.5}$$

where u_i is the component of velocity using the Einstein notation, where i and j is 1, 2 and 3 representing the x, y and z directions. θ is the potential temperature; t, the time; ν, the kinetic viscosity ($\nu = \mu/\rho$, where μ is the dynamic viscosity) and α_h, the thermal diffusivity. S_M is the source or sink of momentum that includes contributions due to the body forces, such as Coriolis. In the Equation 1.5, D_h stands for the dissipation function and S_h is the heat source term.

The viscosity brings about the frictional resistance between the adjacent fluid layers (Arya, 2001). The resistance force is referred to as shearing stress (τ_{ij}), which is proportional to the velocity gradient following the Newton relationship:

$$\tau_{ij} = \mu \frac{\partial u_i}{\partial x_j} \tag{1.6}$$

In the lower atmosphere, most of the physical processes are involved in a turbulent flow regime with high Reynold number (Re). In the PBL, turbulent flows typically have Re $\approx O(10^7)$ (Vilà-Guerau de Arellano et al., 2004). The Re number is expressed as UL_{ref}/ν, where U and L_{ref} are the characteristic velocity and the length scale of the mean flow. The turbulence generation might be caused either by the shear production that transforms the mean flow energy into turbulent kinetic energy (k) or by the buoyancy production due to the transformation of potential energy of unstable stratification into turbulent kinetic energy (similarly, stable stratification suppresses turbulence). The contribution of each process is determined by the Richardson number (Ri), expressed by the ratio of the buoyancy and shear terms.

$$Ri = -\frac{g}{T_0}\frac{\partial \theta / \partial z}{(\partial \mathbf{u}/\partial z)^2} \tag{1.7}$$

The turbulent flow is characterised to be highly irregular and rotational, as well as dissipative, because k is continuously dissipated by viscosity. Therefore, flow variables exhibit intermittent variations both in time and space. These fluctuations represent the turbulence contribution, which are commonly represented applying the Reynolds decomposition (Reynolds, 1895). Thus, the instantaneous variable (ϕ) of a turbulent flow is defined as the sum of the mean component ($\Phi \equiv \overline{\phi}$) and its time fluctuation (ϕ'), resulting in $\phi = \Phi + \phi'$. The mean component is calculated using $\Phi = \frac{1}{\Delta T}\int_0^{\Delta T} \phi \, dt$, where ΔT is the sampling time and, the time average of fluctuations is always zero ($\overline{\phi'} = 0$). Figure 1.4 represents the turbulent fluctuation of velocity at a local point.

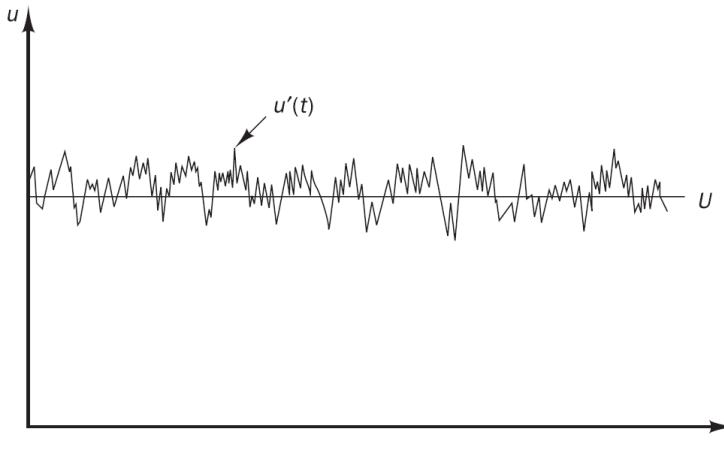

Figure 1.4: Representation of the turbulent fluctuation of the velocity at a local point. Source: Versteeg and Malalasekera (2007).

Therefore, the mean components provide information about the mean structure of the flow, and its fluctuation represents the turbulence structure. The statistical parameters calculated on the turbulent fluctuations report the exchanges processes in the turbulence structure. The variances of the simplest fluctuations of the velocity components ($\overline{u'^2}$, $\overline{v'^2}$, $\overline{w'^2}$) provide the turbulent kinetic energy through $k = \frac{1}{2}(\overline{u'^2} + \overline{v'^2} + \overline{w'^2})$. In addition, the covariances of time fluctuations ($\overline{u_i' u_j'}$, $\overline{u_i' \theta'}$...) give rise to the turbulent fluxes of momentum, heat or mass. The momentum turbulent fluxes are the result of the covariances of the velocity fluctuations in all directions, $\tau_{ij} = -\rho \overline{u_i' u_j'}$, so-called Reynolds Stress tensor. These turbulent stresses have been reported to be much larger in magnitude than the corresponding mean viscous stresses (Arya, 2001).

Turbulent flows are highly rotational and involve three dimensional vortex-like structures called **eddies**, which are characterised in a wide range of scales depending on the Re number. The characteristic parameter representative of the size of the turbulent eddies is defined by a length scale included in the Re number expression. In this way, two broad categories can be distinguished, the large-eddy scale (l) and the small-eddy scale (η). The former receives the most energy from the mean flow and l is comparable to its characteristic scale without

depending on the fluid properties. In contrast, the small-eddy scale is entirely dependent on the fluid viscosity and the energy dissipation rate (ε). From the Energy Cascade Hypothesis, the essential characteristic of the turbulence is based on a continuous transfer energy from the largest to the smallest scale of eddies. And, assuming the Kolmogorov Hypothesis, the small-scale length is exclusively dependent on $\eta = \nu^{3/4}\varepsilon^{-1/4}$.

1.4 Gas-phase chemistry in urban environments

The urban atmospheric composition is mainly dominated by the incoming air mass to the city, the local emissions associated to the human activities and the chemical processes that take place (Bloss, 2009). All together affect not only the primary emitted pollutants, but also the secondary species formed in short-timescale by chemical reactions. The key pollutants in the urban atmosphere are mostly the nitrogen oxides (NO_x), namely NO (nitric oxide) and NO_2, carbon monoxide (CO) and volatile organic compounds (VOC) and, also, the particulate matter. The concentration of these pollutants are basically dominated by exhaust emissions and the releases from industrial or domestic activities. Figure 1.5 shows the main sources of NO_x, where the road transport sector is the largest contributor, and CO and VOC are mainly emitted from the commercial and industrial sectors, respectively (EEA, 2017).

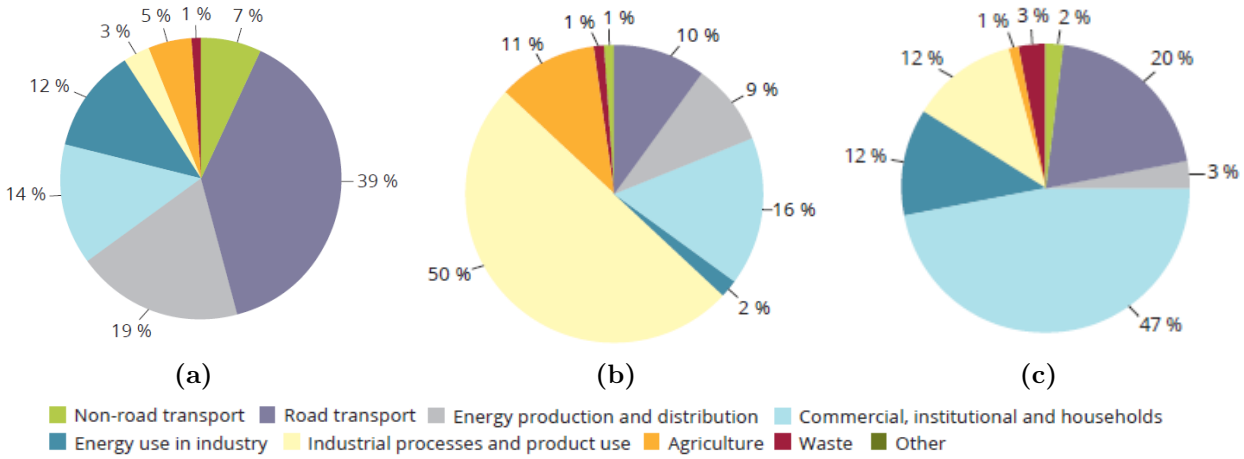

Figure 1.5: Percentage of the source emissions of (a) NO_x, (b) VOC (non-methane) and (c) CO. Source: EEA (2017).

At local scale, the dynamical processes in urban environments play an important role in air composition due to the different time scales of chemistry and turbulence. The turbulent processes can be faster than the chemical reaction. Thus, only the rapid chemical conversions have influence on the pollutant concentrations in the streets. Hence, the reactivity of the compounds is primarily dependent on the turbulent processes, which dominate the mixing

of pollutants. It particularly occur close to the sources where the largest concentrations are found (Vilà-Guerau de Arellano et al., 2004).

The chemical processes in an urban area are fundamentally related with the NO and NO_2. Therefore, the dominant chemical mechanism is the photostationary state that is constituted by the following reactions:

$$O + O_2 + M \longrightarrow O_3 + M \tag{R1}$$

$$O_3 + NO \xrightarrow{k_{NO+O_3}} NO_2 + O_2 \tag{R2}$$

$$NO_2 + h\nu \xrightarrow{J_{NO_2}} NO + O \tag{R3}$$

where J_{NO_2} is the photolysis constant and k_{NO+O_3} the reaction rate constant. M represents a molecule that absorbs the excess of energy without reacting and, thereby, stabilizes the formed ozone (O_3) (Seinfeld and Pandis, 1998). This three-reaction system has timescales of a few minutes or less in daylight conditions in mid-latitude (Bloss, 2009). The reaction R1 is the relevant source of O_3 in the atmosphere and, once formed, the O_3 reacts with NO and regenerates NO_2 (reaction R2). The oxygen atom (O) formed from the NO_2 photolysis (reaction R3) disappears as fast as the reaction R1 occurs since the O is very reactive.

This $NO_x - O_3$ scheme will reach the point where the NO_2 destroyed is reformed so fast that the steady-state cycle is maintained (Seinfeld and Pandis, 1998). The Leighton Relationship represents the chemical equilibrium as follows:

$$\frac{[O_3][NO]}{[NO_2]} = \frac{J_{NO2}}{k_{NO+O_3}} \tag{1.8}$$

This relation determines the anticorrelation between the NO_2 and O_3. It can be clearly observed in urban areas close to the emissions, where the high levels of NO_x, simultaneously lead to the minimum values of O_3 in air.

In addition to the $NO_x - O_3$ system, the NO and NO_2 are involved in chemical conversions with other compounds found in the atmosphere, such as the hydroxyl radical (OH). The OH formation is caused by the reaction of a water molecule and an excited oxygen atom, which was previously produced by the O_3 photolysis in the free atmosphere. The OH is the main oxidant in the atmosphere and, it is the trigger of starting the degradation of the most of organic compounds. In this way, the OH may react with CO or with VOC, turning out the formation of hydroperoxil (HO_2). In presence of NO_x, the HO_2 reacts with NO producing NO_2 and again OH:

$$HO_2 + NO \longrightarrow NO_2 + OH \tag{R4}$$

The intermediate reactions resulting from the interaction of VOC with OH produce organic peroxy radicals that by reacting with the NO also produce NO_2. And thus, this chain drives to the HO_2 formation and the subsequent reaction R4. Finally, this rise of NO_2, without losing O_3 (reaction R2), leads to an increase of O_3 production by the photolysis of NO_2. Figure 1.6 illustrates a simplified scheme of the relevant chemical reactions that involves the NO_x and VOC. Note that the main sink of NO_x in an urban area is the nitric acid (HNO_3) that disappear by rapidly changing to a condense phase (Bloss, 2009).

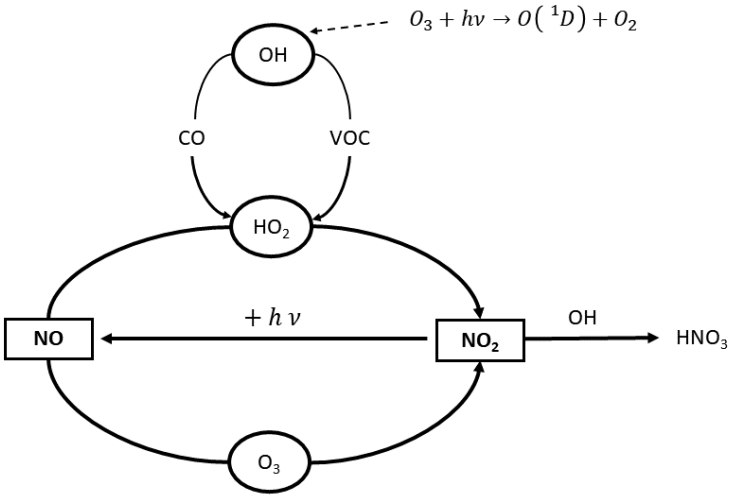

Figure 1.6: Simplified scheme of the reactions involving the NO_x, HO_x and VOC.

In urban environments, the O_3 production can be related either by an airmass rich in O_3 that reaches the city from elsewhere or by the local sources of O_3 precursors: VOC or NO_x. The regime of the O_3 production is dependent on the response of the O_3 to the changes in the abundance of NO_x or VOC. If the O_3 production depends on the increase or decrease of the VOC levels, the O_3 generation is defined as VOC-limited. That occurs with high NO_x levels, the rate of O_3 formation increases both with the CO or VOC levels and with the formation rate of HO_x. However at low NO_x levels, which usually occurs moving further away from the city center, the O_3 formation barely varies with the VOC levels. It is due to the NO_x is the limiting reactant and, the response of the O_3 production is controlled by the NO_x behaviour and, thereby, this system is termed NO_x-limited.

Figure 1.7 shows the diagram of O_3 production as function of the dominate regime. It noteworthy that the O_3 formation by the contribution of NO_x and VOC is highly dependent on the local atmospheric composition, in terms of the NO_x and VOC levels, and the meteorological variables (Bloss, 2009).

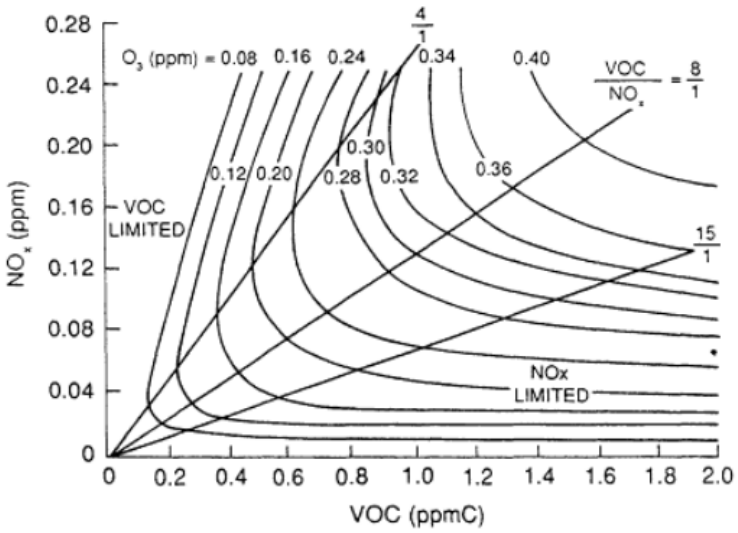

Figure 1.7: At local scale the tendency of production of O_3 by the NO_x and VOC contribution. Source: Council et al. (1992).

As mentioned before, the chemical time scale is important on the understanding of the chemical processes in the urban environments. Typically, the time scales of the reactions involved in the $NO_x - O_3$ photostationary state are around minutes, whereas the O_3 production can range at larger scales (Bloss, 2009). Even so, the influence of the VOC reactions on the O_3 formation in urban areas is primarily dependent on the VOC levels and the NO_x levels of the city, as well as the dynamical behaviour of the flow in the streets.

1.5 Management of urban air quality

The emitted pollutants undergo significant changes caused by the atmospheric processes that take place in the urban atmosphere. In addition, the urban obstacles can improve or worse the dispersion of pollutants giving rise to strong concentration gradients in the streets. All of these factors modulate the air quality in urban areas, which is an important concern for the local and regional governments. Therefore, exhaustive studies are required in an attempt not to exceed the hourly and annual limit values established for pollutants in air. To that end, the understanding of the atmospheric processes that trigger off periods of high concentration levels in the city is needed. Moreover, representative maps of dispersion of pollutants in the streets are very helpful for the appraisal of the annual average concentration. For that reason, the assessment of urban air pollution is tackled from multiple channels in order to establish the most effective strategies for reducing it and mitigating the effects thereof.

Figure 1.8 shows a simple scheme of the procedure to be followed for the management of urban air quality.

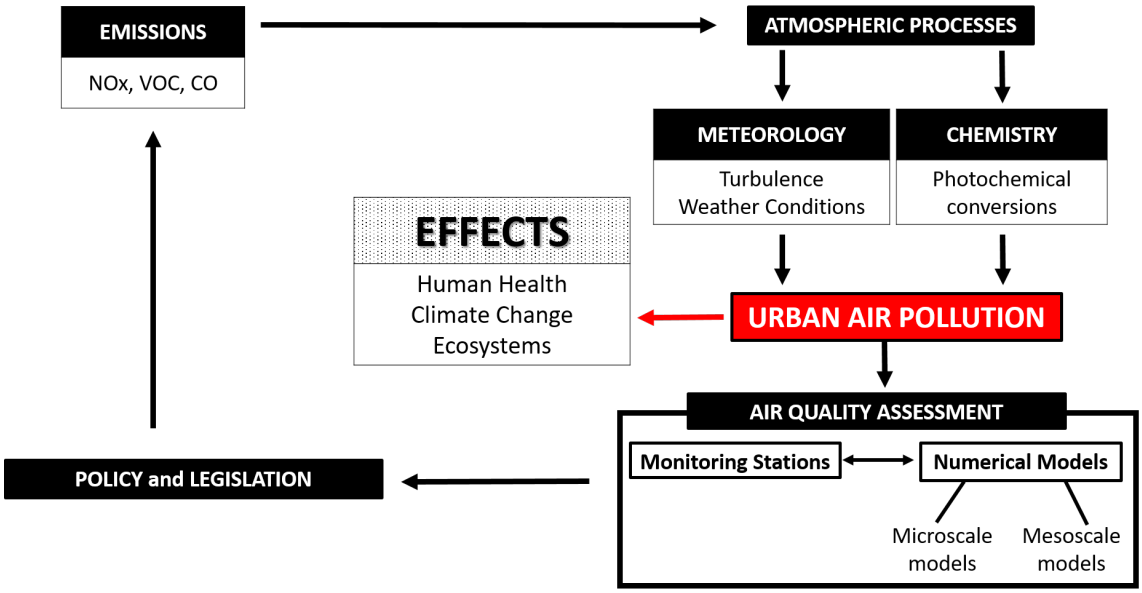

Figure 1.8: Scheme of the management to improve urban air quality.

At city scale, the research methods used to evaluate urban air pollution are fundamentally based on monitoring stations deployed throughout the city and numerical models developed to simulate the relevant processes of the urban atmosphere.

The **monitoring techniques** are based on several air quality stations that record most pollutants all over the city. The advantage of the experimental data is that these provide the actual values of several species at each location. However, their spatial representativeness is limited. And covering the entire city is not feasible since it would entail a big investment in devices and huge outlay. Therefore, the local networks of air quality monitoring stations cannot capture the strong heterogeneities of the distribution of pollutants in the streets.

The lack of spatial information can be complemented with **modelling techniques**. Several numerical models at regional and local scales are used to better understand the physical and chemical processes in urban environments. The **mesoscale models** provide both the dynamical phenomena and the chemical conversions at city scale with a spatial resolution around 1 km^2. Some meteorological mesoscale models are the Weather Research and Forcasting (WRF) or the Regional Atmospheric Model System (RAMS). They provide the meteorological inputs to the mesoscale chemistry-transport models such as the Community Multiscale Air Quality Model (CMAQ), WRF-CHEM, or CHIMERE models so as to complete the pollutants dispersion given by the transport and chemical transformations. These models are suitable for studying large areas or even several countries, and they are able to identify the hot-spots in the city.

However, the buildings, parks, vehicles, tunnels or other components of the city produce irregular patterns of flow and dispersion of pollutants within the area of 1 km^2. To address the

problem, **microscale models**, such as the Computational Fluid Dynamics (CFD) models, can be used to solve the turbulent flow equations at higher spatial resolution (order of meters) in order to reproduce in detail the atmospheric processes in the urban canopy layer. For that reason, performing a CFD simulation demand a large computational load and, thereby, they are used to model short periods of time (several hours). Currently, the CFD models are widely used to investigate specific aspects that affect urban air quality.

Figure 1.9 displays the full system of research methods for the urban air quality assessment. Whereas a mesoscale model provides a value of concentration in 1 km x 1 km, the CFD models resolve in that resolution a detailed distribution of the pollutant concentrations. Subsequently, these results can be evaluated with high precision against the local measurements at the specific point.

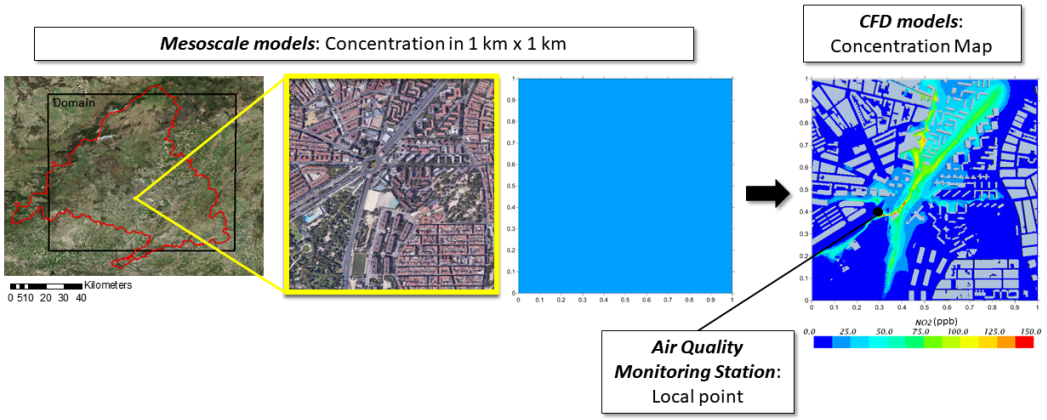

Figure 1.9: Multiscale system of the research methods for urban air quality assessment.

1.6 Research motivation and objectives

Modelling urban meteorology and air quality with high resolution is a growing need. The spatial resolution of CFD simulations provides detailed maps of atmospheric variables in urban areas that are validated at the measurements locations. In a city, this valuable information can be used to assess the dispersion of pollutants at street level and, thus, to determine the pedestrian exposure to urban air pollution. It is really helpful for taking mitigation measures against the high levels of pollutant concentrations in specific areas, e.g. redistribution of the traffic in the streets or planning new strategies in the urban vegetation layout.

The first studies using CFD models were focused on examining the urban atmospheric processes in isolated streets in an attempt to save computational time. Hence the importance of the most relevant processes in the dispersion of pollutants has been extensively studied, e.g. thermal effects, chemical reactions, street configurations, traffic emissions and meteorological

variables (Vardoulakis et al., 2003; Li et al., 2006; Zhong et al., 2016). The influence of the buildings geometry on the ventilation of the street (Santiago and Martin, 2005) as well as the thermal effects on the wind circulations below the canopy (Sini et al., 1996) are widely analysed. Moreover, other components of urban environments can affect the dispersion in the street, e.g. the urban vegetation or the turbulence induced by vehicles. The former brings on both an aerodynamic impact on the flow and a deposition effect reducing the air pollution (Abhijith et al., 2017; Buccolieri et al., 2018). As for the effect of vehicles, their motion increase the turbulence in the street improving the mixing of pollutants (Solazzo et al., 2008). Additionally, the production or loss caused by the chemical reactions on the pollutant concentrations are thoroughly studied in simplified geometries using different chemical mechanisms (Baker et al., 2004; Baik et al., 2007; Bright et al., 2013). Therefore, the composition of the traffic emissions is also an important aspect in the concentration of reactive pollutants (Kwak and Baik, 2012).

However, for reliable and meaningful modelling of pollutant dispersion in urban areas, it is sometimes necessary to perform studies at urban neighbourhood rather than at street canyon scale (Gromke and Blocken, 2015). The rapidly development of the computational resources promotes the use of CFD models to understand the behaviour of atmospheric processes in real urban environments (Blocken et al., 2012; Kwak et al., 2015). Nonetheless, CFD simulations need still be optimized in order to find the best compromise between computational time and accuracy of the results.

The levels of NO_2 in urban environments, mainly caused by the vehicle emissions, are one of objectives to be tackled in the management of urban air quality. Thus far, CFD modelling over urban areas is commonly addressed to study the dispersion of non-reactive pollutants (Amorim et al., 2013; Sanchez et al., 2017; Santiago et al., 2017a). Nevertheless, in case of the NO_2, the fastest chemical reactions can be important in the accuracy of modelling its concentration at street level. The implementation of chemical reactions in the CFD simulation leads to an important rise of computational time. Hence the need to in-depth understand the impact of the chemical interactions on the concentration of pollutants in real streets. This has not been fully addressed in previous studies and, therefore, an exhaustive study about the influence of atmospheric conditions on chemical reactions is essential.

This research is aimed at simulating with high spatial resolution the dynamical and chemical processes that take place in the urban atmosphere using a CFD model. To that end, the most relevant chemical reactions, in gas-phase, for the NO_2 at daytime are implemented in the model. Therefore, the importance of including chemical reactions on modelling the dispersion of pollutants in the streets can be tackled. Additionally, a modelling approach is presented to face the challenge of obtaining detailed maps of concentration over several days. It is worth noting that all simulated results are carefully validated with the available

experimental data in every setting.

The main purpose of this research is achieved by fulfilling the following objectives:

- *The implementation of chemical reactions in the CFD model*: The three-reaction system (NO_x-O_3 reactions) and a more complex chemical mechanism of 23 reactions and 25 species (NO_x-O_x-VOC reactions) are both included in the CFD model. And the chemical terms are evaluated with a chemical box model.
- *The estimation of the resulting error by modelling the NO_2 dispersion under a non-reactive approach instead of using a chemical mechanism*: The deviation in the NO_2 concentration is properly assessed in several urban settings under multiple atmospheric conditions.
- *The analysis of the impact of meteorological variables on the dispersion of reactive pollutants*: The variability of the atmospheric conditions is exhaustively analysed in both simplified geometries and real urban scenarios.
- *The evaluation of the coupled behaviour of turbulent processes and chemical conversions in an urban setting*: The influence of turbulence in the street on the reaction rate is thoroughly examined, both in time and space, in a real urban scenario.
- *The new development of a modelling approach using a meteorological mesoscale and a CFD models in order to obtain detailed concentration maps over long period in real urban areas*: This methodology can be applied in any place of a city and its validation is carried out in an urban hot-spot.

The present work is broken down into chapters that achieve the above-mentioned objectives. The complex system of mathematical expressions and the turbulence closure of the CFD model is fully described in Chapter 2. The implementation of chemical reactions in the CFD model and the subsequent comparison with a chemical box model are also herein explained. Lastly, the procedure to be followed in order to undertake a CFD simulation over urban areas is described in detail. In Chapter 3, the NO_2 dispersion is modelled using the two chemical mechanisms in idealized geometries under different atmospheric conditions. In this way, the impact of specific meteorological scenarios on the chemical activity is analysed through the NO and NO_2 concentrations. It provides quantitative information that helps to select the optimal chemical scheme in terms of computational requirements. In Chapter 4, the influence of the atmospheric chemistry on the NO_2 concentration is evaluated over time throughout a diurnal cycle in a real urban scenario. In this analysis, the coupled behaviour of the chemical and dynamical processes is thoroughly studied. Finally, the ability of CFD models to assess the dispersion of pollutants over long periods of time using a modelling approach is studied in Chapter 5.

Chapter 2

The CFD-RANS model

2.1 Introduction

The application of CFD models become largely used for environmental flows in a great variety of fields, e.g urban air quality and meteorology (Vardoulakis et al., 2003), wind and thermal comfort (Mochida and Lun, 2008), effects of urban vegetation (Buccolieri et al., 2018), emergency response (Antonioni et al., 2012), indoor/outdoor climate design (Zhai and Chen, 2005) and renewable energy such as wind energy (Li et al., 2012).

The main objective of this chapter is to present a brief review of the mathematical equations resolved by the CFD model. Additionally, the procedure to be followed is thoroughly described including each new contribution to simulate the urban atmosphere. Finally, the statistic metrics and the acceptance criteria for an accurate evaluation of modelling results are also presented herein.

This research is carried out using a commercial CFD model (STARCCM+ from SIEMENS) which has been modified in order to include additional phenomena such as the vegetation effects and atmospheric chemistry.

2.2 Governing equations

CFD models are based on the motion equations for the fluid described by the fundamental laws of conservation of mass, momentum and energy expressed by the following equations (Versteeg and Malalasekera, 2007):

$$\frac{\partial u}{\partial x} + \frac{\partial v}{\partial y} + \frac{\partial w}{\partial z} = 0 \tag{2.1}$$

$$\frac{\partial u}{\partial t} + u\frac{\partial u}{\partial x} + v\frac{\partial v}{\partial y} + w\frac{\partial w}{\partial z} = -\frac{1}{\rho}\frac{\partial p}{\partial x} + \nu\,\nabla^2 u + S_{M_x} \tag{2.2}$$

$$\frac{\partial v}{\partial t} + u\frac{\partial u}{\partial x} + v\frac{\partial v}{\partial y} + w\frac{\partial w}{\partial z} = -\frac{1}{\rho}\frac{\partial p}{\partial y} + \nu\,\nabla^2 v + S_{M_y} \tag{2.3}$$

$$\frac{\partial w}{\partial t} + u\frac{\partial u}{\partial x} + v\frac{\partial v}{\partial y} + w\frac{\partial w}{\partial z} = -\frac{1}{\rho}\frac{\partial p}{\partial z} + \nu\,\nabla^2 w + S_{M_z} \tag{2.4}$$

$$\frac{\partial \theta}{\partial t} + u\frac{\partial \theta}{\partial x} + v\frac{\partial \theta}{\partial y} + w\frac{\partial \theta}{\partial z} = -\alpha_h \nabla^2 \theta + S_h \tag{2.5}$$

where ρ is the air density, ν is the kinematic viscosity related to the dynamic viscosity (μ) through $\nu = \mu/\rho$, α_h is the thermal diffusivity (or molecular diffusivity of heat). S_M represents the momentum source for each component x, y, z and S_h is the source term of heat. The Equation 2.1 represents the mass continuity equation in three dimensions. The Equations 2.2-2.4 are the momentum equations widely known as Navier-Stokes equations. And the energy equation (Eq. 2.5) is expressed by means of the transport of temperature.

The atmospheric processes in urban environments are mainly characterized by the turbulent phenomena (Section 1.3). In a turbulent flow, the appearance of eddies with a wide range of length and time scales produce dynamically complex processes (Versteeg and Malalasekera, 2007). Therefore, the mathematical expressions have to be solved applying different numerical methods. There are several models that are able to resolve the turbulent flow equations. Depending on the computational load required, they can be classified from more to less requirements as: the Direct Numerical Simulation (DNS) model, the Large Eddy Simulation (LES) model and the Reynolds-averaged Navier-Stokes equations (RANS) model.

- **The DNS model**: It numerically solves the flow equations without considering any modelling assumption (Coceal et al., 2007). It means that both the mean flow and all turbulent fluctuations of velocity are computed in the simulations. The unsteady Navier-Stokes equations are solved on very fine spatial grids and with time steps sufficiently small to resolve the fastest fluctuations (Versteeg and Malalasekera, 2007). Therefore, DNS simulations require a large computational load that prevents their use in complex geometries, like urban areas, with the current resources.

- **The LES model**: This model involves a spatial filtering operation of the fluid dynamics equations prior to the computations, which tracks the behaviour of larger eddies. The method consists of solving the mean flow and the large eddies. And the effects caused by the smaller structures are included through the so-called sub-grid scale model. Hence, the flow variables are decomposed in the resolved or filtered component (large scale) and the unresolved or sub-filtered component (small scale).

- **The RANS model**: This numerical method is based on resolving the mean flow and the turbulence fluctuations that appear as additional terms in the time-averaged flow equations. To do that, the turbulent terms are not directly computed by the model, but they are parametrized adding a turbulence closure (Versteeg and Malalasekera, 2007).

The main difference between LES and RANS models is that the former need to perform a time-average concentration in order to recover the mean component, which involves simulating a long period of time. In contrast, RANS models directly provide the mean value with no need to do the time average. As for computing requirements, the LES model requires a great volume of calculations demanding a great storage and, thereby, its computational time is fairly large. In contrast, the RANS model does not directly solve the small-scale turbulent fluctuation. It gives a solution for the mean flow variables and, thereby, substantially reduces its computational cost. Tominaga and Stathopoulos (2010) concluded that the RANS method underestimates the turbulent diffusion near the obstacle in comparison with the LES model. Although for mean velocity, the difference between the LES and RANS results are small. Despite the difference in the convergence methods between LES and RANS, they estimated the computational time of LES was around 25 times longer than the RANS model used. This aspect is a very important issue to be considered by modelling flow equations in complex geometries. Santiago et al. (2010) and Dejoan et al. (2010) compared the dispersion of a tracer in an array of obstacles between the LES and RANS results with experimental field data. They concluded that the mean concentration was similar between modelling results and both of them were in a good agreement with the measurements. The main discrepancies between models were close to the edge of the plume due to the effects of small fluctuations. Hence, the LES model provides very accurate results in areas where the instantaneous fluctuations are more relevant. However, the outputs are similar for the mean values evaluated in points further away from the proximity of walls or ground.

The fact that CFD-RANS models require moderate computational load makes them an effective tool to solve the turbulent flow equations in urban environments. Therefore, the CFD-RANS approach is selected to carry out this work.

2.2.1 The Reynolds-averaged Navier-Stokes model

A CFD-RANS model is based on the Reynolds-averaged Navier-Stokes equations that takes into account the time average of the fluid dynamics equation and the turbulence effects on the mean flow properties. By applying the Reynolds decomposition (Section 1.3) to the instantaneous variables of turbulent flow, turns out the addition of the mean component (U, V, Φ...) and its time fluctuation (u', v',ϕ'...):

$$u = U + u' \tag{2.6}$$

$$v = V + v' \tag{2.7}$$

$$w = W + w' \tag{2.8}$$

$$\phi = \Phi + \phi' \tag{2.9}$$

where ϕ represents a scalar variable. If the instantaneous variables in the equations (Eqs. 2.1-2.4) are replaced by the previous definition, result in the so-called Reynolds-averaged Navier-Stokes equations:

$$\frac{\partial U}{\partial x} + \frac{\partial V}{\partial y} + \frac{\partial W}{\partial z} = 0 \tag{2.10}$$

$$\frac{\partial U}{\partial t} + U\frac{\partial U}{\partial x} + V\frac{\partial V}{\partial y} + W\frac{\partial W}{\partial z} = -\frac{1}{\rho}\frac{\partial P}{\partial x} + \nu\,\nabla^2 U + \frac{1}{\rho}\left[\frac{\partial(\overline{u'^2})}{\partial x} + \frac{\partial(\overline{u'v'})}{\partial y} + \frac{\partial(\overline{u'w'})}{\partial z}\right] + S_{M_x} \tag{2.11}$$

$$\frac{\partial V}{\partial t} + U\frac{\partial U}{\partial x} + V\frac{\partial V}{\partial y} + W\frac{\partial W}{\partial z} = -\frac{1}{\rho}\frac{\partial P}{\partial y} + \nu\,\nabla^2 V + \frac{1}{\rho}\left[\frac{\partial(\overline{u'v'})}{\partial x} + \frac{\partial(\overline{v'^2})}{\partial y} + \frac{\partial(\overline{v'w'})}{\partial z}\right] + S_{M_y} \tag{2.12}$$

$$\frac{\partial W}{\partial t} + U\frac{\partial U}{\partial x} + V\frac{\partial V}{\partial y} + W\frac{\partial W}{\partial z} = -\frac{1}{\rho}\frac{\partial P}{\partial z} + \nu\,\nabla^2 W + \frac{1}{\rho}\underbrace{\left[\frac{\partial(\overline{u'w'})}{\partial x} + \frac{\partial(\overline{v'w'})}{\partial y} + \frac{\partial(\overline{w'^2})}{\partial z}\right]}_{Reynolds\ Stress\ tensor} + S_{M_z} \tag{2.13}$$

Using the Einstein notation, the momentum equations can be rewritten as follows:

$$\frac{\partial U_i}{\partial x_i} = 0 \tag{2.14}$$

$$\frac{\partial U_i}{\partial t} + U_j\frac{\partial U_i}{\partial x_j} = -\frac{1}{\rho}\frac{\partial P}{\partial x_i} + \frac{\partial}{\partial x_j}\left[\nu\frac{\partial U_i}{\partial x_j}\right] - \frac{1}{\rho}\frac{\partial \overline{u_i'u_j'}}{\partial x_j} + S_{M_{x_i}} \tag{2.15}$$

The six additional terms, $\tau_{ij} = -\rho\overline{u_i'u_j'}$, comprise the **Reynolds stress tensor**. Based on the Newton's law of viscosity, the viscous stress are taken to be proportional to the rate of deformation of fluid elements. Thus, the Boussinesq hypothesis about eddy viscosity and eddy diffusivity proposed that the Reynolds stress are proportional to the mean strain-rate tensor (Boussinesq, 1877).

$$\tau_{ij} = -\rho\overline{u_i'u_j'} = \mu_t\left(\frac{\partial U_i}{\partial x_j} + \frac{\partial U_j}{\partial x_i}\right) - \frac{2}{3}\rho k\delta_{ij} \tag{2.16}$$

where the **mean strain-rate tensor** (S_{ij}) is:

$$S_{ij} = \frac{1}{2}\left(\frac{\partial U_i}{\partial x_j} + \frac{\partial U_j}{\partial x_i}\right) \tag{2.17}$$

The **turbulent kinetic energy** (k) is defined as $k = \frac{1}{2}\overline{u_i' u_i'}$ and the **turbulent or eddy viscosity** (μ_t) is related to the turbulent or eddy kinematic viscosity as $\nu_t = \mu_t/\rho$, which needs to be determined[‡].

For a scalar variable, the transport equation is expressed as follows:

$$\frac{\partial \Phi}{\partial t} + U_j \frac{\partial \Phi}{\partial x_j} = D\frac{\partial^2 \Phi}{\partial x_j \partial x_j} - \frac{\partial \overline{u_j' \phi'}}{\partial x_j} + S_\phi \tag{2.18}$$

The terms on the left-hand side represents the rate of change and the convective term. On the right-hand side, the first term stands for the diffusive term, where D is the molecular diffusivity. The second term denotes the turbulent transport and the last one, S_ϕ, the source of the scalar.

The turbulent fluxes of any scalar variable, like heat or mass, are also considered proportional to the gradient of the mean value of the scalar transported.

$$-\rho\overline{u_i' \phi'} = K_t \frac{\partial \Phi}{\partial x_i} \tag{2.19}$$

where K_t is the **turbulent or eddy diffusivity**. This parameter for heat and mass is expected to be analogous to the eddy viscosity μ_t for momentum since the turbulent transport of these variables are also controlled by same mechanism of eddy mixing. Therefore, the eddy diffusivity for mass and heat are defined as:

$$K_t = \frac{\mu_t}{\sigma_t} \tag{2.20}$$

where σ_t stands for the turbulent Prandtl number (Pr_t) for heat or the turbulent Schmidt number (Sc_t) for mass.

Therefore, the closure issue is reduced to solve the distribution of μ_t and, for that, it is necessary a turbulence model to resolve the turbulent terms of the RANS equations. The common turbulence closures are classified depending on the number of additional equations needed to solve the RANS flow equations (Versteeg and Malalasekera, 2007). The most simplest model with no extra equation is the **mixing length model**. The main assumption is that the Reynolds stress and the viscous stress are proportional to the fluid deformation

[‡]The second term in Eq. 2.16 includes the Kronecker delta (δ_{ij}=1 if i=j and $\delta_{ij} = 0$ if $i \neq j$)

rate through the turbulent viscosity (μ_t) as proportionality constant. The **Reynolds Stress Model** (RSM) is the most complex model with six additional equations, one for each Reynold stress, which increases the computational load. Finally, an intermediate turbulence model in terms of numerical complexity is the ***k*-ε model**. It only adds two more equations for the turbulent kinetic energy (k) and the turbulent dissipation rate (ε) that are solved together with the RANS equations.

The k-ε turbulence closure is selected in this work for being the most appropriate model that optimise the computing resources without losing accuracy in solving the turbulent processes. It is commonly used for modelling urban air quality (Kim and Baik, 2004; Solazzo et al., 2008; Kwak and Baik, 2012).

2.2.2 The *k*-ε turbulence model

The k-ε turbulence model assumes that the Reynolds stress is proportional to the rate of deformation of fluid elements and, the turbulent viscosity is the proportionality constant for the Reynold stress. This approach is based on modelling two transport equations for the turbulent kinetic energy (k) and for the turbulent dissipation rate (ε). On the basis of the k-ε approach, there are several turbulence closures primarily focused on solving the computation of the effective viscosity and the ε transport equation. The most common turbulence closures are: the Standard k-ε, the Realizable k-ε and the Re-Normalisation Group (RNG) k-ε.

The turbulence closure used in this work is the **Realizable *k*-ε**. It improves the Standard k-ε using the turbulent viscosity deduced by a new analytical expression and the ε equation derived from an exact equation for the transport of the mean-square vorticity fluctuation. Thus, the turbulent viscosity is defined as follows (Shih et al., 1995):

$$\mu_t = \rho C_\mu \frac{k^2}{\varepsilon} \tag{2.21}$$

Unlike the Standard k-ε closure, the parameter C_μ is not constant. It is defined by $C_\mu = 1/(A_0 + A_s U^{(*)} \frac{k}{\varepsilon})$, where $A_0 = 4$, $A_S = \sqrt{6}cos(\xi)$ and $U^{(*)}=\sqrt{\mathbf{S}:\mathbf{S} - \mathbf{W}:\mathbf{W}}$. $\mathbf{S}$ is the mean strain-rate tensor, $\mathbf{W}$ is the rotation rate tensor and $\xi = 1/3\ \mathrm{acos}(\sqrt{6}W)$.

Finally, the governing equations for the **Realizable *k*-ε** model are the following:

$$\frac{\partial k}{\partial t} + u_j \frac{\partial k}{\partial x_j} = \frac{1}{\rho}\frac{\partial}{\partial x_j}\left[\left(\mu + \frac{\mu_t}{\sigma_k}\right)\frac{\partial k}{\partial x_j}\right] + \frac{G_k}{\rho} - \varepsilon + S_k \tag{2.22}$$

$$\frac{\partial \varepsilon}{\partial t} + u_j \frac{\partial \varepsilon}{\partial x_j} = \frac{1}{\rho}\frac{\partial}{\partial x_j}\left[\left(\mu + \frac{\mu_t}{\sigma_\varepsilon}\right)\frac{\partial \varepsilon}{\partial x_j}\right] + C_{\varepsilon 1} S\varepsilon - C_{\varepsilon 2}\frac{\varepsilon^2}{k + \sqrt{\nu\varepsilon}} + S_\varepsilon \tag{2.23}$$

where $\sigma_k = 1$ and $\sigma_\varepsilon = 1.2$ are the turbulent Prandtl numbers for k and ε respectively and $C_{\varepsilon 2}$ is a model constant equal to 1.9. These values for the model constants are shown to be the most suitable for a wide range of turbulent flow at microscale (Launder and Spalding, 1974). The term G_k represents the production of turbulent kinetic energy that is defined as $G_k = \mu_t^2 S^2$, where S is the modulus of the mean strain-rate tensor ($S \equiv \sqrt{2S_{ij}S_{ij}}$) and the constant $C_{\varepsilon 1} = \max\left[0.43, \frac{\eta}{\eta+5}\right]$, with $\eta = S\,k/\varepsilon$.

In words, the terms on the left hand side of the Eqs. 2.22-2.23 represent the rate of change and the convective transport of k and ε. On the right hand side, the first term is the transport of k and ε by diffusion and, the following two terms the production and destruction of k and ε, accordingly. S_k and S_ε represent the source term of k and ε respectively. The differences with other k-ε models are mainly in the production and destruction terms of the ε equation (Eq. 2.23). The present form of the production term is considered to better represent the energy transfer. Unlike other models, the destruction term of ε never vanishes, even if k becomes small values or zero.

From the solution of k and ε, the length scale (l) and the time scale (τ_t) of the turbulence processes can be defined as (Pope, 2001):

$$l = k^{3/2}/\varepsilon \tag{2.24}$$

$$\tau_{turb} = k/\varepsilon \tag{2.25}$$

2.2.3 The Boussinesq approximation

In non-neutral atmospheric conditions, the thermal effects are important and, thereby, the buoyancy terms are included in the CFD model. By considering the air as an incompressible fluid, the Boussinesq assumption consists of the difference between the actual fluid density ρ and the standard aerostatic density ρ_n is small: $|\rho - \rho_n|/\rho << 1$. The use of ρ_n as reference density instead of the actual density produce an error in the description of the inertial forces. In this way, this difference $\rho - \rho_n$ may be important in the description of the gravitational body forces. The Boussinesq approximation holds for the most of the environmental applications in the lower atmosphere (Sini et al., 1996). The density deviation $\rho - \rho_n$ is related to the potential temperature (θ) through the equation of state as follows:

$$\frac{\rho - \rho_n}{\rho_n} = -\beta(\theta - \theta_n) \tag{2.26}$$

where β is the thermal expansion coefficient and it is defined inversely proportional to temperature. Hence, the buoyancy force is defined by $F_{buoyancy} = \rho g \beta(\theta_{ref} - \theta)$, where $g_i = (0, 0, -g)$.

Finally, the flow equations including the buoyancy forces are expressed as:

$$\frac{\partial U_i}{\partial x_i} = 0 \tag{2.27}$$

$$\frac{\partial U_i}{\partial t} + U_j \frac{\partial U_i}{\partial x_j} = -\frac{1}{\rho}\frac{\partial P}{\partial x_i} + \frac{\mu}{\rho}\frac{\partial^2 U_i}{\partial x_j \partial x_j} - \frac{\partial}{\partial x_j}(\overline{u_i' u_j'}) - \rho g_i \beta(\theta_{ref} - \theta) + S_{M_{x_i}} \tag{2.28}$$

$$\frac{\partial \Theta}{\partial t} + U_j \frac{\partial \Theta}{\partial x_j} = \alpha_h \frac{\partial^2 \theta}{\partial x_j \partial x_j} - \frac{\partial \overline{u_j' \theta'}}{\partial x_j} + S_h \tag{2.29}$$

Concerning the turbulence closure, the equations for k and ε are (Hanjalic and Launder, 1972):

$$\frac{\partial k}{\partial t} + U_j \frac{\partial k}{\partial x_j} = \frac{1}{\rho}\frac{\partial}{\partial x_i}\left[\left(\mu + \frac{\mu_t}{\sigma_k}\right)\frac{\partial k}{\partial x_j}\right] + \frac{G_k}{\rho} + \beta g_i \frac{\mu_t}{\sigma_\theta}\frac{\partial \theta}{\partial x_j} - \varepsilon + S_k \tag{2.30}$$

$$\frac{\partial \varepsilon}{\partial t} + U_j \frac{\partial \varepsilon}{\partial x_j} = \frac{1}{\rho}\frac{\partial}{\partial x_j}\left[\left(\mu + \frac{\mu_t}{\sigma_\varepsilon}\right)\frac{\partial \varepsilon}{\partial x_j}\right] + C_{1\varepsilon} S\varepsilon + C_{1\varepsilon}\frac{\varepsilon}{k}\beta\, g_i \frac{\mu_t}{\sigma_\theta}\frac{\partial \theta}{\partial x_j} - C_{2\varepsilon}\frac{\varepsilon^2}{k + \sqrt{\nu\varepsilon}} + S_\varepsilon \tag{2.31}$$

where σ_θ is the turbulent Prandtl number for the temperature.

Table 2.1: Summary of equations using the CFD-RANS model with the k-ε turbulence closure.

Continuity	$\frac{\partial U_i}{\partial x_i} = 0$
Momentum equations	$\frac{\partial U_i}{\partial t} + U_j \frac{\partial U_i}{\partial x_j} = -\frac{1}{\rho}\frac{\partial P}{\partial x_i} + \frac{\mu}{\rho}\frac{\partial^2 U_i}{\partial x_j \partial x_j} - \frac{\partial}{\partial x_j}(\overline{u_i' u_j'}) - g_i \beta(\theta - \theta_n) + S_{M_{x_i}}$
Energy equation	$\frac{\partial \Theta}{\partial t} + U_j \frac{\partial \Theta}{\partial x_j} = k\frac{\partial^2 \theta}{\partial x_j \partial x_j} - \frac{\partial \overline{u_j' \theta'}}{\partial x_j} + S_h$
Transport equation	$\frac{\partial \Phi}{\partial t} + U_j \frac{\partial \Phi}{\partial x_j} = D\frac{\partial^2 \Phi}{\partial x_j \partial x_j} - \frac{\partial \overline{u_j' \phi'}}{\partial x_j} + S_\phi$
k-ε turbulence model	
Turbulent kinetic energy	$\frac{\partial k}{\partial t} + U_j \frac{\partial k}{\partial x_j} = \frac{1}{\rho}\frac{\partial}{\partial x_j}\left[\left(\mu + \frac{\mu_t}{\sigma_k}\right)\frac{\partial k}{\partial x_j}\right] + \frac{G_k}{\rho} + \beta g_i \frac{\mu_t}{\sigma_\theta}\frac{\partial \theta}{\partial x_j} - \varepsilon + S_k$
Turbulent dissipation rate	$\frac{\partial \varepsilon}{\partial t} + U_j \frac{\partial \varepsilon}{\partial x_j} = \frac{1}{\rho}\frac{\partial}{\partial x_i}\left[\left(\mu + \frac{\mu_t}{\sigma_\varepsilon}\right)\frac{\partial \varepsilon}{\partial x_j}\right] + C_{1\varepsilon} S\varepsilon + C_{1\varepsilon}\frac{\varepsilon}{k}\beta\, g_i \frac{\mu_t}{\sigma_\theta}\frac{\partial \theta}{\partial x_j} - C_{2\varepsilon}\frac{\varepsilon^2}{k + \sqrt{\nu\varepsilon}} + S_\varepsilon$

Therefore, the CFD model used in this work is based on the Reynolds-averaged Navier-Stokes equations with the Realizable k-ε turbulence closure. Table 2.1 summarizes the equations to be solved using the CFD-RANS model. These governing equations are discretized by means of the finite volume method in order to be solved using the segregated method. The pressure-velocity coupling is solved by means of Semi-Implicit Method for Pressure-Linked Equations algorithm (SIMPLE). It is based on an iterative process that includes a solution to a Pressure-Correction equation to ensure mass conservation (Patankar, 1980).

2.3 Chemical Mechanisms

The most important reactions of the gas-phase chemistry for the NO_x in urban environments are implemented in the CFD model.

The NO_x chemistry is mainly dominated by the photostationary state involving the NO_x-O_3 interactions. However, there are many other pollutants in the urban atmospheric composition that may interact with NO_x, e.g. the VOC. For that reason, a condensed chemical mechanism involving the relevant interactions of VOC in an urban atmosphere is developed. Accordingly, the two chemical mechanisms implemented in the CFD-RANS model are: the NO_x-O_3 scheme and the reduced NO_x-O_x-VOC scheme.

2.3.1 The NO_x-O_3 scheme

The photostationary state is the most simple chemical mechanism implemented in the CFD-RANS model:

$$NO_2 + h\nu \xrightarrow{J_{NO_2}} NO + O \tag{R5}$$

$$O + O_2 + M \longrightarrow O_3 + M \tag{R6}$$

$$O_3 + NO \xrightarrow{k_{NO+O_3}} NO_2 + O_2 \tag{R7}$$

The steady-state cycle using the NO_x-O_3 scheme is maintained (Section 1.4) and, thereby, the O_3 concentration is related to the NO and NO_2 as follows:

$$[O_3] = \frac{J_{NO2}[NO_2]}{k_{NO+O_3}[NO]} \tag{2.32}$$

The square brackets ([ ]) stands for the concentration of pollutants in ppb (part per billion) or $\mu g\,m^{-3}$ [§]. The photolysis rate constant, J_{NO_2}, is dependent on the zenith solar angle (φ)

[§]In atmospheric conditions of 1 atm and T=298 K: 1 ppb of NO= 1.25 $\mu g\,m^{-3}$, 1 ppb of NO_2= 1.88 $\mu g\,m^{-3}$ and 1 ppb of O_3 = 2 $\mu g\,m^{-3}$

and is defined by $J_{NO_2} = A \exp(B/\cos\varphi)$ (s^{-1}). And the thermal constant rate (k_{NO+O_3}) is computed as $k_{NO+O_3} = A \exp(-(E/R)/T)$ ($ppb^{-1}\ s^{-1}$), where T is air temperature and A, B and E/R are chemical constants established for each chemical reaction (Table 2.3).

2.3.2 The NO_x-O_x-VOC scheme

The chemical processes in the atmosphere involve a vast number of chemical reactions. The most complete chemical scheme is the Master Chemical Mechanism (MCM) with 4531 species and 12691 reactions for representing the degradation of 123 primary VOC species (Saunders et al., 2003; Jenkin et al., 2003). It is highly detailed and it is not feasible to incorporate it in the air quality models because demands a very large computational load. Gery et al. (1989) developed a condensed chemical mechanism focused on urban and regional photochemistry named the Carbon Bond Mechanism IV (CBM-IV) with 33 species and 82 chemical reactions. Stockwell et al. (1997) also presented other chemical mechanism developed to be used in the air quality models known as the Regional Atmospheric Chemistry Mechanism (RACM) which consists of 77 species and 237 reactions.

In any case, these chemical mechanisms are computationally expensive to be implemented in the CFD-RANS model and to carry out many simulations. For that reason, a condensed NO_x-O_x-VOC mechanism has been developed taking into account the VOC reactions without increasing too much the computational time. This NO_x-O_x-VOC scheme has been reduced from the RACM as far as possible without losing much accuracy. It is performed during 30 minutes of simulation for urban conditions in a chemical box model. To that end, the software CHEMATA (CHEmical Mechanism Adaptation to Tropospheric Applications) is used (Junier et al., 2005; Kirchner, 2005). A wide set of different urban pollution conditions was investigated. Special emphasis was given to cases where the results for the RACM mechanism considerably differ from the results of the photostationary steady state.

The species list of the NO_x-O_x-VOC scheme is shown in Table 2.2.

Table 2.2: List of species

Species of the NO_x-O_x-VOC scheme	
O_3	ozone
NO	nitrogen oxide
NO_2	nitrogen dioxide
HNO_3	nitric acid
CO	carbon monoxide
SO_2	sulfur dioxide
N_2	nitrogen
O_2	oxygen
H_2O	water vapour
H_2	hydrogen
O^1D	excited state oxygen atom
HO	hydroxyl radical
HO_2	hydroperoxyl
HCHO	formaldehyde
PAN	peroxyacetyl nitrate
ONIT	organic nitrate
MO_2 (CH_3O_2)	methyl peroxy radical
ACO_3 ($RC(O)O_2$)	acetyl peroxy and higher saturated acyl peroxy
XO_2	accounts for additional NO to NO_2 conversions
XO_2N	accounts for additional NO to NO_2 conversions
ALK	lumping group of alkanes RACM group
OLE	lumping group of olefin RACM group
ARO	lumping group of aromatic RACM group
RACM species used in new integrated species	
Alkanes	
CH_4	methane
ETH	ethane
HC3	alkanes, alcohols, esters, and alkynes †
HC5	alkanes, alcohols, esters, and alkynes *
HC8	alkanes, alcohols, esters, and alkynes **
Olefins	
ETE	ethene
OLT	terminal alkenes
OLI	internal alkenes
Aromatic	
TOL	toluene
XYL	xylene
Radicals	
RO_2	organic peroxy radical

†with HO rate constant (298 K, 1 atm) less than $3.4{\cdot}10^{-12}$ cm^3 s^{-1}

*with HO rate constant (298 K, 1 atm) between than 3 $.4{\cdot}10^{-12}$ cm^3 s^{-1} and $6.8{\cdot}10^{-12}$ cm^3 s^{-1}

**with HO rate constant (298 K, 1 atm) greater than $6.8{\cdot}10^{-12}$ cm^3 s^{-1}

Three main manners of the mechanism reduction are applied:

- Modification of the lumping groups: Several chemical RACM lumping groups are united to a new lumping group. For example, the RACM alkanes (ETH, HC3, HC5 and HC8) are summed up in the new species ALK. The RACM olefins (ETE, OLT and OLI) are lumped to the new specie OLE and the RACM aromatic compounds, TOL and XYL, are integrated in the new species ARO.

- Modification of the organic peroxy radical parametrisation: instead of using the 20 RACM RO_2 species, the approach described by Kirchner (2005) is applied for the RO_2 species CH_3O_2 (called MO_2) and $RC(O)O_2$ (called ACO_3), as well as for the two operator species, XO_2 and XO_2N, which work in the following way shown bellow. The real reactions:

$$\mathrm{R{-}H + HO \longrightarrow R^* + H_2O} \tag{R8}$$
$$\mathrm{R^* + O_2 \longrightarrow RO_2} \tag{R9}$$
$$\mathrm{RO_2 + NO \longrightarrow a\ RONO_2 + b\ (RO + NO_2)} \tag{R10}$$
$$\mathrm{RO \longrightarrow Products} \tag{R11}$$

  are parameterised by:

$$\mathrm{R{-}H + HO \longrightarrow a\ XO_2N + b\ (XO_2 + products)} \tag{R12}$$
$$\mathrm{XO_2 + NO \longrightarrow NO_2} \tag{R13}$$
$$\mathrm{XO_2N + NO \longrightarrow RONO_2} \tag{R14}$$

- Elimination of reactions and species which are not crucial for simulating under the given conditions (time of about 30 minutes, urban pollution conditions, daytime). Focusing on daytime simulations, the species NO_3 (nitrate radical) and all its reactions are eliminated because of the NO_3 is rapidly photolyzed in presence of light (Finlayson-Pitts and Pitts Jr, 1999). Also, low reactive species as methane (CH_4) and H_2 can be eliminated under urban conditions.

The resulting $NO_x{-}O_x{-}$VOC scheme consists of 23 species and 25 chemical reactions involved in Table 2.3. Compared to the $NO_x{-}O_3$ scheme, it includes the peroxy radical production from VOC, CO and SO_2 as well as NO_x loss processes by the formation of PAN, HNO_3 and organic nitrates. Whereas the peroxy radical production increases the NO_2/NO ratio and, thus, the NO_2 concentrations, the NO_x loss processes decrease NO_x and, therefore, NO_2 concentrations. As well, O_3 loss by the reaction with olefins is considered.

This condensed chemical mechanism is particularly developed for this work with aim of optimizing the computational time by undertaking the CFD-RANS simulations.

Table 2.3: The $NO_x - O_x - VOC$ scheme: The rate constants of first order reactions are calculated on $J = A * \exp(B/\cos\varphi)$ (s^{-1}). The rate constants for the second order reactions called "thermal" by $k = A * \exp[(-E/R)/T]$, for the "Troe" reactions by $k_{reac} = \{k_0(T)[M])/(1 + (k_0(T)[M]/k_\infty(T))\}0.6^{\{1+[log_{10}(k_0(T)[M]/k_\infty(T))]^2\}^{-1}}$, and for the "troe-equilibrium" by $k = Aexp(-B/T) \times \{k_0(T)[M]/(1 + (k_0(T)[M]/k_\infty(T)))\} \cdot 0.6^{\{1+\log_{10}[k_0(T)[M]/k\infty(T)]^2\}^{-1}}$, where $k_0(T) = {k_0}^{300}(T/300)^{-n}$ and $k_\infty(T) = {k_\infty}^{300}(T/300)^{-m}$. The units of the second order reactions are $cm^3\ s^{-1}$.

NO_2	NO + O_3	photodissociation (A=1.45E-2, B=-0.4)
O_3	O^1D	photodissociation (A=1.48E-4, B=-1.65)
HCHO	CO	photodissociation (A=6.65E-5, B=-0.6)
HCHO	CO + 2 HO_2	photodissociation (A=5.40E-5, B=-0.79)
ALD	CO + HO_2 + MO_2	photodissociation A=1.35E-5, B=-0.94
$O^1D + N_2$	O_3	thermal(A=1.80E-11, E/R=-110.0)
$O^1D + O_2$	O_3	thermal(A=3.20E-11, E/R=-70.0)
$O^1D + H_2O$	2 HO	thermal(A=2.20E-10, E/R=0.0)
HO + NO_2	HNO_3	troe(${k_0}^{300}$=2.60E-30,n=3.2, ${k_\infty}^{300}$=2.40E-11, m=1.3)
HO_2 + NO	NO_2 + HO	thermal(A=3.70E-12, E/R=-250.0)
O_3 + NO	NO_2	thermal(A=2.00E-12, E/R=1400.0)
HO + SO_2	HO_2	troe(${k_0}^{300}$=3E-31,n=3.3, ${k_\infty}^{300}$=1.50E-12, m=0)
CO + HO	HO_2	K = 1.5d-13*(1.+2.439e-20*airc)
ALK + HO	0.931 XO_2 + 0.842 HO_2 + 0.011 CO + 0.011 HO + 0.019 HCHO + 0.051 MO_2 + 0.378 ALD + 0.096 XO_2N	thermal(A=8.05E-12, E/R=237.0)
OLE + HO	1.001 XO_2 + 0.998 HO_2 + 1.011 HCHO + 0.002 ACO_3 + 0.747 ALD	thermal(A=5.69E-12, E/R=-474.5)
ARO + HO	0.950 XO_2 + 0.950 HO_2 + 1.860 ALD + 0.050 XO_2N	thermal(A=5.35E-12, E/R=-355.0)
ALD + HO	ACO_3	thermal(A=5.55E-12, E/R=-331.0)
HCHO + HO	HO_2 + CO	thermal(A=1.00E-11, E/R=0.0)
OLE + O_3	0.344 HO_2 + 0.383 CO + 0.303 HO + 0.135 XO_2 + 0.682 HCHO + 0.092 MO_2 + 0.007 ACO_3 + 0.630 ALD	thermal(A=1.28E-15, E/R=907.1)
NO_2 + ACO_3	PAN	troe(${k_0}^{300}$=9.70E-29, n=5.6,${k_\infty}^{300}$=9.30E-12, m=1.5)
PAN	NO_2 + ACO3	troe-equil (${k_0}^{300}$=9.70E-29, n=5.6, ${k_\infty}^{300}$=9.30E-12, m=1.5, A=1.16E28, B=13954.)
XO_2 + NO	NO_2	thermal(A=4.00E-12, E/R=0.0)
MO_2 + NO	NO_2 + HO_2 + HCHO	thermal(A=4.20E-12, E/R=-180.0)
ACO_3 + NO	NO_2 + 0.046 HO_2 + 0.046 CO + 0.954 MO_2	thermal(A=2.00E-11, E/R=0.0)
XO_2N + NO	0.939 ONIT	thermal(A=4.45E-12, E/R=-39.9)

2.4 Modelling reactive pollutants

2.4.1 Transport equation

Modelling a reactive pollutant requires to include the chemical term in the transport equation. These additional terms represent the formation and depletion, depending on the chemical reactions in which the reactant appears. Hence, the transport equation is added in the CFD-RANS for each compound (ϕ_i) as follows:

$$\frac{\partial \phi_i}{\partial t} + U_i \frac{\partial \phi_i}{\partial x_j} = D \frac{\partial^2 \phi_i}{\partial x_j \partial x_j} + \frac{\partial}{\partial x_j}\left(K_c \frac{\partial \phi_i}{\partial x_j}\right) + \Delta\phi_i\Big)_{Chem} + S_{\phi_i} \tag{2.33}$$

where ϕ_i is the concentration of the *ith* specie and D and K_c are molecular diffusivity and eddy diffusivity for mass, respectively. The chemical term, $\Delta\phi_i\Big)_{Chem}$, is modelled as the rate of production or loss of each chemical compound depending on the chemical mechanism. The chemical term of the NO_2 using the photostationary state is written as:

$$[\Delta \mathrm{NO_2}]_{Chem} = -\mathrm{J_{NO2}}[\mathrm{NO_2}] + \mathrm{k_{NO+O_3}}[\mathrm{NO}][\mathrm{O_3}] \tag{2.34}$$

In contrast, in the $NO_x{-}O_x{-}$VOC scheme, its chemical term increases as a consequence of the number of chemical reactions (i) in which the NO_2 intervenes. Therefore, its chemical term in the transport equation increases as:

$$[\Delta \mathrm{NO_2}]_{Chem} = -\mathrm{J_{NO2}}[\mathrm{NO_2}] \pm \sum_i k_i \mathrm{R_A\, R_B} \tag{2.35}$$

where $\mathrm{R_A}$ and $\mathrm{R_B}$ are the reactants of the *ith* chemical reaction involving the production or loss of NO_2.

The same numerical solver for resolving the governing equations is used to model the dispersion of reactive pollutants. The terms in each transport equation, including the chemical terms, are solved with a second-order discretization. Therefore, to properly solve the transport considering chemical reactions, a sensitivity test of the time step required is evaluated using the $NO_x{-}O_3{-}$VOC scheme in a single street-canyon (Sanchez et al., 2016). The concentration of reactive pollutants is analysed for different time steps (0.1 s, 1 s and 2 s). During the first period of the simulation, the turbulent dynamic is simulated at a time step of 1 s, without including chemical interactions. After that, the chemical reactions are implemented in the CFD simulation carrying out every time step case (t_s =0.1 s, t_s = 1 s and t_s = 2 s). Finally, in the steady state, the deviation of concentration was computed from the case t_s = 1 s, and the the differences are lower than 0.007 % in comparison with

t_s=0.1 s (Sanchez et al., 2016). Therefore, the time step of 1 s was considered appropriate to solve both the turbulence and chemical reactions through the CFD-RANS model.

In terms of computational time, modelling reactive pollutants increases the time required not only caused by the additional chemical terms in the transport equation, but also with the number of coupled transport equations. The estimated time for modelling NO_2 as a reactive pollutant, with the NO_x-O_3 scheme, instead of a non-reactive in urban areas might approximately reach a factor 1.5, whereas might be four times as much using the NO_x-O_x-VOC scheme. It is noteworthy that it is an approximation because it also depends on the number of grid points, the complexity of the domain and the available computational resources.

2.4.2 Box model validation

The implementation of a chemical scheme in the CFD model is evaluated with the chemical box model (chemBM) used to developed the NO_x-O_x-VOC scheme. To that end, the CFD model is also run as a box model using the NO_x-O_x-VOC scheme using a time step of 1 s. The same conditions both in the CFD model and in the chemical box model are used to perform the simulation for 30 min. The chemical constants are calculated with a constant air temperature T=293 K and a zenith angle fixed in $\varphi = 40°$. The imposed initial conditions are based on concentrations similar to atmospheric conditions and traffic emissions of an urban area (Table 2.4).

Table 2.4: Initial values of concentration of pollutants in ppb.

NO	5	OLE	1
NO_2	12	ALK	2
O_3	20	H_2O	10^7
CO	300	O_2	$2.095\ 10^8$
HCHO	0.1	N_2	$7.808\ 10^8$
ARO	1		

Figure 2.1 displays the time evolution and the scatter plots of several pollutants resulted from the chemical box model and the CFD model.

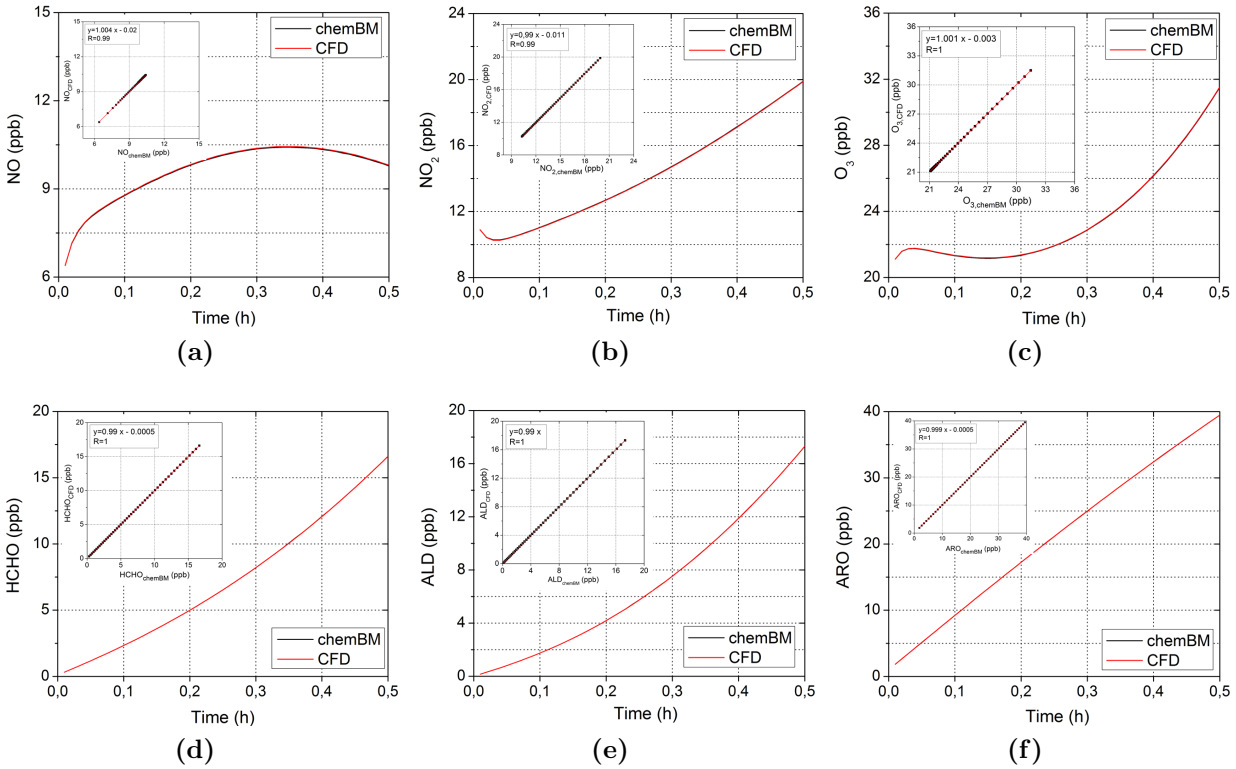

Figure 2.1: Time series and scatter plots of NO, NO_2, O_3, HCHO, ALD and ARO (in ppb) from the chemical box model and from the CFD model.

The results obtained from the CFD model are practically the same that the outputs of the chemical box model. Indeed, the maximum relative errors of concentration for NO, NO_2 and O_3 are respectively 0.28 %, 0.18 % and 0.085 %, associated to simple numerical errors. Therefore, the chemical terms included in the transport equations are appropriately solved by the CFD model.

2.4.3 Chemical and turbulent time scales

The pollutants dispersion in urban environments is mainly dominated by the turbulent processes. In addition, the reaction rate is dependent on the ability of the turbulence to mix the reactants in the PBL (Vilà-Guerau de Arellano et al., 2004). The relation between the turbulent mixing and the chemical reactions is given by the Damkhöler number (Da), which is defined by the ratio of their corresponding time scales.

$$Da = \frac{\tau_{turb}}{\tau_{react}} \tag{2.36}$$

τ_{turb} represents the time scale of the turbulent processes and τ_{react} the time scale of the chemical reactions. Da < 1 means that the chemical processes are relatively slow respect to the turbulent phenomena and, the species become well mixed more rapidly than the chemical

reaction take place. Values of Da$\approx O(1)$ represent that the turbulence is not efficient enough to properly blend the reactants, being able to affect the chemical balance. For Da > 1, the influence of the chemical reactions grows in importance against the turbulent phenomena.

As previously defined, the turbulent time scale can be computed by the turbulent kinetic energy, k, and its dissipation rate, ε, as follows (Pope, 2001):

$$\tau_{turb} \equiv \frac{k}{\varepsilon} \tag{2.37}$$

Concerning the chemical time scale, for a first-order reaction, it is computed by means of the photolysis rate as $\tau_{react} = (J_i)^{-1}$. For a second-order chemical reaction, the time scale is expressed as $\tau_{react} = (k_i R_i)^{-1}$, where k_i is the reaction rate of the *ith* chemical reaction and R_i the concentration of the reactant in that reaction. To compute the Da number in a chain of chemical reactions, the characteristic time scale is obtained from the slowest chemical reaction.

Additionally, the behaviour between the turbulent processes and the chemical activity is influenced by the chemical equilibrium (Jonker et al., 2004). The reactive species tend to reach a chemical balance between the loss and production of the compounds involved in the chemical mechanism. Nevertheless, in urban environments, the continuous emissions on the surface give rise to a permanent perturbation of the chemical state of the overlying air.

2.5 Modelling urban vegetation

The urban vegetation is an important component that affects the dispersion of pollutants in the streets. In fact, the impact of vegetation in urban areas and its use as mitigation measure for urban air pollution is actually matter of debate. The motivation is related to the complex processes that make difficult to draw general conclusions due to the high dependency on the local conditions. Several modelling techniques, particularly through the CFD, are being applied to study the impact of the urban vegetation on the dispersion of pollutants (Vos et al., 2013; Gromke and Blocken, 2015; Jeanjean et al., 2015; Santiago et al., 2017c; Abhijith et al., 2017). The impact of vegetation is caused by aerodynamic effect, modifying the flow, and by the deposition effect, removing pollutants from air through their deposition on the leaves. Several studies have found that the aerodynamic effect is larger than the pollutants removal by deposition (Vos et al., 2013; Santiago et al., 2017b; Buccolieri et al., 2018).

In the CFD-RANS model, the vegetation is considered as a porous medium, which is limited to simplified geometries of the real trees located in the streets. Its aerodynamic effect is modelled as a sink of momentum caused by the drag force exerted that lead to a sink and

source of k and ε (Santiago et al., 2017b). Hence, these extra terms are added to the equations of momentum (S_{veg,u_i}), turbulent kinetic energy ($S_{veg,k}$) and dissipation rate ($S_{veg,\varepsilon}$).

$$S_{veg,u_i} = -\rho \,\mathrm{LAD}\, C_{d,veg}\, |U| u_i \tag{2.38}$$

$$S_{veg,k} = \rho \,\mathrm{LAD}\, C_{d,veg}\, \left(\beta_p |U|^3 - \beta_d\, |U| k\right) \tag{2.39}$$

$$S_{veg,\varepsilon} = \rho \,\mathrm{LAD}\, C_{d,veg} \left(C_{\varepsilon 4}\, \beta_p \frac{\varepsilon}{k} |U|^3 - C_{\varepsilon 5} \beta_d |U| \varepsilon\right) \tag{2.40}$$

$|U|$ is the magnitude of wind speed and u_i is the wind component in i direction. LAD is the leaf area density of vegetation, which depends on the type of trees (evergreen or caduceus) and, in general terms, on the season. $C_{d,veg}$ is the drag coefficient of vegetation (0.2). β_p is the fraction of the mean kinetic energy converted into k by the drag and takes values between 0 and 1. Based on previous studies (Santiago et al., 2013, 2017b), β_p is equal to 1. The constant β_d is a dimensionless coefficient for the turbulence cascade short-circuiting and $C_{\varepsilon 4}$ and $C_{\varepsilon 5}$ ($C_{\varepsilon 4} = C_{\varepsilon 5}$) are based on the following analytical expressions (Sanz, 2003):

$$\beta_d = C_\mu^{1/2} \left(\frac{2}{\alpha}\right)^{2/3} \beta_p + \frac{3}{\sigma_k} \tag{2.41}$$

$$C_{\varepsilon 4} (= C_{\varepsilon 5}) = \sigma_k \left(\frac{2}{\sigma_\varepsilon} - \frac{C_\mu^{1/2}}{6} \left(\frac{2}{\alpha}\right)^{2/3} (C_{\varepsilon 2} - C_{\varepsilon 1})\right) \tag{2.42}$$

where the constant α is 0.5 (Dalpé and Masson, 2009). For the vegetation expression, the values of C_μ and $C_{\varepsilon 1}$ are regarded as constant values, 0.09 and 1.44 respectively.

2.6 Features on modelling urban areas

To perform a CFD simulation over urban areas requires to follow a determined procedure related to the urban geometry and the computational domain (Section 2.6.1). The first step in the CFD simulation is the geometry of the computational domain. In real urban areas, the complexity of the geometry increases and there are too many obstacles to be designed (buildings, trees, tunnels and so on). After that, the domain is meshed with the appropriate type of cell and also the proper grid resolution. Both steps are carried out bearing in mind the optimization of the CFD simulation in order not to increase too much the number of grid points. Lastly, the features of boundary conditions are selected in the domain.

Modelling the atmospheric processes requires to carry out several assumptions explained in Section 2.6.2. In addition, the implementation of the road traffic emissions are described in Section 2.6.3.

2.6.1 Geometry, mesh and boundary conditions

The size of the computational domain is related to the geometry features of the area of interest and the boundary conditions that will be imposed. The COST Action 732 report (Franke, 2007) encompasses the basic guidelines for performing CFD simulations applied to micrometeorology. The height of the domain top should be at least at 4-5H_{max} above the roof, where H_{max} is the tallest building height. This prevents the influence of the top in the study area. For small blockage, it is acceptable to establish the top of the domain at $4H_{max}$ and for larger blockage around $10H_{max}$. In urban areas, with a vast number of buildings, the vertical extension is recommended to impose it at $5H_{max}$. The lateral extension is dependent on the height of the obstacles and, besides, on the boundary conditions of the flow. In urban areas, the lateral boundaries should be placed at $5H_{max}$ to the buildings region in order not to affect the solution in the research area (Fig. 2.2a). For that reason, commonly, the CFD domain is horizontally reduced to size about 1 km x 1 km.

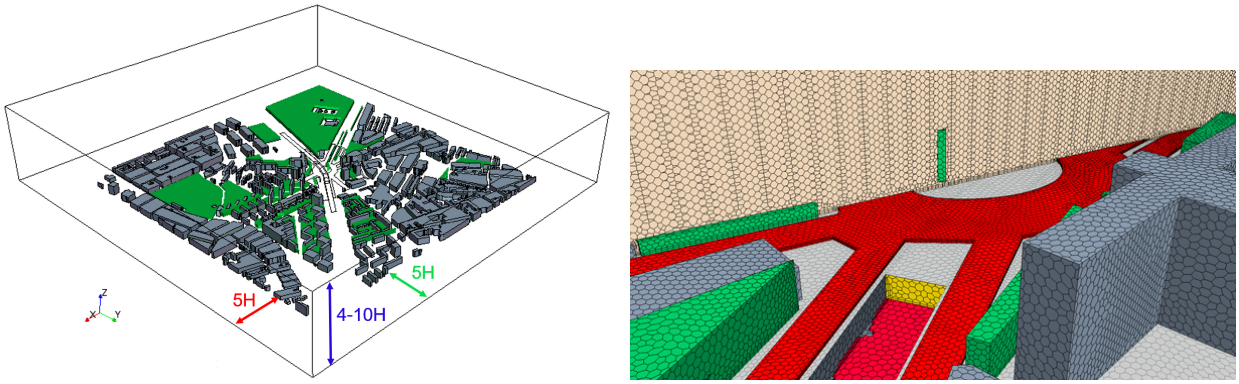

(a) **(b)**

Figure 2.2: (a) Computational domain over an urban area. (b) Polyhedral mesh.

The computational domain is discretized in grid points and the mesh resolution may affect the results. Accordingly, the mesh has to be fine enough to capture the dynamical processes with high resolution without increasing too much the computational load. To that end, the optimization of the mesh is important. The grid stretching should progressively change with a ratio below 1.3 to keep a small truncation error. Depending on the geometry, a recommendable type of the mesh is the tetrahedral shape since introduce small truncation errors and show better convergence (Hirsch et al., 2002). But currently, there are better types of mesh like the polyhedral grid with dodecahedra shapes, very useful for complex and non-uniform geometries (Figure 2.2b). As for the grid resolution, it is completely determined by the research purpose, geometry and the boundary conditions. Thus, a mesh dependency test is recommended in order to check that the outputs are independent of the grid resolution. Additionally, parallel grid lines to the walls with small resolution provide accurate results close to the buildings (Franke, 2007).

The boundary conditions represent the influence of the surroundings on the study area. For that reason, the inflow conditions are imposed at a certain distance in order not to alter the solution inside and, besides, the inlet conditions are able to fully develop. Thus, the top conditions should be imposed to prevent the change on the inflow conditions and, thereby, the symmetry boundary condition is commonly used. This feature enforces a parallel flow to the boundary by forcing the normal component to vanish and, besides, prescribes zero normal derivatives for all dynamics variables. This condition is also often imposed in the lateral boundaries, when the flow is parallel to them to facilitate the numerical convergence. In relation to the outflow, the open boundary conditions are used with a constant static pressure, where the derivative of the flow variables are forced to vanish. As for the wall boundary conditions, smooth and rough walls are considered in urban areas by means of a wall function approach (Wall All Y+ treatment). The ground is considered as a rough surface with a roughness parameter, which should be lower than the vertical grid resolution (Blocken et al., 2007). In urban environments, the effect of the wall functions on the solution away from the wall is considered small (Franke, 2007). In this work, smooth walls on buildings are assumed since the impact on the atmospheric flow caused by its geometry are larger than the roughness of the buildings walls.

2.6.2 Modelling atmospheric inflow conditions

The meteorological variables required at inlet of the CFD simulation are established in base to some assumptions. The lack of the vertical information from experimental data lead to estimate the inflow profiles in a theoretical manner. Assuming near-neutral atmospheric conditions, the inflow is defined by the logarithmic profile law (Eq. 1.2), whereas the inlet conditions of the turbulence parameters, k and ε, are computed as follows (Richards and Hoxey, 1993):

$$u_{in}(z) = \frac{u_*}{\kappa} ln\left(\frac{z + z_0}{z_0}\right) \tag{2.43}$$

$$k_{in} = \frac{{u_*}^2}{{C_\mu}^{1/2}} \tag{2.44}$$

$$\varepsilon_{in}(z) = \frac{{C_\mu}^{3/4} {k_{in}}^{3/2}}{\kappa z} \tag{2.45}$$

In this way, in urban areas, the flow vertical profiles can be derived from the wind speed measured at a certain height. It should be noted that the roughness length has to be established in the inlet wind profile according to the roughness imposed at ground.

In urban environments, this assumption can be suitable when the thermal effects are small. Consequently, the UBL is thermally in near-neutral conditions and the wind flow is basically

modified by the surface roughness (buildings or any obstacles). However, this atmospheric condition does not strictly occur. Indeed, the wind and temperature conditions irregularly change in height on account of the thermal gradients between surface and atmosphere. In stability conditions further away from neutral atmosphere, the vertical profiles of wind and turbulence considerably differ from the previous expressions (Equations 2.43-2.45). In these cases, the mesoscale models can provide the meteorological variables in order to impose more accurate boundary conditions into the CFD-RANS simulations. Therefore, in these cases, in addition to the wind and turbulent parameters, the vertical profile of temperature is also required at inlet.

2.6.3 Road traffic emissions

Road traffic is the main source of air pollution in urban areas, being the primary emitted pollutants in gas-phase: NO_x (NO and NO_2), CO and VOC. The emission rate per vehicle is dependent on several factors linked to the vehicle or the driving behaviour, e.g. the motor internal combustion, namely, the kind of combustible petrol or diesel, the type or size of vehicle and, as well, the driving speeds.

The emission factors are broadly classified taking into account the velocity and the type of vehicle (HBEFA, 2010). In general terms, the standard emission of NO_x for a passenger car travelling at 30 km h^{-1} is around 0.5 g km^{-1} (Baker et al., 2004), but this NO_x rate changes depending on the type of vehicle (motorcycle, light or heavy vehicle, bus and so on). Initially, few years back, the most part of NO_x emissions was considered NO, meaning that the emitted NO was markedly superior to the NO_2 (NO−to−NO_2=10:1) (Buckingham, 1997). However, the trend of this ratio shows a decrease in last years (Carslaw, 2005). Nowadays, the emission ratio of NO_2/NO_x might be considered around 30% (Borge et al., 2014). Additionally, the VOC are other important component in the vehicle exhaust emissions. Overall, the proportions of the emitted pollutants associated with the road traffic of Madrid are shown in Fig. 2.3a. Regarding to the driving in heavy trafficked areas in the city center, the emission ratio VOC-to-NO_x may be around 1/6 or 1/5 according to the emission inventories reports of Madrid (Madrid-Council, 2014). Nevertheless, this ratio may differ not only as a consequence of the driving features (different speed limits, traffic lights and so on), but also of the type of vehicle.

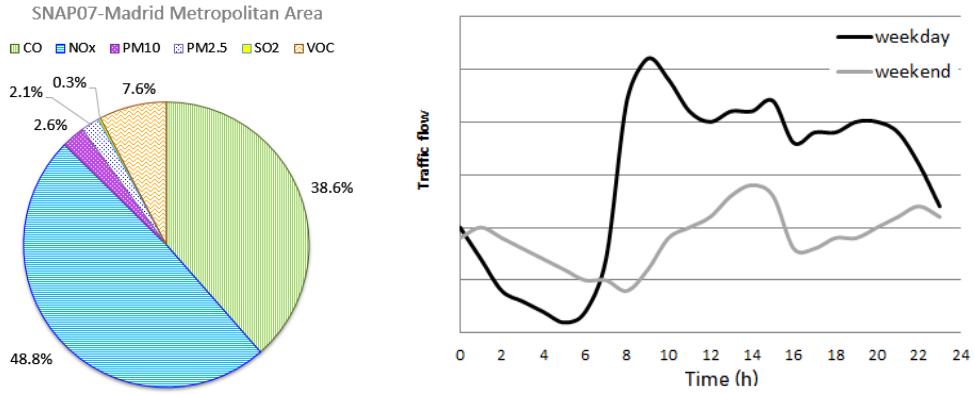

(a) (b)

Figure 2.3: (a) Ratio of the emitted pollutants by road transport reported in the Emission Inventories of Madrid. Source: (Madrid-Council, 2014). (b) Representative daily traffic pattern in a European city, e.g. Madrid (Quaassdorff et al., 2016).

Figure 2.3b illustrates a representative traffic flow pattern in an urban hot-spot in Madrid (Quaassdorff et al., 2016). The traffic flow (veh/h) usually varies depending on the features (population, commercial activities, etc) and the human activities of the urban area. However, the daily trend of a weekday is usually marked by two maximum values in the morning and in the evening with another slight maximum at the central hours of the day.

In the CFD simulations, the traffic emissions are limited to the road areas and the emission rate is added as a source term in the transport equation (Eq. 2.33). On the one hand, the emission rate is commonly computed through the number of vehicles on each street. Overall, this information is usually provided by the annual average daily traffic (AADT) or, otherwise, it can be also derived from specific experimental campaigns. Therefore, the emission rate is computed with the previous emissions factors and is uniformly distributed along the streets.

On the other hand, microscale traffic models combined with an emission model provide the traffic emission with high spatial and temporal resolution in the streets (Abou-Senna et al., 2013; Quaassdorff et al., 2016). The traffic model computes detailed trajectories that describe the behaviour of individual vehicles considering drivers' reaction times, route selection logic and lane change logic. It provides essential information about braking-acceleration patterns that have a huge influence on the amount of pollutants emitted and their distribution in space and time. The emission estimations are based on very detailed fleet composition and vehicle flow data in the research area obtained from an intensive measurement campaign with cameras (Quaassdorff et al., 2016). Therefore, the NO_x release is obtained with resolution of meters and, besides, the temporal variation of the spatial distribution over time.

Figure 2.4 displays the spatial difference of the NO_x emissions for a particular scenario by using both procedures. In the first case, the pollutant emission is uniformly distributed along

the street depending on the number of vehicles at that hour. In contrast, for the same hour, in the outputs from the microscale traffic models, the NO_x emissions spatially change due to the specific features in this region, such as traffic lights or crosswalks.

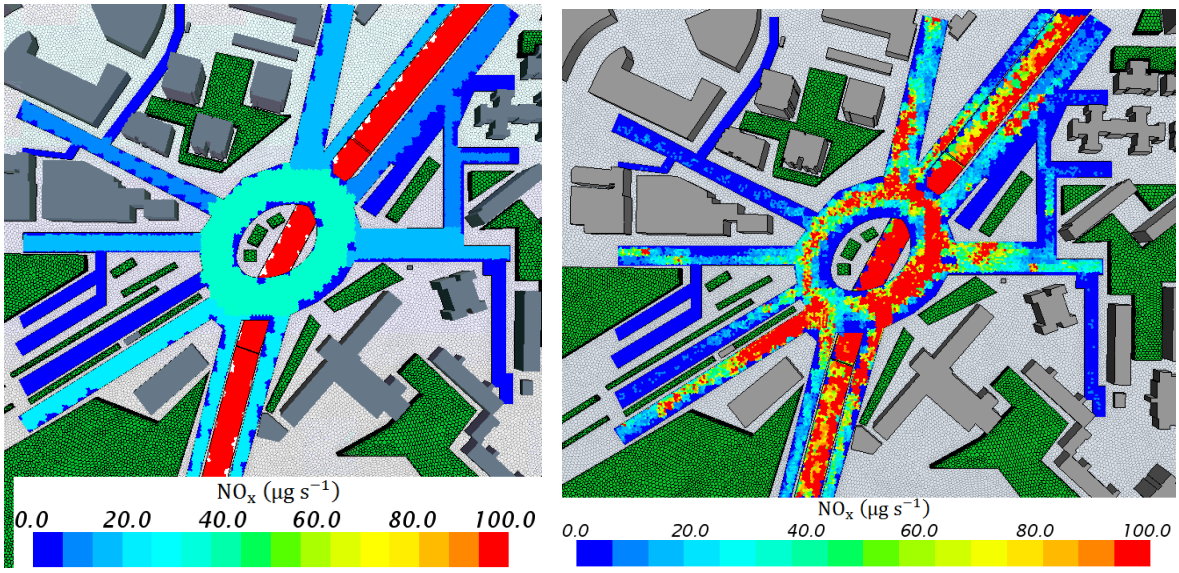

Figure 2.4: Examples of (a) uniform traffic emission layout and (b) detailed spatial distribution of the traffic emissions.

2.7 Statistical model evaluation

This section is addressed to present the statistical analysis for the CFD models applied to air quality assessment. The management of urban air quality in the decision-making on air pollution mitigation calls for reliable results of the modelling techniques.

In urban environments, the dispersion of pollutants in the streets is fundamentally controlled by turbulent processes. Thus, the random nature of the turbulence gives rise to a great spatial and temporal variability, which hinders a fully accurate simulation of the atmospheric processes. In addition to that, the internal numerical errors and the assumptions related to boundary conditions also contribute to the uncertainty of the modelling results. Nevertheless, the outputs of CFD models have been widely validated with experimental data in multiple scenarios, turning out good results of the atmospheric processes. Therefore, the CFD models are able to reproduce the dynamical and chemical processes in distinct scenarios but its evaluation with measurements is an essential requirement.

For further quantitative detail, a statistical analysis helps to determine the accuracy of the modelling results. In the framework of the microscale modelling for urban air quality, Chang and Hanna (2004) proposed criteria for the statistical parameters in order to characterise the

reliability of the outputs. To that end, the most characteristic statistical indicators are: the Normalized Mean Square Error (NMSE), the Fractional Bias (FB), the correlation coefficient (R) and the the factor 2 (FAC2), whose mathematical expressions are the following:

$$\text{NMSE} = \frac{\sum_{i=1}^{n}(O_i - P_i)^2}{\sum_{i=1}^{n}(O_i P_i)} \tag{2.46}$$

$$\text{FB} = \frac{\overline{P} - \overline{O}}{0.5(\overline{P} + \overline{O})} \tag{2.47}$$

$$\text{R} = \frac{\sum_{i=1}^{n}[(O_i - \overline{O})(P_i - \overline{P})]}{\left[\sum_{i=1}^{n}(O_i - \overline{O})^2\right]^{1/2}\left[\sum_{i=1}^{n}(P_i - \overline{P})^2\right]^{1/2}} \tag{2.48}$$

$$\text{FAC2} = \text{fraction of data that satisfy } 0.5 \leq P_i/O_i \leq 2 \tag{2.49}$$

where O_i represents the observed values and P_i the modelling results, and $\overline{O}$ and $\overline{P}$ their corresponding mean values. The NMSE estimates the overall deviation between the modelling results and the observations. The FB indicates the underestimations or overestimations of the observed values. The correlation coefficient reflects the linear relationship between the outputs and measurements, and it is not individually a decisive parameter, but it is necessary to conclude good outcomes. Lastly, the FAC2 only indicates a deviation range, and it is not influenced by the high and the low outliers. A perfect outcome would mean a value of R and FAC2 equal to 1, and the FB and NMSE equal to 0. The influence of the random nature of the atmospheric processes together with the modelling uncertainties prevent from obtaining a perfect model for air quality assessment.

The previous statistical metrics are classified in ranges that determine the accuracy of the results based on the values associated to a perfect model. Table 2.5 shows the acceptance criteria established in Chang and Hanna (2004) and in Goricsán et al. (2011) for the evaluation of air quality modelling results.

In a recent study, Hanna and Chang (2012), proposes new acceptance criteria for urban applications with ranges more flexible for the modelling results. Nevertheless, in this work, the stricter ranges are considered to evaluate the outputs of the CFD-RANS simulations. It is worth noting that the approximation of the model to the real atmospheric processes might be considered appropriate or not depending on the study purpose. For instance,. The management of urban air quality is interested in the distribution of pollutants in the streets during long periods (weeks, months or even a year). Thus, in these cases, the exact values of high concentrations are usually less important than their locations for regulatory applications (Chang and Hanna, 2004).

Table 2.5: Acceptance criteria of the statistical metrics for the modelling evaluation (Chang and Hanna, 2004, 2005). Adapted from Goricsán et al. (2011).

Validation metrics	Range	Membership function
Normalise Mean Square Error (NMSE)	NMSE < 4	Good
	9<NMSE<16	Fair
	NMSE>25	Poor
Fractional Bias (FB)	-0.3<FB<0.3	Good
	1<FB<1.2	Fair, Underestimation
	-1.2<FB<-1	Fair, Overestimation
	FB<-1.33 or FB>1.33	Poor
Correlation Error (R)	| R |>0.8	Good
	0.5<| R |<0.8	Fair
	|R|<0.5	Poor
FAC2	0.5< FAC2 <2	Good
	0.3< FAC2 <0.4	Fair
	FAC2 <0.2	Poor

Chapter 3

Modelling dispersion of reactive pollutants in simplified geometries with the chemical schemes: NO_x-O_3 and NO_x-O_x-VOC

3.1 Introduction

In urban environments, the proximity between sources and receptors in the street entails that only the fastest chemical reactions have an impact on pollutant concentrations. First studies focus on modelling chemical reactions on the pollutant dispersion at street level in simplified geometries. Baker et al. (2004) and Baik et al. (2007) studied the dispersion of reactive pollutants in a street canyon considering the NO_x-O_3 photostationary state. Both researches concluded that the O_3 concentration was faster depleted within the canopy due to the high NO emission at ground level. Moreover, Baik et al. (2007) found that the magnitude of the chemical terms was comparable to the advection or turbulent diffusion for the O_3. In contrast, for the NO or for NO_2 concentrations, the dynamical terms were larger than the chemical ones. Nevertheless, these studies underlined the importance of including the O_3 photochemical reaction in the study of the dispersion of NO and NO_2 within the canopy.

Additionally, the VOC related to traffic emissions are also involved in urban air pollution. This makes it necessary to include a more complex chemical scheme by modelling the interactions among NO, NO_2, O_3 and VOC. In recent studies, complex chemical mechanisms have been implemented in CFD models in order to reproduce the NO and NO_2 dispersion in isolated streets. Kwak and Baik (2012) included the CBM-IV mechanism in a CFD model and evaluated the O_3 sensitivity with respect to different emissions of VOC and NO_x. The

high levels of NO in regards to the NO_2 at street level concluded that the O_3 loss, by reaction with NO, prevails over its formation by NO_2 photolysis. Hence the O_3 sensitivity is weakly related to the VOC emission level and negatively correlated with the NO_x behaviour. Kwak et al. (2013) obtained the same results about the relation between the O_3, NO_x and the VOC emission levels. They examined the dispersion and photochemical evolution of reactive pollutants in a street canyon with different canyon aspect ratios. Note that it is the ratio between building-height and the street-width. They found a relation with the wind speed whereby its increase enhances the exchange with overlying air that promote the downward O_3 transport into the street. These studies highlight the importance of the O_3 oxidation process by assessing the photochemical reactions in the street. Similar major aspects of the relation NO_x, VOC and O_3 are obtained in three-dimensional street canyons by Park et al. (2015). However, small variations are locally found caused by the flow patterns resulting from the geometry of the domain.

The model sensitivity to the chemical mechanism used in the simulation is also thoroughly analyzed. Kim et al. (2012) compared, in identical conditions, the hourly concentration of NO, NO_2 and O_3 resulted from the photostationary steady state and a full chemical mechanism (110 species and 343 reactions). The outputs provided similar concentrations of NO and NO_2 by using any of the mechanisms, whereas for the O_3 concentration, with the simple mechanism turns out lower than with the full scheme. Bright et al. (2013) compared the $O_3 - NO_x$ scheme with a more complex mechanism (51 chemical species and 136 reactions) using a LES model. They found that the values of NO, NO_2 and O_3 differ from the photostationary state by using a more detailed chemistry, which reflects the additional transformation of NO into NO_2, resulting from the intrinsic VOC degradation processes.

The purpose of this chapter is to study the importance of chemical reactions on the dispersion of reactive pollutants in two simplified settings in a 2D- and 3D- geometries. Focusing on the chemistry of NO and NO_2, two chemical schemes are considered: the NO_x-O_3 and the NO_x-O_x-VOC mechanisms. Hence the dispersion of NO and NO_2 are modelled: with no chemical scheme, with the NO_x-O_3 scheme and with the NO_x-O_x-VOC mechanism. Additionally, the influence of atmospheric conditions on the chemical activity is particularly examined through different cases of wind speed, solar position and VOC/NO_x emission ratio.

The implementation of chemical reactions in the CFD model increases the computational load. Therefore, this study is also addressed to quantify the chemical influence in several atmospheric scenarios and, thus, to find the best compromise between the purpose to be reached and the available computational resources. It is worth mentioning that the NO_x-O_x-VOC scheme involves more than twice the computational time required by the photostationary steady state.

Accordingly, the outcomes of this work provide further details about the coupled behaviour of chemical and dynamic processes in order to be able to respond the following research questions:

- How does the dispersion of NO and NO_2 in the urban canopy layer change by including the NO_x-O_3 and NO_x-O_x-VOC schemes in the CFD simulation?
- Which is the impact of the meteorological conditions on the reactive pollutants dispersion?

3.2 CFD model description

The CFD-RANS model with the Realizable k-ε closure, described in Section 2.2.2, is used to analyse the reactive pollutant dispersion in simplified geometries in order to characterise the chemical behaviour by imposing different atmospheric conditions.

3.2.1 Simulation setup

Figure 3.1 illustrates the computational domains: a single street-canyon (2D-geometry) and a staggered array of cubes (3D-geometry) and their respective sizes in x, y and z directions are: 24 m x 40 m x 64 m and 64 m x 64 m x 64 m.

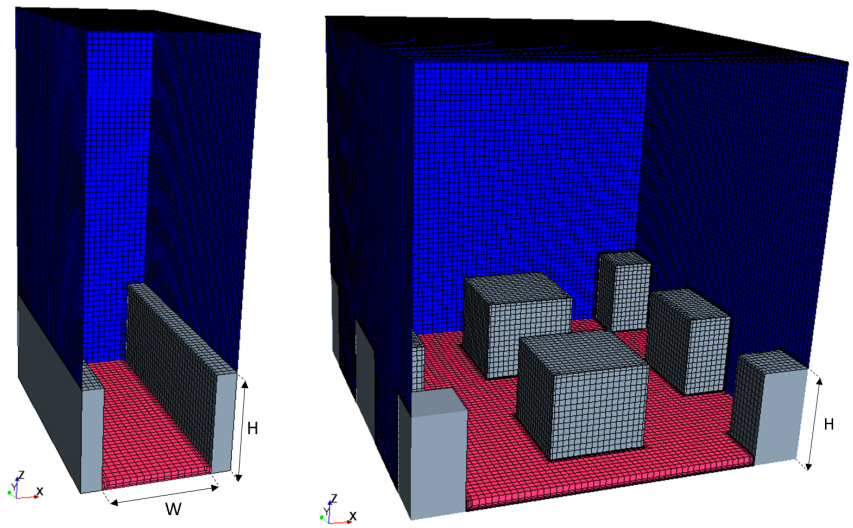

(a) **(b)**

Figure 3.1: (a) Domain of the street canyon with $H = W$ =16 m (2D-geometry). (b) Domain of the staggered array of cubes with $H = W = L$ =16 m (3D-geometry). Pink region stands for the emission location.

The aspect ratio, defined as the ratio of building height (H) to the street width (W), is $H/W = 1$ in both geometries. The domain top is fixed at $4H$ considered high enough to not affect the dynamical processes at street level (Coceal et al., 2006). The 3D-geometry is represented by staggered array of cubes with the width of the buildings equal to their height (L=H), giving rise to a building packing density $\lambda_p = 0.25$, which is a typical value of real urban areas (Grimmond and Oke, 1999). Note that λ_p is expressed by the ratio between the plan area of buildings and the total surface area. The mesh resolution of 1 m in all directions was selected after performing a grid independence test and selecting an optimized mesh for carrying out multiple simulations.

The same boundary conditions are imposed to both geometries. Symmetry conditions are established in the spanwise direction (y-direction) and at the top of the domain, which enforce parallel flow and zero normal derivatives for the dynamic variables. Cyclic boundary conditions are imposed in the streamwise direction, which represents the simulation of an infinite number of streets. Assuming isothermal condition (T=298 K), the flow is driven in x-direction by a pressure gradient equal to $\rho u_\tau^2/4H$, where u_τ is a reference velocity (Santiago and Martilli, 2010). In this study, two values of u_τ are considered: u_τ=0.45 m s^{-1} and u_τ=0.225 m s^{-1}. In this way, the wind speed at 1.5H resulted from using u_τ=0.225 m s^{-1} is 1.9 m s^{-1} and 1.5 m s^{-1} in the 2D-geometry and the 3D-geometry, respectively. As the wind speed is proportional to u_τ, imposing u_τ=0.45 entails that the wind speed is twice as large as the previous case.

Regarding the pollutant concentrations, this study focuses on modelling the NO and NO_2 using different chemical approaches: (a) no chemistry, (b) the NO_x-O_3 scheme and (c) the NO_x-O_x-VOC scheme. The chemical mechanisms are described in detail in Section 2.3.2. And, as explained in Section 2.4.1, the same time step, $t_s = 1$ s, is used to simulate both chemical and dynamical processes, reaching the quasi-steady state in all simulations.

The source of pollutants is located at ground level in both domains (Fig. 3.1). The NO_x emission is assumed at 0.5 g km^{-1} per vehicle (Baker et al., 2004; Baik et al., 2007). The emission ratio used was based on previous studies with ratio $NO-to-NO_2$ equal to 10:1 (Buckingham, 1997). Hence the NO and NO_2 rate are fixed at 112 μg m^{-1} s^{-1} and 17 μg m^{-1} s^{-1} respectively, which is equivalent to 930 vehicles per hour. In addition, the VOC emissions are included by applying the NO_x-O_x-VOC scheme. In this study, two emission ratios of VOC/NO_x are simulated: 1/5 and 1/2. The $VOC/NO_x = 1/5$ is the last value registered in Madrid (Madrid-Council, 2014) but, even so, a higher value ($VOC/NO_x = 1/2$) is also considered. As explained in Section 2.3.2, some VOC are lumped in terms of specific functional groups. The VOC species related to traffic emissions are: OLE, ARO, ALK, ALD and HCHO; and their volumetric proportions are established, based on the emission factors of HBEFA (2010), at: 28.6 %, 23.1 %, 38.6 %, 4.0 % and 5.6 %, respectively.

The boundary conditions for solving the transport equations are considered as cyclic and symmetry conditions along x- and y-directions respectively. In these conditions, the pollutant concentrations imposed at the top of the domain plays an important role on the chemical reactions, except for the NO_x and VOC, because their concentrations in the street are practically due to the traffic emissions. Therefore, the concentrations fixed at the top for NO, NO_2, CO and SO_2 are respectively 16, 35, 200 and 2 ppb in all scenarios, similar values can be found in the urban atmosphere. As for the VOC concentration, the same ratio VOC/NO_x imposed for the emissions is used at the top, and it is deduced from the NO_x value (51 ppb) holding the emitted proportion for each specie of VOC. Hence the concentration of VOC in air is considered fully associated to the traffic emissions. Finally, the O_3 concentration at the top of the domain is computed by the Leighton Relationship (Eq. 2.32). To analyse the influence of the available O_3 on the NO and NO_2 levels in the street, two particular cases of background O_3 are studied, at rush hour, when high concentrations of NO_x are expected. The photolysis rate, J_{NO_2}, is calculated depending on the solar zenith angle (Table 2.3). Hence, a representative solar zenith angle (in mid-latitudes) in winter ($\varphi_w = 78°$) and another one in summer ($\varphi_s = 46°$) are considered to compute the O_3 established at top of the domain. This results in two different cases of background O_3 at the top of the domain: 10 ppb and 40 ppb.

In this chapter, the solar position has been only used to compute the photolysis rate and, the thermal effects on flow and the shadow effects of building on photochemistry are neglected. Including shading effects would imply to study the shadows and the temperature distribution within the street canyon, depending on solar position and street orientation. In shaded zone, the reaction rates decrease (slower chemical reactions) due to the lower radiation and temperature in comparison with the sunlit space. Kwak and Baik (2014) considered the impact of the shadows, which were represented in a simple way, on photochemistry in a street canyon. This is an interesting issue to be study in future works, however, in order to limit the atmospheric conditions analysed, it has been considered out of scope of this research.

3.2.2 CFD model evaluation

Controlled experiments of pollutant dispersion in simplified urban configurations are carried out in wind-tunnel, where only non-reactive pollutants can be studied. Note that the implementation of the chemical mechanisms has been previously evaluated in a box model configuration (Section 2.4.2). Therefore, in this section, the dispersion of the non-reactive pollutants, in the 2D-geometry, is compared against the measurements from a wind tunnel experiment performed in a similar street-canyon (Meroney et al., 1996).

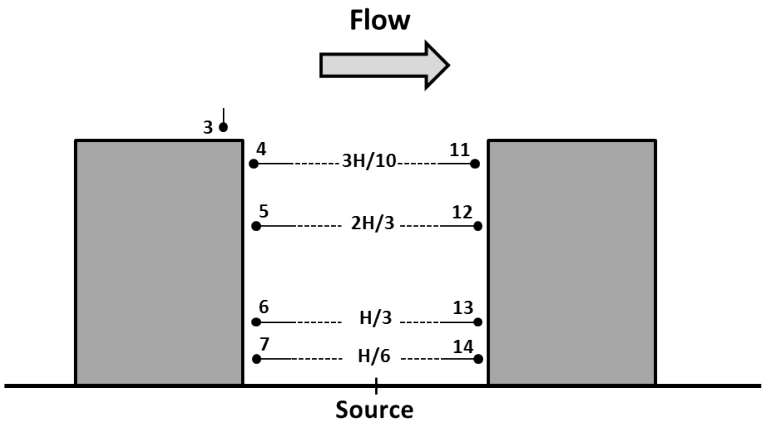

Figure 3.2: Location of the comparison points with measurements from Meroney et al. (1996)

The experimental system consists on a single 2D street canyon with $H/W = 1$ (Fig. 3.2). The wind blows perpendicular to the canyon in x-direction and the emission source is located at the bottom of the domain. This scenario is similar to CFD simulation in the 2D-geometry without imposing the cyclic boundary conditions in streamwise direction. For the comparison with experimental data, just the concentration of the traffic emissions are considered and the concentration gradients within the canyon are evaluated among the points nearby the walls (Fig. 3.2). Therefore, the concentration at each measurement point is normalized with respect to the concentration at the point 7 within the street (C/C_7). The same normalization was used in Santiago and Martín (2008) to evaluate the CFD model results with the same experiment. Figure 3.3 displays the comparison of the normalized concentration from the simulation against the experimental values.

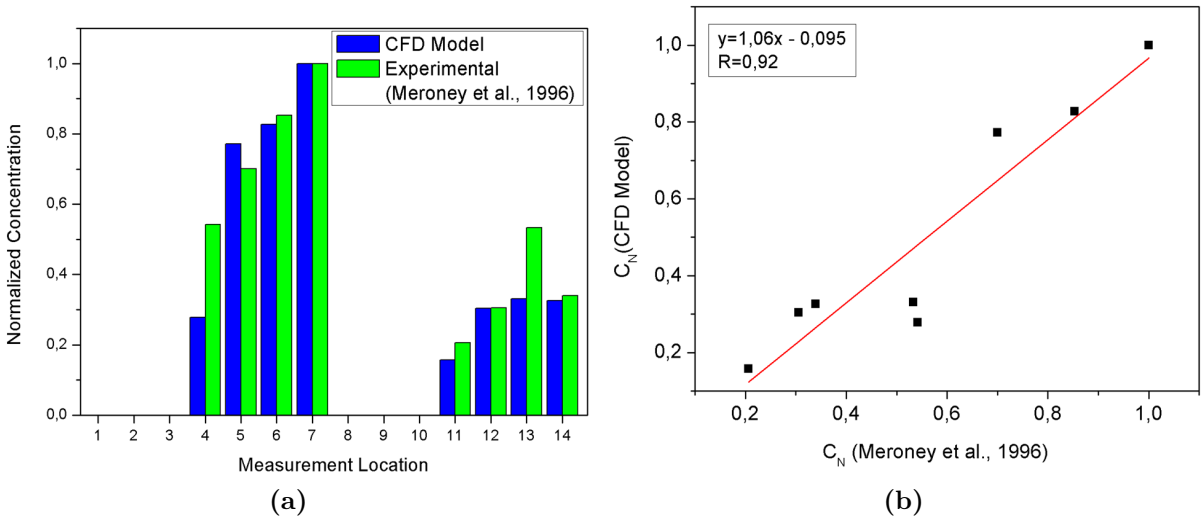

Figure 3.3: Comparison between simulation results and experimental data (Meroney et al., 1996). (a) Comparison between modeled concentration and experimental measurements at each location. (b) Linear fit between experimental measurements and modeled concentrations.

Overall, a good agreement is obtained in spite of the slight difference at points 4 and 13, where

the concentration is lower than experimental data. Besides, the linear regression concludes a good correlation coefficient (R=0.92) between the measurements and the simulated results. For further quantitative information, the statistical parameters of NMSE, FB and the FAC2 are computed following the Eqs. 2.46-2.49. The statistical results are: NMSE=0.03 (NMSE<1.5), FB= 0.068 (-0.3<FB<0.3) and the FAC2=100%, which reveal a good fit between simulated and experimental data with a very small underestimation. Therefore, the pollutant dispersion is accurately simulated in base to the model acceptance criteria summarized in Section 2.7.

3.3 Impact of the atmospheric conditions on the dispersion of reactive pollutants

In this section, a thorough study about the influence of some relevant atmospheric variables on the dispersion of reactive pollutants is presented. To that end, several chemical approaches are assumed: (a) non-reactive pollutants, (b) with just the chemical reactions of the NO_x-O_3 scheme and (c) including the VOC interactions using the NO_x-O_x-VOC scheme.

This study focuses on analysing the impact of the atmospheric conditions on the NO and NO_2 taking into account not only the reaction with O_3, but also the influence of the VOC (Section 1.4). The VOC in an urban area are emitted by different sources (industry, commercial, etc.) but, in this study, are just considered those whose release is associated to the traffic emissions. And the impact of the VOC levels is analysed using the NO_x-O_x-VOC scheme, considering two traffic emission ratios of NO_x/VOC equal to 1/5 and 1/2. Finally, the influence of the wind speed and the solar position on the reactive pollutants dispersion is studied (Table 3.1).

Additionally, the coupling of the dynamical and chemical processes are studied on the dispersion of NO and NO_2 in simplified settings: in 2D- and 3D-geometries. Table 3.1 summarizes the atmospheric cases in which the four chemical scenarios are simulated in both computational domains: no chemical scheme, with NO_x-O_3 scheme (PSS), NO_x-O_x-VOC scheme with traffic emission NO_x/VOC=1/5 (CCM1/5) and NO_x-O_x-VOC scheme with the traffic emission NO_x/VOC=1/2 (CCM1/2).

Table 3.1: Summary of the atmospheric cases in which the chemical scenarios are simulated in each domain.

Chemical Scenarios	
Non-reactive	
NO_x−O_3 scheme	(PSS)
NO_x−O_x−VOC scheme with VOC/NO_x=1/5	(CCM1/5)
NO_x−O_x−VOC scheme with VOC/NO_x=1/2	(CCM1/2)

Atmospheric Conditions		
	Solar Position / Background O_3	Reference velocity
Case 1	φ_s/O_3=40 ppb	u_τ=0.45 m s^{-1}
Case 2	φ_s/O_3=40 ppb	u_τ=0.225 m s^{-1}
Case 3	φ_w/O_3=10 ppb	u_τ=0.45 m s^{-1}
Case 4	φ_w/O_3=10 ppb	u_τ=0.225 m s^{-1}

In this analysis, the deviation of the NO and NO_2 caused by the chemical reactions is analysed through the relative concentration differences from the non-reactive pollutant (tracers), given by the following expressions:

$$\delta\mathrm{NO}(\%) = \frac{\mathrm{NO_R} - \mathrm{NO_T}}{\mathrm{NO_T}} \cdot 100 \qquad ; \qquad \delta\mathrm{NO_2}(\%) = \frac{\mathrm{NO_{2R}} - \mathrm{NO_{2T}}}{\mathrm{NO_{2T}}} \cdot 100 \tag{3.1}$$

where NO_R and NO_{2R} are the concentration for the simulated NO and NO_2 as reactive pollutants and NO_T and NO_{2T}, the simulated concentration for the non-reactive scenario. Thus, the relative differences provide how the concentration of a reactive pollutant can differ from the non-reactive assumption under the same atmospheric conditions.

In addition, the impact of atmospheric conditions on the reactive pollutants is, in turn, studied by means of the normalized concentrations. In this way, the results are non-dependent on the traffic emissions, the wind speed or the value imposed at the top. Accordingly, the normalized concentration of NO and NO_2 provides their general behaviour through the comparison of all the cases. The concentration for both pollutants is normalized by the emission area (A_{Em}), the reference velocity (u_τ) and the source emission rate for NO and NO_2 (Q_{NO} and Q_{NO_2}) as follows:

$$\mathrm{NO_N} = \frac{(\mathrm{NO} - \mathrm{NO_{top}})\ \mathrm{u_\tau}\ \mathrm{A_{Em}}}{\mathrm{Q_{NO}}} \qquad ; \qquad \mathrm{NO_{2,N}} = \frac{(\mathrm{NO_2} - \mathrm{NO_{2,top}})\ \mathrm{u_\tau}\ \mathrm{A_{Em}}}{\mathrm{Q_{NO_2}}} \tag{3.2}$$

where NO_N and NO_{2N} are the normalized concentrations of NO and NO_2 respectively.

Note that the normalized concentrations of the non-reactive pollutants take the same value ($NO_N \equiv NO_{2,N}$ for a tracer) (Appendix 6.2).

3.3.1 Description of the flow patterns

The simulations are performed in two computational domains: the 2D-geometry is a single street-canyon, whereas the 3D-geometry is an idealized configuration of a staggered array of cubes. Both of them are formed by the same features of the obstacles that consists of buildings with the same height (H=16 m) and width (W=16 m) and, thereby, with an aspect ratio H/W=1. In all simulations, the flow pattern corresponds to the perpendicular wind direction to the domain, giving rise to the flow pattern depicted in Fig. 3.4.

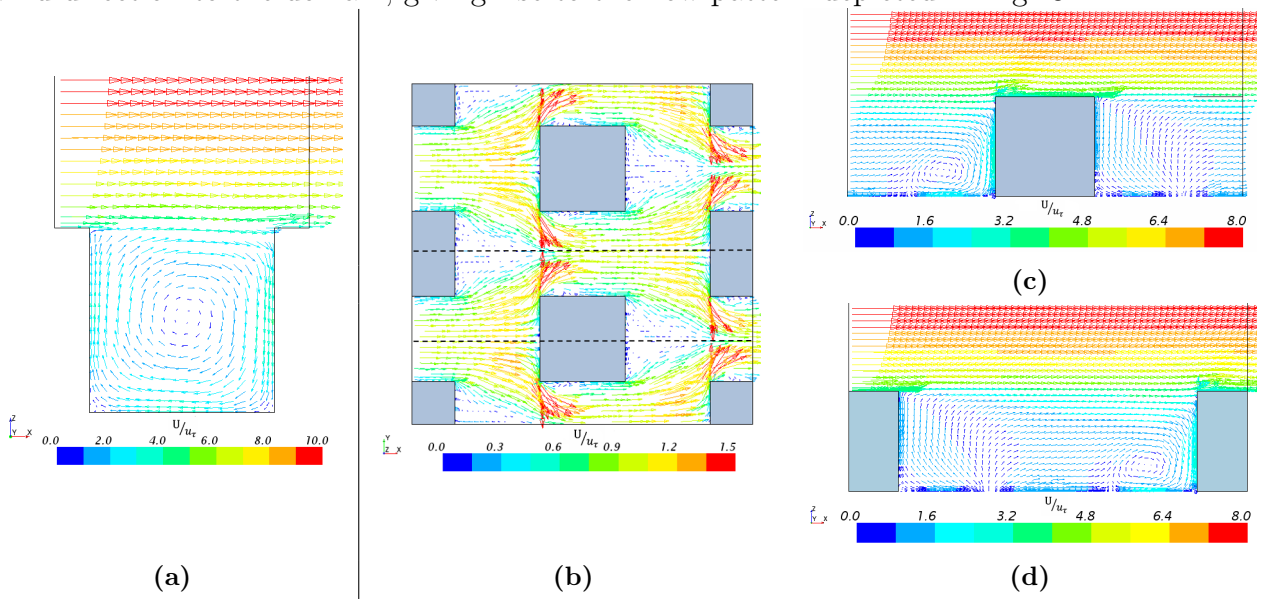

Figure 3.4: (a) Vertical section of U/u_τ in the 2D-geometry, (b) horizontal section of U/u_τ at 3 m in the 3D-geometry and (c-d) the vertical sections at the dashed lines.

In the 2D-geometry, the flow pattern displays a main vortex in the centre of the street at a height of $H/2$ (Fig. 3.4a). As for the 3D-geometry (Fig. 3.4b), the wind in horizontal section shows irregular patterns from the windward side and leeward of the centred cubes, with a symmetrical behaviour in y-direction. Figure 3.4c-d displays the vertical flow distribution at leeward and windward in the canopy, caused by the interaction with the cubes, which improves the vertical exchange of pollutants. Herein, the height of the canopy top is assumed at the height of buildings.

An overview of the dynamical variables in both domains is obtained with the vertical profiles of the horizontal spatial average (<>) of the normalized wind speed (U/u_τ) and the turbulent kinetic energy ($< k > /u_\tau^2$). Larger turbulence and, thereby, greater turbulent mixing below the canopy top, is turned out in the 3D-geometry (Fig. 3.5).

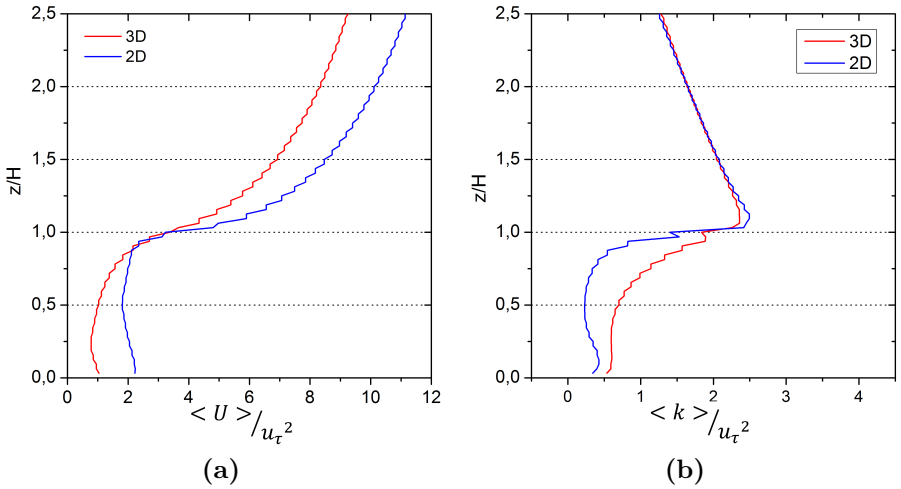

Figure 3.5: Vertical profiles of (a) $< U > /u_\tau$ and (b) $< k > /u_\tau^2$ in the 2D-geometry and 3D-geometry.

3.3.2 Ozone influence on reactive pollutants

As explained in Section 1.4, the O_3 concentration is generally dependent on the photochemical regime but, in the street, it is also affected by the chemical interactions with the NO_x and VOC levels due to traffic emissions. In addition, the photochemical reactions are dependent on the solar position and, as a result of the equilibrium state, two values of the O_3 background are imposed at the top (Case 2 and Case 4 in Table 3.1). Therefore, NO_R and NO_{2R}, from each chemical scenario, are compared against the NO_T and NO_{2T} in order to determine the atmospheric conditions that give rise to the largest impact on the concentration of the reactants.

Figure 3.6 shows a vertical section of NO_T and δNO for the Case 2 and Case 4 in the 2D-geometry. In the Case 4, δNO obtained from any of the reactive approaches is less than 3-4%, without a significant variation among them below the canopy top. In contrast, δNO increases to nearly 10% in the Case 2 and, only a small difference of 2-4% exists between the scenario CCM1/2 and the others (PSS and CCM1/5).

Likewise, δNO_2 is calculated with the PSS, CCM1/5 and CCM1/2 for the Case 2 and Case 4 (Fig. 3.7). In the latter, δNO_2 shows analogous values from all chemical scenarios, below 15-16% in the street. Accordingly, reactions involving VOC have hardly an impact on the NO and NO_2 levels in comparison with the result of the PSS. In the Case 2, δNO_2 rises up to 50% of difference from the non-reactive scenario. Actually, in this case, the use of the CCM1/2 results in larger deviation for the NO_2 concentration against the NO_x−O_3 mechanism (PSS).

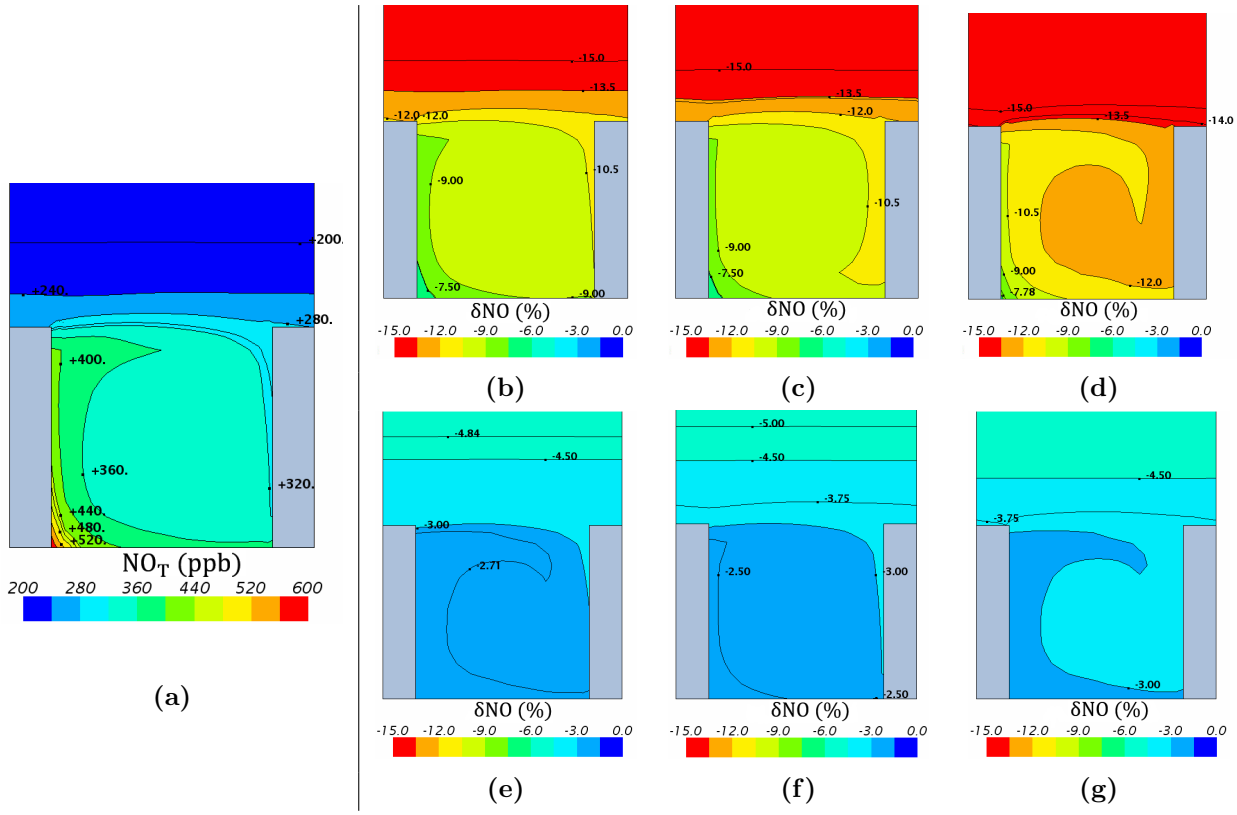

Figure 3.6: (a) Vertical section of NO_T in ppb. Vertical section of δNO (%) obtained respectively from the PSS, CCM1/5 and CCM1/2 chemical scenarios for (b-d) the Case 2 and (e-g) the Case 4.

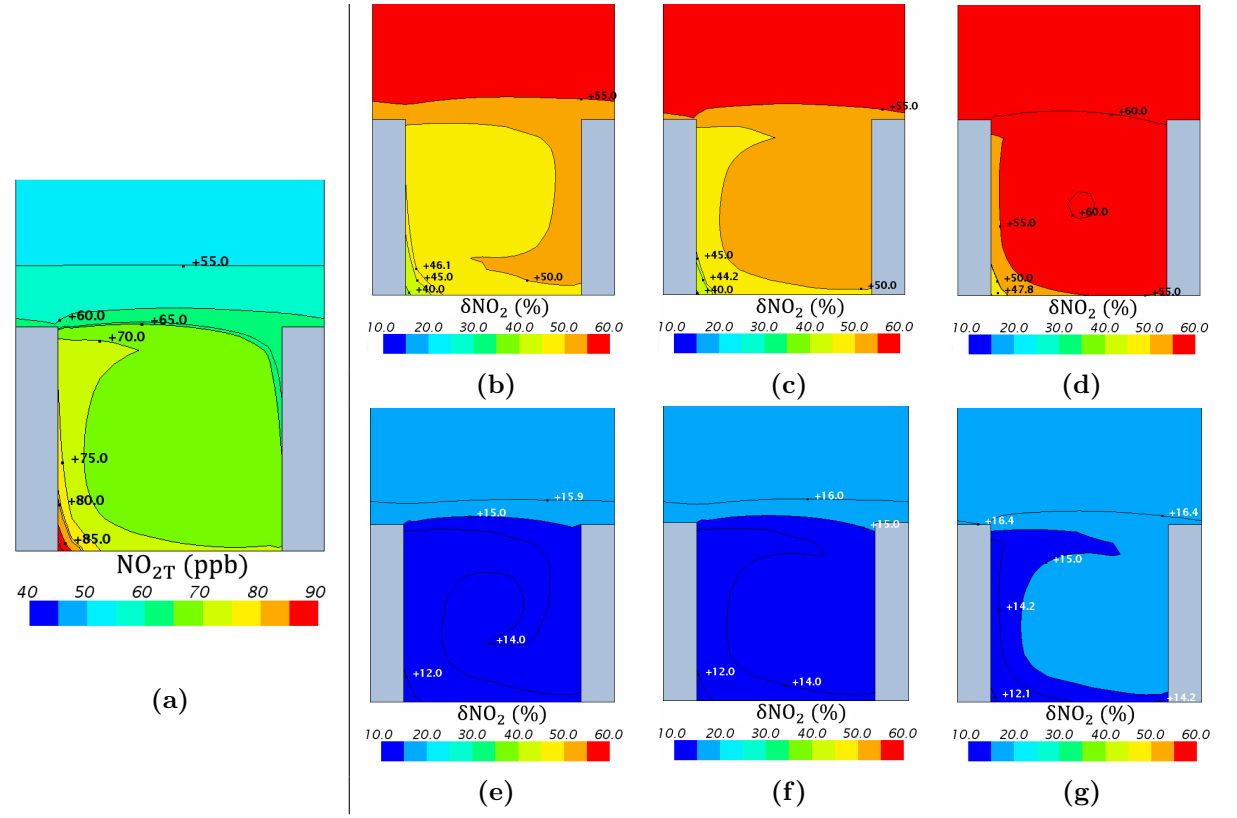

Figure 3.7: (a) Vertical section of NO_{2T} in ppb. Vertical section of δNO_2 (%) obtained respectively from the PSS, CCM1/5 and CCM1/2 chemical scenarios for (b-d) the Case 2 and (e-g) the Case 4.

Similar to the 2D-geometry, the chemical deviation through δNO and δNO_2 are analysed in a horizontal section, at 3 m above the ground level (AGL), in the 3D-geometry. Given that the largest chemical deviations are previously obtained in the Case 2, δNO and δNO_2 are just depicted in these conditions for the 3D-geometry in Fig. 3.8.

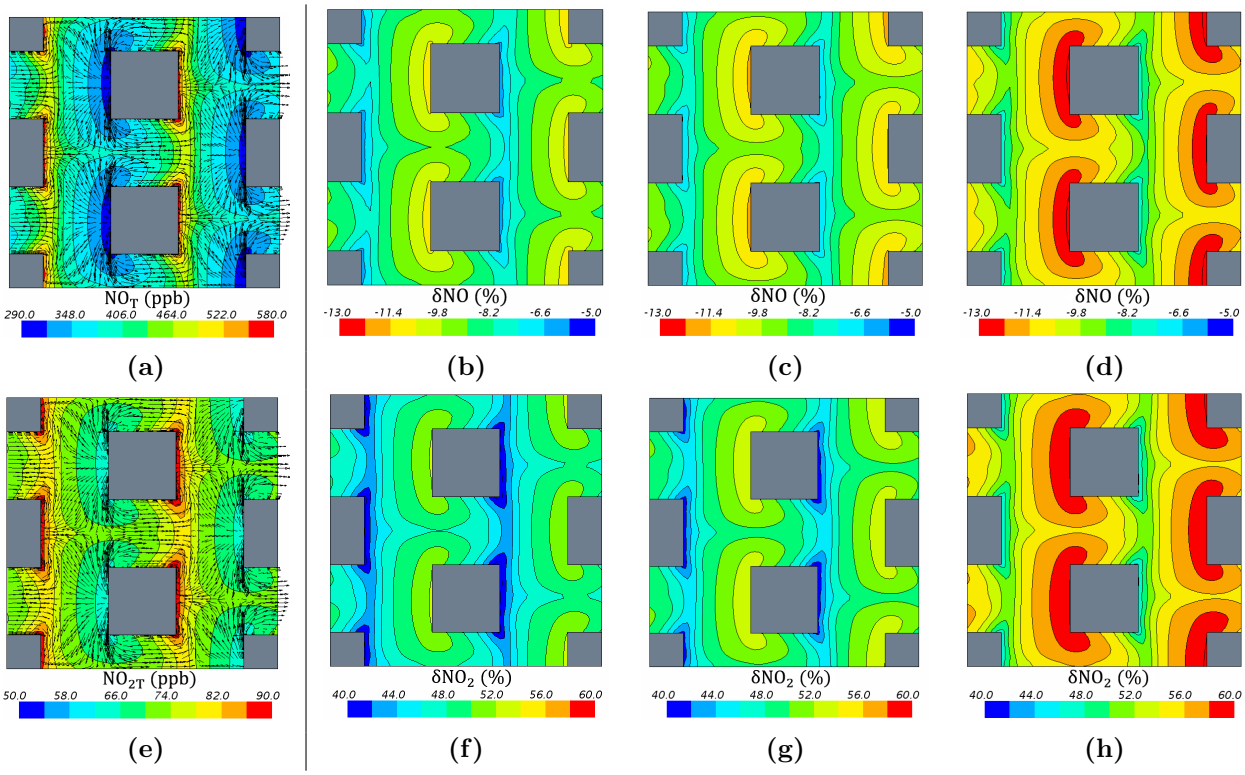

Figure 3.8: Horizontal section at 3 m AGL for the Case 2 of: (a) NO_T (ppb); (b-d) δNO (%) from PSS, CCM1/5 and CCM1/2 respectively; (e) NO_{2T} (ppb) and (f-h) δNO_2 (%) from PSS, CCM1/5 and CCM1/2 respectively.

At street level (3 m AGL), both δNO and δNO_2 hardly show differences by implementing either the PSS or the CCM1/5. By increasing the VOC emissions with the CCM1/2, the concentrations of NO and NO_2 faintly rise from the PSS. The overall values in terms of the spatial average, at 3 m, of δNO with the PSS, CCM1/5 and CCM1/2 yields 8.9%, 9.4% and 10.9% respectively, whereas for δNO_2 reaches values of 47%, 49% and 55% in the Case 2. Hence, an important growth in the reactive NO_2 levels is obtained in this case. In addition, similar differences are achieved in the 2D-geometry close to the ground. Regarding to the VOC influence, the O_3 gained by including VOC reactions is analysed in the 3-D geometry, at 3 m, for the case 2 (Fig. 3.9).

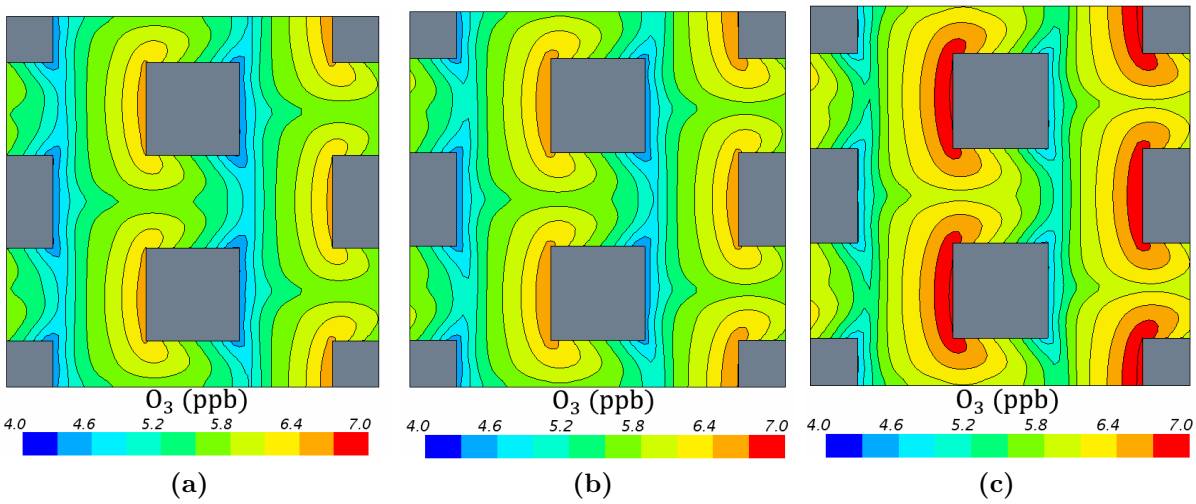

Figure 3.9: Maps at 3 m of the O_3 concentration (ppb) for the (a) PSS, (b) CCM1/5 and (c) CCM1/2 in the Case 2.

The O_3 map of the CCM1/2 show the increase of the O_3 concentration with the CCM1/2. The VOC reactions increase the NO_2 levels and, thus, the photolysis of NO_2 promotes the O_3 production.

For an overview of all chemical scenarios in the Case 2 and Case 4, the normalized concentrations are computed (Eqs. 3.2). Hence, the profiles of the horizontal spatial average of the normalized concentration, $< NO_N >$ and $< NO_{2N} >$, are depicted in Fig. 3.10. Note that the red line represents the normalized concentration of the non-reactive pollutant, which is the same for the NO and NO_2.

The differences on the $< NO_N >$ and $< NO_{2N} >$ profiles between the domains are basically caused by the flow pattern. Whereas in the 3D-geometry the pollutants are progressively reduced from the bottom, in the 2D-geometry, the average concentration holds practically constant in height up to the top of the canopy. It corresponds to the vertical profiles of wind speed and k, resulted from the interaction of the flow and the obstacles (Fig. 3.5). Below the canopy top, the values of k are larger in the 3D configuration than in the 2D geometry, which encourages the turbulent mixing. Nevertheless, regarding to the chemical influence, the same general conclusions are obtained in both domains, independently of the type of configuration. Secondly, the vertical distributions bear out the previous outcomes, where the difference from the non-reactive approach is clearly larger in the Case 2 (with larger background O_3). On the other hand, there is no difference among the chemical scenarios (PSS, CCM1/5, CCM1/2) in the Case 4 (with lower background O_3) whereas in the Case 2, small variations in the NO and NO_2 are obtained with the CCM1/2 with respect to PSS and CCM1/5. Even the results of CCM1/5 hardly differ from the PSS.

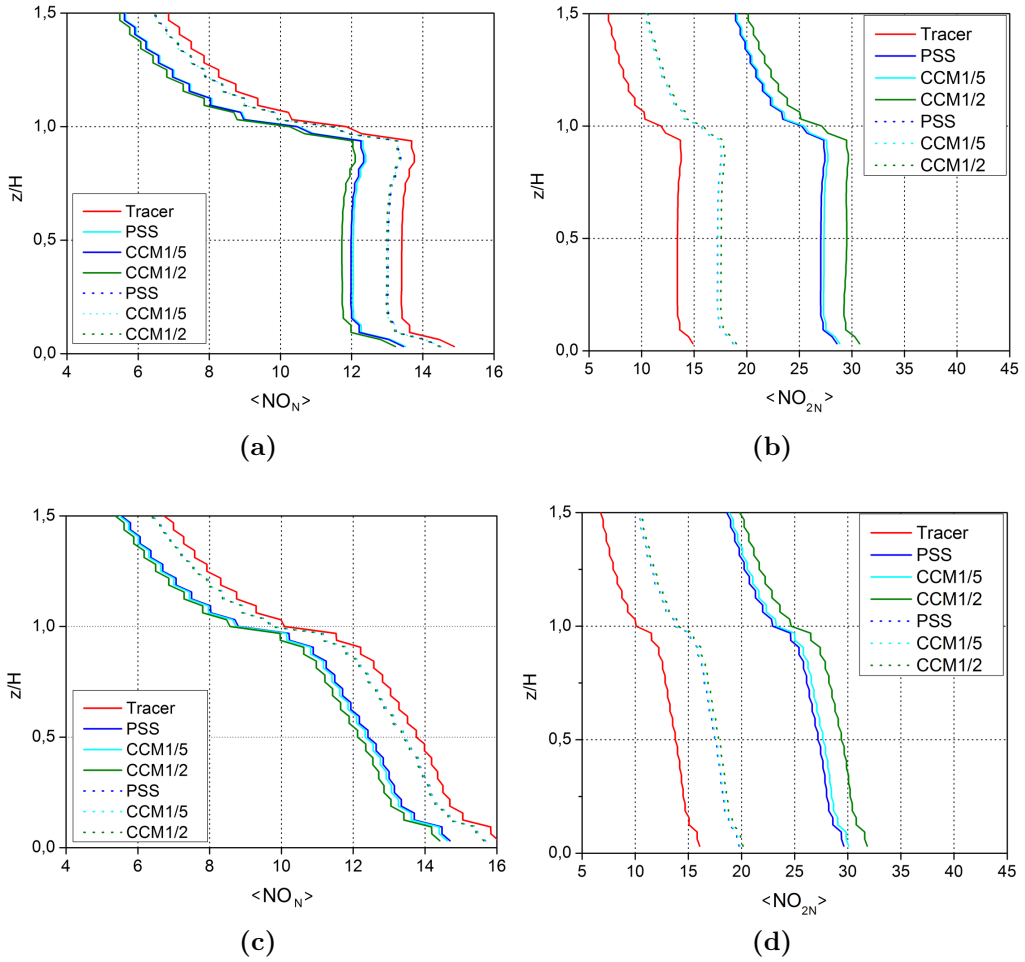

Figure 3.10: Vertical profiles of horizontal spatial average of $< NO_{R,N} >$ and $< NO_{2N} >$ for all chemical scenarios in Case 2 (solid line) and Case 4 (dotted line) in (a,b) the 2D-geometry and (c,d) the 3D-geometry.

To summarize these outcomes, the atmospheric conditions related to the solar position and the ambient O_3 give rise to important variations on the NO_R and NO_{2R} concentrations. With lower O_3 (Case 4), the relative differences of concentration between the reactive and non-reactive approaches are smaller with values below 15% (Fig. 3.7). Nonetheless, in the Case 2, the concentration of the NO_{2R} significantly increases up to values above 60% from the NO_{2T} in both geometries (Fig. 3.7-3.9).

Concerning the influence of the VOC, the NO_2 and O_3 levels from these atmospheric cases reveal a slight impact using the NO_x-O_x-VOC scheme, even with greater ambient O_3 (Case 2). However, by increasing the VOC release, slight differences are obtained on the NO and NO_2 levels in comparison with using the NO_x-O_3 scheme. It is due to the NO_x levels are substantially elevated against the VOC. Hence, the NO_x levels tend to inhibit the O_3 formation and, thus, to limit the O_3 production owing to the VOC reactions. In turn, the available O_3, from the background, promotes the loss of NO. For that reason, the influence of the VOC in the lower O_3 case is negligible whereas, with enough available O_3, its importance

is slightly noticeable.

3.3.3 Wind speed influence on reactive pollutants

In this section, the impact of wind speed on the chemical influence is analysed with the largest background O_3 (Case 1 and Case 2 in Table 3.1). To do that, different wind speeds, u_τ=0.45 m/s and u_τ=0.225 m/s, are simulated keeping constant the rest of atmospheric variables. Based on previous results, the cases of the greatest background O_3 are here studied given that larger chemical influence is obtained within the canopy. The concentration of a tracer (non-reactive compound) is inversely proportional to wind speed by subtracting the background concentration (Appendix 6.2). However, the non-linearity of the chemical reactions brings about changes in this behaviour. The deviation in concentration of reactive pollutants, at street level, is dependent on both the dispersion within the canopy and the exchange with the overlying air, linked to the street ventilation.

Concerning the chemical influence, the same conclusions are obtained for the NO and NO_2. Hence, just the NO_2 results are shown in this section (more detail about the NO results in Sanchez et al. (2016). Figure 3.11 displays the comparison of δNO_2 for the Case 1 and Case 2 in the 2D-geometry.

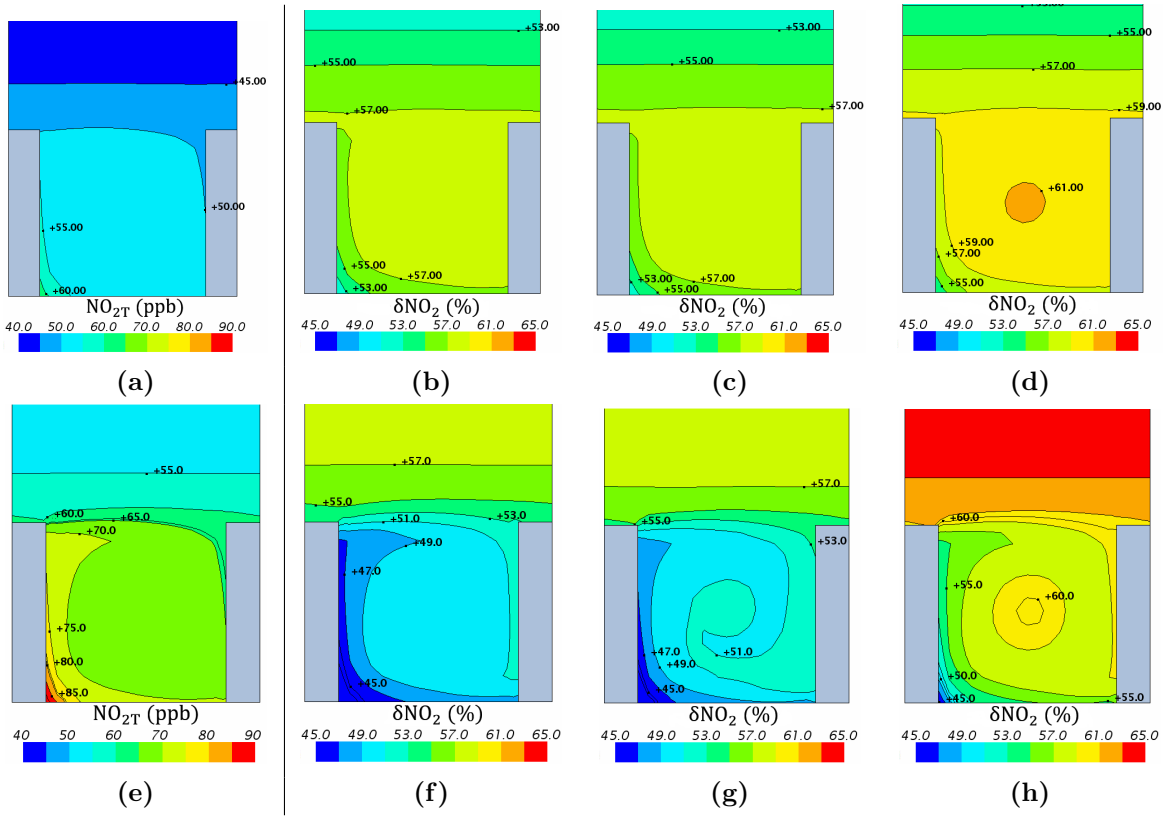

Figure 3.11: For the Case 1: (a) NO_{2T} (ppb) and (b-d) δNO_2 (%) from PSS, CCM1/5 and CCM1/2. For the Case 2, (e) NO_{2T} (ppb) and (f-h) δNO_2 (%) from PSS, CCM1/5 and CCM1/2.

Despite the NO_{2T} within the canopy is lower in the Case 1 than in the Case 2, around 50 ppb versus 70 ppb, δNO_2 turns out close values. Nevertheless, the values of δNO_2 are around 55-60% in the Case 1 and slightly lesser in the Case 2. The main particularity between both cases focuses at the bottom, close to the emissions. In the Case 1, the faster wind speed enhances the street ventilation, which boosts the mixing of pollutants and triggers the main interactions between NO_x and O_3. As a consequence, greater chemical influence from the non-reactive approach are obtained. On the other hand, the larger differences between CCM1/2 and PSS are found in the Case 2, even above the canopy.

At street level, δNO_2 is examined in the 3D-geometry. Figure 3.12 displays δNO_2 resulted from the PSS, CCM1/5 and CCM1/2, both in the Case 1 and the Case 2.

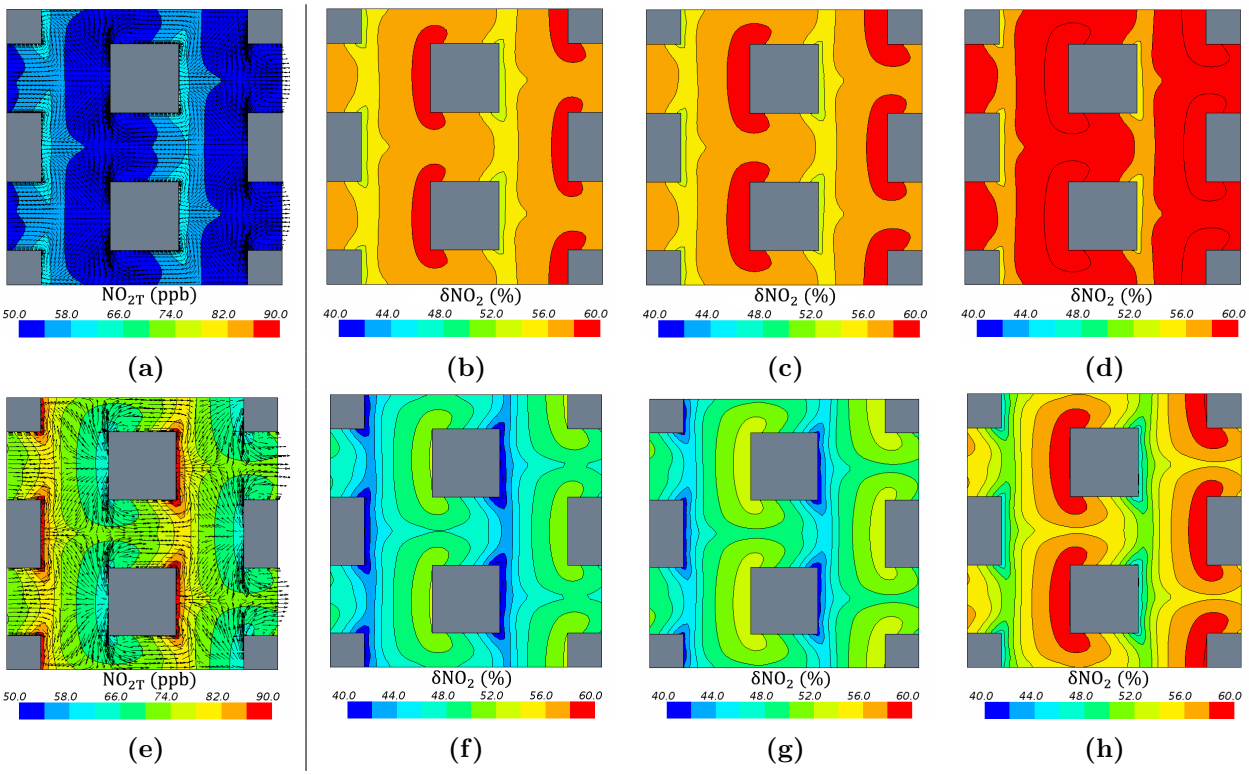

Figure 3.12: Horizontal section at 3 m AGL of: (a) NO_{2T} (ppb) and (b-d) δNO_2 (%) from PSS, CCM1/5 and CCM1/2 respectively, in the Case 1. For the Case 2: (e) NO_{2T} (ppb) and (f-h) δNO_2 (%) respectively from the PSS, CCM1/5 and CCM1/2.

In the 3D-geometry, comparing with the non-reactive approach, δNO_2 shows larger differences in the Case 1, as in the 2D-geometry. The rapid flow enhances the pollutant withdrawal from the street and encourages the pollutant mixing with the overlying air. Thus, the O_3 inflow to the street rises triggering the conversion of NO into NO_2. As a result, greater deviations of reactants with respect to the non-reactive approach is obtained. As for the influence of VOC reactions, both cases show similar δNO_2 for the PSS and CCM1/5 and it is slightly larger from CCM1/2.

The average concentration at 3 m of δNO_2 yields 57%, 57% and 59% for the PSS, CCM1/5 and CCM1/2 in the Case 1 whereas in the Case 2, it is respectively 47%, 49% and 55%. There is low difference in δNO_2 from both wind cases, being greater with larger O_3 entrainment into the street (Case 1). However, the influence of VOC on the NO_2 concentration is more relevant with lower wind speed (Case 2). Whereas in the Case 1 the chemical activity in the street is basically dominated by the photostationary state, in the Case 2 the VOC interactions become important in the NO conversion to NO_2.

Lastly, the vertical profiles of $< NO_{2N} >$ in each domain is depicted in Fig. 3.13.

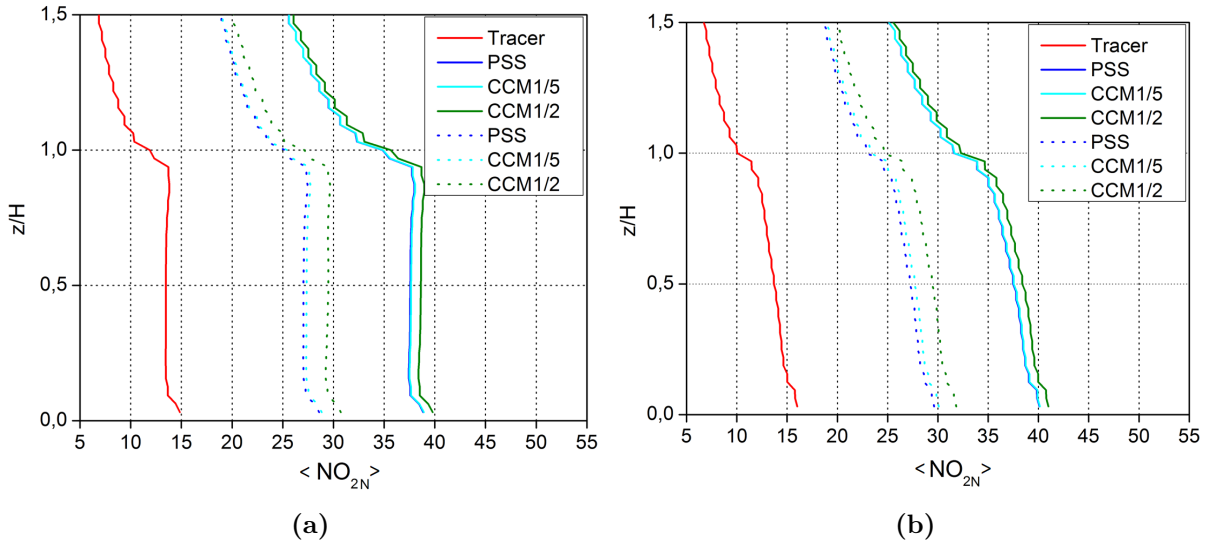

Figure 3.13: Vertical profiles of $< NO_{2N} >$, for all chemical scenarios, in the Case 1 (solid line) and Case 2 (dotted line) for: (a) the 2D-geometry and (b) the 3D-geometry.

The behaviour of the chemical influence in response to vary the wind speed is examined comparing the vertical distributions. For a non-reactive pollutant, the same profile of $< NO_{2N} >$ is obtained for the different wind speeds (red line). However, the $< NO_{2N} >$ profiles from any of the chemical schemes exhibit the non-linearity of chemistry by increasing the wind speed twice as much. Therefore, the reduction of the wind speed by half does not result in the double of the chemical influence. The differences between chemical approaches are consistent with the results previously discussed. This reveals that the impact of the chemical reactions on pollutant concentrations is dependent on a set of atmospheric factors, particularly in this study, on the wind speed and the available O_3 jointly .

3.4 Vertical transport

In this section, all atmospheric cases are analysed by means of the vertical concentration fluxes. In this way, both the removal of pollutants from the street and entrainment into the

street are analysed in each atmospheric condition. Given that the global conclusions of the chemical behaviour are similar in both domains, this section only depicts the vertical fluxes in the 3D-geometry.

The total flux ($F_{T,i}$) is expressed by the sum of the mean flux ($F_{m,i}$) and the turbulent flux ($F_{t,i}$). The horizontal spatial average (<>) of the vertical concentration fluxes for the NO, NO_2 and O_3 are performed every 1 m in height. Hence, $F_{T,i}$ for ith species is computed as follows:

$$F_{T,i} =< \overline{w\,C} >= F_{m,i} + F_{t,i} \tag{3.3}$$

$$F_{m,i} =< \overline{w}\,\overline{C_i} > \tag{3.4}$$

$$F_{t,i} =< \overline{w'\,C_i'} >= - < K_c \frac{\partial C_i}{\partial z} > \tag{3.5}$$

Here $\overline{w}$ and w' are the mean component of the vertical velocity and its fluctuation respect to the mean. And C_i and C_i' are the corresponding components to the concentration of ith species.

For a harmonious study of the NO and NO_2, the vertical fluxes are normalized in order to properly compare the results with the non-reactive approach. To do that, the concentration imposed at the top is dismissed in the computation of the fluxes. The concentracion fluxes are normalized following the method developed for an inert pollutant in Martilli et al. (2013). Hence, the $F_{T,i}$ for non-reactive species, considering an homogeneous emission, the steady state and neglecting vertical changes in the air density, is normalized as:

$$\textit{below the canopy top}, \quad < \overline{w\,C} >_N = \frac{< \overline{w}\,\overline{C} > + < \overline{w'\,C'} >}{S_{em}} \tag{3.6}$$

$$\textit{above the canopy top}, \quad < \overline{w\,C} >_N = \frac{< \overline{w}\,\overline{C} > + < \overline{w'\,C'} >}{S_{em}} \frac{A_{street} + A_{roof}}{A_{street}} \tag{3.7}$$

where S_{em} is the constant emission flux (ppb $m^2 s^{-1}$) at the surface. A_{street} and A_{roof} are the horizontal areas of the streets and the building roofs respectively. Note that the average total flux of a non-reactive pollutant is equal in all atmospheric conditions, turning out one only profile for the NO_T and another one for the NO_{2T}. Hereafter, the horizontal spatial average of the normalized total fluxes of NO and NO_2 is referred to as $< \overline{w\,NO} >_N$ and $< \overline{w\,NO_2} >_N$.

Figure 3.14 illustrates the vertical profiles of $< \overline{w\,NO} >_N$, $< \overline{w\,NO_2} >_N$ and $< \overline{w\,O_3} >$ for the CCM1/2 and PSS in the 3D-geometry. The results from the CCM1/5 are not shown since they are practically equal to that the PSS.

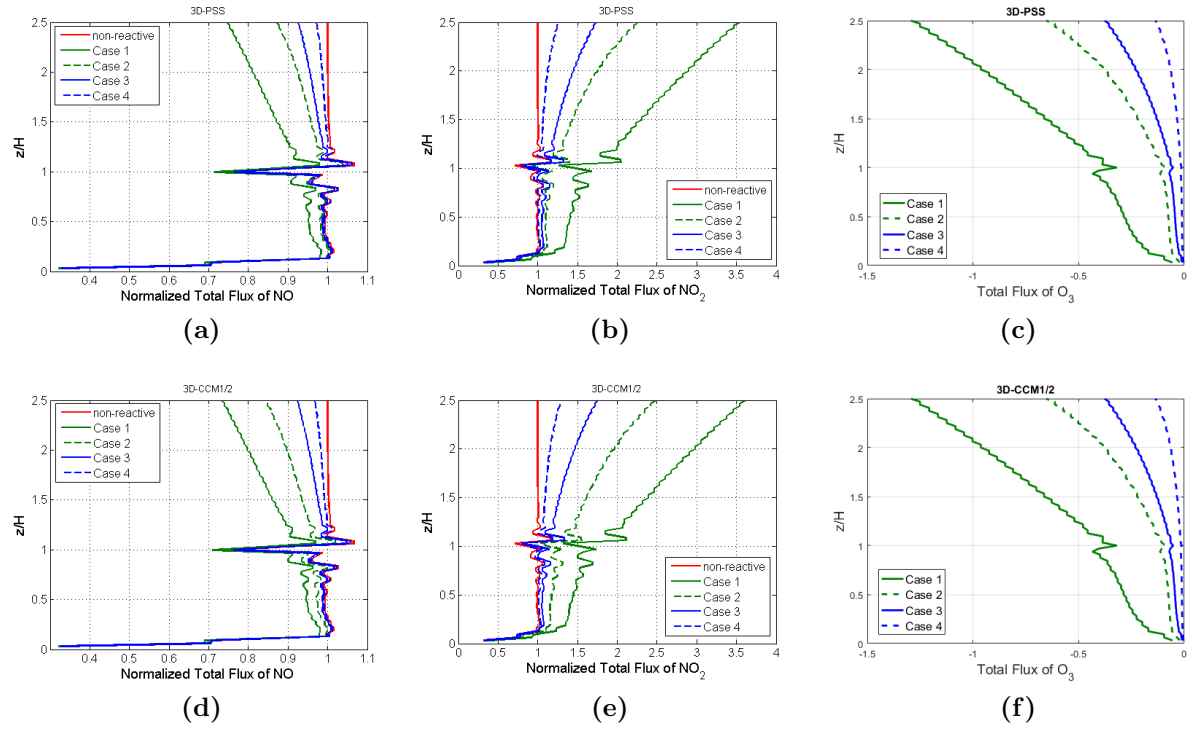

Figure 3.14: Vertical profiles of $< \overline{w\,\mathrm{NO}} >_N$, $< \overline{w\,\mathrm{NO_2}} >_N$ and $< \overline{w\,\mathrm{O_3}} >$ (ppb m s^{-1}) respectively for (a-c) the PSS and (d-f) the CCM1/2.

The vertical transport of a non-reactive pollutant above the canopy top is mainly dominated by the turbulent processes because the mean vertical velocity is zero, but instead, in the street, the vertical motions are mainly controlled by the mean flux. The dispersion of the reactive pollutants is also managed by these dynamical processes, being in turn affected by chemical interactions with O_3 and VOC.

Both in the CCM1/2 and PSS scenarios, the largest deviation of $< \overline{w\,\mathrm{NO}} >_N$ and $< \overline{w\,\mathrm{NO_2}} >_N$ from the non-reactive profile is obtained for the Case 1 and Case 2 (green lines), essentially associated with a highest O_3 inflow in the street (Fig. 3.14c-f). In contrast, for the Case 3 and Case 4 (blue lines), the vertical transport of the reactants is fairly similar to the non-reactive approach within the canopy. In these cases, the influence of introducing chemical mechanisms just can be observed above the canopy top, where the O_3 concentration is not rapidly reduced by the high NO levels in the street. Therefore, the greatest impact of the chemical activity on pollutants is obtained in atmospheric conditions that promote the vertical mixing of pollutants. Comparing $< \overline{w\,\mathrm{NO}} >_N$ and $< \overline{w\,\mathrm{NO_2}} >_N$ obtained from the PSS and CCM1/2, VOC reactions barely produce changes in the outflows of NO and NO_2 for the Case 2.

Lastly, the rapid conversion of NO into NO_2 is studied by the ratio NO_{2N}/NO_N for the PSS, CCM1/5 and CCM1/2 in all atmospheric cases in the 3D-geometry. Figure 3.15a shows

the average concentration within the canopy of the ratio NO_{2N}/NO_N in comparison with the total flux of O_3 at roof level ($< \overline{w\,O_3} >$). Thus, the chemical influence is distinguished as a consequence of the deviation from the non-reactive behaviour (NO_{2N}/NO_N=1). With larger O_3 entrainment, the chemical deviation from the non-reactive behaviour is larger, being the maximum differences (NO_{2N}/NO_N ≈3.5) associated with faster wind speed (red filled symbols). In contrast, when the O_3 levels are not enough with respect to the strong NO_x emissions, the reactants behaviour barely differ from the non-reactive approach.

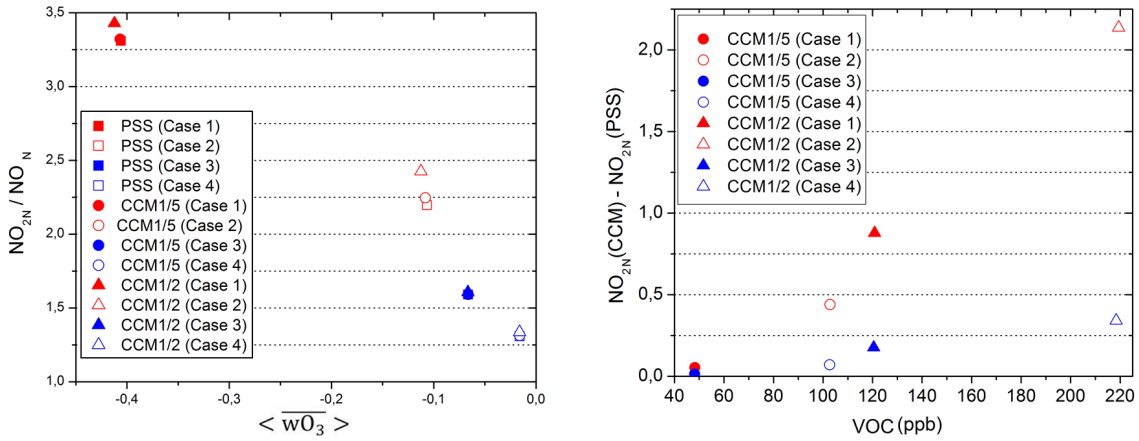

(a) **(b)**

Figure 3.15: (a) Average concentration within the canopy of NO_{2N}/NO_N against the total flux of O_3 at roof level and (b) variation of the average concentration within the canopy of NO_{2N} with CCM1/5 and CCM1/2 from that the PSS over the average concentration of VOC.

Secondly, the deviation of NO_{2N}, after including the VOC reactions, is analysed depending on the VOC levels within the canopy (Fig. 3.15b). These results show that the influence of the VOC on the NO_2 concentration depends on both the NO_x levels and the available O_3 in the street. With higher O_3 within the canopy, the NO_2 levels from the CCM1/2 scenario increasingly differ from the PSS as the VOC emissions increase. In addition, with lower wind speeds, that deviation rises caused by the emitted VOC hold retained within the canopy and, thereby, the residence time of pollutants in the street increases. However, the results from the CCM1/5 show similar outcomes to PSS since the VOC levels are not enough to provide a significant deviation in the NO_2 resulted from the PSS.

3.5 Summary and conclusions

Modelling the dispersion of NO and NO_2 require to include the chemical reactions that take place in the urban atmosphere. The NO_2 concentration is mainly dominated by the interactions with NO and O_3, according to the photostationary state. Nonetheless, there is a more complex chain of chemical reactions, in which the VOC are involved, that should also be considered.

The purpose of this study is to evaluate the importance of the chemical reactions on the NO and NO_2 dispersion considering three chemical approaches in the CFD simulation: (a) non-reactive pollutants, (b) the $NO_x - O_3$ scheme and (c) the NO_x−O_3−VOC scheme. For the latter scenario, two options of traffic emission ratios are deemed: VOC/NO_x=1/2 and VOC/NO_x=1/5. In this way, the effect of including the VOC interactions on analysing the reactive NO_2 is compared with the results from the photostationary state. In addition, the influence of the background atmospheric conditions on the chemical reactions is tackled through the variation of the wind speed and the solar position, which is linked to the ambient O_3. This analysis is carried out both in a single street canyon (2D-geometry) and in the staggered array of cubes (3D-geometry) in order to draw general conclusions with no dependence on the geometry. Therefore, the impact of several atmospheric variables on the dispersion of reactive pollutants can be examined within the canopy in simplified urban configurations.

The results show that the available O_3 in the street determines the difference in the dispersion of the NO and NO_2 as reactive species against the non-reactive approach. In turn, the wind speed controls the vertical transport and therefore, the pollutants exchange between the street and the overlying air, which is related with the inflow of O_3 to the street. Based on this, the greatest differences of the reactive NO and NO_2 from the non-reactive scenario are obtained with larger background O_3 (Case 1 and Case 2). Moreover, the faster wind speed promotes that the influence of the chemical activity increases because improving the mixing of pollutants in the canopy. This entails a large O_3 entrainment into the street and outflow of the emitted NO_x. The vertical fluxes proves that the available O_3, regardless of the wind speed in the lowest background O_3 cases (Case 3 and Case 4), is not enough to produce a significant influence of including chemical reactions on the NO and NO_2 concentration. And, just above the canopy top, the chemical deviation from the non-reactive behaviour is perceptible on the vertical profiles.

Concerning the chemical scheme to be used for modelling the NO and NO_2 dispersion, the influence of the VOC interactions is analysed against the results of just using the photostationary state. The greatest deviation of the reactants between the chemical schemes is observed in the Case 2, with low wind speed and large background O_3. Larger VOC release (VOC/NO_x=1/2) helps to rise the difference of NO_2 concentration obtained from the photostationary state. The weaker wind flow retains the VOC concentrations within the canopy, which compete with the O_3 for the NO oxidation and, thereby, it produces NO_2. Hence, the O_3 loss in the street is reduced and, besides, the NO_2 production slightly increases by using the complex chemical scheme. In contrast, the NO and NO_2 concentrations by implementing the NO_x−O_x−VOC scheme with the emission ratio VOC/NO_x=1/5, turn out similar values to those derived from the NO_x−O_3 scheme.

These conclusions of the behaviour of the reactive pollutants can be generalized to atmospheric conditions in urban environments. In atmospheric conditions of weak solar radiation, the ambient O_3 formed is usually low, and the chemical reactions are relatively slower than the rapid dynamical processes characteristic of urban areas. In addition to that, the high concentrations of NO_x, associated to the traffic emissions, give rise to the quick reduction of the O_3 concentration at street level. Accordingly, the implementation of any chemical scheme to simulate NO and NO_2 dispersion may provide small differences in comparison to the non-reactive approach. In contrast, in meteorological conditions of high solar radiation, the background O_3 increases promoting the chemical interactions with the NO and NO_2. It may induce an important impact on the reactive pollutant concentration in the streets with respect to not use a chemical scheme in the CFD simulation. As for considering of NO_x-O_x-VOC scheme instead of the NO_x-O_3 mechanism, the difference in the NO and NO_2 concentrations is dependent on both the presence of the VOC levels in air, in comparison with those of NO_x, and the background O_3. Based on these results, the difference between chemical schemes is intensified by increasing the amount of VOC within the canopy.

The computational resources required to implement a chemical mechanism in the CFD model should be considered. Hence the importance of chemical reactions on the pollutant dispersion has to be analysed in several conditions, since it is affected by many key factors, i.e. the meteorological conditions, the traffic emissions, the urban air composition or the flow pattern representative of the urban area. Therefore, this study provides a better understanding of the chemical influence to seek the best compromise between the complexity of the chemical scheme needed and the computational load required in order to simulate the NO_2 dispersion in urban scenarios.

Acknowledgements

This study has been supported by European Project LIFE $MINO_x$-STREET (LIFE12 ENV/ES/000280) funded by European Union. Authors thank to Frank Kirchner (GAIASENS Technologies) for providing the condensed chemical mechanism (NO_x-O_x-VOC scheme) to be implemented in the CFD model for this study. I would like to grateful with Extremadura Research Centre for Advanced Technologies (CETA-CIEMAT) by helping in using its computing facilities for the simulations. CETA-CIEMAT belongs to CIEMAT and the Government of Spain and is funded by the European Regional Development Fund (ERDF).

Chapter 4

Modelling the dispersion of reactive pollutants in an urban area

4.1 Introduction

The urban air quality is controlled both by the background characteristics of the atmosphere at larger scale and by the dynamical and chemical processes at local scale, basically driven by the turbulence. In urban environments, turbulence primarily dominates the dispersion and mixing of pollutants in the streets. In turn, the emitted pollutants undergo rapid chemical transformations modifying the air composition. Hence, the pollutants advected into the urban area interact with the emitted species from local releases, triggering multiple chemical conversions that can lead to relevant changes in pollutant concentrations. Accordingly, the dispersion of reactive pollutants in urban areas is jointly driven by the turbulence and the chemical processes occurred in the streets.

Many studies focus on analysing the impact of turbulent processes on the chemical activity by means of the Damkhöler (Da) number in the atmospheric boundary layer (Galmarini et al., 1995; Krol et al., 2000; Vilà-Guerau de Arellano et al., 2004). These studies reveal the role that the turbulent mixing plays on the chemical reactions, together with the importance of the chemical balance among reactive species. In particular conditions of turbulence and chemical activity, the chemical terms included in the governing equations can be comparable to the dynamical terms (Vilà-Guerau de Arellano et al., 2004). It means that the time scales of chemical reactions and turbulent mixing are of the same order. Krol et al. (2000) showed that the chemical equilibrium among pollutants also determine the relation between turbulence and chemical activity. In chemical equilibrium among pollutants, the effects of the turbulence on the chemical reaction are reduced. Jonker et al. (2004) concluded that the reactive species are dependent on both the Da number and the chemical balance among

reactants. Vilà-Guerau de Arellano et al. (2004) thoroughly examined the influence of the turbulence on the chemical activity using dimensionless numbers, such as the Da number. They concluded that the turbulent processes dominate the dispersion and mixing of the reactive pollutants in the ABL and, thereby, control the chemical activity of the reactants.

The inhomogeneity of turbulence in urban settings leads to also analyse the influence of the adveccion-diffusion processes on the chemical conversion. In a street canyon, Baker et al. (2004) proved that the chemical terms may be comparable to the advection and diffusion terms in the transport equation for a reactive pollutant. They also proposed the deviation factor from the chemical equilibrium in order to study the efficiency of the reacting mixing at local scale. Zhong et al. (2015) examined the chemical behaviour with a $NO_x - O_3$ mechanism in an idealized deep street canyon (aspect ratio equal to 2). They concluded that the largest deviation from the chemical equilibrium is obtained close to the NO_x emissions, where the imperfect pollutant mixing is greater.

In real urban environments, the impact of dynamical processes on the chemical activity is difficult to study since there are many factors that can affect the chemical transformation, e.g. the meteorological conditions, the ambient concentration, the irregularity of the buildings layout or the traffic emissions. For that reason, the influence of the chemical reactions are analysed by comparing with a non-reactive approach, under the same conditions. Currently, some studies are addressed to model the dispersion of reactive pollutants in urban scenarios through the CFD simulations. Santiago et al. (2017a) examined the effect of including chemical reactions in the CFD model in a peak and off-peak traffic conditions in an urban area at wintertime. They concluded that the modelled concentration of NO_2 shows similar results comparing the reactive and non-reactive assumptions, with differences below 20% at street level. Kim et al. (2012) studied the sensitivity of a CFD model to include chemical mechanisms for simulating the dispersion of the NO, NO_2 and O_3 throughout the day, in an irregular street. Similar concentrations of NO and NO_2 were obtained after considering both a full chemical mechanism and the photostationary state. In contrast, a significant difference in the O_3 concentration under lower pollution conditions was captured. It is worth noting that the VOC/NO_x emission ratio of vehicles was established at 2.7.

In Chapter 3, the overall outcomes revealed small differences on the NO_2 concentration at street level between the $NO_x - O_3$ and $NO_x - O_x - VOC$ schemes. In this study, the emission factors of NO_x and VOC are obtained from the emission inventories for the road transport in Spain (Madrid-Council, 2014), which report larger emissions of NO_x against the VOC release. To ascertain the deviation on the NO_2 concentration in real atmospheric conditions, the use of the $NO_x - O_x - VOC$ scheme was compared with the photostationary state, at 1200 LST (Local Solar Time), in a real urban scenario (see Appendix 6.2). The NO and NO_2 results were evaluated with measurements in situ. The conclusions of the modelled

concentrations revealed small differences between the use of both chemical mechanisms. It may be related to the small VOC levels in air in regards to the NO_x since the VOC/NO_x emission ratio is 1/5. Kwak and Baik (2012) analysed the impact of the VOC/NO_x emission ratio concluding that, as the VOC emission level increased, the NO_2 and O_3 became larger in the street canyon. Accordingly, the need to include the VOC interactions for modelling the NO_2 dispersion is dependent on the atmospheric background composition and the emissions traffic, representative of the urban area to be simulated.

This chapter is addressed to thoroughly analyse the atmospheric factors that affect the influence of the atmospheric chemistry on the NO_2 concentration in a real urban area. To that end, the dispersion of the reactive NO_2 is modelled over time, from 0600 LST to 1600 LST (from 08h to 18h local time) at early-autumn in a real urban scenario. Based on the results obtained in Appendix 6.2, just the NO_x-O_3 scheme is herein considered. Thus, the NO and NO_2 are simulated under the two chemical approaches: no chemistry and NO_x-O_3 scheme. Once the modelling results are validated with measurements, the chemical influence on pollutant concentrations are examined, both in time and space, taking into account the atmospheric variability. Lastly, the impact of dynamical processes on the chemical effect is studied in detail, at local scale, in a real urban environment.

In this way, this work attempts to answer the following research questions:

- Which is the impact of the atmospheric conditions at daytime on modelling the dispersion of NO_2 as a reactive specie in a real street?
- How the turbulence mixing and the chemical processes control the NO_2 dispersion in a real street?

4.2 Study case

This study focuses on an urban area located in Alcobendas, close to the North of Madrid, with geographic coordinates 40° 32' N and 3° 37' W (Fig. 4.1a). The research area (blue square in Fig. 4.1b) is located in a residential area, where the mean buildings height is around 18 m and the tallest one is almost 20 m. The main street within the research area includes a dual carriageway separated by a median strip. The representative traffic intensity, given by the AADT for the studied street is around 2000-4000 veh/day (Alcobendas-Council, 2005).

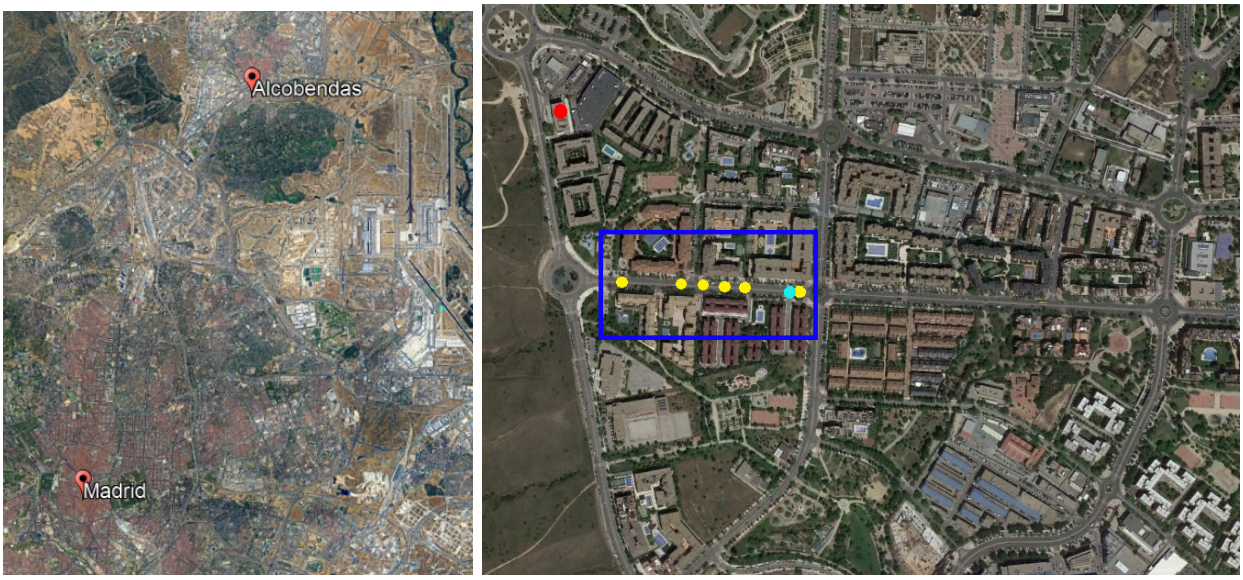

(a) **(b)**

Figure 4.1: (a) Location of the research area around Madrid. (b) Locations of the measurement points (red and yellow points) deployed for the experimental campaign. The blue point represent the location of the camera used for recording the traffic flow in specific days.

In this area, an intensive experimental campaign was carried out from 11th September to 25th October in 2015 (Pujadas et al., 2016) within the framework of the LIFE MINOx-STREET European Project (LIFE12 ENV/ES/000280). For this study, the 29th September 2015 is selected because all the variables needed to undertake the CFD-RANS simulation were collected [§].

The data used for this study are derived from measurements taken at several points deployed along the street and, also, at one sampling point placed on the building's roof, at 20 m AGL. At the reference point (red point in Fig.4.1b), the ambient atmospheric conditions around the research area are intensively recorded every 5 min. In this way, the meteorological variables (wind speed and direction, temperature and solar radiation) together with the concentration of NO, NO_2 and O_3 provides full information of the background conditions. Additionally, six measurement points (yellow points in Fig.4.1b) are deployed on the median strip along the studied street, at 0.4 m AGL, in which both the NO and NO_2 concentrations are taken every 2 min. Besides, the actual traffic flow in the study street was recorded over time for several days throughout the experimental campaign (Pujadas et al., 2016). During this day, the camera was located at east of the street close to the roundabout (blue point in Fig. 4.1b).

[§]For this day, a photocatalytic coating covered a small area (1000 m^2) in the studied street as part of the scope of the project. Both the experimental and the modelling approaches proved the efficiency of the photocatalytic material have a negligible effect on the NO_x concentration in air (Pujadas et al., 2016).

4.3 CFD model description and simulation setup

4.3.1 Geometry and mesh

Figure 4.2a displays the computational domain, whose size is 1600 m x 1000 m, with the top of the domain established at $8H_{max}$, where H_{max} is the height of the tallest building (20 m) (Franke, 2007). The research area (black square in Fig. 4.2a) is vertically quite homogeneous with a packing density of buildings $\lambda_p = 0.3$ and the mean height of buildings around 18 m. A polyhedral mesh is applied with the grid resolution of 2 m in the research area and, externally, it is progressively increased up to 6 meters. The grid size is further reduced to 1 m close to the ground, emissions and buildings resulting in a total of 2.3 10^6 grid points.

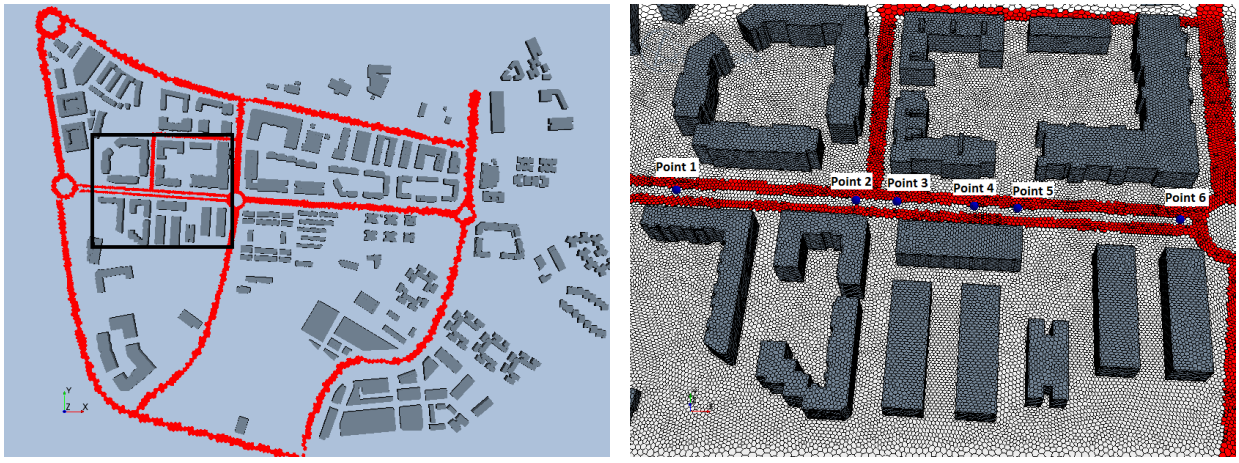

(a) **(b)**

Figure 4.2: (a) Geometry of the computational domain and the research area limited by the black square. (b) Zooming in on the meshed research area and location of the measurements points.

4.3.2 Simulation setup

The CFD-RANS simulation is performed in unsteady conditions for the day 29th September 2015, from 0600 LST to 1600 LST (from 08h to 18h local time). Inlet and outlet boundaries are defined depending on wind direction and symmetry conditions are imposed at the top of the domain.

The inlet conditions are derived from the measurements taken at the reference point on the building's roof. From the experimental data, the wind speed and direction is averaged every 30 min and, thus, the vertical profiles of wind speed, turbulent kinetic energy and turbulent dissipation rate are computed from these data using the Eqs. 2.43-2.45. In these atmospheric conditions, the thermal effects become increasingly important and, thereby, affect the flow distribution. Nonetheless, this aspect has not been considered in this simulation because it

would require include the time-dependent conditions on the solar position, i.e. the variability of the surface heat fluxes. Assuming that this factor modify the dispersion of pollutants in the streets, the isothermal condition has to be assumed in order to perform the simulation in a reasonable computational time.

Concerning the background atmospheric composition, the concentrations of NO, NO_2 and O_3 are obtained from the reference point. The concentration averaged every 30 min is uniformly established at the inlet of the domain (Fig. 4.3). In this study, NO and NO_2 are simulated both as reactive and non-reactive pollutants. For the reactants, the $NO_x - O_3$ scheme is implemented in this simulation changing the chemical constant rates (J_{NO_2} and k_{NO+O_3}, Table 2.3) every hour depending on the solar position and air temperature. Lastly, the same dynamic and chemical time step is 1 s, varying the inlet conditions every 30 min.

Figure 4.3 illustrates the time series of wind speed and direction (at 20 m), the air temperature, the solar position and the concentration of NO, NO_2 and O_3, established as inlet conditions.

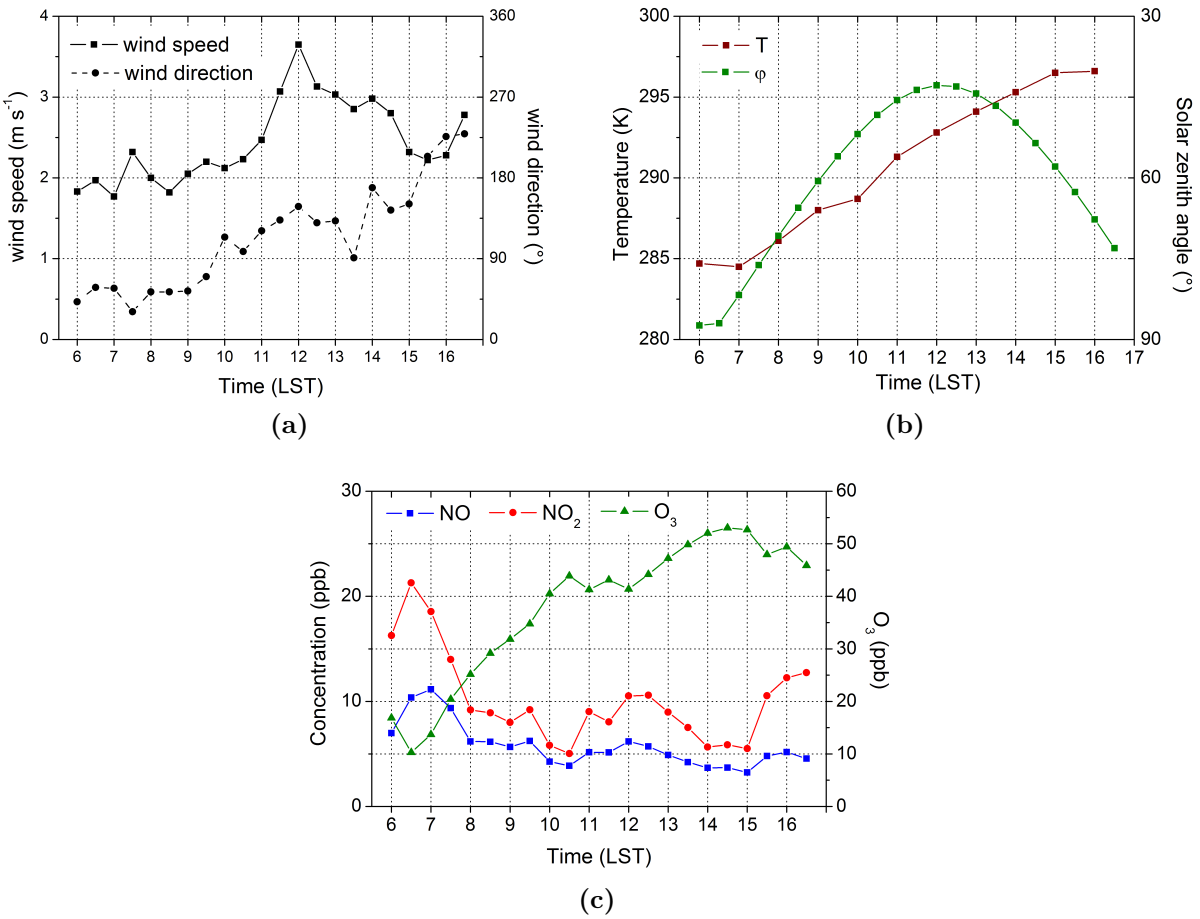

Figure 4.3: Time series of the inlet conditions of: (a) wind speed and direction at 20 m, (b) air temperature and (c) background concentrations of NO, NO_2 and O_3, in ppb.

Lastly, the traffic-related emissions imposed in the simulation are based on the actual traffic flow, recorded in the studied street during the experimental campaign (Pujadas et al., 2016). Hence, this number of vehicles is clustered every hour giving rise to the daily traffic pattern (Fig. 4.4a). Based on that evolution, the amount of vehicles travelling on the rest of the streets is computed keeping the relation of the traffic intensity established by the AADT, reported by the City Council (Alcobendas-Council, 2005). The emitted NO_x per vehicle is established at 0.5 g km^{-1} and the latest emission ratio NO_2/NO_x is considered 0.3 (Section 2.6.3). According to the number of vehicles on each street, the emission rate is uniformly distributed along each street as a result of the computed releases through the traffic intensity (Fig. 4.4b).

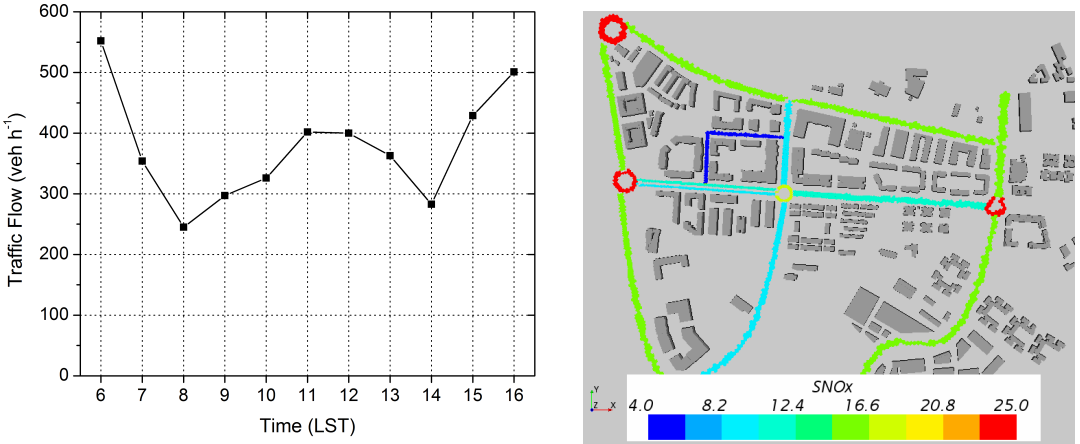

(a) **(b)**

Figure 4.4: (a) Time series of the traffic intensity in the reference street. (b) Uniform distribution of the NO_x emissions (ppb s^{-1}) at 0730 LST depending on the traffic flow representative of each street.

4.4 Validation

4.4.1 Time series at the sampling points

In this section, the modelled NO and NO_2 concentrations are validated with the measurements from 0600 LST to 1600 LST at the sampling points, located along the study street (Fig. 4.5).

Figure 4.5: Location of the measurement points

The proximity of the sampling points to the emission source may introduce perturbations in the measurements that are not reproduced by the model. For that reason, the experimental data of NO and NO_2 are, firstly, filtered by means of the hourly average concentration and its standard deviation. Those values that fall out of the deviation range are dismissed in order to recalculate the average concentration at every hour. Subsequently, the simulated concentrations of NO and NO_2 are also averaged every hour and compared with the measurements at the six points placed along the street. First of all, the NO_x, resulted from the sum of NO and NO_2 is evaluated over time in comparison with the experimental data (Fig. 4.6). Note that the NO_x can be considered as a non-reactive pollutant.

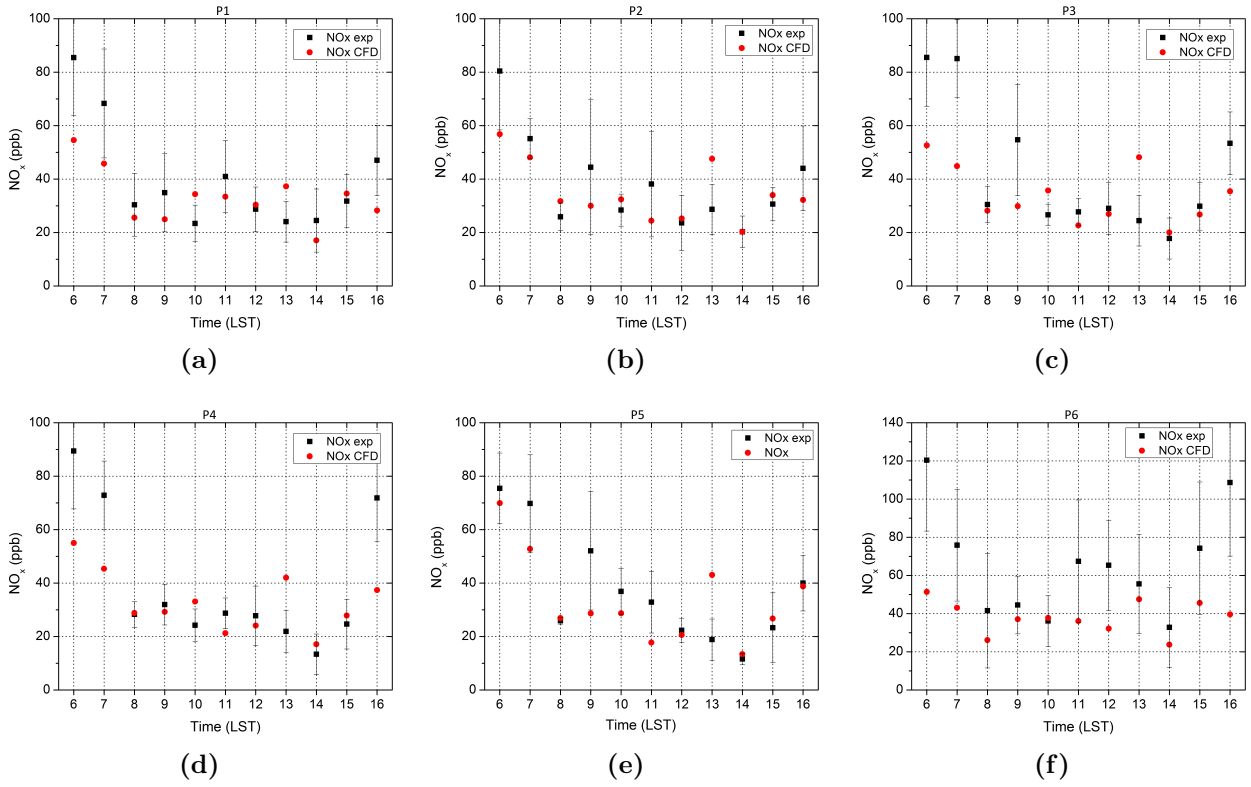

Figure 4.6: (a-f) Time series of the NO_x concentration measured and simulated at the measurement points, in order from P1 to P6. Vertical bars indicate the standard deviation of the measurement, at each hour.

At all the points, the recorded NO_x presents the maximum concentrations at the first and last hours, following the evolution of the traffic intensity and PBL behaviour. The modelled NO_x underestimates those values, specifically at P6. This point is located very close to the roundabout, where accurate data of the traffic flow are not available to estimate the emission and, thereby, it may be the cause of that underestimation. Nevertheless, during the central hours of the day, the modelled NO_x reproduces the temporal evolution, approximately, within the error range of the measurements. The deviation in the simulated NO_x concentration may be caused either by an underestimation of the emissions at that time or by an error in the inlet meteorological variables (e.g. wind direction) or by the atmospheric stability, particularly at first hours of the day. At sunrise, the nocturnal stability is destroyed as the solar radiation increases. Hence, the vertical structure of the lowest atmosphere changes and the temperature and wind profiles differ from the assumed profiles in neutral atmospheric conditions.

For further quantitative details, the statistics NMSE, FB and R (Eq. 2.5) are computed at each point. The NMSE provides information about the overall deviation from the experimental data and, for a good simulation, the threshold is limited below 1.5 (Chang and Hanna, 2004). The FB<0 indicates an underestimation of the simulated concentration against the experimental value. In this case, the resulting NMSE is below 1.5, with a general underestimation and correlation coefficients above 0.6 at all points (Table 4.1). It concludes that the simulation for the NO_x dispersion with respect to the measured NO_x is appropriate.

Table 4.1: Statistical parameters of NMSE, FB and R of the NO_x validation at every points.

	NO_x (P1)	NO_x (P2)	NO_x (P3)	NO_x (P4)	NO_x (P5)	NO_x (P6)
NMSE	0.15	0.09	0.25	0.23	0.11	0.48
FB	-0.18	-0.22	-0.19	-0.11	-0.53	-0.18
R	0.78	0.79	0.66	0.80	0.79	0.65

The NO and NO_2 obtained from both chemical approaches are also evaluated at the sampling points. Hereinafter the NO modelled as reactive and non-reactive pollutants are referred to as NO_R and NO_T respectively. The same notation is used for the NO_2 (NO_{2R} and NO_{2T}). Figure 4.7 displays the validation of the hourly average of the measured NO, NO_R and NO_T at every point. Likewise, the hourly average concentration of NO_{2R} and NO_{2T} against the measured NO_2 is depicted in Fig. 4.8.

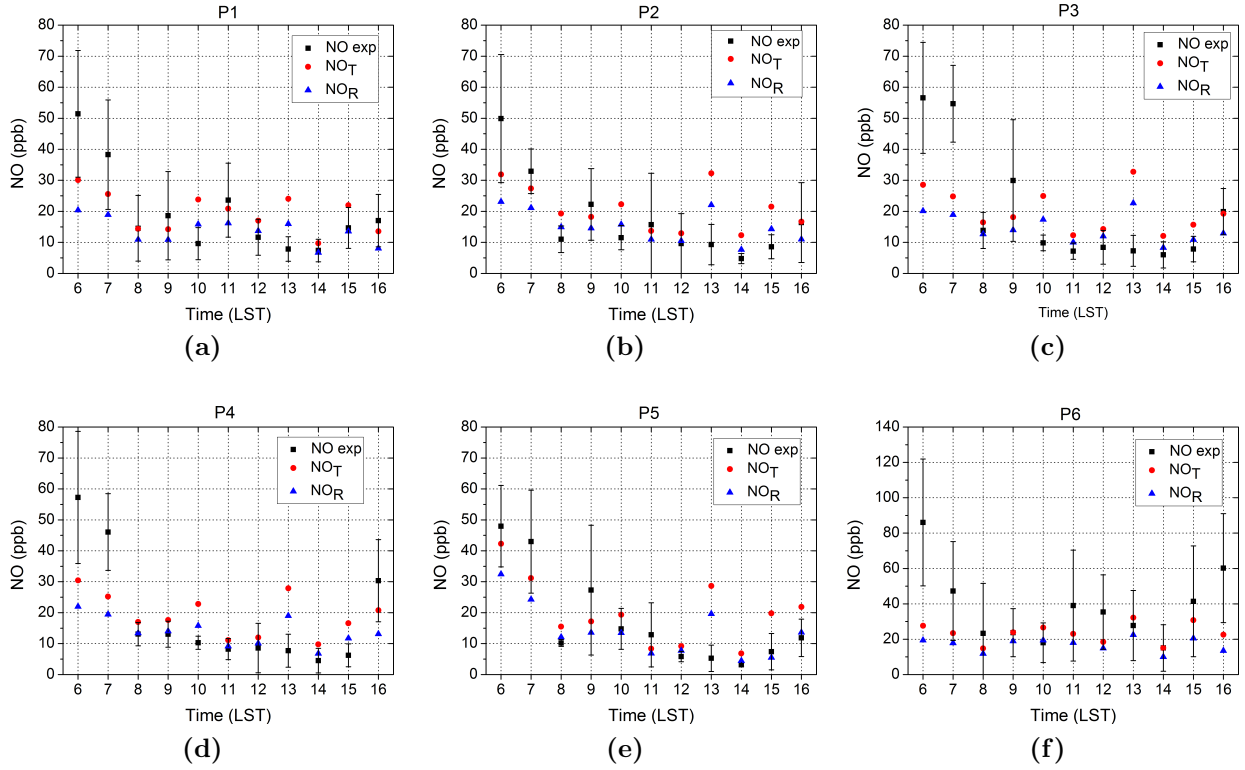

Figure 4.7: (a-f) Hourly average values of the experimental NO, NO_R and NO_T at the sampling points (P1-P6). Vertical bars indicate the standard deviation of the measurements at each hour.

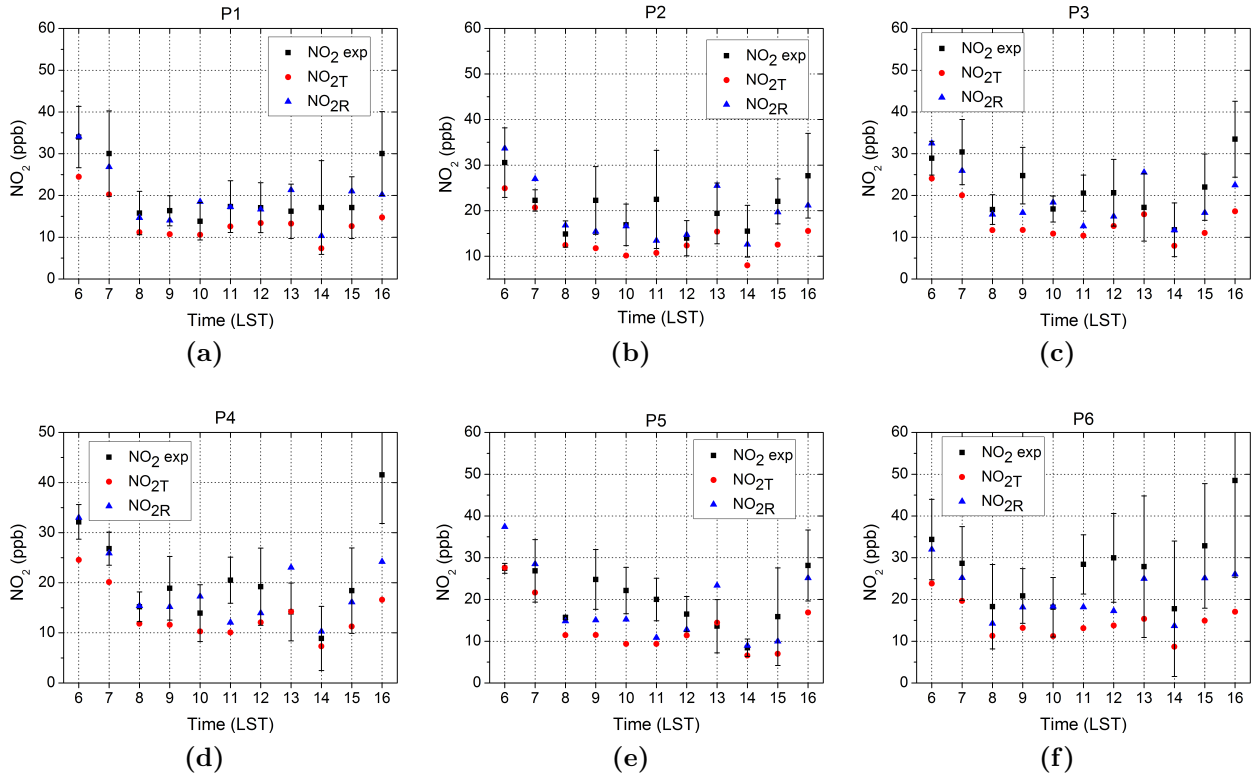

Figure 4.8: (a-f) Hourly average values of experimental NO_2, the NO_{2T} and NO_{2R} at sampling points (P1-P6). Vertical bars indicate the standard deviation of the measurements at each hour.

As the NO_x validation revealed, there is an overall underestimation of the modelled concentrations of the NO and NO_2 at first hours, caused by some uncertainties assumed in the boundaries conditions. Nonetheless, throughout the day, the modelled NO resulted from both the reactive and non-reactive approaches are in a good agreement with the measured NO. Concerning the NO_2 concentration, the NO_{2R} fits slightly better to the experimental value than the NO_{2T}, generally, within the range of the measurement variation.

For a complete ascertainment, the statistical parameters NMSE, FB and R are computed, at each point, for the results of NO (Table 4.2) and NO_2 (Table 4.3).

Table 4.2: Statistical parameters: NMSE, FB and R of NO_T and NO_R at every points.

	P1		**P2**		**P3**	
	NO_T	NO_R	NO_T	NO_R	NO_T	NO_R
NMSE	0.25	0.50	0.29	0.36	0.57	0.88
FB	0.0030	-0.35	0.17	-0.14	-0.010	-0.32
R	0.62	0.66	0.57	0.65	0.46	0.52

	P4		**P5**		**P6**	
	NO_T	NO_R	NO_T	NO_R	NO_T	NO_R
NMSE	0.42	0.70	0.23	0.28	0.61	1.24
FB	0.028	-0.28	0.15	-0.21	-0.47	-0.76
R	0.68	0.72	0.74	0.83	0.32	0.21

Table 4.3: Statistical parameters NMSE, FB and R of NO_{2T} and NO_{2R} at every points.

	P1		**P2**		**P3**	
	NO_{2T}	NO_{2R}	NO_{2T}	NO_{2R}	NO_{2T}	NO_{2R}
NMSE	0.19	0.047	0.16	0.047	0.27	0.089
FB	0.39	0.045	0.32	-0.018	0.46	0.14
R	0.86	0.78	0.72	0.76	0.73	0.60

	P4		**P5**		**P6**	
	NO_{2T}	NO_{2R}	NO_{2T}	NO_{2R}	NO_{2T}	NO_{2R}
NMSE	0.29	0.11	0.23	0.11	0.50	0.13
FB	0.42	0.11	0.40	0.082	0.61	0.27
R	0.73	0.69	0.69	0.67	0.64	0.71

From the simulated concentrations, the NMSE results in all cases below 1.5. For the NO_R, the negative values of FB denote an underestimation of the experimental data at all locations, whereas the NO_T slightly overestimates the measurement. The statistics of the modelled NO_2 concentrations from both chemical approaches yield values of the NMSE below 1.5 and

correlation coefficients above 0.6 in all points. However, unlike the NO_{2T}, the FB for the NO_{2R} holds within the acceptance criteria (-0.3<FB<0.3, Table 2.5) at all sampling points.

For a better understanding of the difference between the chemical approaches, the ratio NO-to-NO_2 is computed over time at every point. The ratio NO-to-NO_2 describes the fast conversion of NO into NO_2 by reacting with O_3. Therefore, it reveals the impact of the chemical reactions. Figure 4.9 shows the time series of the NO-to-NO_2 calculated with both chemical approaches in comparison with that obtained from the experimental data. As explained above, the experimental ratio NO-to-NO_2, at first hours, is not captured by any chemical approach. Throughout the day, the result of NO-to-NO_2 from the reactive approach turns out closer values to that obtained from the experimental data. Accordingly, it remarks that the reactive approach better capture the ratio NO-to-NO_2 in air, showing the fast the NO is converted to NO_2, at the measurement height.

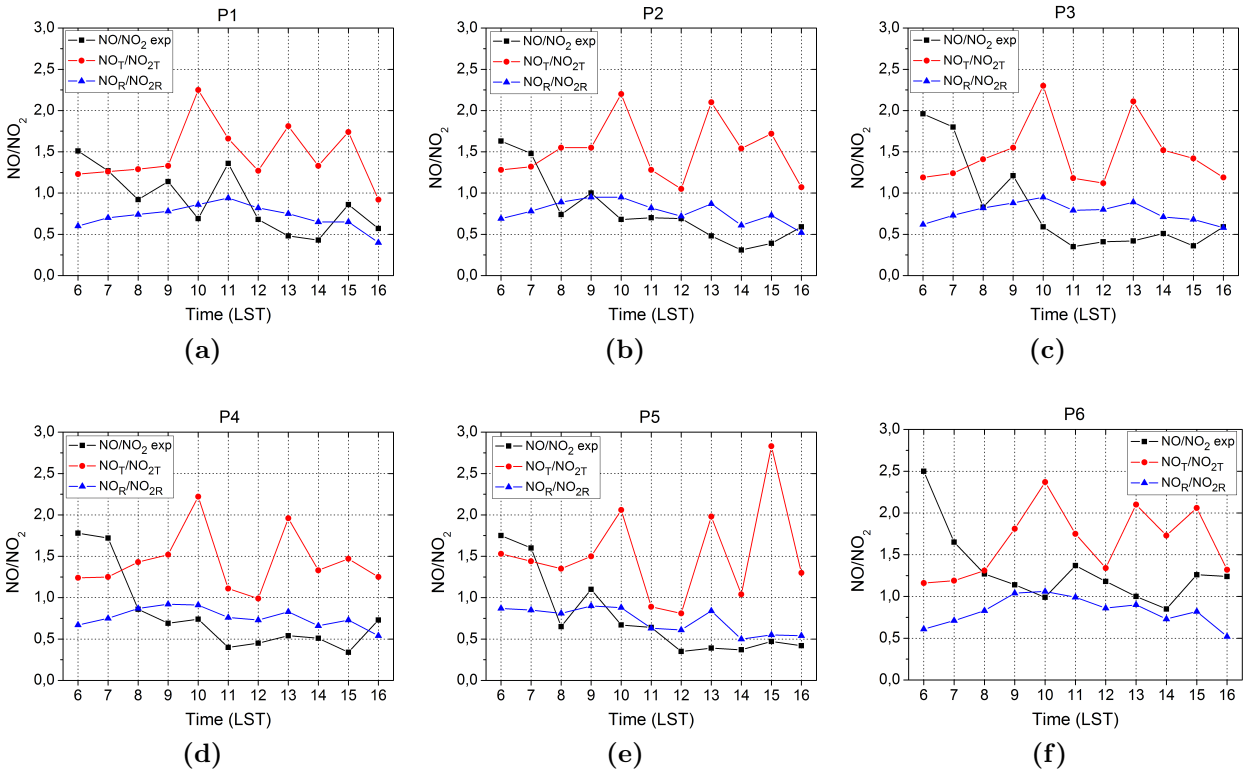

Figure 4.9: (a-f) Time series of the ratios: NO-to-NO_2, the NO_R-to-NO_{2R} and the NO_T-to-NO_{2T} at the measurement points from P1 to P6.

4.4.2 Daytime mean concentration at the sampling points

Additionally, the time-averaged concentration ($\overline{C_i}$) of the NO_x, NO and NO_2 (hereafter referred to as $\overline{NO_x}$, $\overline{NO_R}$ and $\overline{NO_{2R}}$), simulated from 0600 LST to 1600 LST, is evaluated against the mean experimental values, at every point, in Fig. 4.10.

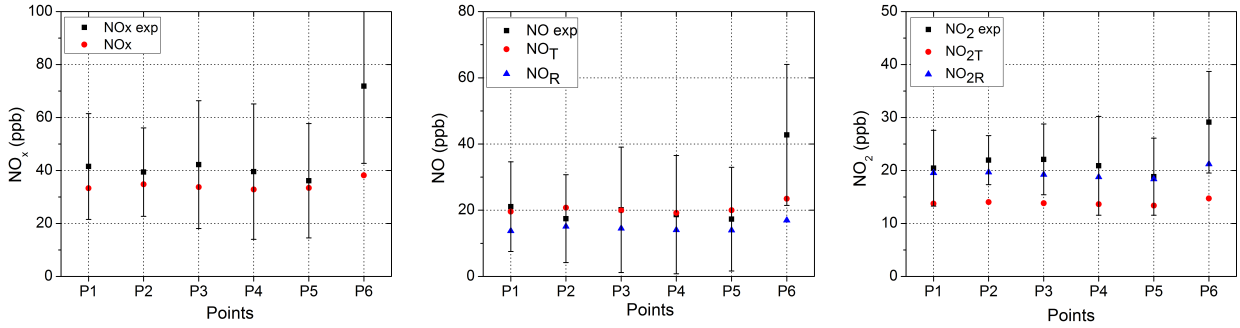

Figure 4.10: At the sampling points from P1 to P6: (a) $\overline{NO_x}$ (ppb), (b) $\overline{NO}$ (ppb) and (c) $\overline{NO_2}$ (ppb) from the experimental data and the simulated reactive and non-reactive pollutants.

The NO_x concentration resulted from the simulation fits quite well to the experimental data with a slight underestimation at most of the points. As for the NO concentration, both the $\overline{NO_R}$ and $\overline{NO_T}$ turn out close values to the measurement within its variation range (except for the P6). In contrast, the results of the $\overline{NO_{2R}}$ differ from the $\overline{NO_{2T}}$ in regards to the experimental values, providing better results when the chemistry is considered.

The statistical parameters (Table 4.4) associated to this analysis reveal high correlations with the experimental data using both modelling approaches. However, the FB yield underestimations in the concentrations of NO_R and NO_{2T} slightly less to the value established in the acceptance criteria (-0.3<FB<0.3). Note that it is mainly due to the result obtained at P6, where the modelled values are out of the variation range of measurements.

Table 4.4: Statistical parameters for NO_x, NO_T, NO_R, NO_{2T} and NO_{2R} at every points.

	NO_T	NO_R	NO_{2T}	NO_{2R}	NO_x
NMSE	0.14	0.38	0.25	0.031	0.14
FB	-0.11	-0.43	-0.46	-0.13	-0.27
R	0.91	0.88	0.97	0.94	0.93

Therefore, including chemical reactions in order to particularly model the NO_2 improves the results by comparing with the measured concentration value. Although the differences between the reactive and non-reactive approaches seem small, is worth noting that the sampling points are located very close to the vehicle exhausts and, thereby, the chemical reactions may have short time to happen.

Figure 4.11 depicts the mean maps of NO_x, NO_R and NO_{2R} and the experimental results, at the sampling points.

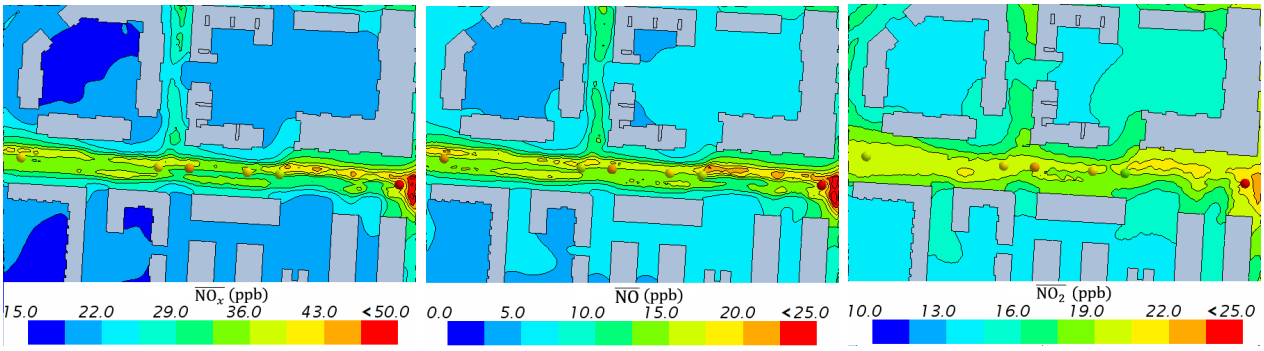

(a) **(b)** **(c)**

Figure 4.11: Time-average concentration map of the simulated (a) $\overline{NO_x}$, (b) $\overline{NO_R}$ and (c) $\overline{NO_{2R}}$ at the height of the sampling points with its corresponding mean experimental value depicted at every point.

Despite the fact that the measurement points are located in areas of strong concentration gradients, the mean maps show that the modelled values properly capture the recorded concentration for the NO_x, NO and NO_2, throughout the day. Accordingly, based on a comprehensive validation of pollutant concentrations, the simulation properly reproduce the dispersion of pollutants in the study street, both in terms of time and space.

4.5 Difference between chemical approaches at pedestrian level

This section is addressed to study the behaviour of reactive pollutants in a real street. To do that, the chemical influence on the pollutant concentrations is temporally and spatially analysed at daytime. In addition, the coupling between the dynamical and chemical processes is thoroughly analysed in the street, at pedestrian level.

This height is commonly established at 3 m AGL as a representative level of the air breathed by pedestrians. Usually, air quality is assessed at 3 m AGL in the monitoring stations deployed throughout the city. It is considered a reasonable height, in which the pollutant concentrations are representative of the air composition in the streets and, for which, the potential impact on pedestrian human health is evaluated.

4.5.1 Daytime behaviour of NO and NO_2 at pedestrian level

Firstly, the chemical influence is studied over time, as a function of the temporal variability of the atmospheric conditions, at daytime. Hence the difference of the NO and NO_2 concentrations, caused by the chemical conversions, is computed at pedestrian level in the study street (Fig. 4.12).

Figure 4.12: Area of the study street.

The concentration of NO and NO_2 is spatially averaged (<>) at every hour, within the selected area (Fig. 4.12). Figure 4.13 displays the $< NO_T >$, $< NO_R >$, $< NO_{2T} >$, $< NO_{2R} >$ and, also, the relative differences $< \delta NO >$ and $< \delta NO_2 >$ (Eq. 3.1).

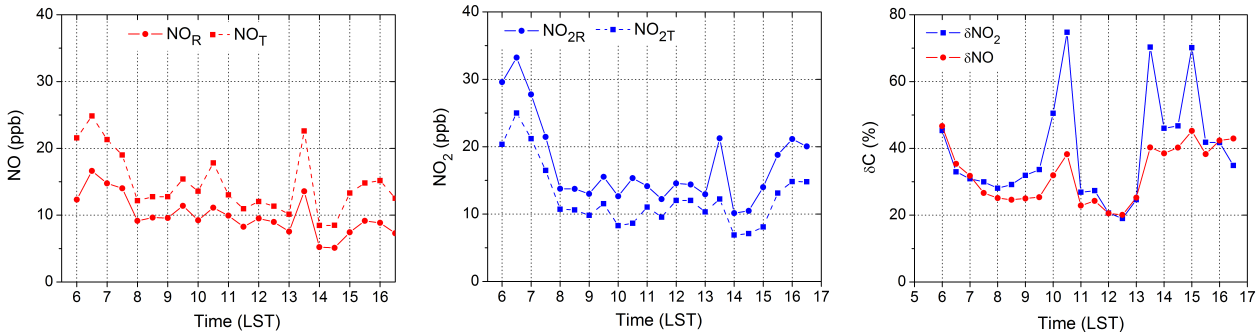

Figure 4.13: At 3 m AGL, time series of: (a) $< NO_T >$ and $< NO_R >$ in ppb, (b) $< NO_{2T} >$ and $< NO_{2R} >$ in ppb and (c) $< \delta NO >$ and $< \delta NO_2 >$ in %.

In the early hours (from 0600 LST to 0800 LST), the time series of $< \delta NO >$ and $< \delta NO_2 >$ show a decrease in the chemical influence from 50% to 30%. It is directly caused by the temporal evolution both of the traffic emissions and the solar radiation. At first hour, the solar radiation is lower and, thereby, the NO_2 loss by photolysis is quite small. In turn, the traffic emissions are higher and the emitted NO reacts with O_3, rising the NO_2 production. It hinders the chemical equilibrium among pollutants, which gives rise to an increase of the difference between the reactive from non-reactive approaches. This behaviour is reduced as the solar radiation increases and, thus, the NO_2 formation tends to balance the loss of NO_2.

At certain hours, $< \delta NO_2 >$ reaches values above 50%, which is mainly related to the flow pattern in the street. At 1330 LST, east wind blows parallel to the study street (Fig. 4.14a) and drag the pollutants from the surroundings areas. Consequently, $< \delta NO_2 >$ is

more affected by the chemical deviation obtained from the pollutants mixing between the emissions and the overlying air in the surroundings. On the other hand, at 1500 LST (Fig. 4.14b), the decrease of the wind speed and the vortexes developed in the street increasing the residence time of pollutants. These conditions promote the chemical interactions among pollutants increasing the value of $< \delta NO_2 >$.

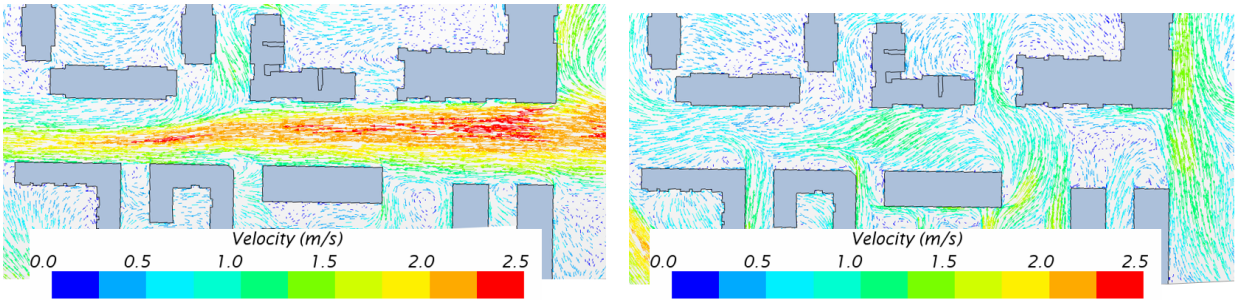

(a) **(b)**

Figure 4.14: Wind flow at pedestrian level at (a) 1330 LST and (b) 1500 LST.

Despite the NO and NO_2 concentrations are not overly high, because this street is not regarded as a heavily trafficked area, the temporal evolution of the chemical deviation turns out values above 20% at all hours. This value is established as the threshold from which the influence of the chemistry is considered significant. This is based on the legal error allowed for pollutant measurements by European Air Quality Directive 2008/50/EC, which ranges from 15% to 25% depending on the pollutant. The same threshold (20%) is used as the concentration similarity criteria for other purposes, e.g. by computing the spatial representativeness area of air quality monitoring stations (Santiago et al., 2013; Martin et al., 2014; Piersanti et al., 2015).

Accordingly, in these atmospheric conditions, the influence of including chemical reactions in order to model the dispersion of NO and NO_2 seems to be significant in the daylight hours.

At daytime, the traffic emissions are larger and the chemical reactions of the photostationary state mainly reflect the NO and NO_2 interactions. However, at night, the photolysis of NO_2 ceases and the traffic emissions are considerably reduced. Therefore, the overall deviation obtained at daytime in these atmospheric conditions is quantify through the daytime mean map, from 0600 LST to 1800 LST. Figure 4.15 illustrates the map at pedestrian level of $\overline{NO_T}$, $\overline{NO_R}$, $\overline{NO_{2T}}$, $\overline{NO_{2R}}$ and, their corresponding chemical deviations $\Delta\overline{C}$ $(\overline{C_R} - \overline{C_T})$, $\delta\overline{NO}$ and $\delta\overline{NO_2}$. Note that the difference $(\Delta\overline{C})$ takes the same value for the NO and NO_2 $(\overline{NO_R} - \overline{NO_T} = \overline{NO_{2R}} - \overline{NO_{2T}})$.

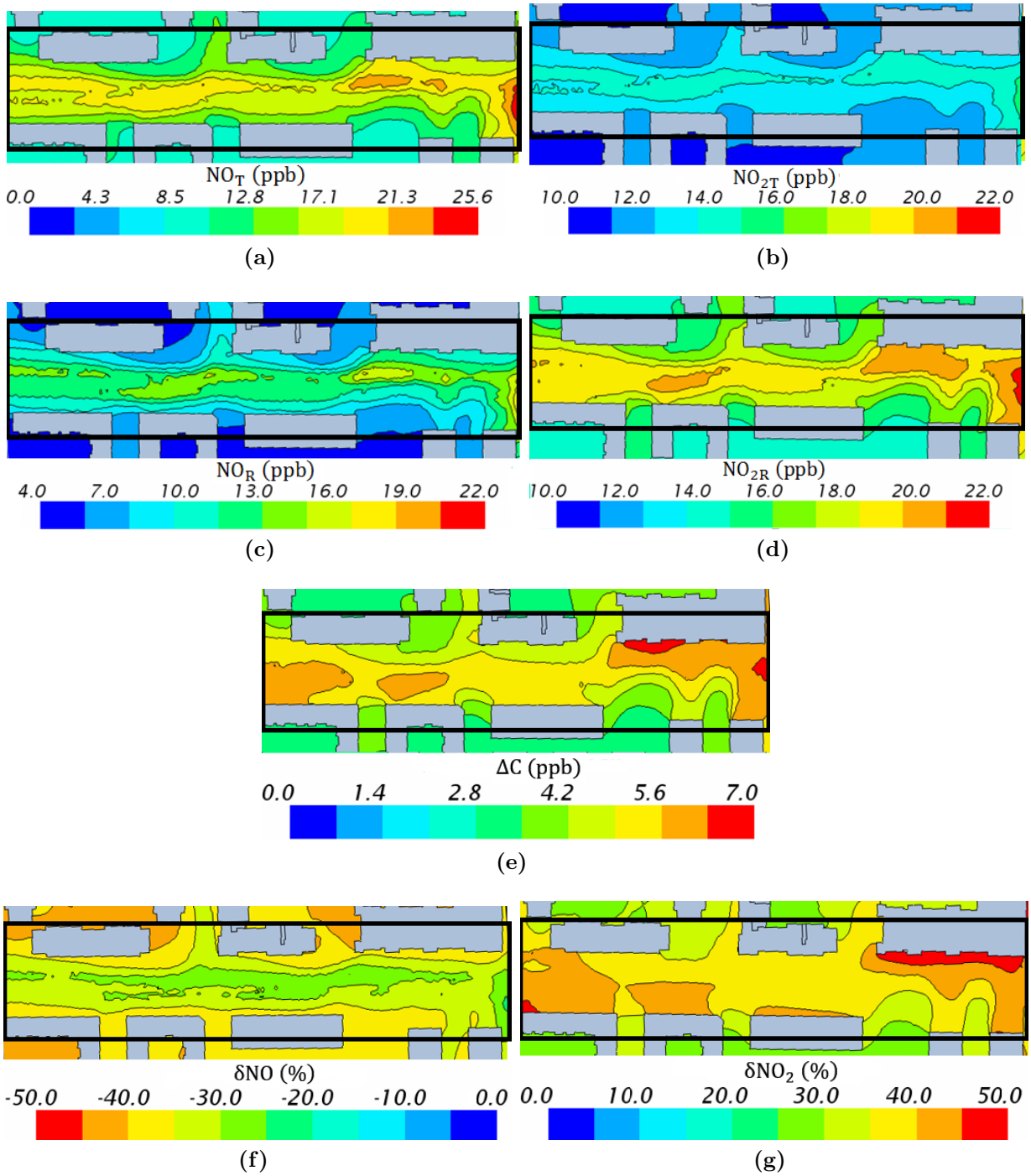

Figure 4.15: Maps of (a) $\overline{\mathrm{NO_T}}$ (ppb), (b) $\overline{\mathrm{NO_{2T}}}$ (ppb), (c) $\overline{\mathrm{NO_R}}$ (ppb), (d) $\overline{\mathrm{NO_{2R}}}$ (ppb), (e) $\Delta\overline{\mathrm{C}}$ (ppb), (f) $\delta\overline{\mathrm{NO}}$ (%) and (g) $\delta\overline{\mathrm{NO_2}}$ (%), at pedestrian level.

Concerning the dispersion in the street, the mean maps reveal that both the non-reactive assumption and the reactive approach reproduce similar concentration distributions at pedestrian level. However, the concentrations of $\mathrm{NO_R}$ and $\mathrm{NO_{2R}}$ turn out lower and larger values respectively from the non-reactive approach, highlighting the influence of the chemical conversions. In addition, $\Delta\overline{C}$ shows the maximum values in the street over the traffic emission area (around 5-7 ppb). It concludes that the importance of the chemical activity

varies according to the distance to the source. Overall, both $\delta\overline{\mathrm{NO}}$ and $\delta\overline{\mathrm{NO_2}}$ take values above 20% in the entire street, even the 50% is reached in some areas depending on the characteristic flow in the street. Therefore, modelling NO_2 as a non-reactive pollutant lead to a relevant difference in the NO_2 concentration at daytime. Based on these results, the evaluation of a particular abatement strategy for the NO_2 levels would be necessary to consider the chemical reactions in modelling accurate NO_2 concentrations.

As previously showed, the variability of the atmospheric conditions, e.g. wind flow or the solar position modified the chemical influence on the pollutants concentration in the streets. In the following section, the dynamical processes and its importance in the chemical activity are in-depth studied in the street.

4.6 Chemical and dynamical processes in an urban area

In urban environments, the dynamical processes control the transport of pollutants in the streets. The advective term determines the flow pattern and, thus, the residence time of pollutants in the street. In turn, the turbulence is a key factor that dominate the mixing of pollutants. As for the chemical processes, the reactive pollutants tend to seek the chemical equilibrium up to reach the point, where the removal is equivalent to the formation of the reactants. Nevertheless, in urban areas, the fresh emission in the streets is continuously disturbing the reach of a chemical balance. Therefore, the dynamical processes play an important role in the mixing of the emissions and the ambient pollutants that promote to achieve the chemical equilibrium.

In this study, the importance of the turbulence in the chemical activity is examined through the concentration differences between the reactive and the non-reactive approaches. That deviation represents the influence of the chemical conversions, involving both the advective and turbulent-diffusive terms (assuming the molecular diffusion is irrelevant with respect to the turbulent). In this way, the contribution of the turbulence to the chemical influence is analysed by the Da number (Section 2.4.3). This dimensionless number provides the relation between the turbulent processes and the reaction rate, as a function of the turbulent time scale (τ_{turb}) and the chemical time scale (τ_{react}). Using the $NO_x{-}O_3$ mechanism, the characteristic time scale of the steady state is computed for the slowest chemical reaction; in this case, using the NO concentration and the reaction rate constant k_{NO+O_3}:

$$\tau_{react} = (\mathrm{k_{NO+O_3}NO})^{-1} \quad ; \quad \tau_{turb} \equiv \frac{k}{\varepsilon} \tag{4.1}$$

$$Da = \frac{\tau_{turb}}{\tau_{react}} = \frac{k/\varepsilon}{1/(\mathrm{k_{NO+O_3}} \cdot \mathrm{NO})} \tag{4.2}$$

Another important aspect is the deviation from the chemical equilibrium (δ_{eq}). Based on the the Leighton relation (Eq. 1.8), δ_{eq} can be computed as follows:

$$\delta_{eq} = 1 - \left(\frac{\mathrm{J_{NO_2}} \cdot \mathrm{NO_2}}{\mathrm{k_{NO+O_3}} \cdot \mathrm{NO} \cdot \mathrm{O_3}} \right) \tag{4.3}$$

If δ_{eq} ≈1, the chemical state of pollutants is completely out of the chemical equilibrium, whereas if δ_{eq} ≈0, there is a balance between the NO_2 photolysis and its formation by the NO and O_3 interaction. Nonetheless, if other chemical processes become more important, triggering additional loss processes, the chemical equilibrium does not hold. At sunset and sunrise, the deviation of the chemical equilibrium are expected fairly high. In these conditions, the NO_2 photolysis is considerably small and the steady-state relation of chemical equilibrium is not fulfilled (Calvert and Stockwell, 1983; Finlayson-Pitts and Pitts Jr, 1999).

Due to the chemical influence varies as a result of the proximity to the source, two locations at pedestrian level are selected for this study (Fig. 4.16). The first point (P_S) is placed at centre of the street near the road. The second one (P_B) is located further away from the NO_x release, which may be representative of the ambient composition.

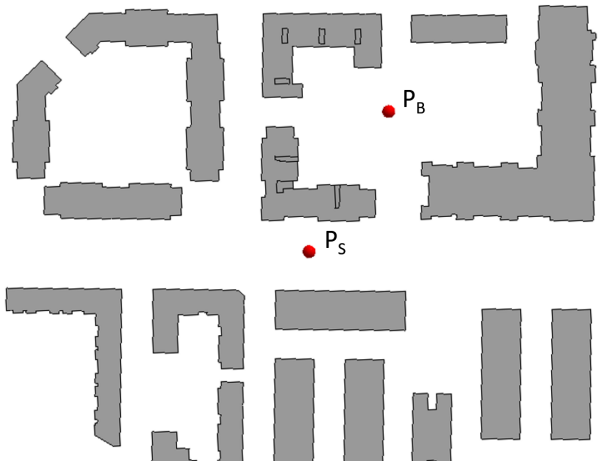

Figure 4.16: Location of the study points in the streets: P_S, near the road and P_B, further from the traffic emissions.

At these points, the relation between turbulent mixing and equilibrium state and its influence on the chemical activity is analysed over time. This allows to understand the reasons that cause the variability of the chemical influence on the dispersion of pollutants in the street. To that end, the difference in NO_2 from the reactive and non-reactive approaches (ΔNO_2=NO_{2R}-NO_{2T}), the Da number and δ_{eq} are depicted, at P_S and P_B, in Fig. 4.17.

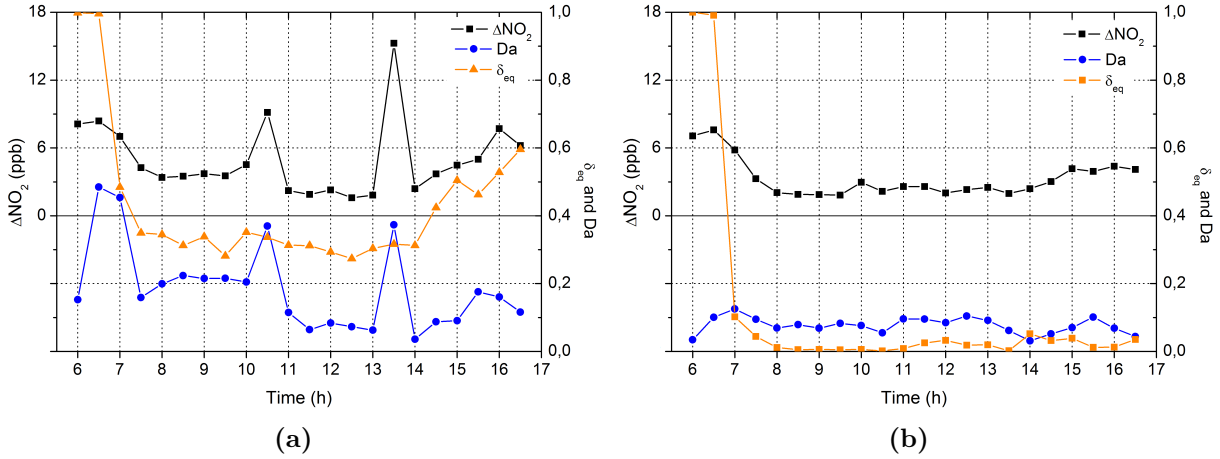

Figure 4.17: Temporal evolution of the ΔNO_2 (=NO_{2R}−NO_{2T}), Da number and δ_{eq} in (a) P_S and (b) P_B.

Firstly, ΔNO_2 exhibits a clear difference between both locations and, therefore, an evidence of the spatial variation owing to the chemical influence in urban environments. In addition, the chemical state of the ambient pollutants (δ_{eq}) at P_B shows that the species are close to the chemical balance along the day except at first hours. However, at P_S, the reactants are usually further from the chemical equilibrium. Likewise, the results of the Da number reveal different behaviours at P_S from the P_B. In the latter, the Da number takes low values (Da≈0.1) that corresponds to the small variations of ΔNO_2. This represents that the turbulent processes are efficiently able to well mix the pollutants up to reach the chemical equilibrium ($\delta_{eq} \approx 0$). At P_S, the time series of the Da number correlates with the evolution of the largest variations of ΔNO_2, except at the first hour. Therefore, an increase in the chemical influence reveals the turbulent processes are not able to properly merge the emitted pollutants with the overlying air. Thus, at P_S, the Da number exhibits that the relation between turbulence and chemical activity affects the dispersion of reactant in the street.

At first hours, both at P_S and P_B, the reactants are completely out of the chemical equilibrium ($\delta_{eq} \approx 1$) since the NO_2 photolysis does not make up for the NO_2 production by the reaction of NO with O_3. In these conditions, the concentration difference with the reactive approach is basically caused by the reaction of the continuous NO emissions and the background O_3. Hence there is no influence of the turbulent mixing on the chemical rate as the Da number shows. And ΔNO_2 close to the release (P_S) hardly differs from the value at P_B.

The spatial variation in the streets of ΔNO_2, δ_{eq} and Da number are depicted at 0630 LST, 1200 LST and 1330 LST, at pedestrian level, in Fig. 4.18.

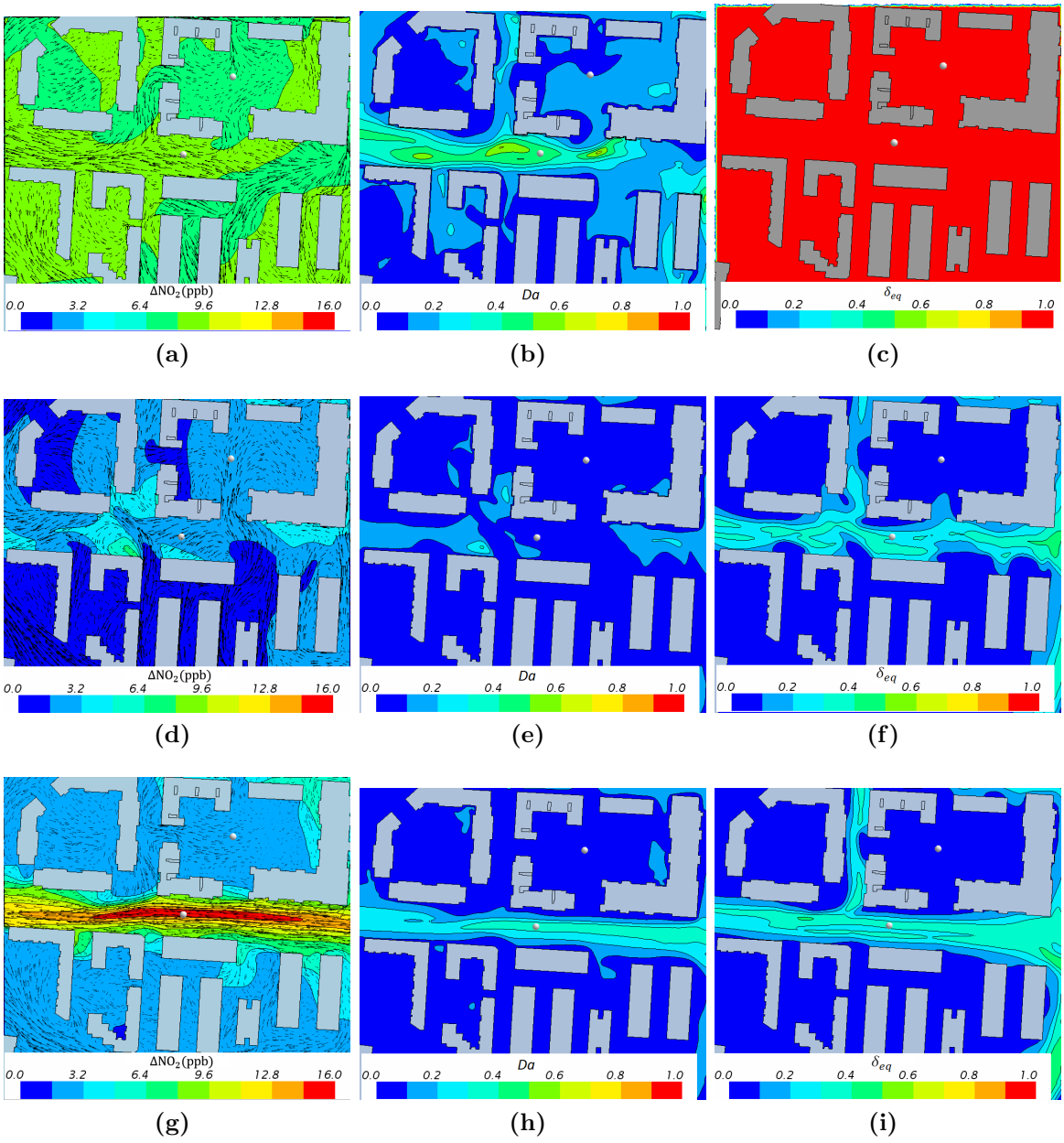

Figure 4.18: (*From left to right*) Map at pedestrian level of ΔNO_2 (ppb), the Da Number and δ_{eq} at (a-c) at 0630 LST, (d-f) 1200 LST and (g-i) at 1330 LST.

At 0630 LST (4.18a-c), δ_{eq} displays that pollutants are not in a chemical equilibrium throughout the entire domain. At this time, the solar position is fairly low since it corresponds to the sunrise. As a consequence, the NO_2 photolysis is slow or almost non-existent, which prevents to reach the chemical balance (Eq. 4.3). Using the photostationary state, ΔNO_2 cannot be related to the influence of the turbulence in the street. The loss of O_3 is not being chemically replaced by the NO_2 photolysis and, therefore, the pollutants mixing cannot improve the chemical conversions. Therefore, the chemical influence is not dynamically affected and ΔNO_2 is only dependent on the reaction of NO and O_3, depending on the background O_3 imposed in the CFD simulation and the emitted NO.

In these atmospheric conditions, other chemical reactions regarding the NO_3 interactions become more important, giving rise to a more complex chemical system (Stockwell and Calvert, 1983).

At 1200 LST (4.18e-f), the largest δ_{eq} is just located close to the traffic releases area in the streets. In most part of the domain, the chemical balance is maintained being disturbed in the proximity of NO_x sources. The maximum importance of the chemical difference, namely maximum ΔNO_2, is locally found in areas where the Da number is higher. However, Da number is generally low in the street, which reveals that the turbulence is able to rapidly mix the emissions with the overlying pollutants. Therefore, at this time, the efficient mixing drives to small deviations between chemical approaches, given that NO_2 removal is quickly replaced by the reaction of NO and O_3.

The highest values of ΔNO_2 are obtained in the study street at 1330 LST (Fig. 4.18g). As at 1200 LST, the largest deviation from the chemical equilibrium is located over the traffic emissions. However, in this case, the Da number represents the inefficiency of the turbulence to quickly blend the reactants in the emissions areas. The chemical and turbulent time scale are comparable. It entails that the reaction of NO and O_3 cannot make up for the loss of NO_2. In this case, the flow pattern (Fig. 4.14a) drags the pollutants from the surroundings streets, which are not efficiently mixed with the ambient pollutants, and significantly increases the difference between NO_{2R} and NO_{2T}. Accordingly, in these atmospheric conditions, the importance of the chemical reactions increases with respect to the turbulent phenomena.

Therefore, the influence of the chemistry on the reactive pollutants is closely related to the advective-turbulent processes in the streets. In turn, the perturbation of the emissions in the chemical balance from the overlying air determines the concentration difference, given by the chemical reactions, in which the turbulence in the street is a key factor. At sunrise and sunset, the turbulence effect is limited because ΔNO_2 is mainly controlled by the reaction rates and the chemical balance of the background pollutants imposed at inlet in the simulation.

However, as the solar radiation and temperature increase together with the background O_3, the chemical equilibrium is quickly reached. In the streets, that chemical balance is disturbed by the local emissions. With an effective turbulent mixing able to efficiently mix the NO_x emission and the ambient pollutants, the influence of the chemical interactions is reduced. In contrast, a poor mixing gives rise to the chemical reactions concentration difference in the streets between the reactive and non-reactive approaches.

4.7 Summary and conclusions

This chapter is addressed to study the coupled behaviour of dynamic and chemical processes in a real street and, thereby, how the turbulence can modify the influence of chemical interactions on pollutant concentrations. To that end, the dispersion of NO and NO_2 is simulated considering two chemical approaches: no chemistry and $NO_x{-}O_3$ mechanism. Accordingly, the effect of the chemistry is examined depending on the atmospheric variability at daytime. In this way, the differences between the chemical approaches are quantified for these conditions at pedestrian level.

Firstly, the time series of the pollutant concentrations are compared against the experimental data, at sampling points, along the study street. Despite the assumption of neutral atmospheric conditions, without including thermal effects, the NO_x validation shows that the transport is properly reproduced by the simulation. However, at first hour, there are some errors derived from the uncertainties of traffic emissions or the atmospheric stability. Overall, the validation reveals a good agreement of the modelled concentrations for the NO, NO_2 and NO_x. As for the difference between chemical approaches, small differences are obtained. Nevertheless, the NO_2 concentration is better captured using chemical reactions. The improvement of the reactive approach is obtained by comparing the ratio NO-to-NO_2 in air with the measurements. Unlike the non-reactive approach, the ratio obtained from the reactive pollutants follows the same tendency than the experimental one.

Once the simulation is evaluated, the daytime behaviour of the chemical influence is also analysed, both in time and space, in the study street. The diurnal variability of the atmospheric parameters are a key component in the reaction rates such the solar position and the air temperature. First of all, the relative differences in concentration between the two chemical approaches are analysed over time at pedestrian level. Overall, the temporal evolution of $< \delta\mathrm{NO} >$ and $< \delta\mathrm{NO_2} >$ in the study street yield above 20% throughout the day and, even, $< \delta\mathrm{NO_2} >$ reaches up to 70%, at some hours. On the other hand, the mean maps of NO and NO_2 show broadly similar horizontal gradients of the dispersion of pollutants in the street. However, in terms of concentration, the NO_R and NO_{2R} take respectively lower and larger values above 20% than those obtained using the non-reactive approach. Therefore, these results conclude that the spatial distribution in the streets is approximately captured using both the reactive and non-reactive approaches. Nonetheless, in these atmospheric conditions, the values of concentration are significantly modified by using chemical reactions in the simulation.

Lastly, the relation of the turbulence with the chemical influence is thoroughly examined. To do that, the variability in the difference between the reactive and non-reactive approaches is explained through the changes of the Da number and the deviation from the chemical

equilibrium.

At sunrise and sunset, the NO_2 photolysis decreases and the steady-state system (represented by $NO_x - O_3$) is no longer fulfilled. Consequently, other chemical reactions can prevail in the NO_2 transformations. In the simulation, the lack of chemical balance among the ambient pollutants reveals that the turbulence has not effect on the deviation caused by chemical reactions.

As the solar radiation increases, the chemical equilibrium in the overlying air is rapidly reached, and just disturbed by the local emissions in the streets. Therefore, the difference between the reactive and non-reactive approaches is related to the efficiency of the turbulence to properly blend the emitted and ambient pollutants in the streets. For a turbulent time scale lower enough than the characteristic chemical time, the turbulent processes are able to suitably mix the pollutants in the streets. This involves that the NO and O_3 reaction replaces the loss of NO_2 as fast as the photolysis occurs. In these conditions, the chemical influence on the dispersion of a reactive pollutant is small in comparison with the non-reactive approach. On the contrary, for an inefficient pollutant mixing, the importance of the chemical reactions increases. In this way, the NO_2 photolysis is not balanced by the reaction of NO and O_3, giving rise to larger differences in concentration between the approaches. Moreover, that difference rises in case of the perturbation of the traffic emissions increases.

Accordingly, the assessment of particular mitigation measure for the abatement of NO_2 concentration requires to introduce the chemical reactions in CFD modelling. It improves the value of NO_2 concentration obtained from the simulation. Nonetheless, the representative distributions of the pollutants in the streets is similarly reproduced by using any of the chemical approaches in the CFD modelling.

Acknowledgments

This study has been supported by European Project LIFE MINO$_x$-STREET (LIFE12 ENV/ES/000280). Thanks to the colleagues of the Atmospheric Pollution Characterization and POC Group from CIEMAT for providing the experimental data used in the validation of the CFD-RANS simulation. The authors are also grateful to Extremadura Research Centre for Advanced Technologies (CETA-CIEMAT) by helping in using its computing facilities for the simulations. CETA-CIEMAT belongs to CIEMAT and the Government of Spain and is funded by the European Regional Development Fund (ERDF).

Chapter 5

Modelling approach for air quality assessment in an urban hot-spot in winter conditions

5.1 Introduction

Broadly half of the global population currently lives in urban areas and this share is projected to increase to two thirds by 2050. In Europe, this percentage is even higher, with a 73% of urban population and a projected share of 82% by 2050 (EEA, 2015). EEA (2015) established that 9% of European urban population lives in areas in which the annual NO_2 EU threshold was exceeded in 2013. Current European air quality legislation (Directive 2008/50/EC) establishes the need to assess air quality and apply plans to improve air quality in non-compliant areas. However, high population exposure is often associated to hot-spots with high emission intensity from road traffic and reduced natural ventilation (Vardoulakis et al., 2003). Therefore, more detailed studies about urban air pollution are required by policymakers to effectively mitigate the population exposure.

Urban monitoring station networks are not dense enough to capture these heterogeneities, making it difficult to understand and manage urban air quality issues. Indeed, the spatial representativeness of urban air quality monitoring stations (i.e. the area around the station where the pollutant concentration does not differ significantly from the concentration measured at the station) is currently an important concern (Martín et al., 2015). Hence, high resolution maps of average concentration over long periods of time, ideally annual or several weeks at least, are necessary for air quality management and the assessment of local abatement measures taking into account the variability of emissions and meteorological conditions.

Experimental campaigns with passive samplers have been carried out to evaluate air pollution levels in several urban zones (Krochmal and Kalina, 1997; Vardoulakis et al., 2002, 2005; Ott et al., 2008; Parra et al., 2010). This experimental deployment with a large amount of passive samplers allows obtaining time-average concentration maps during several weeks for a given pollutant, usually the NO_2. These samplers are cheaper and easier to install than monitoring stations, although they lack temporal resolution. Concentration maps can be obtained applying interpolation methods from the measurements points. However, these results may differ from the real maps owing to the complex geometry with a large number of obstacles in urban areas and the irregular distributions of pollutants sources (Deligiorgi and Philippopoulos, 2011).

CFD models are an effective tool to simulate airflow and pollutant dispersion with 1-m resolution in urban environments. However, the temporal evolution of pollutant concentration during several days, weeks or months cannot be simulated using a CFD model due to the huge computational requirements. Nevertheless, recent studies (Parra et al., 2010; Solazzo et al., 2011; Santiago et al., 2013, 2017a) have developed a numerical methodology based on a combination of a set of steady CFD-RANS simulations to generate the time-average concentration map over a long period. In this way, the temporal evolution of the pollutant is composed of several simulated scenarios involving the actual wind data and the traffic emission conditions derived from experimental data at every hour. The main assumption of this methodology is that the pollutants are regarded as non-reactive, which is not fulfilled in case of the NO_2.

This work focuses on obtaining the spatial distribution of NO_2 concentration averaged over several weeks in a heavily trafficked urban area in Madrid (Spain) using a CFD-RANS model. In this scenario, the modelling results are compared against measurements recorded in an intensive experimental campaign in wintertime. Firstly, the influence of chemical reactions on the NO_2 concentration is evaluated at daytime for a particular day. To do that, the NO_2 is modelled as a inert pollutant and a reactive compound, using the $NO_x{-}O_3$ mechanism. Secondly, the NO_2 mean map is obtained using the numerical methodology based on the sequence of steady-state simulations. In this chapter, some novelties are included in the numerical approach for improving the microscale results. On one hand, the use of mesoscale variables for the required meteorological data. On the other hand, the traffic emissions are derived from a microscale simulation system that combines a traffic and emission models (Quaassdorff et al., 2016). In that way, emissions with high spatial resolution are implemented in the CFD simulation. Lastly, the time average map of NO_2 concentration is compared against the experimental data obtained from 72 passive samplers deployed throughout this urban hot-spot.

Therefore, the following research questions are raised to be solved in this chapter:

- Which is the error in modelling NO_2 as a non-reactive pollutant in winter conditions?
- Can we use meteorological mesoscale models in order to improve the CFD modelling of urban air quality?
- Are the concentration fields obtained with this methodology reliable?

5.2 Experimental Campaign

The research area is located in a heavily trafficked roundabout with a freeway crossing it through a tunnel in Fernández Ladreda Square at south of Madrid (Fig. 5.1a). The selected location is a highly contaminated microenvironment with a very complex geometry and intense presence of pedestrians (more than 12 000 pedestrians/hour at peak hours) that makes this location a representative traffic hot-spot where urban air quality issues commonly occur. The study of the air quality in this location is encompassed within the framework of TECNAIRE-CM Project (S2013/MAE-2972).

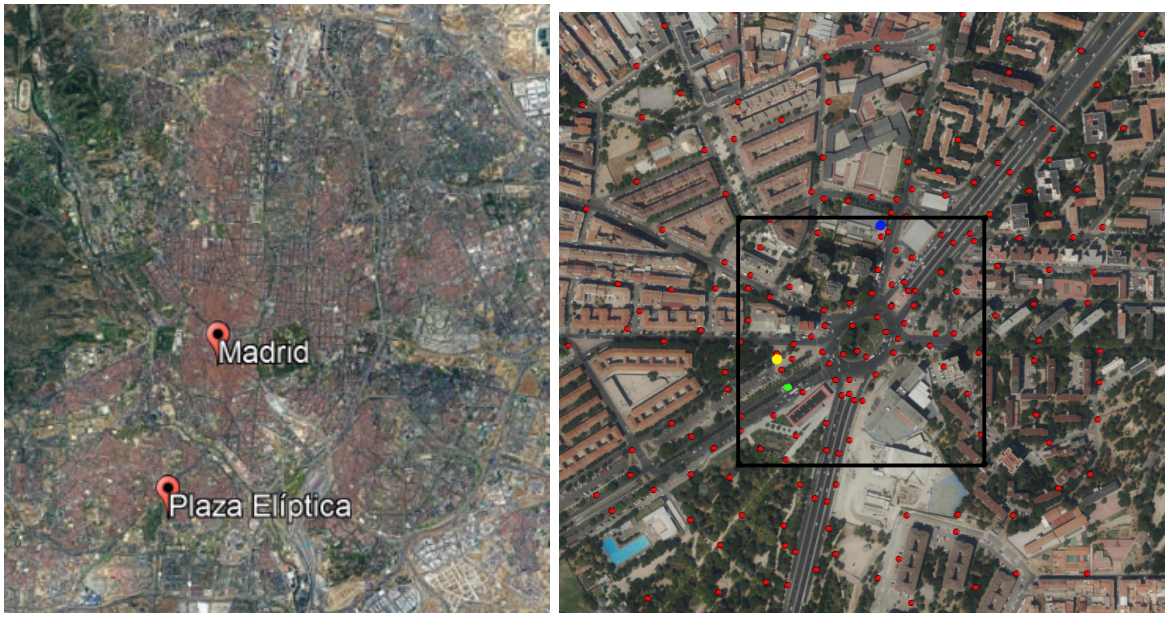

(a) **(b)**

Figure 5.1: (a) Location of the research area at south-west of Madrid (Spain). (b) Locations of measurements sites in the research area: red dots stand for the passive samplers; yellow dot for the air quality monitoring station; blue dot for the meteorological station and green dot represents the sonic anemometers location.

An intensive measurement campaign was carried out from 9th to 27th February, 2015 in this urban area to study the spatio-temporal variations of the main pollutants and its implication

for population exposure (Borge et al., 2016). This experimental campaign included the characterization of NO_2 spatial gradients through a dense network of Palmes-type passive diffusion tubes (PDT). Altogether, 206 PDT were homogeneously distributed throughout the roundabout (in lampposts, traffic signs, etc.) at red points in Fig. 5.1b and approximately deployed at 3 m AGL.

The time series of pollutant concentrations are measured at the air quality monitoring stations that belongs to the measurement network of the Madrid Council. This station (yellow point in Fig. 5.1b) is classified as traffic urban station and is called Fernández Ladreda station (hereafter referred to as FL station). In addition, the two closest monitoring stations to the research area are used to obtain the background concentration, named Farolillo and Retiro stations, which are categorised as urban background stations. The former is located at 1.5 km at North-West from the research area, hereinafter referred to as NW-UB station. The second one is placed at 4.5 km of distance from the FL station in the North-East direction, hereinafter called NE-UB station. All monitoring stations measure the concentration of NO, NO_2 and O_3 every hour, at 3 m AGL.

Additionally, the meteorological parameters were recorded from 17th February to 2nd March, 2015 (Borge et al., 2016). The meteorological station was located on the roof of a building, at 18 m AGL (blue point in Fig. 5.1b) and the variables instantaneously recorded were wind speed and direction, air temperature, relative humidity, pressure, precipitation and global solar radiation. The meteorological data were originally integrated into 10-min averages and, subsequently, averaged through a vectorial mean of 1-h periods for modelling evaluation purposes. In addition, the velocity components and temperature were measured by two sonic anemometers deployed at 6 m and 8 m at the second location (green point in Fig. 5.1b). Thus, micrometeorological parameters such as the turbulent kinetic energy and the turbulent heat flux were calculated from the measurements recorded with a high sampling frequency (20 Hz).

Accordingly, two periods are considered for this study: for the concentration measurements from 9th to 27th February, 2015 and, as regards the meteorological data, from 17th to 27th February, 2015.

5.3 Geometry, mesh and boundary conditions

The simulations are carried out using the CFD-RANS model with the Realizable k-ε turbulence closure. The size of the computational domain over the research area is, approximately, 1300 m x 1300 m (Fig. 5.2). The geometry consists of several characteristic regions: a tunnel located at the center of the square, vegetation zones (green part), buildings

(dark grey part) and a traffic emission region (red part). The base resolution of the polyhedral irregular mesh used is around 5 meters, with a smaller resolution of 2 meters within the region of 400 m x 400 m located at the center of the square (black square). Within this zone, the cell size is even smaller than 1 m close to the ground and buildings and in the emission region. As a consequence, the mesh holds 8.3 10^6 grid points in total. A mesh independence test was performed using fine (14 10^6 grid points) and coarse (1.8 10^6 grid points) meshes and the results turn out that the medium grid resolution is enough to properly simulate the flow and dispersion in this scenario. Therefore, the medium mesh was selected for this work in order to obtain the best compromise between accuracy and computational load.

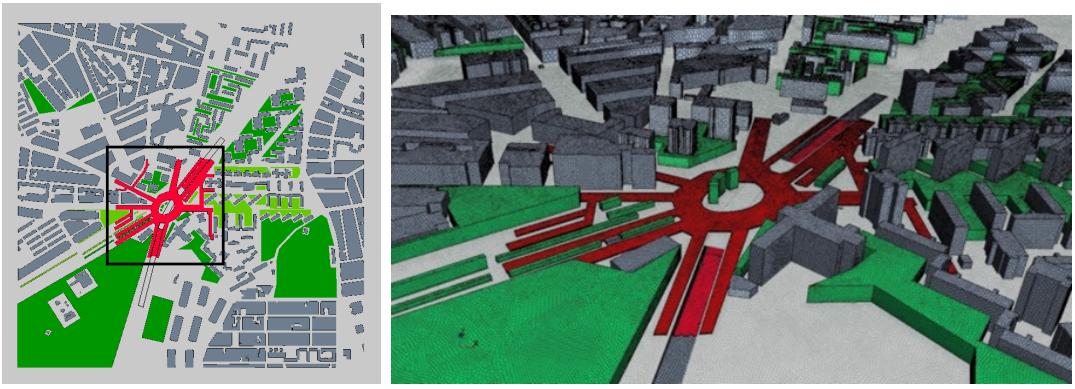

(a) **(b)**

Figure 5.2: (a) Domain of the research area (black square). (b) Mesh of the central square. Green regions represent the vegetation zones and the red part, the traffic emission region in the research area.

In wintertime, the evergreen urban vegetation may affect pollutants dispersion in the streets. Hence, it is included by means of a simplified geometry (green regions in Fig. 5.2). The vegetation effect is modelled assuming trees as a porous medium, just considering its dynamical effects with a value of leaf area density of 0.5 m^2 m^{-3} (Section 2.5).

On the other hand, the red region (Fig. 5.2) marks out the traffic emission zone of 300 m x 300 m with 1m-height AGL, where spatially non-uniform source have been implemented. These detailed emissions of NO_x are derived from a microscale traffic emission model (Quaassdorff et al., 2016). The traffic model computes detailed trajectories that describe the behaviour of individual vehicles considering drivers' reaction times, route selection logic and lane change logic. It provides essential information about braking-acceleration patterns that have a huge influence on the pollutants emitted and their distribution in space and time. For this study, emissions are computed through the TNO ENVIVER high-resolution post-processor that links the emissions model VERSIT+micro, based on VERSIT+ model (Smit et al., 2007), to speed-time profiles generated by the PTV VISSIM microscale traffic model. The emission estimations are based on very detailed and specific fleet composition and vehicle flow data in

the square, obtained from an intensive measurement campaign with cameras (Quaassdorff et al., 2016). Therefore, 13 emission scenarios of 1-h length, representative of different traffic composition and flow conditions, are computed to complete the weekly pattern (Fig. 5.3). For instance, similar traffic flow and driver's behaviour is considered for Monday, Tuesday and Wednesday at 08:00 a.m. and, thereby, the same scenario is assigned at that hour (S2).

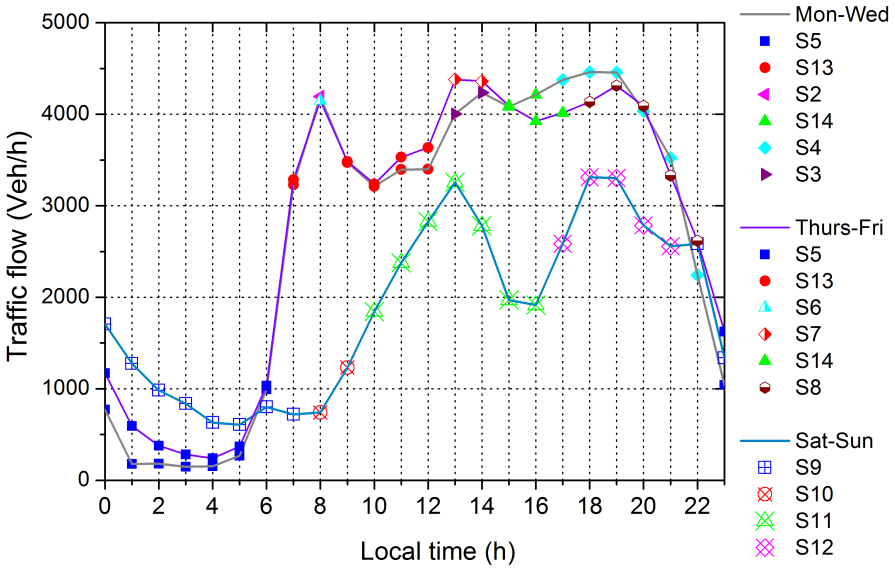

Figure 5.3: Daily traffic flow in local time for each emission scenarios (Quaassdorff et al., 2016).

Table 5.1 gathers the allocation of the emission scenario to every hour.

Table 5.1: Hourly distribution of the traffic emission scenarios along a week in local time.

Day \ Hour	0	1	2	3	4	5	6	7	8	9	10	11	12	13	14	15	16	17	18	19	20	21	22	23
Monday	S5	S5	S5	S5	S5	S5	S5	S13	S2	S13	S13	S13	S13	S3	S3	S14	S14	S4	S4	S4	S4	S4	S4	S5
Tuesday	S5	S5	S5	S5	S5	S5	S5	S13	S2	S13	S13	S13	S13	S3	S3	S14	S14	S4	S4	S4	S4	S4	S4	S5
Wednesday	S5	S5	S5	S5	S5	S5	S5	S13	S2	S13	S13	S13	S13	S3	S3	S14	S14	S4	S4	S4	S4	S4	S4	S5
Thursday	S5	S5	S5	S5	S5	S5	S5	S13	S6	S13	S13	S13	S13	S7	S7	S14	S14	S14	S8	S8	S8	S8	S8	S5
Friday	S5	S5	S5	S5	S5	S5	S5	S13	S6	S13	S13	S13	S13	S7	S7	S14	S14	S14	S8	S8	S8	S8	S8	S5
Saturday	S9	S9	S9	S9	S9	S9	S9	S9	S10	S10	S11	S11	S11	S11	S11	S11	S11	S12	S12	S12	S12	S12	S9	S9
Sunday	S9	S9	S9	S9	S9	S9	S9	S9	S10	S10	S11	S11	S11	S11	S11	S11	S11	S12	S12	S12	S12	S12	S9	S9

In spatial terms, the NO_x emission are calculated in a resolution of 5 m x 5 m considering the specific release into the tunnel and on the square. In the CFD simulation, the traffic emissions are implemented in the domain according to 1-m resolution for each emission scenario (Fig. 5.4).

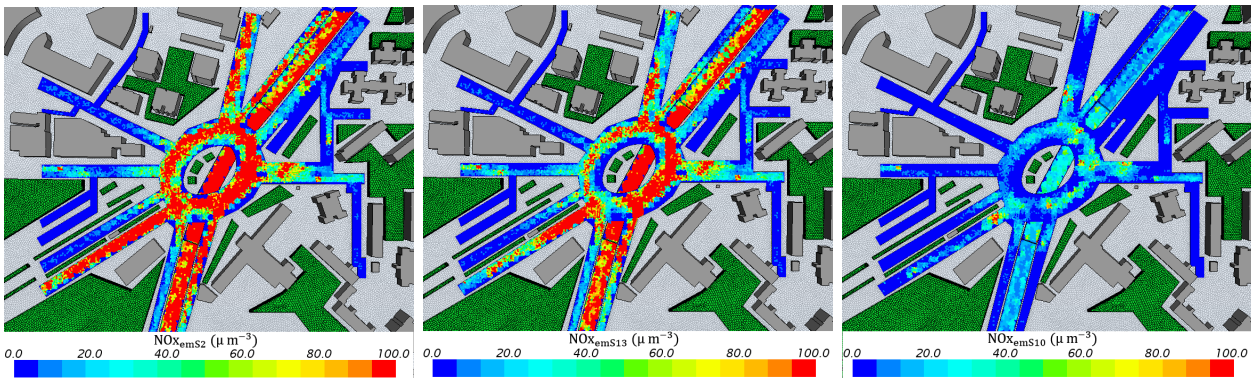

Figure 5.4: From left to right, the spatial distribution of NO_x emitted in $\mu g\ s^{-1}$ from the traffic scenarios S2, S13 and S10 (see Table 5.1) implemented into the CFD simulations.

The daytime variation of air temperature in winter atmospheric conditions is smooth without strong thermal gradients in the streets. For that reason, the assumption of isothermal condition may be appropriate and, thereby, the mathematical expressions for neutral atmosphere stability are applied in the CFD simulations. Thus, the vertical profiles of wind speed (u), turbulent kinetic energy (k) and turbulent dissipation rate (ε) are imposed at inlet, following the expressions:

$$u_{in}(z) = \frac{u_*}{\kappa} ln\left(\frac{z+z_0}{z_0}\right) \qquad k_{in} = \frac{{u_*}^2}{{C_\mu}^{1/2}} \qquad \varepsilon_{in}(z) = \frac{{C_\mu}^{3/4}{k_{in}}^{3/2}}{\kappa z} \tag{5.1}$$

where κ is the von Karman constant (0.4); C_μ, the constant (0.09); z_0, the roughness length (0.03 m) and u_*, the friction velocity (m s^{-1}).

The turbulence induced by traffic and the thermal effects give rise to a greater turbulent diffusion. However, they are not considered in these CFD simulations. Accordingly, the diffusion of pollutants is modelled considering a low value of turbulent Schmidt number, $Sc_t = 0.3$, in order to minimize the underestimation in the dispersion of pollutants. The most common values used to simulate the pollutant dispersion are between 0.7 and 0.9. Nevertheless, Tominaga and Stathopoulos (2007) concluded that the optimum values of Sc_t are in a range from 0.2 to 1.3, according to various flow properties and geometries. For instance, Vranckx et al. (2015) observed, by comparing CFD simulations with wind tunnel experimental data, that the optimum turbulent Schmidt number depends on the case and ranges from 0.3 to 1.0.

In addition, the research area within the city is also affected by the traffic emission at the surroundings neighbourhoods. Therefore, the background concentration used is derived from the closest air quality stations to the study area, depending on the wind direction (NW-UB and NE-UB).

5.4 Daytime behaviour of NO and NO_2

In this section, the influence of the chemical reactions in the NO_2 levels is examined in wintertime under two approaches: with no chemical reactions and with the NO_x−O_3 mechanism. In winter, maximum NO_2 concentrations are usually measured at night, when the PBL height shrinks down due to the nocturnal stability. Nevertheless, the study of photohemical reactions leads to focus at daytime, in presence of solar light. For that reason, the CFD simulation is carried out from 0700 LST to 1700 LST (from 08:00 a.m. to 18:00) on Wednesday, 18th February 2015, within the period of the experimental campaign. This day is selected because the largest NO_2 concentrations are recorded at FL station throughout daylight hours, within the period of the experimental campaign.

5.4.1 Simulation setup

The CFD-RANS simulation is performed in unsteady conditions with 1 s time step and the boundary conditions are changed at every hour. The inlet meteorological conditions are obtained from the hourly-averaged data recorded at the meteorological station on a building roof at 18 m AGL (blue point in Fig. 5.1b). The wind speed and direction at 18-m-height are used to compute the inlet vertical profiles for wind, turbulent kinetic energy and turbulent dissipation rate assuming neutral atmospheric conditions (Eq. 5.1).

For the reactive approach, the chemical constants, J_{NO_2} and k_{NO+O_3}, are computed over time through the hourly variation of air temperature and solar position (Section 2.3.1). As for the background pollutant concentrations, the values of NO, NO_2 and O_3 are obtained from the air quality station NE-UB station since, for the selected day, north-east wind is the prevailing direction. Lastly, the emission scenarios corresponding to daily pattern on Wednesday are simulated over time. The NO_2 release is calculated taking into account the emission ratio NO_2-to-NO_x equal to 0.3, derived from the Madrid emission inventories (Borge et al., 2014).

Figure 5.5 shows the inlet conditions over time for the wind speed and direction (at 18 m AGL), the air temperature and the background concentration of NO, NO_2 and O_3.

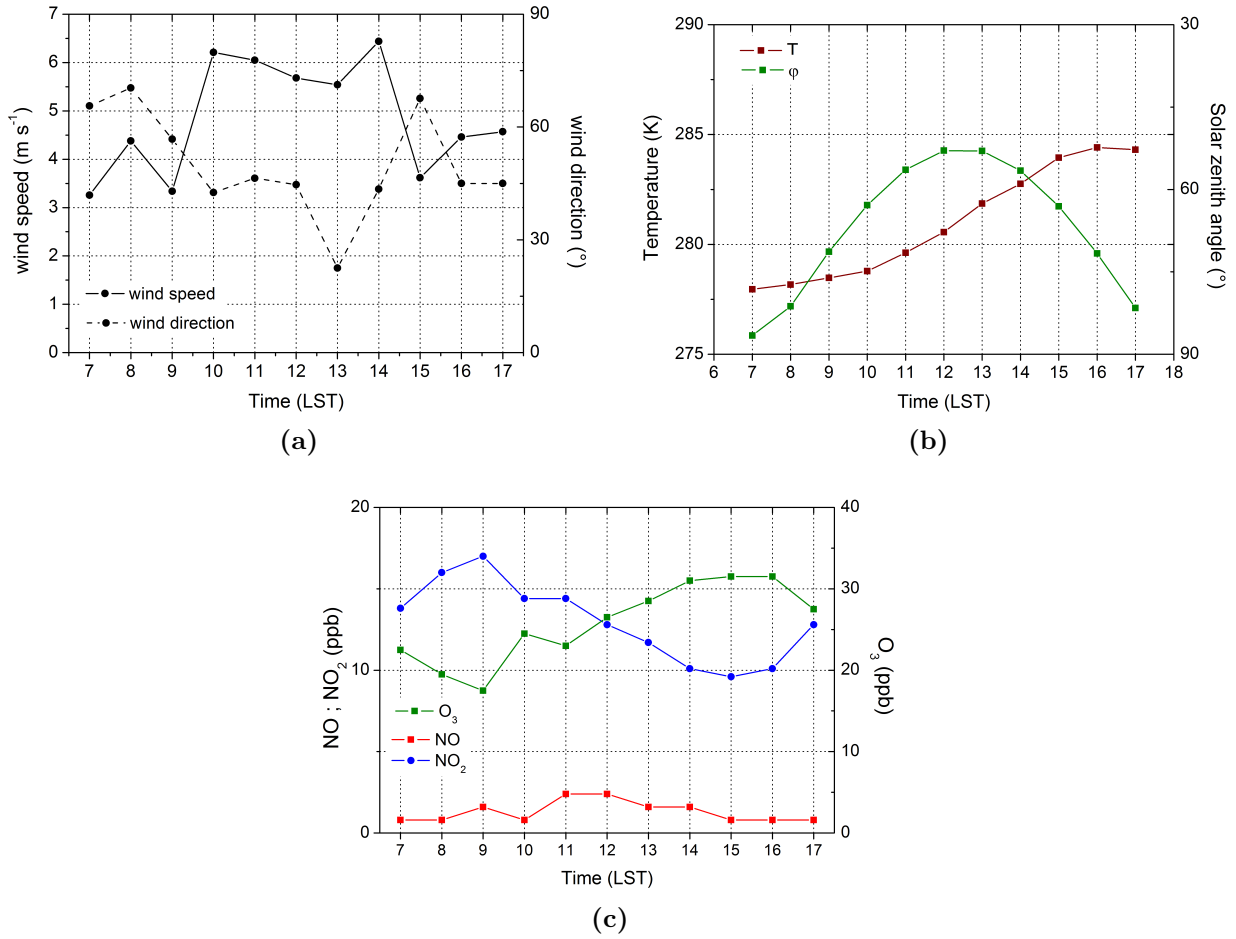

Figure 5.5: Inlet values of: (a) wind speed and direction at 18 m, (b) air temperature and solar zenith angle and (c) background concentrations of NO, NO_2 and O_3 derived from NE-UB station.

5.4.2 Validation

The meteorological and turbulent parameters obtained from the CFD simulation are evaluated against the experimental data taken in the sonics anemometers, at 8 m and 6 m AGL (green dot in Fig. 5.1b). For the validation, the measurements are hourly averaged.

Figure 5.6 illustrates the time series of wind speed and direction and turbulent kinetic energy resulted from the simulation against the experimental value.

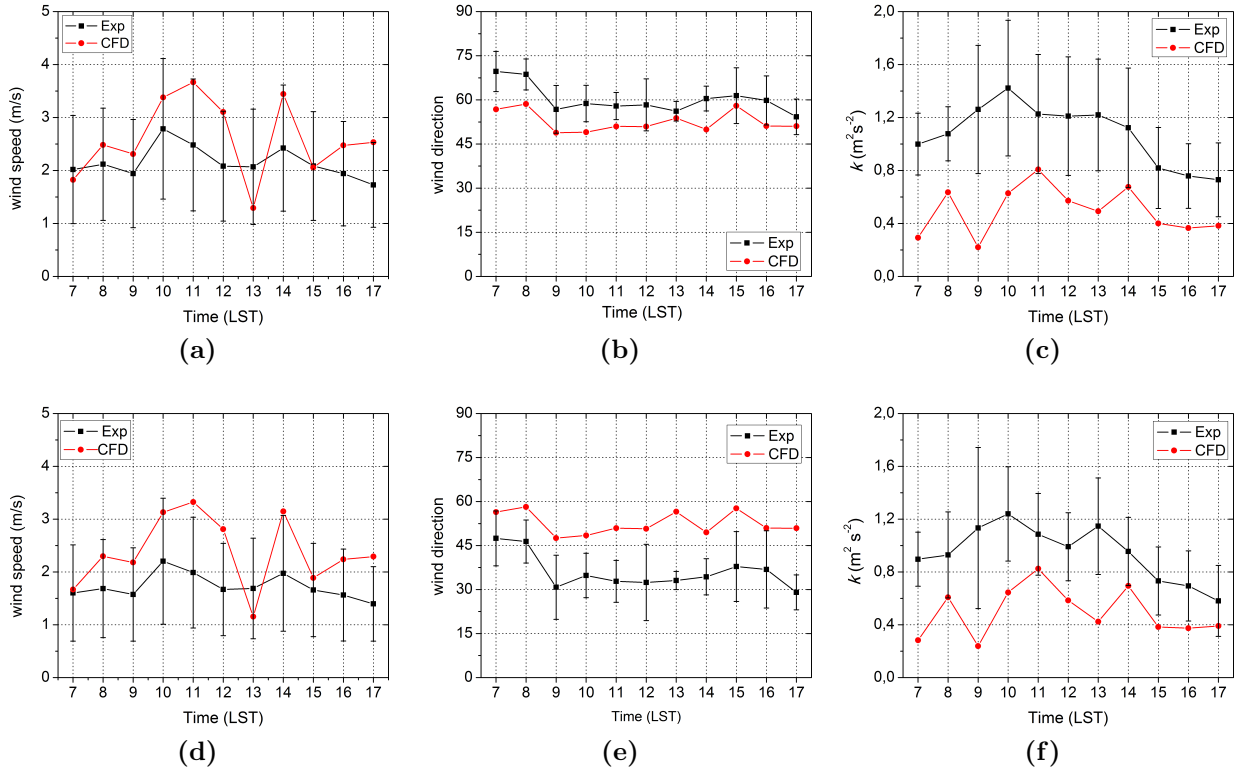

Figure 5.6: Time series of wind speed, wind direction and turbulent kinetic energy (k) respectively, (a-c) at 8 m AGL and (d-f) at 6 m AGL. The errors bars means the standard deviation of the measurement at every hour.

At both points, the wind direction is well reproduced by the simulation, being slightly better at 8 m. At that height, the modelled wind speed remains within the variation range of measurement every hour whereas, at 6 m, the outputs show overestimations at certain hours. In contrast, the modelled turbulent kinetic energy clearly underestimate the experimental values.

For further quantitative information, the statistics NMSE, FB and R are calculated for wind speed and turbulent kinetic energy at 8 and 6 m (Table 5.2).

Table 5.2: Statistical parameters for wind speed (U) and turbulent kinetic energy (k).

	U (z=8 m)	k(z=8 m)	U (z=6 m)	k(z=6 m)	Acceptance Criteria
NMSE	0.09	0.57	0.69	0.52	NMSE<1.5
FB	0.19	-0.32	-0.74	-0.62	-0.3<FB<0.3
R	0.64	0.65	0.44	0.35	R>6

Better results for wind speed and turbulent kinetic energy are obtained at 8 m, where all statistics are within the acceptance criteria established in Chang and Hanna (2004). The NMSE reveals an overall small deviation of the modelled value from the observation. At 8

m, the FB shows a slight overestimation of the wind speed and a larger underestimation of turbulent kinetic energy close to acceptance threshold. Likewise, for both variables, R above 0.6 exhibits a fair correlation between the outputs and the observations. In contrast, at 6 m, whereas the experimental wind speed and turbulent kinetic energy are slightly lower than at 8 m, the modelling results provide similar values. This little difference between both points is mainly caused by the mesh resolution of the CFD simulation. Improving this error would require to reduce the grid size in order to better reproduce the vertical gradient in that short distance. In addition, there is vegetation close to the experimental deployment, which may introduce an error in the simulation since its features geometry are modelled in a simplified way.

The validation of the concentrations of NO_x, NO, NO_2 and O_3 is performed with the measurements recorded at FL station (blue dot in Fig. 5.1b).

Figure 5.7 displays time series of the experimental and simulated NO_x concentrations. Except to first hour, the simulated NO_x follows the same trend of the measured NO_x, obtaining values of NMSE and FB equal to 0.17 and -0.064. The error in the NO_x concentration at 0700 LST may be related to an overestimation of the traffic emission for that particular day, or to the uncertainties associated to atmospheric stability at that time.

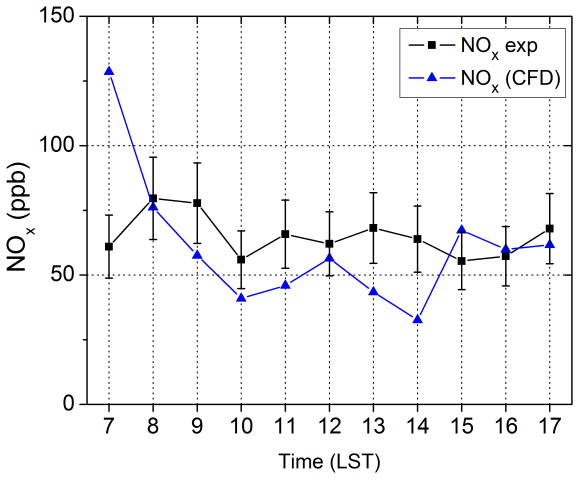

Figure 5.7: Time series of measured and modelled concentration of NO_x (ppb) at FL station. The error bars represent the 20% of experimental data.

Figure 5.8 shows the temporal evolution of NO, NO_2 and O_3 obtained from the simulation and the measurements at FL station. The NO and NO_2 modelled as reactive pollutants are hereafter referred to as NO_R and NO_{2R} and, as non-reactive, NO_T and NO_{2T}. It is noteworthy that the error bar is the 20% of the measurements related to the legal error allowed for the measurements by the UNION et al. (2008), without considering the variability of concentration during the hour.

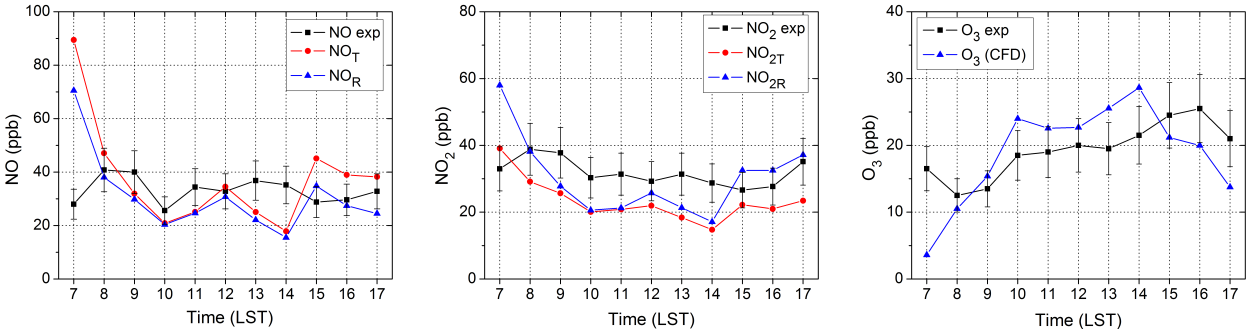

Figure 5.8: Time series of the measured and modelled concentrations (ppb) at FL station for: (a) NO, (b) NO_2 and (c) O_3. The error bars represent the uncertainty of the measurement (20%).

Unlike the first hour, the modelled concentrations reproduce the same behaviour that the measurements at FL station. Overall, the statistical analysis for the NO_T and NO_R yield similar values of the NMSE, 0.36 and 0.25 respectively and the FB equal to 0.13 and -0.08, which concludes a good approximation of both approaches. Likewise, for the NO_{2T} and NO_{2R}, the NMSE is 0.13 and 0.12 respectively whereas the FB shows a slight underestimation with values of -0.31 and -0.05 respectively. Even so, despite the error made at 0700 LST, both chemical approaches considered in the simulation seem to provide a good result of the daytime behaviour for both the NO and the NO_2.

5.4.3 Impact of the chemical approach on concentration at pedestrian level

This section is addressed to examine the deviation of modelling NO and NO_2 as reactants instead of non-reactive pollutants at pedestrian level over the research area (Fig. 5.9).

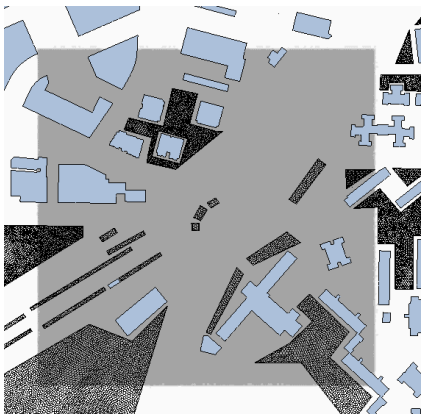

(a)

Figure 5.9: Research area of 300 m x 300 m.

Firstly, the spatial average (<>) concentrations over the research area (300 m x 300 m) is computed at every hour for: NO_T, NO_R, NO_{2T} and NO_{2R} and the relative differences, δNO and δNO_2 (Eq. 3.1). Figure 5.10 depicts the temporal evolution of: $< NO_T >$, $< NO_R >$, $< \delta NO >$ and $< NO_{2T} >$ and $< NO_{2R} >$ and $< \delta NO_2 >$.

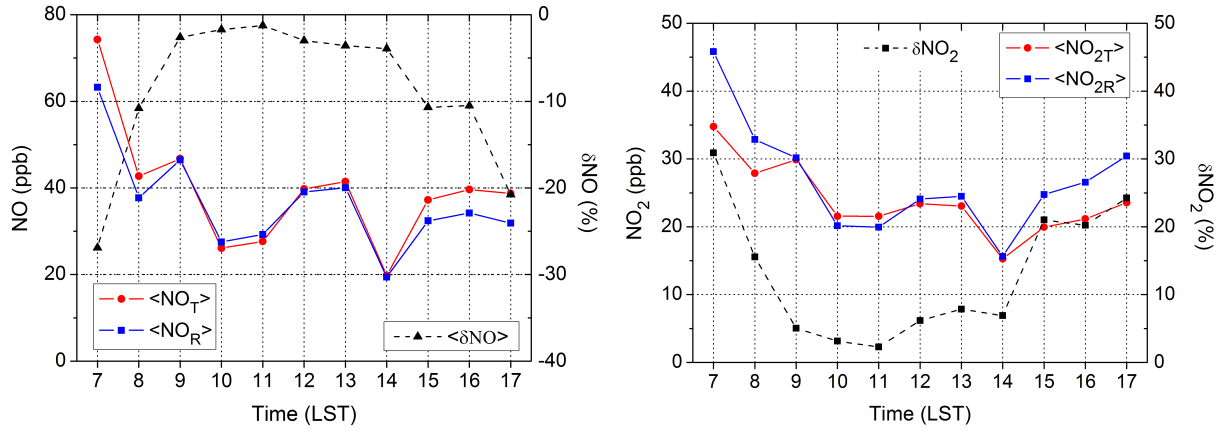

Figure 5.10: Time series over the research area, at 3 m AGL, of (a) $< NO_T >$, $< NO_R >$ and $< \delta NO >$ and (b) $< NO_{2T} >$, $< NO_{2R} >$ and $< \delta NO_2 >$.

Overall, the results of NO and NO_2 show the same temporal trend with barely differences, below 20%, between the reactive and the non-reactive assumptions, particularly from 0800 LST to 1600 LST. At midday, the ambient O_3 and the NO_2 photolysis are larger and, thereby, the deviation from the chemical equilibrium is lower in the overlying airmass.

However, at sunrise (0700 LST), the NO_2 photolysis is smaller and, thereby, there is no possibility to reach a chemical balance using the $NO_x - O_3$ mechanism (as described in Chapter 4). In these cases, $< \delta NO >$ and $< \delta NO_2 >$ increases up to 30% mainly caused by the NO and O_3 reaction. Similarly, at last hour, the photolysis of NO_2 decays, regarding the reaction between NO and O_3 since the temperature and the background O_3 is still larger (Fig. 5.5). In this case, $< \delta NO_2 >$ slightly exceeds 20% of difference. Overall, $< \delta NO >$ and $< \delta NO_2 >$ reveal an small impact of the chemical reactions.

Comparing the spatial layout, NO_{2R} and δNO_2 are depicted at 0700 LST and 1200 LST at pedestrian level in Fig. 5.11.

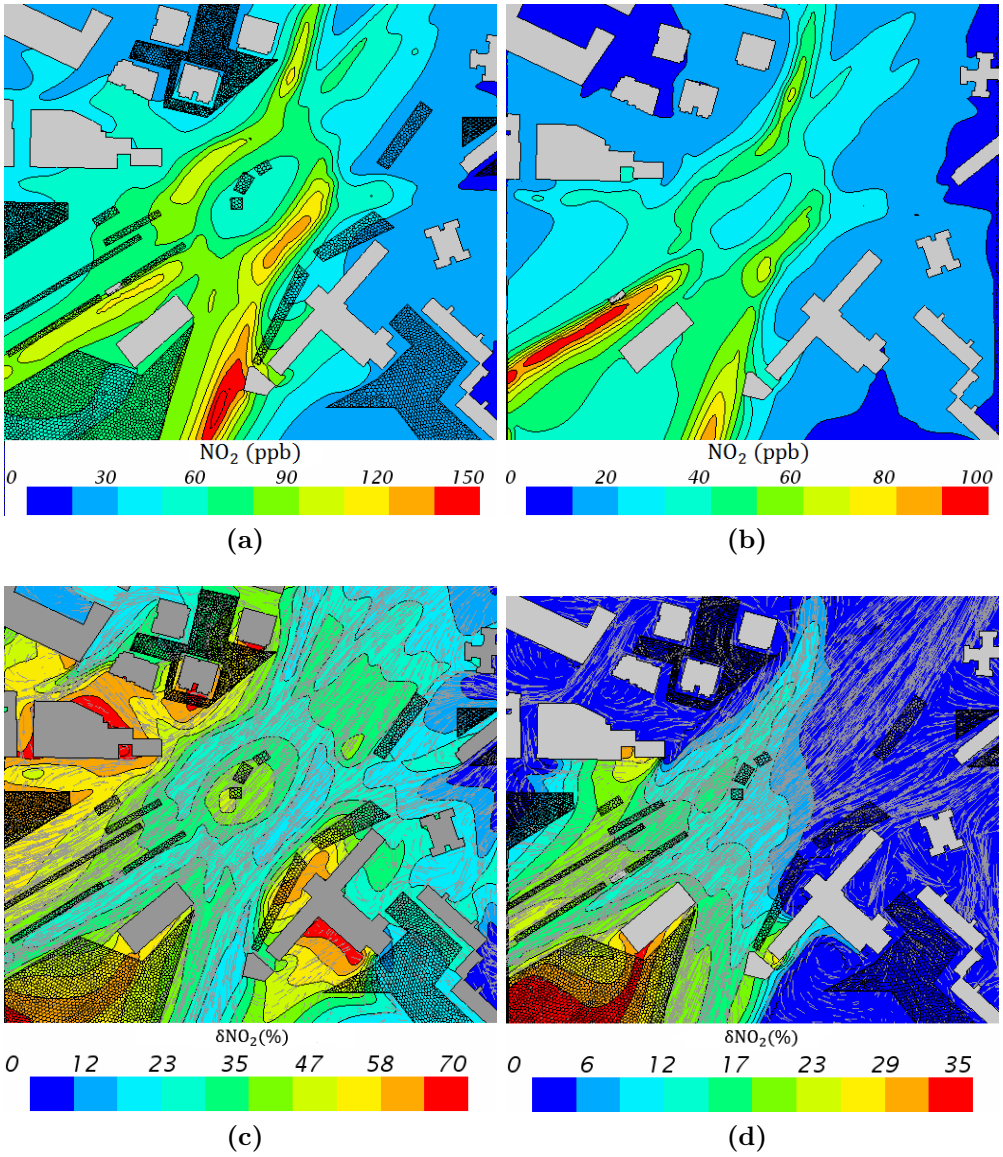

Figure 5.11: Maps at pedestrian level of (a-b) NO_{2R} (ppb) and (c-d) δNO_2 (%) respectively at 0700 LST and 1200 LST. Grey arrows indicate the flow fields corresponding to the NE direction.

The maps of δNO_2 show that the smallest differences are located around the emission region in both cases. However, the largest δNO_2 are obtained further away from emissions, where the NO_2 concentration is lower. At 0700 LST, δNO_2 displays an overall increase in the concentration of NO_{2R}, that provides local deviations significantly higher. At 1200 LST, δNO_2 rises in the wind flow direction (NE), as the emissions interact with the ambient pollutants, disturbing the chemical equilibrium of the overlying air. As a consequence of the flow pattern, the concentration of reactive pollutants differ from the non-reactive approach, especially in areas with larger residence time, e.g. in the vortexes produced in the street or in the vegetation region.

The average error throughout the day in the NO and NO_2 is examined through the daytime mean maps. Figure 5.12 shows the time-average concentration from 0700 LST to 1700 LST

for the NO_T, NO_R, NO_{2T}, NO_{2R} in the research area, at pedestrian level.

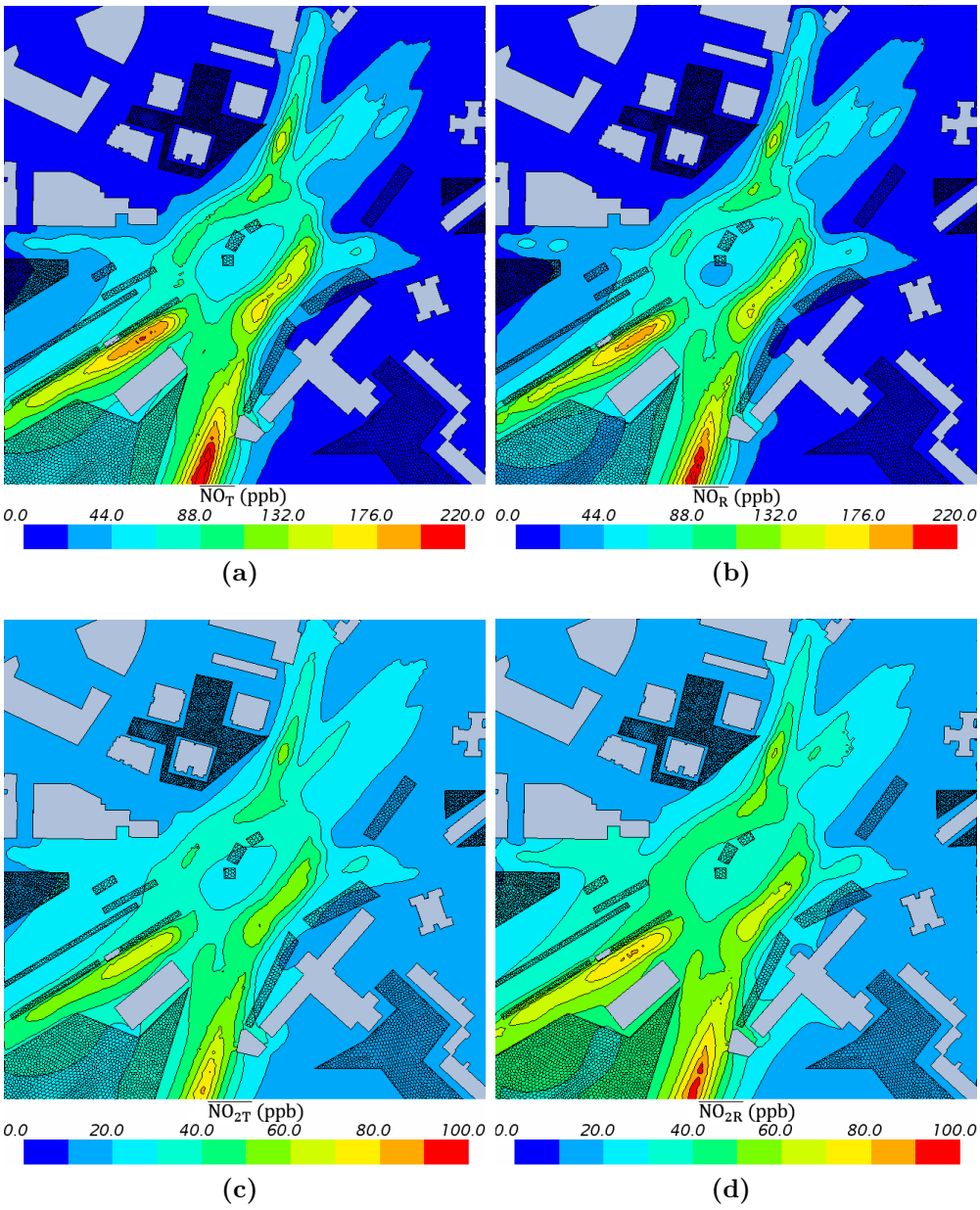

Figure 5.12: Maps at pedestrian level of (a) $\overline{NO_T}$ (ppb), (b) $\overline{NO_R}$ (ppb), (c) $\overline{NO_{2T}}$ (ppb) and (d) $\overline{NO_{2R}}$ (ppb).

The concentration mean maps show similar distributions of pollutants dispersion in the streets using any of the two chemical approaches, though an increase of NO_{2R} concentration is appreciable. $\Delta\overline{C}$ $(=\overline{C_R} - \overline{C_T})$ displays the largest values at south-west of the square, due to the flow pattern produced by the prevailing wind direction (North-East) along the day (Fig. 5.13a). It is noteworthy that the maximum difference is around 14 ppb with concentration values of 80 ppb for the NO and 40 ppb for the NO_2. The significant values of $\delta\overline{NO}$ and $\delta\overline{NO_2}$ above 20% are only limited to certain areas, also caused by the flow (Fig. 5.13b-c). In general, low differences between the two modelling chemical approaches are

obtained in most part of the domain. The spatial average over the research area results in $< \delta\overline{NO} >$ around 6.3 %, whereas the $< \delta\overline{NO_2} >$ reaches a value of 11.5 %.

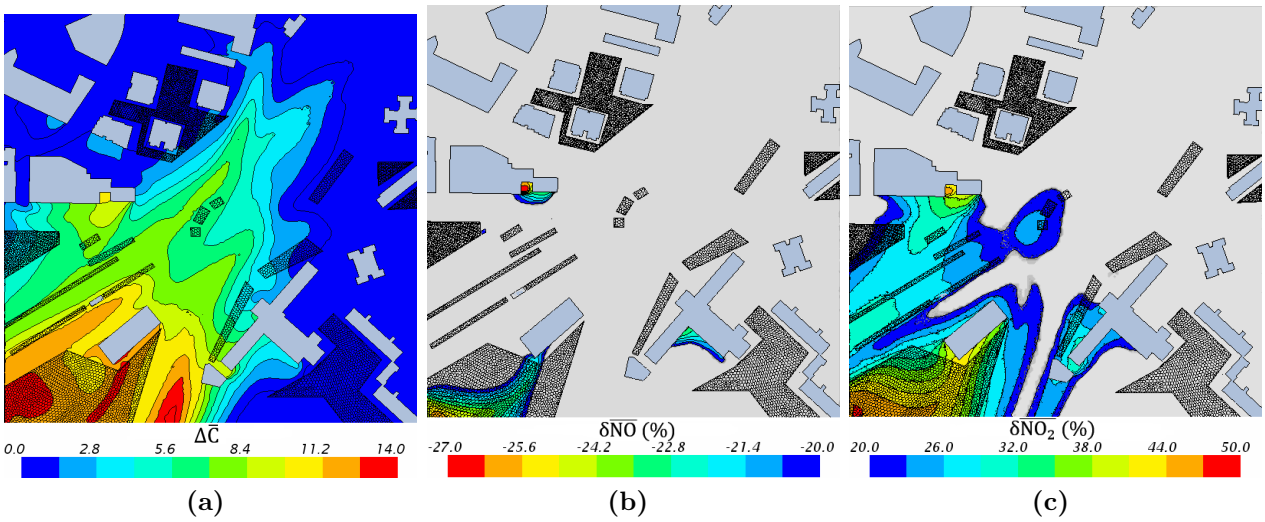

Figure 5.13: Daytime map at pedestrian level of: (a) $\Delta\overline{C}$ (ppb), (b) $\delta\overline{NO}$ (%) and (c) $\delta\overline{NO_2}$ (%). Grey color represents relative values below 20% of difference.

The conversion of NO to NO_2 over the total NO_x is analysed by means of the ratio NO_2-to-NO_x in air. Figure 5.14 displays the $\overline{NO_{2T}}$-to-$\overline{NO_x}$ and $\overline{NO_{2R}}$-to-$\overline{NO_x}$ at pedestrian level.

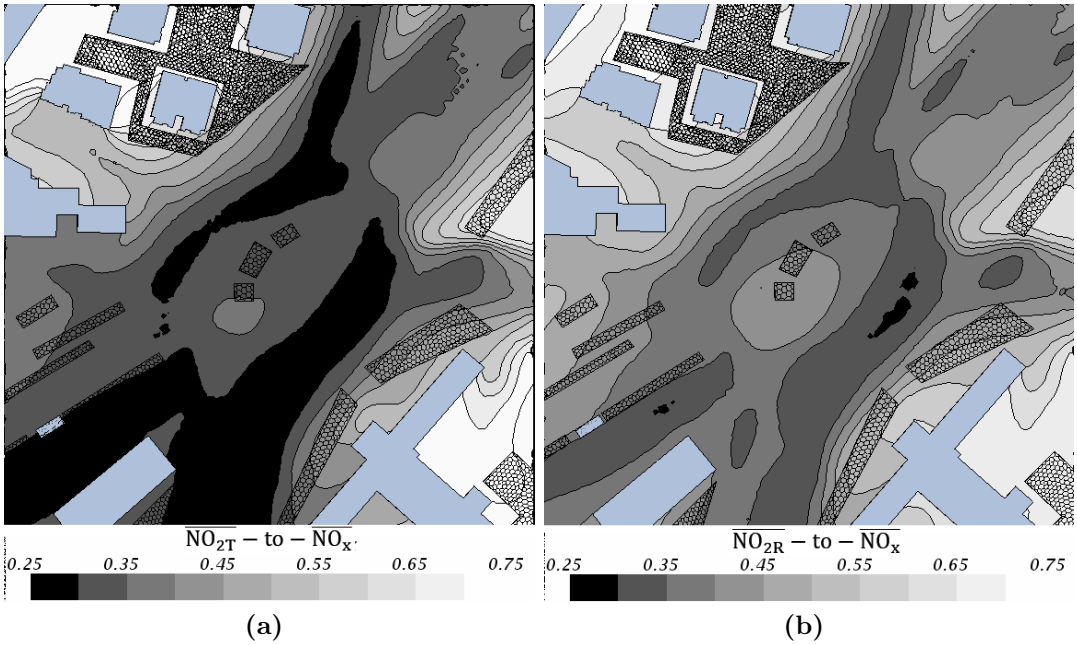

Figure 5.14: Maps at pedestrian level of: (a) $\overline{NO_{2T}}$-to-$\overline{NO_x}$ and (b) $\overline{NO_{2R}}$-to-$\overline{NO_x}$.

The ratio $\overline{NO_{2T}}$-to-$\overline{NO_x}$ slightly differs from the ratio imposed at the source (NO_2/NO_x=0.3). The horizontal gradients show that the ratio grows as the distance from the emission increases, which is mainly caused by dynamical processes (Fig. 5.14a). The inclusion of

chemical reactions displays smoother horizontal gradients but the $\overline{NO_{2R}}$-to-$\overline{NO_x}$ takes closer values to the non-reactive approach (Fig. 5.14b).

Accordingly, in these atmospheric conditions, the difference obtained between the two chemical approaches is reduced throughout day and, also, in the daytime mean maps (below 20%). However, there are local differences above 20% in certain areas, mainly as a consequence of the flow pattern. Therefore, as the error obtained for the NO_2 concentration is small, NO_2 can be modelled as a non-reactive pollutant in order to reproduce the NO_2 dispersion in the streets for long periods.

5.5 Modelling approach for urban air quality assessment

Air quality assessment in urban environments demands representative distributions of wind flow and dispersion of pollutants in the streets during long periods (weeks, months and even years).

This section is addressed to develop a modelling approach through the CFD-RANS simulations in an attempt to obtain the NO_2 mean map over several weeks in the research area. The resulting NO_2 map is validated with the NO_2 concentration obtained from the 72 samplers placed around the square, from 9^{th} to 27^{th} in February, 2015 (Section 5.2).

5.5.1 Modelling approach

The numerical approach used is based on the Weighted Average methodology using a CFD-RANS model (WA CFD-RANS methodology) proposed by Santiago et al. (2013, 2017a). The main assumptions of this methodology are the following:

1. The pollutants have to be strictly considered as non-reactive specie. In this way, in neutral atmospheric conditions, the modelled concentration is directly and inversely proportional to the emissions and wind speed respectively (see Appendix 6.2). Although some differences are found between the reactive and non-reactive approaches by modelling NO_2 concentration, this error can be assumed small in winter conditions (δNO_2 <20%). Moreover, the non-linearity of chemical reactions prevents the application of this modelling approach.

2. The pollutant concentration just depends on emissions, wind speed and background concentration at every hour. Therefore, there is no influence from one hour to the next, which is implicitly considered in the background concentration applied at every hour.

3. Neutral atmospheric conditions have to be assumed and, thereby, thermal effects are not included in the CFD-RANS simulations. The strong mechanical turbulence, generated by the presence of buildings, makes that the thermal effects can be negligible, particularly in wintertime, when the solar forcing is not very intense.

The numerical approach consists in modelling neutral atmospheric conditions for each wind direction sector (such as N, NNE, and so on), in which is included all emission scenarios. Subsequently, the temporal evolution is performed from a sequence of those CFD simulations, depending on the wind sector and emission scenario at every hour. Finally, the adjustment of the selected simulations to the actual conditions of every hour is carried out using a reference velocity. Figure 5.15 illustrates a scheme of the procedure to be followed for the application of the numerical approach.

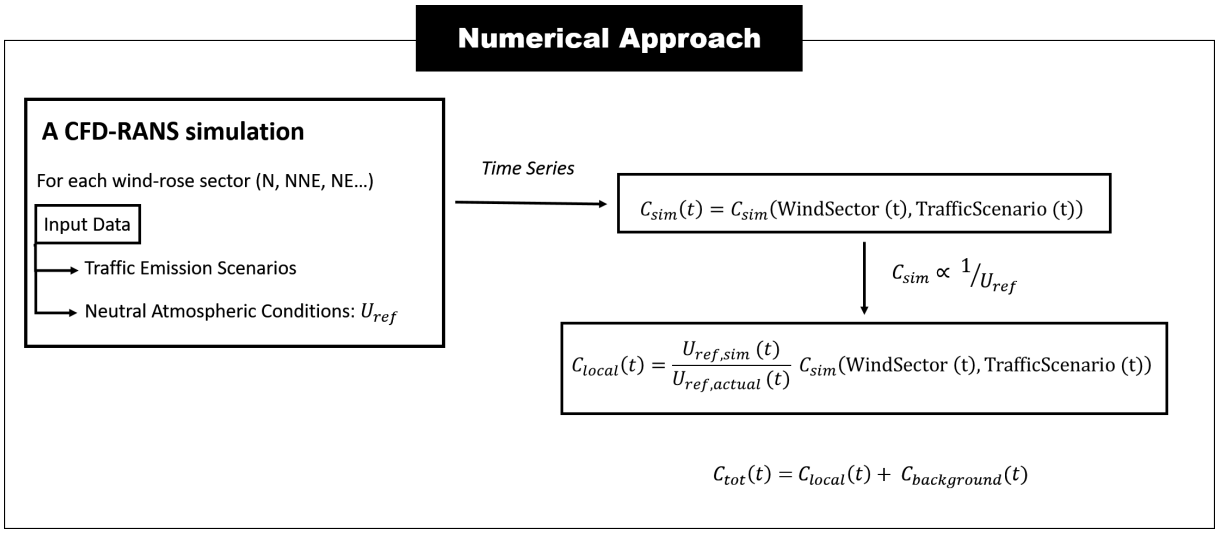

Figure 5.15: Scheme of the procedure of the numerical methodology.

The CFD simulations are carried out for each wind rose sector, in neutral stability conditions (Eqs. 5.1). To do that, the friction velocity is fixed (u_*=0.22 m s^{-1}) and the steady state is reached. For each wind direction sector, all emission scenarios involved in the weekly traffic pattern are simulated (Table 5.1).

For applying this methodology, the temporal evolution of the meteorological conditions at every hour is needed. In this work, the use of variables from a meteorological mesoscale model is proposed to improve the final result.

The mesoscale model (WRF) used is particularly adapted to simulate the urban atmosphere (Chen et al., 2011) by including the urban roughness sublayer parametrization (BEP-BEM) (Martilli et al., 2002; Salamanca et al., 2010). In particular, the grid point (1 km x 1 km) corresponding to the research area is classified as Compact Mid rise. This type of urban zone is characterized by a building packing density of 0.58 and building height distribution

of 25 % of buildings of 10 m, 45 % of 15 m, 20% of 20 m and 10% of 25 m (Stewart and Oke, 2012). Note that these are not the real morpholological parameters of the area. With the aim of covering the entire experimental campaign (Section 5.2), the mesoscale simulation starts at 1800 LST of the 8$^{\text{th}}$ February 2015 and ends at midnight of the 28$^{\text{th}}$ of February 2015 (Sanchez et al., 2017).

Therefore, for the composition of the microscale maps, the wind direction is selected at every hour from the mesoscale results, at the grid point corresponding to the microscale domain. Likewise, for that hour, the emission scenario is chosen based on the traffic flow pattern (Table 5.1). Consequently, the wind direction sector and the emission scenario corresponding to every hour are suitably associated throughout the entire experimental campaign.

$$C_{sim}(t) = C_{sim}(W_{sect}(t), S_{traff}(t)) \tag{5.2}$$

where C_{sim} is the simulated concentration of a non-reactive pollutant, and $W_{sect}(t)$ and $S_{traff}(t)$ are the wind direction sector and the traffic emission scenario corresponding to the time t.

As a second step, the simulated concentration ($C_{sim}(t)$) has to be transformed into the local concentration ($C_{local}(t)$) over time through the ratio of reference velocities (Fig. 5.15). This approximation is based on the concentration is inversely proportional to wind speed. Therefore, the concentration is transformed according to the actual wind speed at every hour.

In previous studies (Santiago et al., 2013, 2017a), the wind speed is used as reference velocity, which is obtained from a nearby meteorological station that is not perturbed by buildings. However, when thermal effects become significant in comparison with dynamical effects, the shape of the wind profile significantly differ from the neutral profile. In these cases, the use of the wind speed introduce some errors in the computation. To face this issue, the mesoscale model provides additional information about meteorological conditions. For that reason, the friction velocity (u_*) at the top of the canopy is proposed to be used as reference velocity. The height of the canopy top is considered at mean height of buildings. The friction velocity is defined by the turbulent momentum fluxes so that it provides information concerning vertical transport at that level.

In the microscale simulations, the u_* is computed by the spatial average ($< >$) of turbulent momentum fluxes given by:

$$u_* = \left[(< u'w' >)^2 + (< v'w' >)^2\right]^{(1/4)} \tag{5.3}$$

where the turbulent momentum fluxes in the CFD-RANS model are computed as:

$$u_i' u_j' = -\frac{\mu_t}{\rho}\left(\frac{\partial u_i}{\partial x_j} + \frac{\partial u_j}{\partial x_i}\right) \tag{5.4}$$

Likewise, the u_* from the mesoscale grid point is computed through the turbulent momentum fluxes in the horizontal surface at the selected level (around 30 m). Note that the mesoscale model takes into account the momentum and heat exchanges as a consequence of the presence of buildings. However, the u_* from the CFD simulation just considers the drag forces produced by the obstacles. In this way, several effects neglected in the CFD simulations are implicitly involved in the friction velocity derived from the mesoscale simulation. Finally, the ratio of the velocities obtained from the mesoscale and microscale outputs is computed at every hour. This provides the adjustment of the vertical transport at the height of the canopy top (h_{canopy}).

The ratio $u_{*,CFD}(t)/u_{*,WRF}(t)$ is used to transform the $C_{sim}(t)$ into $C_{local}(t)$, adjusted to the atmospheric conditions given by the mesoscale simulation at that time t. Moreover, the air composition from the surroundings of the research area is considered in the background concentration, C_{back}. It is obtained from the NW-UB station since the North-West is the prevailing wind direction during the experimental campaign. Hence the total concentration, $C_{tot}(t)$, is computed at every hour from the sum of the local contribution and the background concentration, expressed as follows:

$$C_{tot}(t) = \left.\frac{u_{*,CFD}(t)}{u_{*,WRF}(t)}\right)_{z=h_{canopy}} \cdot C_{sim}(W_{sect}(t), S_{traff}(t)) + C_{back}(t) \tag{5.5}$$

In atmospheric conditions of neutral stability, this approach is equivalent to use the wind speed as reference value since the wind speed is proportional to the u_* (logarithmic profile). However, when thermal effects become important, the use of u_* minimizes the error induced by the differences in the vertical wind profile.

This discussion about the suitable reference velocity to use in this modelling approach is analysed in the following section.

5.5.2 Evaluation of the modelling approach against measurements

The application of the previous modelling approach is firstly evaluated with the meteorological data measured at 18 m height on the building roof (blue point in Fig.5.1b). Secondly, the estimation of the NO_x concentration, using both the wind speed at a certain

height and the friction velocity, is compared with measurements recorded at FL station. For this analysis, NO_x is chosen since it is commonly considered as non-reactive pollutant.

Time series of meteorological variables

The meteorological variables are not recorded during the entire experimental campaign. For that reason, the evaluation of the modelling results is focused on full days, from 17th to 27th February, 2015. The outputs are compared against the wind data, averaged over 1-h periods, at 18 m height.

Once the inlet wind sector is selected, the temporal evolution of the wind direction from the CFD simulation is analysed against the experimental data at the sampling point (Fig. 5.16a). Overall, the outputs approximately capture the experimental wind direction over time, except in some hours. These differences are related to the mesoscale modelling errors as well as to the discretization of the inlet conditions of wind direction in the CFD simulations. Note that the continuous values derived from the mesoscale simulation is classified into the 16 wind sectors simulated with the CFD model.

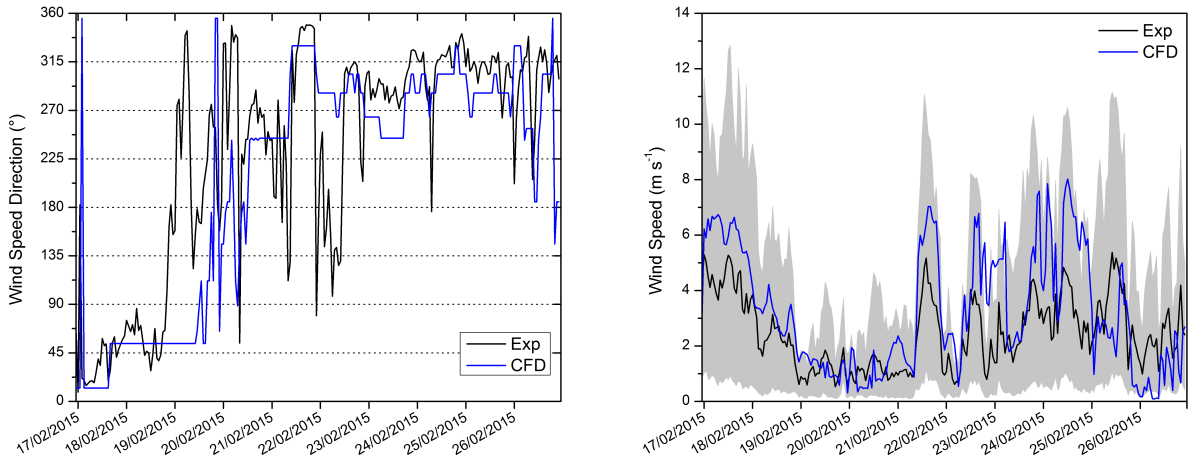

(a) **(b)**

Figure 5.16: (a) Time series of wind direction from CFD results (blue line) and measurements (black line) at meteorological station site. (b) Time series of the computed wind speed from CFD results (blue line) and measurements (black line). Grey area represents the interval between the maximum and minimum values recorded at every hour.

In addition, the wind speed is computed following the modelling approach (u_{comp}), but taking into account that the wind speed is directly proportional to the friction velocity:

$$u_{comp}(t) = \left.\frac{u_{*,WRF}(t)}{u_{*,CFD}(t)}\right)_{z=h_{canopy}} \cdot u_{sim}(W_{sect}(t)) \tag{5.6}$$

Figure 5.16b illustrates the temporal evolution of u_{comp} and the wind speed obtained from

experimental data at the same point. The u_{comp} reproduces the time evolution of the experimental data within the maximum and minimum values (grey area in Fig. 5.16b) recorded at every hour. For further details, the statistical parameters: NMSE, FB, R are computed together with the fraction of predictions within the factor 2 of observations (FAC2). The values obtained for the NMSE ans FB are respectively 0.31 and 0.27, which show a small deviation from the experimental data with a slight overestimation within the range of the acceptance criteria (NMSE<1.5 and -0.3 <FB< 0.3 (Chang and Hanna, 2004; Goricsán et al., 2011). In addition, the FAC2 equal to 71.25% and a correlation coefficient of 0.69 conclude that the modelling approach used for the wind speed (u_{comp}) is appropriate.

Time series of NO_x concentration at FL station

In this section, the use of the friction velocity or the wind speed as reference velocities to apply the modelling approach is evaluated. To that end, the NO_x concentration is computed through the two methods and is evaluated against the NO_x measured at the FL station, from 9^{th} to 27^{th} of February, 2015 (Fig. 5.17). The friction velocity is computed at the top of the canopy (h_{canopy}) from the mesoscale data. Instead, the wind speed used as reference velocity is selected at 180 m ($6h_{canopy}$), where the vertical profile approximately holds constant in height from mesoscale outputs.

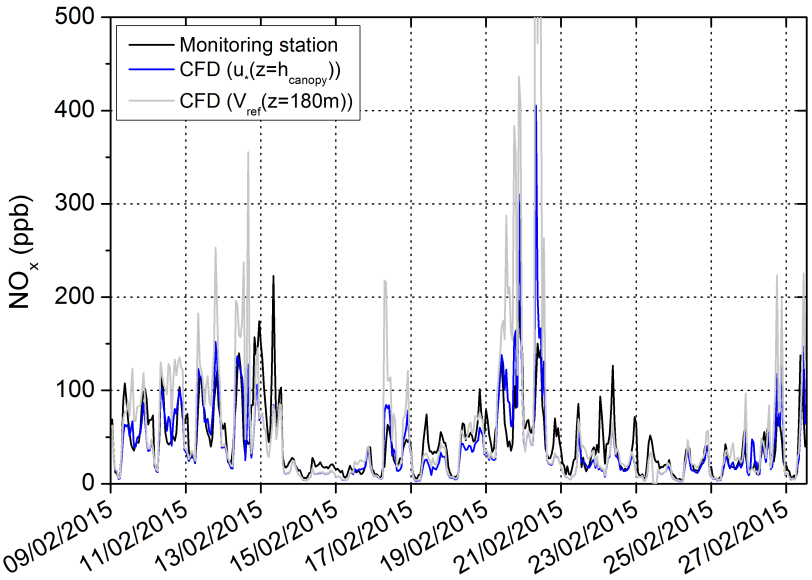

Figure 5.17: Time series of the measured NO_x (black line) and the computed NO_x with the $u_*(z = h_{canopy})$ (blue line) and $V(z = 180$ m) (grey line) at the FL station in the research area.

In general, the time series of the measured NO_x is well reproduced with the computed NO_x in both cases. During several days, the notable overestimations of the NO_x calculated with the wind speed ($V_{ref}(z = 180$ m)) are significantly reduced using the friction velocity as reference

velocity. This was study for wind speeds at several heights giving similar behaviours.

There are some uncertainties caused not only by the assumptions established in the CFD simulations, but also by the unavoidable numerical errors from the models. The assumption of neutral atmospheric conditions is one of the reason of those overestimations. The atmospheric stability broadly varies over time. Consequently, when the atmospheric stability changes to unstable or stable conditions, the wind profile ceases to be logarithmic and the error in the equivalence of the ratio of velocities increases. Therefore, the atmospheric stability is estimated over time from the mesoscale outputs by means of the parameter z/L defined in the Monin-Obukhov similarity theory (Section 1.2), where L is expressed as:

$$L = \frac{{u_*}^3}{\frac{g}{T_{ref}} \frac{Q_h}{\rho C_p}} \tag{5.7}$$

In this case, Q_h is the total heat flux defined by the heat from all urban surfaces divided by the horizontal area (W m^{-2}). L stands for the thickness of the layer close to the surface, where the production of turbulent kinetic energy by shear is greater than by buoyancy.

Therefore, the temporal variation of the atmospheric stability is calculated at the top of the canopy (h_{canopy}/L). For neutral atmospheric conditions, the adimensional number h_{canopy}/L is zero. Instead, higher values represent a greater importance of the buoyant forces and, thereby, the atmospheric conditions are further from the neutral atmosphere. Figure 5.18 shows the time series of h_{canopy}/L and the difference of the computed NO_x through $u_*(z = h_{canopy})$ and $V_{ref}(z = 180$ m) from the measured NO_x.

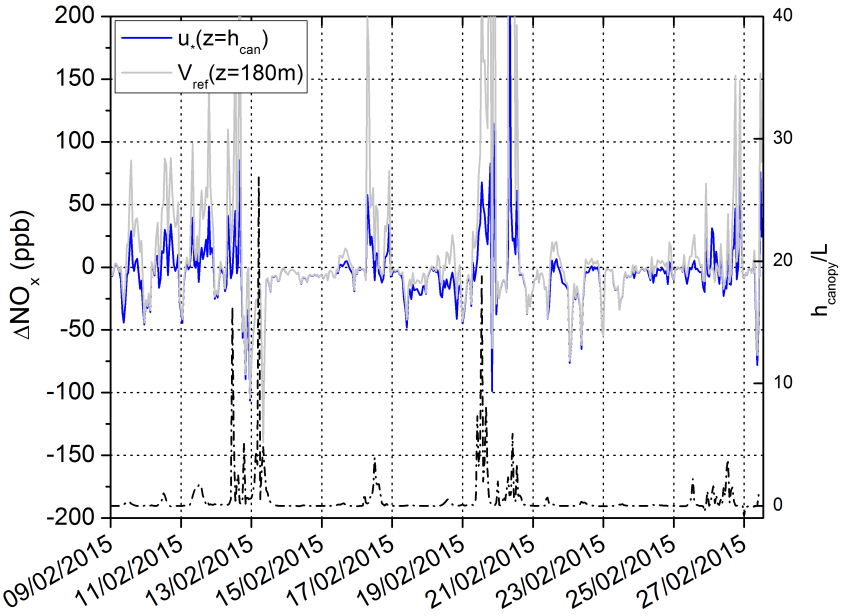

Figure 5.18: Time series of: h_{canopy}/L (dashed line) and the differences in concentration of the computed NO_x against the experimental data using the friction velocity (blue line) and the wind speed at z=180 m (grey line).

For both reference velocities, the maxima differences correspond to high values of h_{canopy}/L, which represents that the atmospheric stability is further from neutral conditions. High values of h_{canopy}/L indicate that buoyant forces are prevailing against the inertial force in the production of turbulent kinetic energy. It gives rise to the vertical transport is considerably modified below the canopy top. Therefore, if the wind speed as reference velocity is replaced by the friction velocity at the top of the canopy, the greatest overestimations in concentration are smoothed (e.g on 20$^{\text{th}}$ February in Fig. 5.18). For lower values of h_{canopy}/L, where the thermal effects are slightly larger than inertial forces, the use of u_* enhances the computed concentration, e.g. from 25$^{\text{th}}$ to 27$^{\text{th}}$ February (Fig. 5.18). This improvement is because to a certain extent, thermal effects are accounted for by the mesoscale model in the estimation of u_*. However, for high h_{canopy}/L values, this methodology fails and the explicit inclusion of thermal effects in the CFD simulations becomes necessary.

The scatter plots of the NO_x obtained from both methods against the measured NO_x are depicted in Fig. 5.19 and, the statistical parameters are contained in Table 5.3.

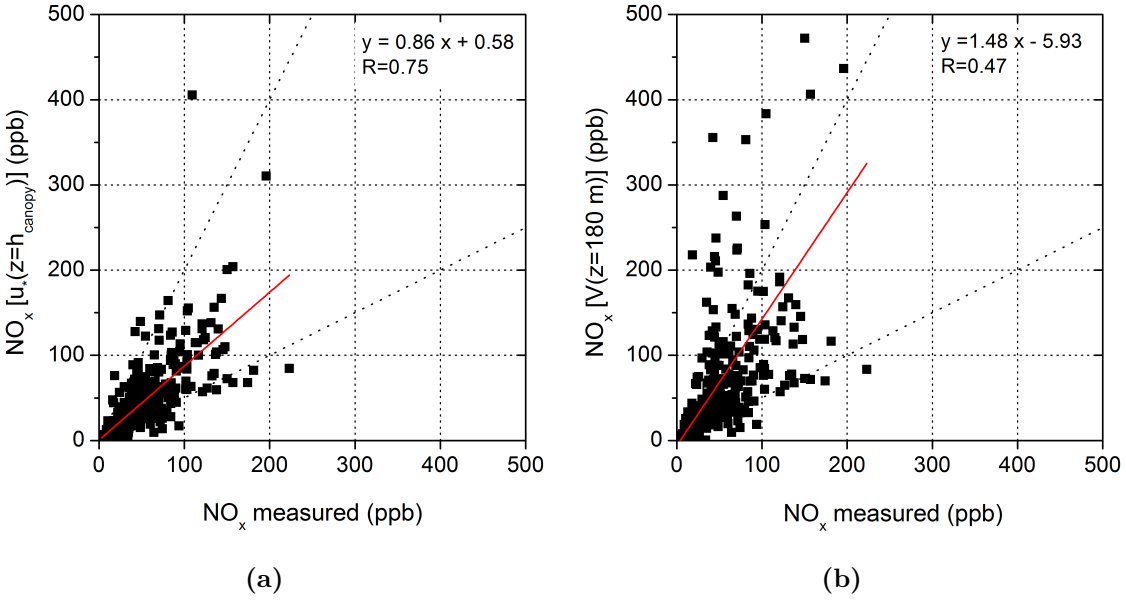

Figure 5.19: (a) Scatter plot of NO_x computed using the friction velocity. (b) Scatter plot of NO_x computed using a specific wind speed, at z = 180 m.

Table 5.3: Statistic metrics obtained for the validation of using u_* and $V(z = 180$ m) in the modelling approach. Acceptance criteria for urban configuration proposed by Chang and Hanna (2004) and Goricsán et al. (2011).

	Values u_*	Values $V(z = 180m)$	Acceptance Criteria
NMSE	0.28	2.40	NMSE< 1.5
FB	-0.13	-0.29	-0.3 < FB < 0.3
R	0.75	0.47	0.5<R<0.8

The use of u_* improves the results in comparison with the experimental, proving statistical parameters within the acceptance range established in Chang and Hanna (2004). The correlation coefficient increases from 0.47 to 0.75 by using the friction velocity and, besides, the fraction of values within a factor 2 improve from 77.3% to 88.6%. This analysis concludes that better results are obtained using the modelling approach with the friction velocity.

5.5.3 Validation with passive samplers

In this section, the modelling approach, using the u_*, is applied in order to obtain the NO_2 mean map in the research area. The NO_2 mean map for the entire experimental campaign (from 9^{th} to 27^{th} February 2015) is computed through two different procedures. The results are evaluated in 72 sampling points of NO_2 placed in the streets in an attempt to provide the best approximation for the NO_2.

- **Case 1**

  On the basis of NO_x can be considered as a non-reactive pollutant, the modelling approach is applied for the NO_x concentration. Hence the NO_x mean map is transformed to NO_2 through the time-average of the ratio NO_2/NO_x recorded at FL station, which is assumed equivalent to the entire research area. Therefore, the NO_2 mean map is resulted from the product of the NO_x mean map and the ratio $\overline{NO_2/NO_x}$=0.57 measured at the FL station.

- **Case 2**

  In this case, the NO_2 is regarded as a non-reactive pollutant, assuming that there is no significant influence of chemical reactions in the concentration. Hence the modelling approach is directly applied over the NO_2. It involves simulating the NO_2 dispersion, for each wind direction sector, taking into account the traffic emission ratio NO_2/NO_x equal to 0.3. Thereupon, the modelling approach is performed in the same way considering, in this case, the background concentration of NO_2.

Thereafter, the time average of the computed NO_2 using both procedures (Case 1 and Case 2) is evaluated with the NO_2 recorded at every point (Fig. 5.20). The NO_2 resulted from both cases fits fairly well to the experimental value in most points. However, there is an overall underestimation of the NO_2 concentration that may be related, among other reasons, to not consider chemical reactions (Fig. 5.21).

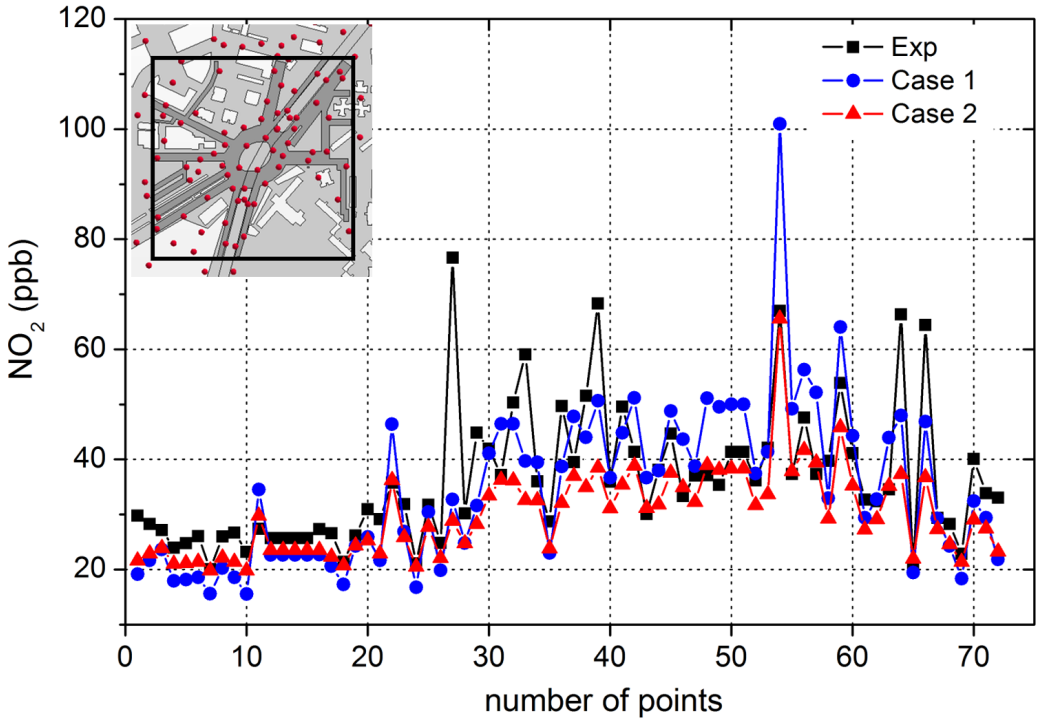

Figure 5.20: Time average value of the computed NO_2 concentration resulted from the Case 1 (blue point) and Case 2 (red point) and the experimental value (black point), at every location of the passive samplers, within the research area.

The scatter plots of the NO_2 from each case against the measurements reveal good results with the same correlation coefficient (R=0.72 in Fig. 5.21). Likewise, statistics NMSE and FB turn out 0.09 and -0.05, for the Case 1, and 0.1 and -0.2, for the Case 2. In general, it concludes a good adjustment to the experimental data with a slight underestimation for the Case 1, being larger for the Case 2.

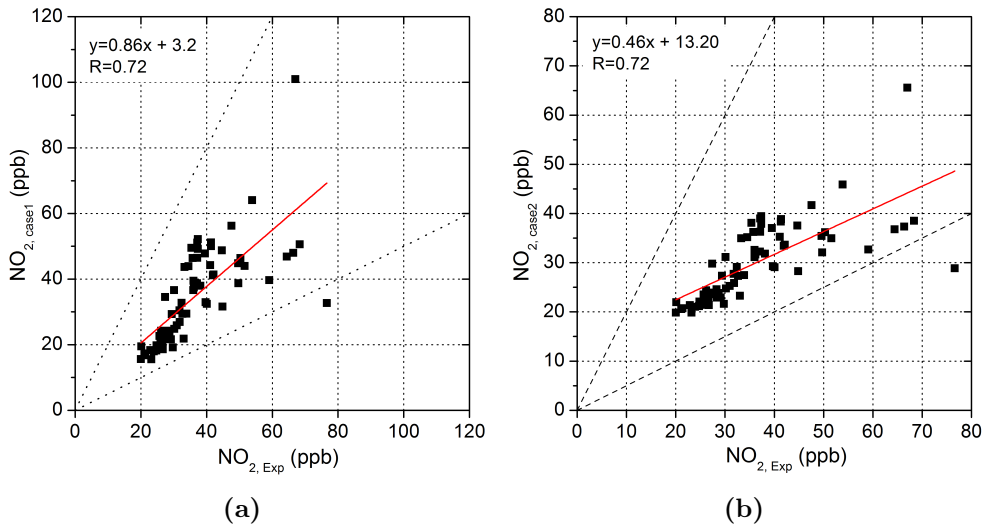

Figure 5.21: Scatter plots of the NO_2 concentration at sampling points for the (a) Case 1 and (b) Case 2.

Lastly, the spatial distribution of NO_2 obtained from both cases is compared in Fig. 5.22 a-b. In the Case 1, the NO_2 map exhibits areas of larger concentration than that obtained in the Case 2. Most sampling points are located close to the road, where the concentration gradients are stronger. Hence the difficulty to capture the accurate value using the CFD model, even with high resolution emissions.

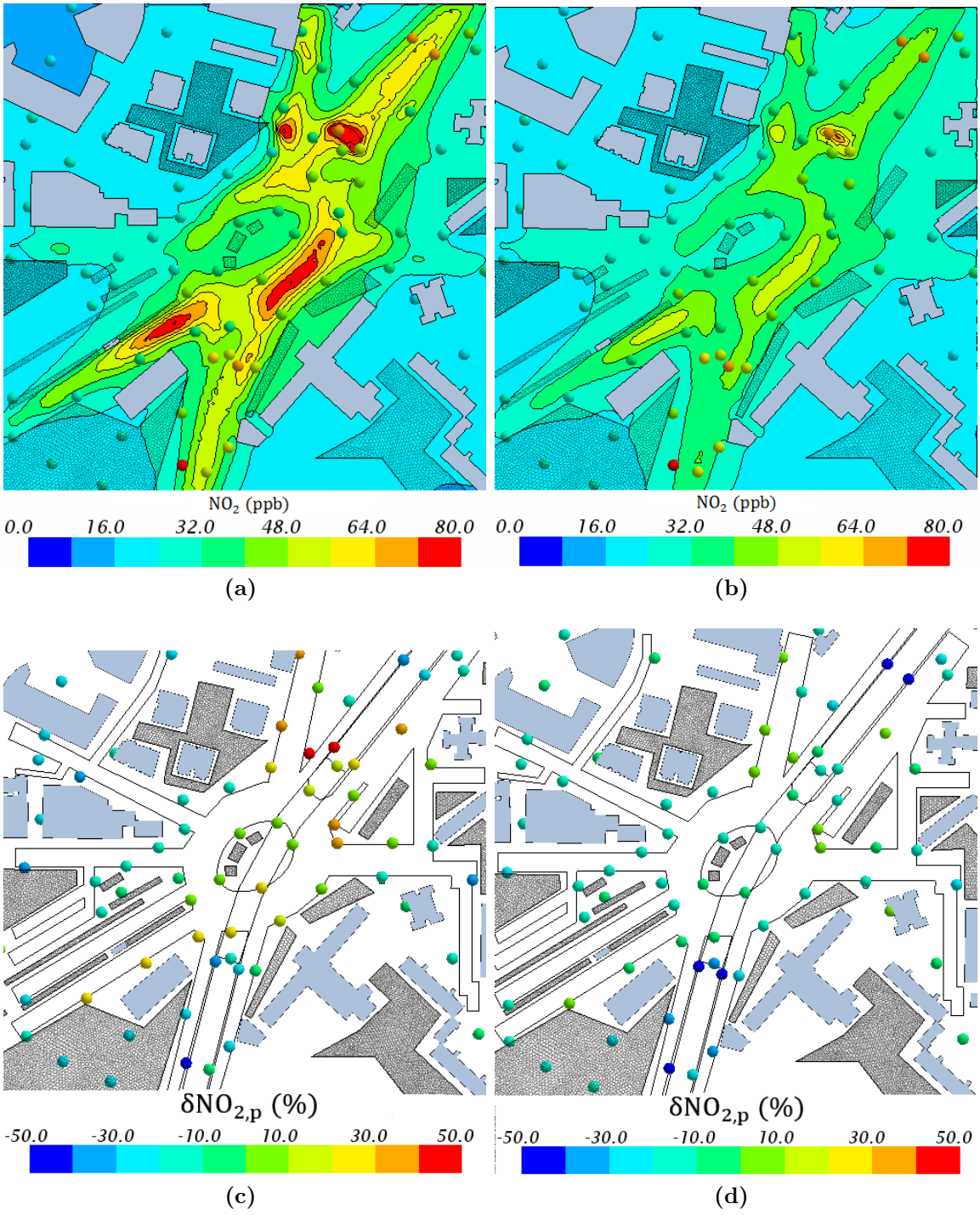

Figure 5.22: NO_2 mean map in comparison against the concentration taken by the passive samplers (coloured dots) located in the research area, for the (a) Case 1 and (b) Case 2. The $\delta NO_{2,p}$ at each measurement point, (c) for the Case 1 and (d) for the Case 2.

To analyse point-to-point, the relative differences of NO_2 with respect to the experimental data ($\delta NO_{2,p}$) is depicted at every location in Fig. 5.22 c-d. Overall, for both cases, the NO_2 differs from the measurements less than $\pm 20\%$ in most points. On the contrary, in the closest areas to the road, the values are above $\pm 20\%$ at some points. Moreover, there are some spatial differences between the NO_2 resulted from the Case 1 and the Case 2. In the latter, the largest $\delta NO_{2,p}$ are limited to the exits from the tunnel, however, in the Case 1, the deviation provides overestimations above 20% at some points along the main streets. In this case, the $\pm 30\%$ differences are located close to the emission areas, e.g. north-east of the roundabout or in the street the south-west of the domain. This is fundamentally related with the assumption of applying the ratio NO_2/NO_x at the FL station over the entire area. The ratio NO_2/NO_x in air spatially changes as result of chemical reactions and dispersion (Section 5.4.3).

Therefore, in the Case 2, the NO_2 is well reproduced throughout the roundabout, turning out some underestimations in the areas beyond the emissions from the tunnel. Although the global results from the Case 1 show better values in the statistical analysis, the relative differences display higher values in the interest areas. Focusing on near areas to the source, the relative difference shows a better approximation by applying the modelling methodology, assuming the NO_2 as non-reactive pollutant at wintertime.

This methodology is also used to reproduce the concentration gradients in this urban area during 4 weeks in summertime. The results turn out to be a suitable approximation of the spatial distribution captured by experimental data (Appendix 6.2). It bears out that this modelling approach provides reliable maps of pollutant concentrations in the street with high resolution.

5.6 Summary and conclusions

This work is addressed to evaluate the NO_2 dispersion in an urban hot-spot, at wintertime, using a CFD model. Firstly, the deviation in the NO_2 concentration, caused by chemical reactions, is temporally and spatially examined using the NO_x-O_3 mechanism. The temporal evolution of the NO_2 is modelled under both chemical approaches, being evaluated with the measurements recorded at FL station. The comparative study reveals differences below 20%, in average over the research area, throughout the day. However, the daytime mean map of NO_2 shows significant local differences between NO_{2R} and NO_{2T}, which is basically dependent on the flow pattern. Moreover, although the spatial average of the relative differences turns out lower values, locally, the dependence on the prevailing flow on the chemical reactivity is important. This is due to the formation of vortexes or the exchange of the emissions with the overlying air promote the chemical interactions as the pollutants mixing is growing.

The second part of this study is focused on obtaining the representative map of the NO_2 concentration in the research area covering several weeks. Performing a CFD simulation for a long period would require an important increase of computational load. Hence, an alternative solution to accomplish that mean map was proposed in Santiago et al. (2013). The numerical methodology is based on a combination of simulations, which entails making some assumptions: considering the NO_2 as a non-reactive pollutant and disregarding the thermal effects in the simulations. This methodology is improved with some novelties and thoroughly compared against experimental data (Sanchez et al., 2017). This new approach includes the variation of the meteorological conditions derived from a mesoscale simulation. Thus, the use of the friction velocity (u_*) at the top of the canopy is regarded as the reference velocity in the estimation of the time evolution of the NO_2 concentration. This seems to be crucial for a good estimation of NO_2 concentration, specially when the atmospheric stability changes from the assumed neutral conditions. With the ratio of the friction velocities, the vertical transport is forced to be equivalent at the canopy top, drawing other physical processes into the computation. In this way, the impact of the thermal effects on the flow, which are not considered in the CFD model, is indirectly taken into account in the u_* obtained from mesoscale. The temporal validation of the NO_x at FL station shows a better agreement with the measurement by using the friction velocity in the computation of the pollutant concentrations.

Therefore, this modelling approach is applied to obtain high resolution maps of NO_2 concentration, averaged over several weeks. To do that, two different procedures are followed. In the Case 1, the modelling approach is applied for the NO_x, considered as a non-reactive. After that, the resulting mean map of NO_x is transformed to NO_2 map, assuming the ratio NO_2-to-NO_x obtained at FL station for the entire map. On the other hand, for the Case 2, the NO_2 mean map is directly computed assuming the NO_2 as a non-reactive pollutant. Finally, the time-average concentration of NO_2, obtained from both procedures, is spatially evaluated against the experimental data from passive samplers. The corresponding scatter plots exhibit a good fit of the NO_2 concentration to the measurements, with an overall underestimation that may be related, among other reasons, to the fact that chemical reactions are not considered. The statistical parameters are within the ranges established in the acceptance criteria, with a high correlation coefficient (R = 0.72) in both cases. Nonetheless, locally, the relative differences of the NO_2 concentration obtained from the Case 2 are lower than in the Case 1.

The main limitation of applying this modelling approach is the need to establish some assumptions. However, the assessment shows that the methodologies used provide a good approximation to the experimental data, which conclude the validity of the assumptions for these atmospheric conditions. The link of mesoscale outputs with CFD simulations is

an useful system to analyse the NO_2 dispersion in urban areas with high spatial resolution. Moreover, the application of this modelling approach can be extended to any part of the city, independently of the existence of a meteorological station in the research area. Nevertheless, the modelling techniques should be complemented with experimental campaigns in order to show the accuracy of the simulated results.

Accordingly, these high resolution maps of pollutant concentrations are useful to assess the urban air quality, allowing to carry out a more detailed evaluation of the population exposure. In addition, if mesoscale models previously provide the outputs of chemical and weather forecasting at larger scale, this modelling approach could be applied for air quality forecasting at microscale.

Acknowledgments

This study has been supported by the TECNAIRE-CM research project (S2013/MAE-2972) funded by The Regional Government of Madrid and the Madrid City Council. Authors thank to C. Yague, C. Román-Cascón, G. Maqueda and M. Sastre (University Complutense of Madrid) for providing the meteorological data used in this work. The authors are also grateful to Extremadura Research Centre for Advanced Technologies (CETA-CIEMAT) by helping in using its computing facilities for the simulations. CETA-CIEMAT belongs to CIEMAT and the Government of Spain and is funded by the European Regional Development Fund (ERDF).

Chapter 6

Concluding remarks

6.1 Summary and conclusions

CFD models provide high spatial resolution results for the assessment of urban air pollution. To reach this goal, millions of computational cells are required to properly resolve atmospheric dynamics. As a consequence, these simulations demand large computational resources. The development of more powerful computers promotes that CFD simulations gradually incorporate more physical processes, e.g. the chemical interactions among air pollutants, with the aim of modelling the dispersion of reactive species in urban areas.

This work encompasses a comprehensive study of the chemical and dynamical processes that take place in the urban atmosphere using a CFD-RANS model. To that end, the most relevant chemical reactions in urban environments are considered. Hence the chemical mechanisms, NO_x-O_3 and NO_x-O_3-VOC, are implemented in the model. The multiple and combined chemical interactions among pollutants lead to a significant rise of computational time. Accordingly, in the course of this work, the importance of chemical reactions on modelling the NO_2 dispersion is thoroughly analysed in numerous atmospheric conditions and different urban settings. This study covers not only simplified urban configurations, but also real urban areas. The impact of the chemistry on pollutant concentrations in urban environments is variable depending on several factors that can affect the chemical conversions, e.g. meteorological conditions, urban air composition, geometry of urban area and, also, the traffic emission pattern. From this comprehensive study, the following conclusions are drawn:

- *Implementation of chemical reactions in the CFD-RANS model.*

  The chemical reactions of a simple chemical mechanism, the NO_x-O_3 scheme, and a more complex mechanism, NO_x-O_3-VOC scheme, have been properly implemented

in the CFD model.

CFD modelling of chemical reactions of the NO_x-O_3-VOC mechanism is successfully validated with a chemical box model. Additionally, the NO_x-O_3-VOC mechanism is evaluated in real urban environments using the CFD model. This analysis concludes suitable results that remark the potential of the CFD model to simulate the dispersion of pollutants including chemical reactions.

- *Influence of the chemical mechanism on the NO_2 dispersion at street level: NO_x-O_3 scheme and NO_x-O_3-VOC scheme.*

  The use of both chemical mechanisms (with and without VOC) allow to analyse the influence of including the VOC interactions on modelling the NO_2 concentration. In this study, the VOC contribution is just considered from traffic emissions. Hence the NO_x levels in air predominate over the VOC.

  In the cases studied, the modelled NO_2 concentration at street level reveals small sensitivity to the VOC levels. However, an increase of the VOC amount results in a greater impact on the NO_2 concentration and, thereby, the available O_3 in the street. Consequently, it rises the difference in the NO_2 concentration from the result of NO_x-O_3 scheme.

  Therefore, the NO_x-O_3 scheme seems appropriate to model the NO_2 dispersion in the streets. Just with a high VOC/NO_x relation and high O_3 background, the NO_x-O_3-VOC mechanism could be required. Accordingly, the sensitivity of modelling the NO_2 dispersion with the NO_x-O_3 scheme or the condensed NO_x-O_3-VOC mechanism rely on the urban atmospheric composition (i.e. levels of NO_x, O_3 and VOC) and even on the emission ratio VOC/NO_x from vehicles exhausts.

- *Impact of the atmospheric conditions on the chemical interactions.*

  The model sensitivity to use the NO_x-O_3 scheme for simulating NO_2 dispersion is widely examined under multiple meteorological conditions and several urban environments.

  Wind flow controls the ventilation of the streets and, thereby, determines the residence time of pollutants. Moreover, the non-uniform layout of buildings generate irregular flow patterns in the streets that are highly variable in time. The variability of chemical influence caused by the wind flow is characterised by the combination of two ways:

  - Greater ventilation of the street promotes the exchange of pollutants, giving rise to a larger O_3 entrainment into the street and, thus, larger chemical impact on the NO_2 concentration.

  - At street level, the spatial variability produces areas with larger residence time (e.g. vortexes) that encourage the chemical interactions, increasing the difference of concentration between the reactive and non-reactive approaches.

In the studied atmospheric conditions, larger values of temperature and solar radiation promote the chemical activity. In turn, those processes are usually related to an increase of the O_3 concentration in the background air. The available O_3 in the street trigger the chemical conversions between NO and NO_2. Hence the impact of chemical reactions on the modelled NO_2 concentration in the street increases with greater levels of background O_3. In contrast, when it is lower, the impact of the chemistry is significantly reduced.

Using the NO_x-O_3 scheme, the studied case with larger available O_3 in the street, the results reveal significant differences (above 20%) between the reactive and non-reactive approaches for the NO_2 and NO concentrations. Therefore, modelling the NO_2 dispersion at daytime demands the need to include a chemical mechanism in order to provide accurate concentration values. In contrast, the importance of chemical reactions in the urban hot-spot at wintertime reveals, in average, smaller differences below 20%. Lower solar radiation and temperature give rise to small deviations between the reactive and non-reactive approaches. However, locally, that difference increases in particular zones of greater residence time as a consequence of the wind flow pattern.

- *Influence of turbulence on chemical activity in urban environments.*

  The variability of atmospheric conditions along the diurnal cycle makes that the chemical influence on pollutant concentrations is changeable. Additionally, the daily pattern of road traffic emissions contribute to that variability. Therefore, the importance of chemical reactions, at street level, is resulted from the interaction of the background atmospheric conditions and the emissions.

  In urban environments, the advection-diffusion processes control the dispersion in the streets, becoming important the role of turbulence on the mixing of pollutants. In turn, the chemical balance is also relevant factor in the difference of NO_2, regarded as reactant instead of a non-reactive compound.

  In a chemical equilibrium state, the loss and production rates of a reactant with the $NO_x - O_3$ mechanism is equivalent. That balance in the overlying air is mainly perturbed by the local emissions. Hence, the deviation from the chemical equilibrium trigger that the concentration of the reactant differ from the non-reactive assumption. In an urban area, the continuous releases prevent reaching the chemical balance, specifically in the vicinity of the traffic emissions. That deviation is to a certain extent controlled by the turbulence as a function of its efficiency to well mix the

emitted pollutants with the overlying air. For an inefficient mixing, the importance of the chemical reactions increases versus the turbulence processes. In these cases, the deviation from the chemical balance rises, giving rise to greater differences between chemical approaches. It commonly occurs with elevated NO_x emissions, where the turbulence is not enough to properly mix the pollutants with the ambient species. On the contrary, when the perturbation of the NO_x emissions is not very high and the turbulence processes are able to suitably mix the compounds, the chemical balance is rapidly reached again. Therefore, the differences between the reactive and non-reactive approaches are reduced.

On the other hand, in cases when the overlying air is completely further from the chemical equilibrium, a different behaviour is found, e.g. at sunset and sunrise. Using the $NO_x{-}O_3$ mechanism, when the solar radiation decays, the NO_2 photolysis ceases and, thereby, the chemical balance is not produced. In these cases, the turbulence has no influence on the chemical activity to achieve a equilibrium state. Therefore, the concentration difference of the reactive from the non-reactive approach increases as the NO and O_3 react.

- *Modelling approach for the assessment of urban air quality for a long period of time.*

  The representative distribution of pollutants in the streets is very useful for the management of air quality in urban areas. In that sense, the capability of reproduce the strong concentration gradients produced in the streets is essential.

  The modelling approach presented in this work involves the use of mesocale results to provide the temporal evolution of the meteorological conditions needed by the CFD simulations. In this case, the non-linearity of chemistry hinders the consideration of chemical reactions in the modelling approach and, thereby, non-reactive pollutants are assumed. Finally, the NO_2 mean map over several weeks is estimated at wintertime in a heavily trafficked area. The spatial validation shows that the developed multiscale system provides reliable maps of mean concentration for a long period of time in an urban area.

The most relevant contribution of this work is the comprehensive study about how the chemical behaviour is depending on the atmospheric conditions and the dynamical processes that take place in the streets. This research improve the understanding of the uncertainties associated with modelling reactive pollutants in urban environments. Therefore, it can help to take decisions related to find the best compromise between accuracy and computational time for futures CFD simulations.

In summary, for specific studies of pollutant dispersion at daytime, modelling the chemical interactions provides a better result in the NO_2 concentration in the streets, e.g. in

cases of unfavourable atmospheric conditions, which are responsible of high pollution episodes. The demand of detailed concentration maps over long periods can be tackled, assuming non-reactive pollutants, through a multiscale approach using CFD and mesoscale simulations. Therefore, these modelling approaches (for short and long periods of time) are useful for planning mitigation measures in urban environments (e.g. the redistribution of the traffic in the streets or planning new strategies in the urban vegetation layout).

6.2 Future research

The most relevant atmospheric processes in urban environments are already included. However, there are some aspects to be improved:

- The introduction of thermal effects, resolving the surface heat fluxes as a function of the solar position and radiation. High values of heat fluxes and the impact of buildings shadow can considerably modify the flow patterns and, thereby, the dispersion of pollutants, especially at summertime. Additionally, the chemical reactions would be also affected by solar radiation and temperature fields within the streets.
- The implementation of the turbulence induced by vehicles on the roads. It would improve the common underestimations of the turbulent kinetic energy, which would promote the mixing and diffusion of pollutants in the emission region.

On the other hand, the off-line coupling of the mesoscale outputs as boundary conditions of CFD simulations is a big challenge. This multiscale system can assess the pollutant dispersion over time in any part of a city. The multiple variables computed in mesoscale models provide additional information about the vertical structure of the atmosphere unlike that obtained from the standard experimental data. In that sense, the inlet conditions of the CFD simulations are better suited to the time to be simulated. Although the simulation of consecutive hours requires a large computational time, this multiscale approach is feasible and useful for short-time studies. Note that one simulated hour demands around 3 real hours, using around 200 computational cores. Hence this approach constitute an useful tool for examining the causes of high concentration values in urban areas that exceed the hourly limit value established. In this study, a first attempt for coupling mesoscale and microscale model is carried out in order to show the advantages of this approach. The first results of applying this multiscale system over several hours in summer conditions are shown in Appendix 6.2.

PUBLICATIONS

The main contributions of this research have been published in the following articles:

- Sanchez, B., Santiago, J.-L., Martilli, A., Palacios, M., Kirchner, F., 2016. *CFD modeling of reactive pollutant dispersion in simplified urban configurations with different chemical mechanisms.* Atmospheric Chemistry and Physics 16 (18), 12143-12157. URL http://www.atmos-chem-phys.net/16/12143/2016/

- Sanchez, B., Santiago, J.-L., Martilli, A., Martin, F., Borge, R., Quaassdorff, C., de la Paz, D., 2017. *Modelling NO_x concentrations through CFD-RANS in an urban hot-spot using high resolution traffic emissions and meteorology from a mesoscale model.* Atmospheric Environment 163 (155-165).

Other contributions related to this work:

- Santiago, J., Borge, R., Martin, F., de la Paz, D., Martilli, A., Lumbreras, J., Sanchez, B., 2017. *Evaluation of a CFD-based approach to estimate pollutant distribution within a real urban canopy by means of passive samplers.* Science of the Total Environment 576, 46-58.

- Santiago, J.-L., Rivas, E., Sanchez, B., Buccolieri, R., Martin, F., 2017. *The impact of planting trees on NOx concentrations: The case of the Plaza de la Cruz neighbourhood in Pamplona (Spain).* Atmosphere 8 (7), 131.

- Buccolieri, R., Santiago, J.-L., Rivas, E., Sanchez, B., 2018. *Review on urban tree modelling in CFD simulations: Aerodynamic, deposition and thermal effects.* Urban Forestry & Urban Greening 31, 212-220.

- Borge, B., Santiago, J.-L., de la Paz, D., Martín, F., Domingo, J., Valdés, C., Sanchez, B., Rivas, E., Rozas, M.T., Lázaro, S., Pérez, J., Fernández, A., 2018. *Application of a short term air quality action plan in Madrid (Spain) under a high-pollution episode - Part II: Assessment from multi-scale modelling.* Science of The Total Environment (*in press*).

Appendix A

Relation between modelled concentration and wind speed

In the CFD model based on the Reynolds-averaged Navier-Stokes equations, the modelled concentration of a non-reactive pollutant hold a linear relation with the wind speed and its release in isothermal conditions. Thus, the inlet vertical profiles for the the wind speed, k and ε are defined by:

$$u_{in}(z) = \frac{u_*}{\kappa} ln\left(\frac{z+z_0}{z_0}\right);\ k_{in} = \frac{{u_*}^2}{{C_\mu}^{1/2}};\ \varepsilon_{in}(z) = \frac{{C_\mu}^{3/4}{k_{in}}^{3/2}}{\kappa z} \tag{1}$$

where, κ is the von Karman constant (0.4), C_μ is the constant (0.09), z_0 are the roughness length and u_* the friction velocity.

The transport equation of a scalar variable ϕ ($\equiv \Phi + \phi'$), in this case the concentration of a non-reactive pollutant (in ppb), is expressed by,

$$\frac{\partial \Phi}{\partial t} + U_j \frac{\partial \Phi}{\partial x_j} = D\frac{\partial^2 \Phi}{\partial x_j \partial x_j} - \frac{\partial \overline{u_j' \phi'}}{\partial x_j} + S_\phi \tag{2}$$

where D is the molecular diffusion, S_ϕ the scalar source (in ppb s^{-1}) and the turbulent flux is expressed as,

$$\overline{u_j' \phi'} \equiv K_\Phi \frac{\partial \Phi}{\partial x_j} = \frac{\mu_t}{\rho Sc_t}\frac{\partial \Phi}{\partial x_j} \tag{3}$$

where the turbulent viscosity is $\mu_t = \rho C_\mu \frac{k^2}{\varepsilon}$. Assuming that the molecular diffusion ($D<<$) is significantly lower than the turbulent diffusion, the transport equation can be rewritten

for a steady state ($\frac{\partial \Phi}{\partial t} = 0$) as follows,

$$\frac{\partial}{\partial x_j}\left(U_j\Phi - \frac{\mu_t}{\rho Sc_t}\frac{\partial \Phi}{\partial x_j}\right) = S_\phi \tag{4}$$

To ascertain the assumption of the modelled concentration of the non-reactive compound by the dimensionless variables (expressed with *).

$$\varepsilon = {U_{ref}}^3 \cdot L_{ref}^{-1} \cdot \varepsilon^* \tag{5}$$

$$k = U_{ref}^2 \cdot k^* \tag{6}$$

$$u = U_{ref} \cdot u^* \tag{7}$$

$$x = L_{ref} \cdot x^* \tag{8}$$

$$\mu_t = \rho \cdot C_\mu \cdot U_{ref} \cdot L_{ref} \cdot \mu_t^* \tag{9}$$

Hence the Eq. 2 can be rewritten as,

$$\frac{\partial \Phi}{\partial x_j^*}\left(u^* \cdot \Phi - \frac{\mu_t^*}{Sc_t}\frac{\partial \Phi}{\partial x_j^*}\right) = S_\phi \cdot L_{ref} \cdot U_{ref}^{-1} \tag{10}$$

Finally, the concentration of a non-reactive pollutant, without considering the background concentration, can be normalized by the following expression Eq. 11, which stands for the concentration inversely proportional to wind speed and proportional to the source.

$$\Phi = \Phi^* \frac{L_{ref} \cdot S_\phi}{U_{ref}} \tag{11}$$

Appendix B

Modelling the NO_x-O_3 and the NO_x-O_x-VOC mechanisms in an urban area

The temporal evolution of the dispersion of reactive pollutants is carried out with the NO_x-O_3 scheme and the NO_x-O_x-VOC mechanism in a real urban area using a CFD-RANS model (LIFE MINOx-STREET Report). The outputs are validated with measurements recorded in an experimental campaign within the framework of the LIFE MINOx-STREET Project (LIFE12 ENV/ES/000280). The study case corresponds to an urban area of Alcobendas, a nearby city from Madrid. Figure 1 represents the computational domain highlighting the research area (black square).

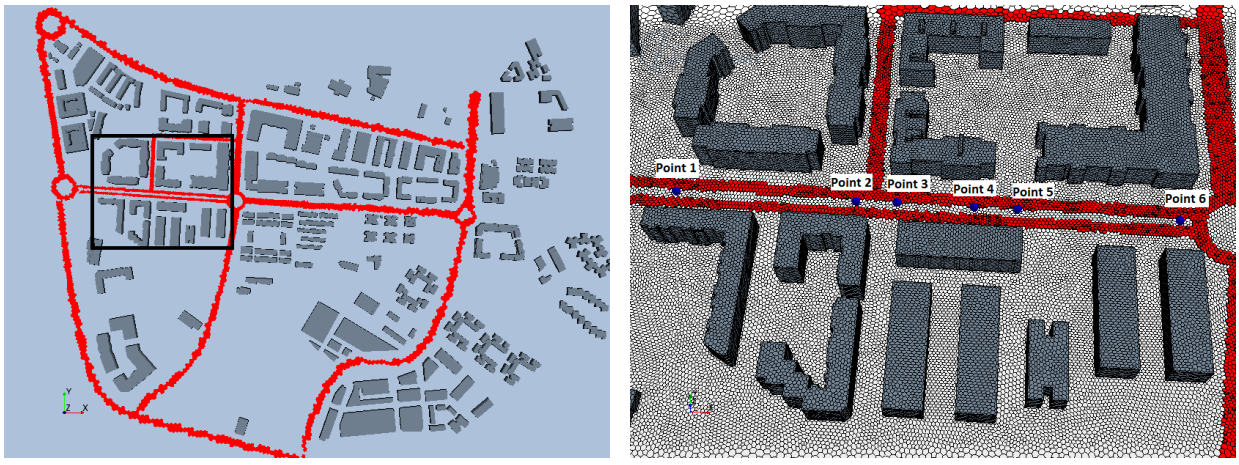

(a) **(b)**

Figure 1: (a) Geometry of the computational domain and the research area limited by the black square. (b) Mesh of the research area and location of the measurements points.

In this domain, two simulations are performed from 1200 LST to 1300 LST on 29th

September (2015) including both chemical approaches to model the NO_2 dispersion with the same boundary conditions. Thus, both the background atmospheric variables and the traffic emissions are derived from experimental data taken at that time in the research area (Table 1). In case of NO_x-O_x-VOC mechanism, the traffic emissions of the VOC are regarded as VOC/NO_x=1/5 in accordance with the emission inventories (Madrid-Council, 2014). The simulations are performed in unsteady conditions changing the boundary conditions every 5 min.

Table 1: Time average of the inlet concentration for all pollutants (in ppb) from 1200 LST to 1300 LST (14:00 to 15:00).

Inlet pollutants	ppb
NO	5.88
NO_2	10.48
O_3	41.76
CO	436.68
HCHO	0.42
SO_2	0.38
ARO	4.18
ALK	0.14
OLE	0.17

Subsequently, the validation of the pollutant concentrations is carried out by the time average value of NO and NO_2 at the 6 measurements points deployed along the study street.

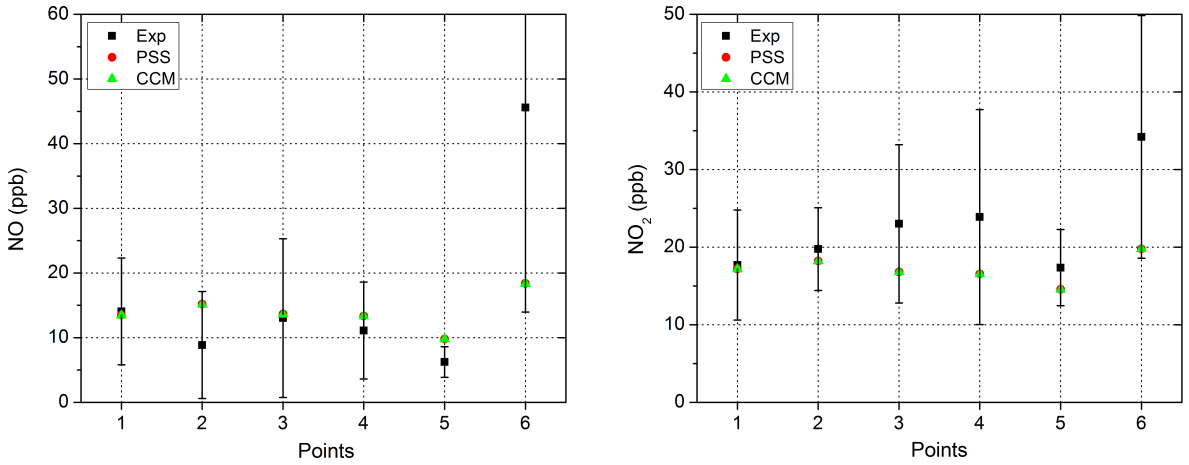

(a) **(b)**

Figure 2: Validation of the time average concentration of (a) NO and (b) NO_2 obtained from the experimental data and the outputs from the NO_x-O_3 and NO_x-O_x-VOC mechanisms at the measurements points.

The results of the NO and NO_2 concentrations turn out almost the same values with

inappreciable differences on the pollutants of concern. It may be related to the atmospheric composition of the research area in terms of the little VOC load in comparison with the NO_x levels. Additionally, the ratio VOC/NO_x of traffic emissions is established at 1/5, and the impact on the NO and NO_2 concentrations was found small in several atmospheric conditions in Chapter 3. Accordingly, due to the increase of the computational time needed to undertake a CFD simulation with the complex scheme, just the photostationary state is used for the longer study carried out in Chapter 4.

References

Madrid-Council, 2014. *Inventario de emisiones de contaminantes a la atmósfera en el municipio de Madrid 1999-2012 (in Spanish).* Area de Gobierno de Medio Ambiente y Movilidad del Ayuntamiento de Madrid, Spain. (website: http://www.madrid.es /unidadesdescentralizadas/sostenibilidad/espeinf/energiaycc/04cambioclimatico/ 4ainventario/ficheros/inventarioeam2012.pdf).

Sanchez, B., Santiago, J.L., Martilli, A., 2017. Modelización con código CFD-química reactiva-velocidad de depósito de NO_x en escenarios urbanos (in Spanish), Progress Report of the LIFE MINO$_x$−STREET Project, CIEMAT, Madrid.

Appendix C

Modelling approach in summer conditions

The modelling approach described in Chapter 5 is also applied in the same research area of Madrid in summertime. An experimental campaign was carried out from 26th June to 20th July in 2015 with passive samplers recording NO_2 concentration throughout the square in the same location depicted in Fig. 5.1b.

Firstly, the temporal evolution is compared with the NO_2 concentration measured at FL station. To that end, the NO_2 concentration is computed by means of both procedures described in Section 5.5.3. In Case 1, the modelling approach is applied for the NO_x in order to after multiplying by the ratio $NO_2-to-NO_x$ obtained from the measurements at FL station. In Case 2, the total NO_2 concentration is directly derived from the modelling approach assuming the NO_2 as a non-reactive compound.

Figure 3 shows the experimental NO_2 and the result of NO_2 for both procedures over time at FL station. The NO_2 concentration obtained from the modelling approach hold the same trend of the NO_2 concentration recorded at FL station. Despite the thermal effects are not considered in this study, the concentration is properly reproduced by applying the modelling approach.

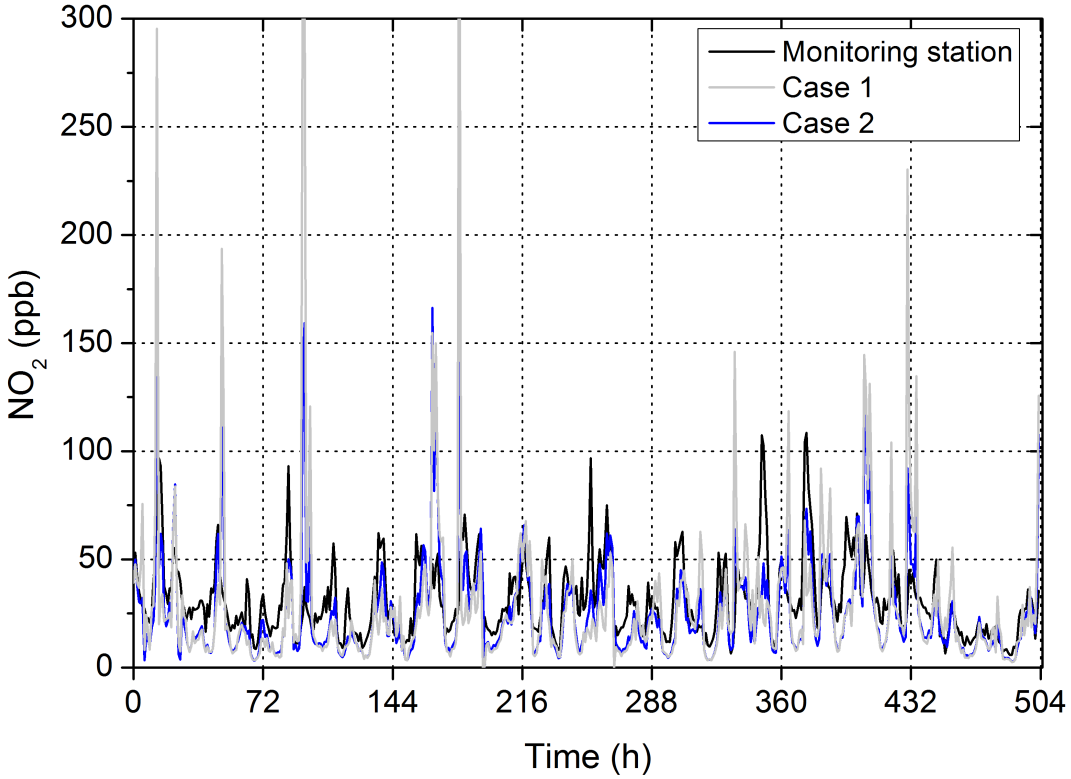

Figure 3: Time series of NO_2 concentration at FL station from experimental data (black line), for the Case 1 (grey line) and for the Case 2 (blue line).

Secondly, the time average concentration of NO_2 for the entire campaign is compared against the NO_2 measured at the sampling points (Fig. 4).

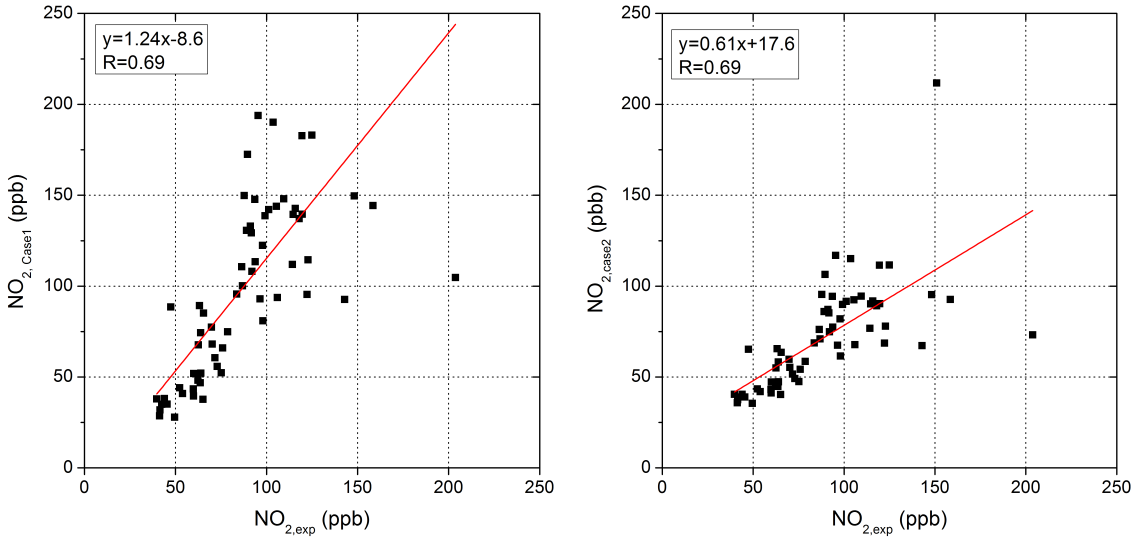

(a) **(b)**

Figure 4: Scatter plots of the NO_2 concentration (ppb) obtained from the (a) Case 1 and (b) Case 2 against the measured NO_2 (ppb).

The results show an overall good approximation with a correlation coefficient above 0.6,

though the linear regression show an overestimation of the NO_2 concentration in Case 1 and an underestimation in Case 2. The statistics NMSE and FB are respectively 0.12 and 0.14 for the Case 1, whereas for the Case 2 yield 0.20 and -0.19 respectively. Both procedures provide good statistical parameters within the acceptance criteria 2.5.

Figure 5 illustrates the relative differences of the computed NO_2 with respect to the measured NO_2 at sampling points.

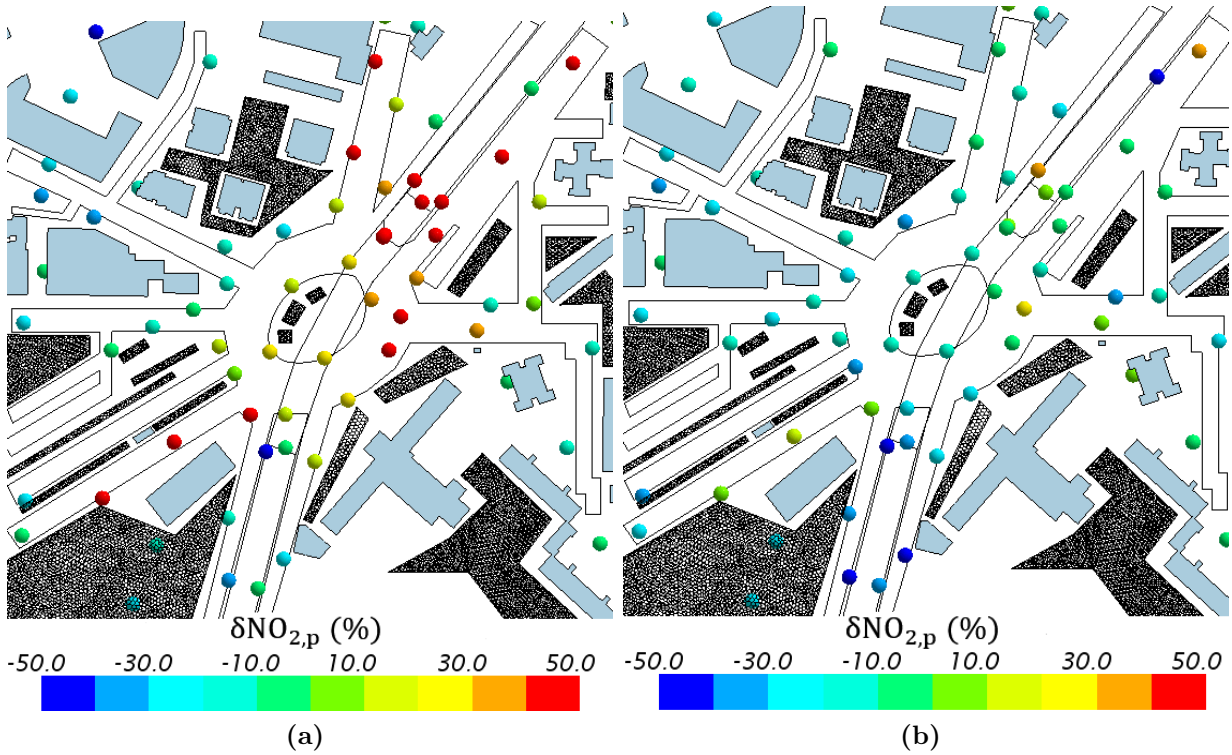

Figure 5: $\delta NO_{2,p}$ at sampling points for (a) the Case 1 and (b) the Case 2.

In summertime, there are more points with errors above ±20% than the results in winter conditions (Fig. 5.13). It is fundamentally caused by the assumptions considered by applying the modelling approach since in summer conditions the thermal effects may be relevant in the dispersion of pollutants. Additionally, the chemical reactions may introduce a larger deviation in the NO_2 concentration caused by an increase of the solar radiation and air temperature, and thereby an increase of the available O_3 in the overlying air.

Appendix D

Multiscale system of WRF-CMAQ and CFD models in an urban hot-spot

A multiscale system of models can become very effective for the study of urban air quality in a great detail. The use of mesoscale models to provide the boundary conditions in the CFD simulation is a big challenge that is still developing. This work presents the first results about modelling reactive pollutants dispersion in an urban hot-spot with a CFD model through the outputs derive from a meteorological and a chemistry-transport mesoscale models.

In this way, the CFD simulation is carried out from 0600 LST to 1800 LST on 1st July (2015) in the same scenario of the Chapter 5, establishing the vertical profiles of the meteorological variables and the background pollutant concentrations derive from WRF and CMAQ models. In addition, the surface heat flux is imposed at ground in the CFD model based on the outputs obtained from the WRF model. The wind, temperature and the turbulent parameters are evaluated against the measurements taken in this urban area turning out a high accuracy of the CFD model. As for the pollutant concentrations, the inclusion of a chemical mechanism in the CFD simulation proves a better fit to the NO_2 concentration measured at the air quality monitoring station.

These outcomes show the advantage of using the mesoscale outputs as input of a microscale model since it increases the possibility of simulating any part of the city using a CFD model. Nevertheless, some discrepancies arise in the turbulent closures between the mesoscale and the CFD models that has to be thoroughly investigated. Hence, a full connection between these models would allow expanding the utility of the CFD models in order to capture the heterogeneities of the wind flow and dispersion characteristic of any city. This multiscale system is useful for different purposes: urban air quality assessment, planing mitigation measures (e.g. traffic reduction) or air quality forecast. It was presented at 18th International Conference on HARMO18, 9-12 October 2017, Bologna, Italy.

18th International Conference on
Harmonisation within Atmospheric Dispersion Modelling for Regulatory Purposes
9-12 October 2017, Bologna, Italy

Modelling reactive pollutants dispersion in an urban hot-spot in summer conditions using a CFD model coupled with meteorological mesoscale and chemistry-transport models

B. Sanchez[1], J.L. Santiago[1], F. Martín[1], A. Martilli[1], C. Quaassdorff[2], D. de la Paz[2], R. Borge[2]

[1] *Research Center for Energy, Environment and Technology (CIEMAT), Madrid, Spain*
[2] *Laboratory of Environmental Modelling, Technical University of Madrid (UPM), Madrid, Spain*

beatriz.sanchez@ciemat.es

Abstract: Air quality assessment requires detailed studies about urban air pollution. In a city, the interaction between atmosphere and urban morphology induces complex flow pattern which leads to irregular spatial distributions of pollutants in the streets. In addition, the influence of chemical reactions and the atmospheric variability make difficult to reproduce the reactive pollutants dispersion at microscale, especially in summer conditions. In this season, the thermal effects acquire greater importance than in winter since that considerably modify the air flow and therefore, the pollutants dispersion in the streets. Furthermore, the chemical constants are linked with the air temperature and solar radiation, hence, the inclusion of chemical mechanism to model the NO and NO_2 dispersion in an urban hot-spot becomes necessary. The aim of this work is to simulate reactive pollutants dispersion during several hours in summer conditions in an urban hot-spot using a computational fluid dynamics (CFD) model. To achieve this purpose, the vertical profiles resulted from a meteorological mesoscale simulation (WRF) are used as inputs in the CFD simulation. Besides, in relation to the background concentration of pollutants, the outputs of a chemistry-transport simulation (CMAQ) are also imposed as inlet condition at microscale. Additionally, detailed traffic emissions of NO and NO_2 are implemented into the CFD simulation based on the results of a microscale traffic emission model. Lastly, focusing on studying the NO_2 dispersion, the photostationary state mechanism is implemented in the CFD simulation. Thus, the time series of meteorological variables and pollutants concentration resulting from the CFD simulation are thoroughly evaluated against measurements at several points from an experimental campaign carried out in the research area (in the framework of TECNAIRE project). Regarding the air quality assessment, the deviation of NO_2 concentration including chemical reactions in the CFD simulation is quantified in comparison with a non-reactive pollutant. In this way, the improvements included in the CFD modelling and the conclusions obtained from this analysis provide information on how to simulate reactive pollutant dispersion in an urban hot-spot in summer conditions.

Key words: *CFD-RANS model, reactive pollutants, mesoscale models, WRF, CMAQ*

1. INTRODUCTION

Air quality assessment in urban areas through a CFD model is in continuous development owing to its high resolution to solve the air flow and pollutants dispersion in the real geometry of a city. One of the main sources of uncertainties are the boundary conditions used in the simulation. In that regard, the use of outputs from a mesoscale model can provide more complete information about the atmospheric conditions and improve the input data of the microscale simulation. Kwak et al. (2015) developed an integrated system of mesoscale models with the weather research and forecasting (WRF) model and the community multiscale air quality (CMAQ) model providing the time-dependent boundary conditions to the CFD simulation. They have shown that the use of a CFD model improves the accuracy for the NO_2 and O_3 concentration at street level compared to the outputs of CMAQ, because the spatial heterogeneity is better reproduced.

The impact of the use of boundary conditions increasingly detailed in the CFD simulations is tackled in this study. For that, an unsteady CFD simulation from 06 to 18UTC over an urban hot-spot in summer conditions is performed coupling the outputs from WRF and CMAQ simulations in that area. The time series of meteorological variables and turbulent parameters are validated at several points with experimental data. And as for the pollutants concentration, the deviation produced by the chemical reactions is also analyzed and evaluated with the air quality monitoring station.

2. CASE STUDY

The urban hot-spot selected is located in a large square of Madrid (Spain) which consists of a heavily trafficked roundabout crossed by a main exit road through a tunnel. The meteorological deployment is composed of an anemometer at a building's roof (18m above ground level) and two sonic anemometers close to a main road at a height of 8 and 6 m (yellow and blue points in Fig.1a, respectively). The concentration of pollutants is recorded at the air quality monitoring station that belongs to the Madrid Council and is located in the research area. More detail can be found in Borge et al. (2016).

3. MODELING APPROACH

The modelling system consists of coupling the outputs from the mesoscale simulations into the CFD simulation so as to model the reactive pollutants dispersion in the streets over time in summer conditions.

3.1. Mesoscale Models Description

The mesoscale simulations are carried out during the experimental campaign from 29th June to 20th July 2015. The meteorological mesoscale model (WRF) used is a model particularly adapted to simulate the urban atmosphere (Chen et al, 2011). The five nested domains are 48, 16, 4, 1 and 500m. In the lowest levels, it takes into account the strong gradients of mean variables, the turbulent fluxes and even the heat in buildings and its exchange with air in order to obtain a high understanding of the physical processes in urban roughness sublayer (BEP-BEM, Martilli et al. (2002) and Salamanca et al. (2010)). In regard to the pollutants concentration, the chemistry-transport model used is Community Multiscale Air Quality (CMAQ) (Byun and Schere, 2006).

3.2. CFD Simulation Setup

The CFD model used is based on the Reynolds-averaged Navier-Stokes equations (RANS) with the realizable k-ε turbulence closure. In addition, the buoyancy terms are included with the Boussinesq's approximation. The size of the computational domain over the research area is approximately 1300mx1300mx270m. The polyhedral irregular mesh used has a base resolution of 5 m. Besides, the grid size applied within the central region of 400mx400m is 2 m and even 1 m close to the ground and buildings (Sanchez et al., 2017).

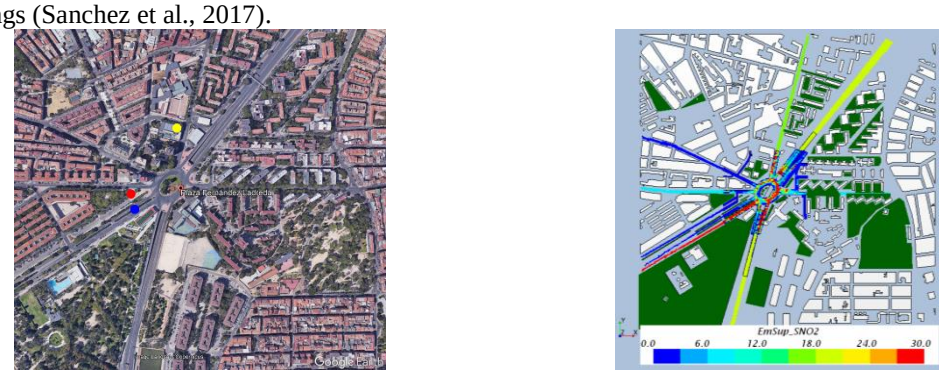

(a) (b)

Figure 1. (a) Research area from Google Earth. At the yellow and blue points are the meteorological stations and at the red point is air quality monitoring station (b) Computational domain of the CFD simulation.

The CFD simulation is performed in unsteady conditions and covers from 06UTC to 18UTC of 1st July, 2015. The vertical profiles of horizontal wind components, air temperature and turbulent kinetic energy (k) derived from WRF for a grid cell corresponding to the CFD domain, are imposed at inlet in the microscale simulation. The boundary conditions for the turbulent dissipation rate (ε) are computed as, $\varepsilon_{in} = {C_\mu}^{3/4}\, {k_{in}}^{3/2}/(\kappa z)$. The surface heat flux derived from WRF is established at ground of the CFD domain since in summer conditions the thermal effects are important and considerably modify the flow pattern and therefore, the pollutants dispersion. The boundary conditions for pollutants are also obtained from the CMAQ simulation for the corresponding grid cell, and used as inputs for the CFD simulation. All boundary conditions are changing every 1h. On the other hand, the detailed traffic emissions in an area of 300mx300m centered on the square are obtained from a microscale traffic emission model (Quaassdorff et al., 2016) with a resolution of 5mx5m; and they are uniformly extended to the rest of the

domain. The daily pattern of traffic emission is considered and the emission scenario is changing every hour. The emitted ratio NO_2-to-NO_x is 0.3 based on the Madrid emission inventories (Borge et al., 2014). Lastly, the chemical interactions between the primary emitted pollutants NO and NO_2 are considered in the CFD simulation through the photostationary state.

4. RESULTS

4.1. Meteorological variables

Some meteorological variables from modelling outputs are validated against the experimental data. The results in the WRF cell and in the specific point corresponding to the location of the measurement point of the CFD domain are compared with the experimental data. Thus, the WRF results are also analyzed in order to show the accuracy of inputs in the CFD simulation. Figure 2 shows the time series of wind speed and direction and temperature at **18 m** above ground level (AGL).

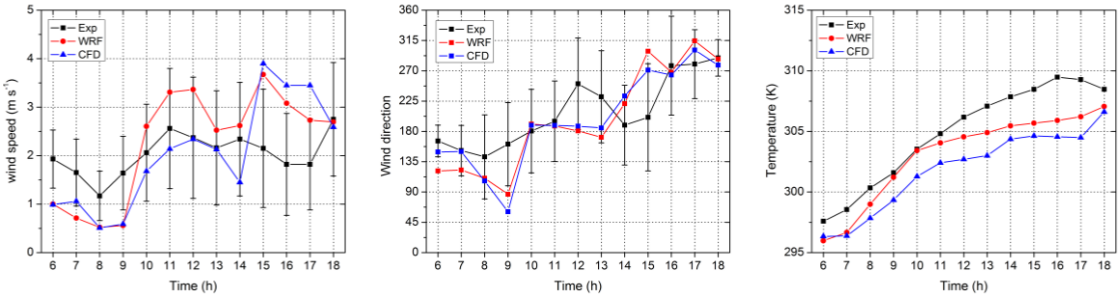

(a) (b) (c)

Figure 2. Time series of the experimental data, WRF and CFD results of: (a) wind speed, (b) wind direction and (c) temperature at 18 m (yellow point in Fig. 1).

In general, the modelling results fit quite well to the measurement within its error range. As for the hourly mean wind direction, either the mesoscale or the microscale results reproduce the wind behavior along the day. Note that experimental wind direction is constantly varying during each hour being these variations greater than 45º in some cases. Even so, the wind speed simulated exhibits a good agreement to the experimental data with the NMSE equal to 0.15 and 0.22 and a FB of 0.10 and 0.006 respectively from WRF and CFD results. The slightly underestimation of temperature by both models is obtained for all hours. In the microscale case, part of this error is due to the fact that the surface heating of buildings is not taken into account and it is only imposed at ground.

Figure 3 shows the same variables but at **8 m** AGL (blue point in Fig. 1). Similarly, at this point, the evolution of wind direction and temperature is captured over time by the models. For the wind speed the statistical parameters NMSE, FB and the correlation coefficient are 0.13, -0.05 and 0.87 for the WRF results and 0.08, -0.24 and 0.91 for the CFD outputs. It represents a small deviation from the experimental data with a slight underestimation, which entails in a high correlation coefficient.

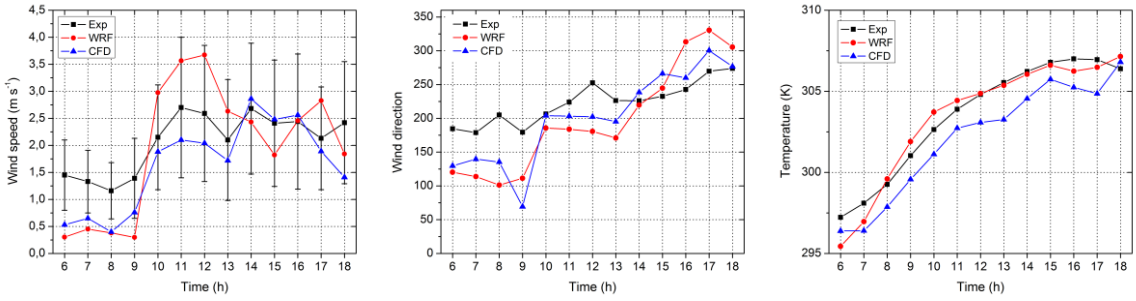

(a) (b) (c)

Figure 3. Time series of experimental data, WRF and CFD results of: (a) wind speed, (b) wind direction and (c) temperature at 8 m (blue point in Fig. 1)

To further ascertain the validation, the turbulent parameters such as the turbulent kinetic energy (k) and the heat flux (HF) are also analyzed at 8 m (Fig. 4). In regard to the HF, either WRF or CFD reveal precise outcomes with a NMSE 0.26 and 0.0.11 and FB 0.36 and -0.08 respectively. However, the time

series of *k* simulated by the CFD model is improved from the WRF results and its fit to the experimental data is quite accurate. The NMSE is 1.09 and 0.11 and the FB is 0.79 and -0.09 from WRF and CFD outputs respectively. Therefore, the use of boundary conditions in the CFD simulations derived from a mesoscale model provides appropriate results that reproduce the micrometeorology in the research area.

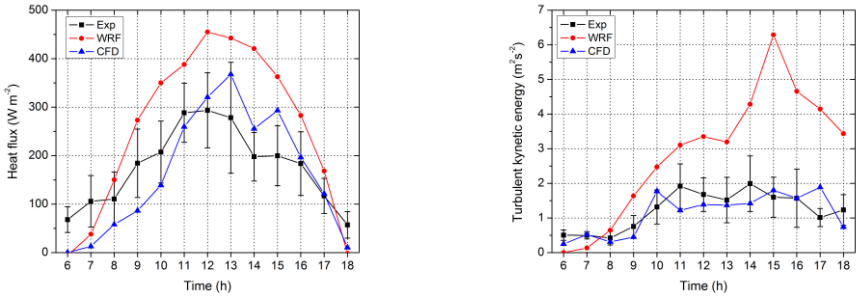

(a) (b)

Figure 4. Time series of WRF and CFD results against to the experimental data of: (a) HF and (b) *k*

4.2. Pollutants concentration

The time series of the concentration of NO, NO_2 and O_3 are analyzed at the air quality monitoring station. The results of NO and O_3 (not shown) reveals a good agreement with a correlation coefficient of 0.89 and 0.95 respectively. Focusing on NO_2, which is simulated as reactive (NO_{2R}) and inert (NO_{2T}) pollutant, the time series of NO_2, the ratios NO-to-NO_2 and the NO_2-to-NO_x is compared with measurements (Fig. 5).

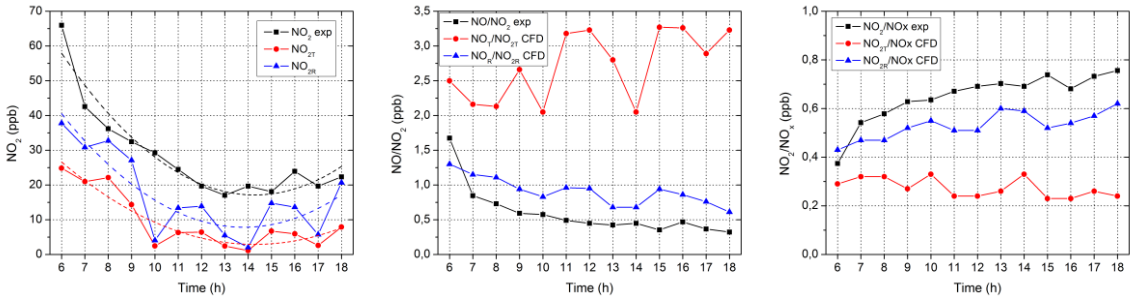

(a) (b) (c)

Figure 5. Time series of: (a) NO_2 concentration (ppb), (b) NO-to-NO_2 and (c) NO_2-to-NO_x registered at air quality monitoring station (black) and the CFD results by simulating the pollutants as inert species (red) and reactive compounds (blue)

The evolution of NO_2 simulated, either NO_{2R} or NO_{2T}, show sharp variations in comparison with the experimental data as well as an underestimation of the measurements. The sharp changes are due to the fact that the wind direction fluctuates over time during 1 h and here, hourly mean values are used to simulate each hour. If these variations were taken into account to simulate the pollutants dispersion, the time series of pollutant would be likely smoothed. With the objective of mitigating that variation and extracting the tendency followed, either the experimental data or the values simulated are adjusted to a polynomial equation (dashed line in Fig. 5.a.). It reveals that the pollutants modelled have the same behavior that the experimental, however the NO_{2R} is higher and closer to the experimental result. In turn, the comparison of the ratio NO-to-NO_2 with that of the air quality station, shows the importance of including chemical reactions in the simulation in order to capture the conversions of NO and NO_2. Besides, the NO_{2T}-to-NO_x shows little variations over time but always around the ratio NO_2-to-NO_x imposed into the emissions (0.3). In contrast, the NO_{2R}-to-NO_x is closer to the value computed from experimental data. This slight difference on NO_2 concentration over time might be related to an underestimation from CMAQ of the background concentration of NO_2 and O_3 or by a deviation in the computation of the chemical constants either by temperature or by solar radiation due to the assumptions considered. Figure 6 shows the distribution of NO_2, NO_{2R}-NO_{2T} and the NO_{2R}/NO_{2T} in order to spatially evaluate the importance of including chemical reactions in summer conditions. At 06UTC, the solar radiation and temperature are lower than at 12UTC and consequently, the chemical constants rate are lower leading to little differences in modelling NO_2 as a tracer instead of a reactive pollutant. For that, the

deviation from tracer is higher at 12 than 06 UTC. In both cases, that difference increases with distance from the traffic emission area because of the high NO emission there. But even at 12UTC the NO_{2r} is up to a factor 1.5 from tracer in this area partly because there is higher available O_3 and the chemical activity is more reactive. It is possible to conclude that modelling NO_2 as reactive pollutant in summer conditions is important to develop the diurnal variation of this pollutant and so to obtain an accurate map of the NO_2 in an urban hot-spot.

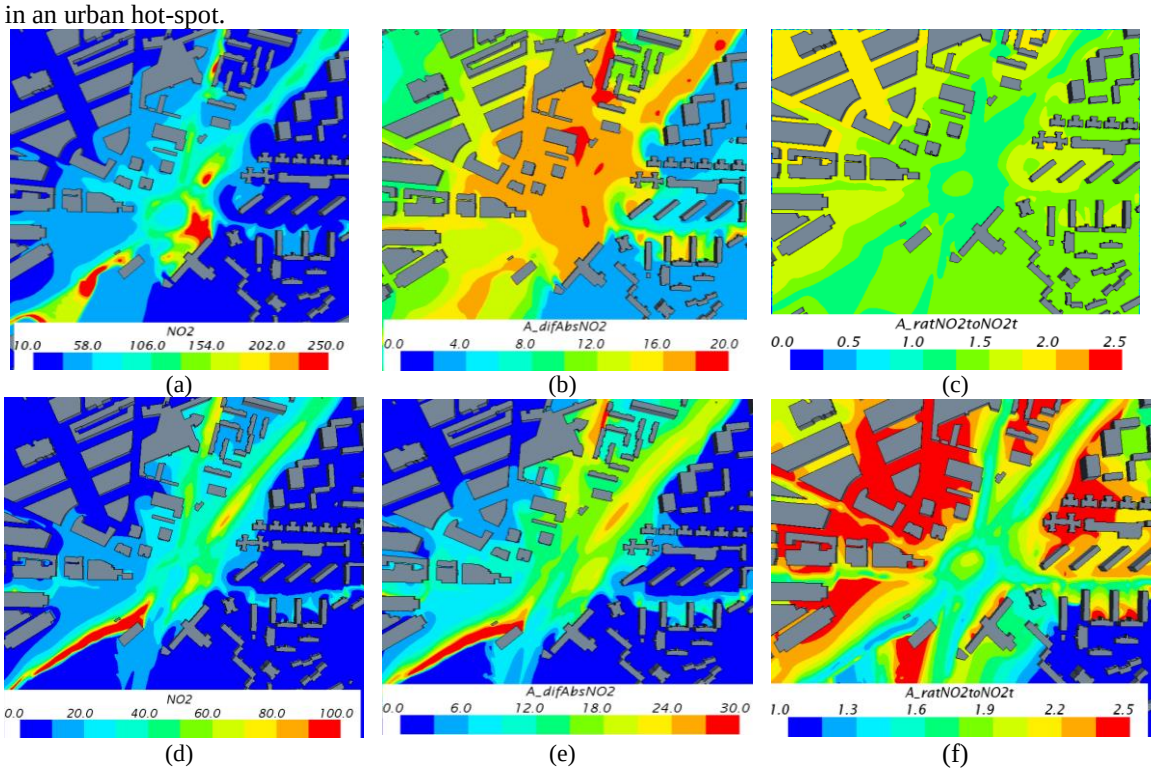

Figure 6. (*left to right*) The spatial distribution of NO_{2r} concentration (ppb), the differences (NO_{2R}-NO_{2T}) of concentration and the ratio NO_{2R}-to-NO_{2T} at (above) 06UTC and (bellow) 12UTC.

5. CONCLUSIONS

- Using the vertical profiles of the atmospheric variables derived from the mesoscale models as boundary conditions for the CFD result in a good agreement of the CFD results with the point experimental data and it allows to obtain a better approximation of atmospheric conditions.
- In summer conditions due to the high air temperature and solar radiation it is important to simulate the NO_2 as reactive pollutant to better represent the concentration in the streets. Although the inclusion of a chemical mechanism increases the computational load, to accurately capture the diurnal variation of NO_2 should be included at least the photochemical scheme.
- The hourly CFD results would improve by changing the boundary conditions every 30 min. It would enhance the pollutants concentration and the meteorological variables representative of every hour.

REFERENCES

Borge et al., 2014. *Sci. Total Environ*. 466-467, 809-819.
Borge et al., 2016. *Atmos. Environ*. 140, 432-445.
Byun DW, Schere KL, 2006. Appl Mech Rev 59:51-77.
Chen et al., 2011. *Int. J. Climatol*. 31 (2), 273-288.
Kwak et al, 2015. *Atmospheric Environment*, 100, 167-177.
Martilli et al., 2002. *Boundary-Layer Meteorol*. 104 (2), 261-304.
Quaassdorff et al., 2016. *Sci. Total Environ*. 566, 416-427.
Salamanca et al., 2010. *Theor. Appl. Climatol*. 99 (3-4), 331-344.
Sanchez et al., 2017. *Atmos. Environ*. 163, 155-165.

ACKNOWLEDGEMENTS

This study has been supported by the TECNAIRE-CM research project (S2013/MAE-2972) funded by The Regional Government of Madrid. The authors are also grateful to Madrid City Council and to C.Yague, C. Roman Cascon, G. Maqueda and M. Sastre (University Complutense of Madrid) for providing the meteorological data used in this work and to Extremadura Research Center for Advanced Technologies (CETA-CIEMAT) by helping in using its computing facilities for the simulations.

References

Abhijith, K., Kumar, P., Gallagher, J., McNabola, A., Baldauf, R., Pilla, F., Broderick, B., Di Sabatino, S., Pulvirenti, B., 2017. Air pollution abatement performances of green infrastructure in open road and built-up street canyon environments–a review. Atmospheric Environment 162, 71–86.

Abou-Senna, H., Radwan, E., Westerlund, K., Cooper, C. D., 2013. Using a traffic simulation model (vissim) with an emissions model (moves) to predict emissions from vehicles on a limited-access highway. Journal of the Air & Waste Management Association 63 (7), 819–831.

Alcobendas-Council, 2005. Plan de movilidad urbana. Ayuntamiento de Alcobendas, Madrid (in Spanish).
URL `website: http://www.alcobendas.org/recursos/doc/Urbanismoinfraestructura/Informesmedioambientales/13115900311201413103 8.pdf`

Amorim, J., Rodrigues, V., Tavares, R., Valente, J., Borrego, C., 2013. Cfd modelling of the aerodynamic effect of trees on urban air pollution dispersion. Science of the Total Environment 461, 541–551.

Antonioni, G., Burkhart, S., Burman, J., Dejoan, A., Fusco, A., Gaasbeek, R., Gjesdal, T., Jäppinen, A., Riikonen, K., Morra, P., et al., 2012. Comparison of cfd and operational dispersion models in an urban-like environment. Atmospheric environment 47, 365–372.

Arya, P. S., 2001. Introduction to micrometeorology. Vol. 79. Academic press.

Baik, J.-J., Kang, Y.-S., Kim, J.-J., 2007. Modeling reactive pollutant dispersion in an urban street canyon. Atmospheric Environment 41 (5), 934–949.

Baker, J., Walker, H. L., Cai, X., 2004. A study of the dispersion and transport of reactive pollutants in and above street canyonsa large eddy simulation. Atmospheric Environment 38 (39), 6883–6892.

Blocken, B., Janssen, W., van Hooff, T., 2012. Cfd simulation for pedestrian wind comfort and wind safety in urban areas: General decision framework and case study for the eindhoven university campus. Environmental Modelling & Software 30, 15–34.

Blocken, B., Stathopoulos, T., Carmeliet, J., 2007. Cfd simulation of the atmospheric boundary layer: wall function problems. Atmospheric environment 41 (2), 238–252.

Bloss, W., 2009. Atmospheric chemical processes of importance in cities. Issues in Environmental Science and Technology 28, 42.

Borge, R., Lumbreras, J., Pérez, J., de la Paz, D., Vedrenne, M., de Andrés, J. M., Rodríguez, M. E., 2014. Emission inventories and modeling requirements for the development of air quality plans. application to madrid (spain). Science of the Total Environment 466, 809–819.

Borge, R., Narros, A., Artíñano, B., Yagüe, C., Gómez-Moreno, F. J., de la Paz, D., Román-Cascón, C., Díaz, E., Maqueda, G., Sastre, M., et al., 2016. Assessment of microscale spatio-temporal variation of air pollution at an urban hotspot in madrid (spain) through an extensive field campaign. Atmospheric Environment 140, 432–445.

Boussinesq, J., 1877. Essai sur la théorie des eaux courantes. Imprimerie nationale.

Bright, V. B., Bloss, W. J., Cai, X., 2013. Urban street canyons: Coupling dynamics, chemistry and within-canyon chemical processing of emissions. Atmospheric Environment 68, 127–142.

Britter, R., Hanna, S., 2003. Flow and dispersion in urban areas. Annual Review of Fluid Mechanics 35 (1), 469–496.

Buccolieri, R., Santiago, J.-L., Rivas, E., Sanchez, B., 2018. Review on urban tree modelling in cfd simulations: Aerodynamic, deposition and thermal effects. Urban Forestry & Urban Greening 31, 212–220.

Buckingham, C., 1997. London atmospheric emissions inventory. London Research Centre.

Calvert, J. G., Stockwell, W. R., 1983. Acid generation in the troposphere by gas-phase chemistry. Environmental science & technology 17 (9), 428A–443A.

Carslaw, D. C., 2005. Evidence of an increasing no 2/nox emissions ratio from road traffic emissions. Atmospheric Environment 39 (26), 4793–4802.

Chang, J., Hanna, S., 2004. Air quality model performance evaluation. Meteorology and Atmospheric Physics 87 (1), 167–196.

Chang, J. C., Hanna, S. R., 2005. Technical descriptions and users guide for the boot statistical model evaluation software package, version 2.0. Harmonisation within atmospheric dispersion modelling for regulatory purposes.

Chen, F., Kusaka, H., Bornstein, R., Ching, J., Grimmond, C., Grossman-Clarke, S., Loridan, T., Manning, K. W., Martilli, A., Miao, S., et al., 2011. The integrated wrf/urban modelling system: development, evaluation, and applications to urban environmental problems. International Journal of Climatology 31 (2), 273–288.

Coceal, O., Dobre, A., Thomas, T. G., 2007. Unsteady dynamics and organized structures from dns over an idealized building canopy. International Journal of Climatology 27 (14), 1943–1953.

Coceal, O., Thomas, T., Castro, I., Belcher, S., 2006. Mean flow and turbulence statistics over groups of urban-like cubical obstacles. Boundary-Layer Meteorology 121 (3), 491–519.

Council, N. R., et al., 1992. Rethinking the ozone problem in urban and regional air pollution. National Academies Press.

Dalpé, B., Masson, C., 2009. Numerical simulation of wind flow near a forest edge. Journal of wind engineering and industrial aerodynamics 97 (5), 228–241.

Dejoan, A., Santiago, J., Martilli, A., Martin, F., Pinelli, A., 2010. Comparison between large-eddy simulation and reynolds-averaged navier–stokes computations for the must field experiment. part ii: effects of incident wind angle deviation on the mean flow and plume dispersion. Boundary-layer meteorology 135 (1), 133–150.

Deligiorgi, D., Philippopoulos, K., 2011. Spatial interpolation methodologies in urban air pollution modeling: application for the greater area of metropolitan Athens, Greece. INTECH Open Access Publisher.

EEA, 2015. Air Quality in Europe-2015 Report. EEA Technical Report No 5/2015. ISBN: 978-92-9213-701-4 702-1. Tech. rep., European Environment Agency (EEA).
URL `Available online at: http://www.eea.europa.eu//publications/air-quality-in-europe-2015.`

EEA, 2017. Air Quality in Europe-2017 Report. EEA Technical Report No 13/2017. ISBN: 978-92-9213-921-6. Tech. rep., European Environment Agency (EEA).
URL `Available online at: http://www.eea.europa.eu//publications/air-quality-in-europe-2017.`

Finlayson-Pitts, B. J., Pitts Jr, J. N., 1999. Chemistry of the upper and lower atmosphere: theory, experiments, and applications. Academic press.

Franke, J., 2007. Best practice guideline for the CFD simulation of flows in the urban environment. Meteorological Inst.

Galmarini, S., De Arellano, J. V.-G., Duynkerke, P., 1995. The effect of micro-scale turbulence on the reaction rate in a chemically reactive plume. Atmospheric environment 29 (1), 87–95.

Gery, M. W., Whitten, G. Z., Killus, J. P., Dodge, M. C., 1989. A photochemical kinetics mechanism for urban and regional scale computer modeling. Journal of Geophysical Research: Atmospheres 94 (D10), 12925–12956.

Goricsán, I., Balczó, M., Balogh, M., Cződer, K., Rákai, A., Tonkó, C., 2011. Simulation of flow in an idealised city using various cfd codes. International journal of Environment and Pollution 44 (1-4), 359–367.

Grimmond, C., Oke, T. R., 1999. Aerodynamic properties of urban areas derived from analysis of surface form. Journal of applied meteorology 38 (9), 1262–1292.

Gromke, C., Blocken, B., 2015. Influence of avenue-trees on air quality at the urban neighborhood scale. part ii: Traffic pollutant concentrations at pedestrian level. Environmental pollution 196, 176–184.

Hanjalic, K., Launder, B., 1972. A reynolds stress model of turbulence and its application to thin shear flows. J. Fluid Mech 52 (4), 609–638.

Hanna, S., Chang, J., 2012. Acceptance criteria for urban dispersion model evaluation. Meteorology and Atmospheric Physics 116 (3-4), 133–146.

HBEFA, 2010. Handbook Emission Factors for Road Transport. Tech. rep., Tech. rep., INFRAS, HBEFA 3.1.
URL Available online at: http://www.eea.europa.eu//publications/air-quality-in-europe-2017.

Hirsch, C., Bouffioux, V., Wilquem, F., 2002. Cfd simulation of the impact of new buildings on wind comfort in an urban area. In: Workshop proceedings, cost action C. Vol. 14. pp. 3–4.

Jeanjean, A. P., Hinchliffe, G., McMullan, W., Monks, P. S., Leigh, R. J., 2015. A cfd study on the effectiveness of trees to disperse road traffic emissions at a city scale. Atmospheric Environment 120, 1–14.

Jenkin, M., Saunders, S., Wagner, V., Pilling, M., 2003. Protocol for the development of the master chemical mechanism, mcm v3 (part b): tropospheric degradation of aromatic volatile organic compounds. Atmospheric Chemistry and Physics 3 (1), 181–193.

Jonker, H. J., Vilà-Guerau de Arellano, J., Duynkerke, P. G., 2004. Characteristic length scales of reactive species in a convective boundary layer. Journal of the atmospheric sciences 61 (1), 41–56.

Junier, M., Kirchner, F., Clappier, A., van den Bergh, H., 2005. The chemical mechanism generation programme chematapart 2: Comparison of four chemical mechanisms for mesoscale calculation of atmospheric pollution. Atmospheric Environment 39 (6), 1161–1171.

Kim, J.-J., Baik, J.-J., 2004. A numerical study of the effects of ambient wind direction on flow and dispersion in urban street canyons using the rng k–ε turbulence model. Atmospheric Environment 38 (19), 3039–3048.

Kim, M. J., Park, R. J., Kim, J.-J., 2012. Urban air quality modeling with full $o_3 - no_x - voc$ chemistry: Implications for o_3 and pm air quality in a street canyon. Atmospheric Environment 47, 330–340.

Kirchner, F., 2005. The chemical mechanism generation programme chematapart 1: The programme and first applications. Atmospheric Environment 39 (6), 1143–1159.

Krochmal, D., Kalina, A., 1997. Measurements of nitrogen dioxide and sulphur dioxide concentrations in urban and rural areas of poland using a passive sampling method. Environmental pollution 96 (3), 401–407.

Krol, M. C., Molemaker, M. J., Arellano, J. V. G., 2000. Effects of turbulence and heterogeneous emissions on photochemically active species in the convective boundary layer. Journal of Geophysical Research: Atmospheres 105 (D5), 6871–6884.

Kwak, K.-H., Baik, J.-J., 2012. A cfd modeling study of the impacts of nox and voc emissions on reactive pollutant dispersion in and above a street canyon. Atmospheric environment 46, 71–80.

Kwak, K.-H., Baik, J.-J., 2014. Diurnal variation of nox and ozone exchange between a street canyon and the overlying air. Atmospheric Environment 86, 120–128.

Kwak, K.-H., Baik, J.-J., Lee, K.-Y., 2013. Dispersion and photochemical evolution of reactive pollutants in street canyons. Atmospheric Environment 70, 98–107.

Kwak, K.-H., Baik, J.-J., Ryu, Y.-H., Lee, S.-H., 2015. Urban air quality simulation in a high-rise building area using a cfd model coupled with mesoscale meteorological and chemistry-transport models. Atmospheric Environment 100, 167–177.

Launder, B. E., Spalding, D. B., 1974. The numerical computation of turbulent flows. Computer methods in applied mechanics and engineering 3 (2), 269–289.

Li, X.-X., Liu, C.-H., Leung, D. Y., Lam, K., 2006. Recent progress in cfd modelling of wind field and pollutant transport in street canyons. Atmospheric Environment 40 (29), 5640–5658.

Li, Y., Paik, K.-J., Xing, T., Carrica, P. M., 2012. Dynamic overset cfd simulations of wind turbine aerodynamics. Renewable Energy 37 (1), 285–298.

Madrid-Council, 2014. Inventario de emisiones de contaminantes a la atmsfera en el municipio de Madrid 1999-2012 (in Spanish). Area de Gobierno de Medio Ambiente y Movilidad del Ayuntamiento de Madrid, Spain. (website: http://www.madrid.es/unidadesdescentralizadas/sostenibilidad/espeinf/energiaycc/04cambioclimatico/4ainventario/ficheros /inventarioeam2012.pdf).

Martilli, A., Clappier, A., Rotach, M. W., 2002. An urban surface exchange parameterisation for mesoscale models. Boundary-Layer Meteorology 104 (2), 261–304.

Martilli, A., Santiago, J. L., Salamanca, F., 2013. On the representation of urban heterogeneities in mesoscale models. Environmental Fluid Mechanics 15 (2), 305–328.

Martin, F., Fileni, L., Palomino, I., Vivanco, M. G., Garrido, J. L., 2014. Analysis of the spatial representativeness of rural background monitoring stations in spain. Atmospheric Pollution Research 5 (4), 779 – 788.

Martín, F., Santiago, J. L., Kracht, O., García, L., Gerboles, M., 2015. FAIRMODE Spatial representativeness feasibility study. Report number: Report eur 27385 en. Affiliation: European Commission Joint Research Centre Institute for Environment and Sustainability.

Meroney, R. N., Pavageau, M., Rafailidis, S., Schatzmann, M., 1996. Study of line source characteristics for 2-d physical modelling of pollutant dispersion in street canyons. Journal of Wind Engineering and Industrial Aerodynamics 62 (1), 37–56.

Mochida, A., Lun, I. Y., 2008. Prediction of wind environment and thermal comfort at pedestrian level in urban area. Journal of wind engineering and industrial aerodynamics 96 (10-11), 1498–1527.

Oke, T. R., 1997. Urban environments. McGill–Queens University Press.

Ott, D. K., Kumar, N., Peters, T. M., 2008. Passive sampling to capture spatial variability in pm 10–2.5. Atmospheric Environment 42 (4), 746–756.

Park, S.-J., Kim, J.-J., Kim, M. J., Park, R. J., Cheong, H.-B., 2015. Characteristics of flow and reactive pollutant dispersion in urban street canyons. Atmospheric Environment 108, 20–31.

Parra, M., Santiago, J., Martín, F., Martilli, A., Santamaría, J., 2010. A methodology to urban air quality assessment during large time periods of winter using computational fluid dynamic models. Atmospheric Environment 44 (17), 2089–2097.

Patankar, S., 1980. Numerical heat transfer and fluid flow. CRC press.

Piersanti, A., Vitali, L., Righini, G., Cremona, G., Ciancarella, L., 2015. Spatial representativeness of air quality monitoring stations: A grid model based approach. Atmospheric Pollution Research 6 (6), 953 – 960.

Pope, S. B., 2001. Turbulent flows.

Pujadas, M., Palacios, M., Nunez, L., German, M., Fernandez-Pampillon, J., Iglesias, J., Santiago, J., 2016. Real scale demonstration of the depolluting capabilities of a photocatalytic pavement in a real urban area. 17th International Conference on Harmonisation within Atmospheric Dispersion Modelling for Regulatory Purposes (HARMO17) (website: http://www.harmo.org/conferences/Proceedings/Budapest/publishedSections/H17-090.pdf).

Quaassdorff, C., Borge, R., Pérez, J., Lumbreras, J., de la Paz, D., de Andrés, J. M., 2016. Microscale traffic simulation and emission estimation in a heavily trafficked roundabout in madrid (spain). Science of The Total Environment 566, 416–427.

Reynolds, O., 1895. On the dynamical theory of incompressible viscous fluids and the determination of the criterion. Philosophical Transactions of the Royal Society of London. A 186, 123–164.

Richards, P., Hoxey, R., 1993. Appropriate boundary conditions for computational wind engineering models using the k-ε turbulence model. Journal of wind engineering and industrial aerodynamics 46, 145–153.

Salamanca, F., Krpo, A., Martilli, A., Clappier, A., 2010. A new building energy model coupled with an urban canopy parameterization for urban climate simulationspart i. formulation, verification, and sensitivity analysis of the model. Theoretical and applied climatology 99 (3-4), 331–344.

Salmond, J. A., McKendry, I., 2009. Influences of meteorology on air pollution concentrations and processes in urban areas. Air Quality in Urban Environments 28, 23.

Sanchez, B., Santiago, J. L., Martilli, A., Martin, F., Borge, R., Quaassdorff, C., de la Paz, D., 2017. Modelling nox concentrations through cfd-rans in an urban hot-spot using high resolution traffic emissions and meteorology from a mesoscale model. Atmospheric Environment 163, 155–165.

Sanchez, B., Santiago, J.-L., Martilli, A., Palacios, M., Kirchner, F., 2016. Cfd modeling of reactive pollutant dispersion in simplified urban configurations with different chemical mechanisms. Atmospheric Chemistry and Physics 16 (18), 12143–12157.
URL http://www.atmos-chem-phys.net/16/12143/2016/

Santiago, J., Borge, R., Martin, F., de la Paz, D., Martilli, A., Lumbreras, J., Sanchez, B., 2017a. Evaluation of a cfd-based approach to estimate pollutant distribution within a real urban canopy by means of passive samplers. Science of The Total Environment 576, 46–58.

Santiago, J., Dejoan, A., Martilli, A., Martin, F., Pinelli, A., 2010. Comparison between large-eddy simulation and reynolds-averaged navier–stokes computations for the must field experiment. part i: study of the flow for an incident wind directed perpendicularly to the front array of containers. Boundary-layer meteorology 135 (1), 109–132.

Santiago, J., Martilli, A., 2010. A dynamic urban canopy parameterization for mesoscale models based on computational fluid dynamics reynolds-averaged navier–stokes microscale simulations. Boundary-layer meteorology 137 (3), 417–439.

Santiago, J., Martín, F., 2008. Slp-2d: A new lagrangian particle model to simulate pollutant dispersion in street canyons. Atmospheric Environment 42 (17), 3927–3936.

Santiago, J.-L., Martilli, A., Martin, F., 2017b. On dry deposition modelling of atmospheric pollutants on vegetation at the microscale: Application to the impact of street vegetation on air quality. Boundary-Layer Meteorology 162 (3), 451–474.

Santiago, J. L., Martin, F., 2005. Modelling the air flow in symmetric and asymmetric street canyons. International journal of environment and pollution 25 (1-4), 145–154.

Santiago, J. L., Martín, F., Martilli, A., 2013. A computational fluid dynamic modelling approach to assess the representativeness of urban monitoring stations. Science of the total environment 454, 61–72.

Santiago, J.-L., Rivas, E., Sanchez, B., Buccolieri, R., Martin, F., 2017c. The impact of planting trees on nox concentrations: The case of the plaza de la cruz neighborhood in pamplona (spain). Atmosphere 8 (7), 131.

Sanz, C., 2003. A note on k-ε modelling of vegetation canopy air-flows. Boundary-Layer Meteorology 108 (1), 191–197.

Saunders, S. M., Jenkin, M. E., Derwent, R., Pilling, M., 2003. Protocol for the development of the master chemical mechanism, mcm v3 (part a): tropospheric degradation of non-aromatic volatile organic compounds. Atmospheric Chemistry and Physics 3 (1), 161–180.

Seinfeld, J. H., Pandis, S. N., 1998. Atmospheric chemistry and physics: from air pollution to climate change. John Wiley & Sons.

Shih, T.-H., Liou, W. W., Shabbir, A., Yang, Z., Zhu, J., 1995. A new k- eddy viscosity model for high reynolds number turbulent flows. Computers & Fluids 24 (3), 227–238.

Sini, J.-F., Anquetin, S., Mestayer, P. G., 1996. Pollutant dispersion and thermal effects in urban street canyons. Atmospheric environment 30 (15), 2659–2677.

Smit, R., Smokers, R., Rabé, E., 2007. A new modelling approach for road traffic emissions: Versit+. Transportation Research Part D: Transport and Environment 12 (6), 414–422.

Solazzo, E., Cai, X., Vardoulakis, S., 2008. Modelling wind flow and vehicle-induced turbulence in urban streets. Atmospheric Environment 42 (20), 4918–4931.

Solazzo, E., Vardoulakis, S., Cai, X., 2011. A novel methodology for interpreting air quality measurements from urban streets using cfd modelling. Atmospheric environment 45 (29), 5230–5239.

Stewart, I. D., Oke, T. R., 2012. Local climate zones for urban temperature studies. Bulletin of the American Meteorological Society 93 (12), 1879–1900.

Stockwell, W. R., Calvert, J. G., 1983. The mechanism of no3 and hono formation in the nighttime chemistry of the urban atmosphere. Journal of Geophysical Research: Oceans 88 (C11), 6673–6682.

Stockwell, W. R., Kirchner, F., Kuhn, M., Seefeld, S., 1997. A new mechanism for regional atmospheric chemistry modeling. Journal of geophysical research: Atmospheres 102 (D22), 25847–25879.

Stull, R. B., 2012. An introduction to boundary layer meteorology. Vol. 13. Springer Science & Business Media.

Tominaga, Y., Stathopoulos, T., 2007. Turbulent schmidt numbers for cfd analysis with various types of flowfield. Atmospheric Environment 41 (37), 8091–8099.

Tominaga, Y., Stathopoulos, T., 2010. Numerical simulation of dispersion around an isolated cubic building: model evaluation of rans and les. Building and Environment 45 (10), 2231–2239.

UNION, P., et al., 2008. Directive 2008/50/ec of the european parliament and of the council of 21 may 2008 on ambient air quality and cleaner air for europe. Official Journal of the European Union.

Vardoulakis, S., Fisher, B. E., Pericleous, K., Gonzalez-Flesca, N., 2003. Modelling air quality in street canyons: a review. Atmospheric environment 37 (2), 155–182.

Vardoulakis, S., Gonzalez-Flesca, N., Fisher, B., 2002. Assessment of traffic-related air pollution in two street canyons in paris: implications for exposure studies. Atmospheric Environment 36 (6), 1025–1039.

Vardoulakis, S., Gonzalez-Flesca, N., Fisher, B. E., Pericleous, K., 2005. Spatial variability of air pollution in the vicinity of a permanent monitoring station in central paris. Atmospheric Environment 39 (15), 2725–2736.

Versteeg, H. K., Malalasekera, W., 2007. An introduction to computational fluid dynamics: the finite volume method. Pearson Education.

Vilà-Guerau de Arellano, J., Dosio, A., Vinuesa, J.-F., Holtslag, A. A., Galmarini, S., 2004. The dispersion of chemically reactive species in the atmospheric boundary layer. Meteorology and Atmospheric Physics 87 (1-3), 23–38.

Vos, P. E., Maiheu, B., Vankerkom, J., Janssen, S., 2013. Improving local air quality in cities: to tree or not to tree? Environmental pollution 183, 113–122.

Vranckx, S., Vos, P., Maiheu, B., Janssen, S., 2015. Impact of trees on pollutant dispersion in street canyons: A numerical study of the annual average effects in antwerp, belgium. Science of the Total Environment 532, 474–483.

Zhai, Z. J., Chen, Q. Y., 2005. Performance of coupled building energy and cfd simulations. Energy and buildings 37 (4), 333–344.

Zhong, J., Cai, X.-M., Bloss, W. J., 2015. Modelling the dispersion and transport of reactive pollutants in a deep urban street canyon: Using large-eddy simulation. Environmental pollution 200, 42–52.

Zhong, J., Cai, X.-M., Bloss, W. J., 2016. Coupling dynamics and chemistry in the air pollution modelling of street canyons: a review. Environmental Pollution 214, 690–704.